UNIVERSITY OF SOUTHAMPTON

Powering Performance of a Self Propelled Ship in Waves

by

Björn Windén

Thesis for the degree of

Doctor of Philosophy

at the Faculty of Engineering and the Environment

June 2014

Powering Performance of a Self Propelled Ship in Waves
Ph.D. thesis

Fluid Structure Interactions Group,
Faculty of Engineering and the Environment,
University of Southampton,
Southampton,
SO17 1BJ,
United Kingdom.

Declaration of Authorship

I, Björn Windén, declare that the thesis entitled 'Powering Performance of a Self Propelled Ship in Waves' and the work presented in the thesis are both my own, and have been generated by me as the result of my own original research. I confirm that:

- this work was done wholly or mainly while in candidature for a research degree at this University;
- where any part of this thesis has previously been submitted for a degree or any other qualification at this University or any other institution, this has been clearly stated;
- where I have consulted the published work of others, this is always clearly attributed;
- where I have quoted from the work of others, the source is always given. With the exception of such quotations, this thesis is entirely my own work;
- I have acknowledged all main sources of help;
- where the thesis is based on work done by myself jointly with others, I have made clear exactly what was done by others and what I have contributed myself;
- parts of this work have been published as: (Windén et al., 2012),(Windén, Turnock and Hudson, 2013*b*),Windén, Turnock and Hudson (2013*a*) and Windén et al. (2014*a*).

Signed: .....

Date: .....

UNIVERSITY OF SOUTHAMPTON

ABSTRACT

FACULTY OF ENGINEERING AND THE ENVIRONMENT
Fluid Structure Interactions Group

Doctor of Philosophy

POWERING PERFORMANCE OF A SELF PROPELLED SHIP IN WAVES

by Björn Windén

The ability to accurately predict the powering performance of a ship when travelling in waves is of high importance for the design of new ships. Almost a century of experience exists regarding how to predict the mean resistance increase in waves compared to calm water. Despite this, improvements in numerical models are still in high demand. Traditionally, the mean increase together with the calm water resistance and propeller open water curves are used to determine the powering performance. This thesis argues that, to achieve better predictions, a more holistic approach can be taken. A RANS based numerical approach to predicting the performance of a self propelled ship in waves is presented. The model is supported by a review of previous literature as well as new experiments to determine what phenomena need to be modelled. It is concluded that the surge force amplitude in waves is something that is not well studied but that has an impact on the propeller performance. The experiments show that this is likely to be harder to predict than the mean increase. Furthermore, the inclusion of RPM control in the model is seen as important to make it better suited for predicting the performance.

In developing the numerical model, it is shown that the amplitude and phase of the viscous surge force are affected to some extent by the way the RANS equations are solved numerically. Recommendations on the choice of schemes are given based on several comparative studies where a limited TVD scheme is found to give the best representation of the flow. Furthermore, detailed analysis on how the boundary layer is affected by the passing waves is presented.

A framework for coupling the RANS solver with a simplified propeller model is presented. This is a powerful tool that allows for a broad range of present and future studies regarding propeller modelling and RPM control for self propelled simulations in waves. The implementation of Blade Element Momentum theory in the framework is outlined and a correction able to achieve a satisfactory run time coupling in terms of identifying the propeller induced velocities from the total wake is presented. The coupled solver is found to be a computationally efficient tool for studying ship performance in waves. It is applied to study the propulsive performance of the KCS in unsteady inflow conditions. Reasonable agreement with experiments is found both for resistance and for propeller performance. Overall, the findings and methods presented here represent a contribution towards better predictions of the performance of self propelled ships in waves.

Contents

List of Figures

List of Tables

Nomenclature

A **bold** symbol denotes a vector or matrix quantity. This is used in most places although for describing the RANS equations, Einstein notation is used as it is more convenient. This list presents unique symbols as well as base symbols. Variations of the base symbols can be obtained by adding the common subscripts mentioned below. Further variations are also possible and where other subscripts are used, their meaning is explained in the text.

Abbreviations and acronyms

2D	Two Dimensional
3D	Three Dimensional
AMG	Algebraic Multi-Grid
AMI	Arbitrary Mesh Interface
BEM	Boundary Element Method
BEMt	Blade Element Momentum theory
CFD	Computational Fluid Dynamics
CPU	Central Processing Unit
C++	C programming language with classes
DES	Detached Eddy Simulation
DNS	Direct Numerical Simulation
DOF	Degree(s) Of Freedom
EEDI	Energy Efficiency Design Index
EFD	Experimental Fluid Dynamics
FV	Finite Volume (method)
ID	Identity
IMO	International Maritime Organization
ITTC	International Towing Tank Conference
JONSWAP	JOint North Sea WAve observation Project
KCS	Korean Container Ship
KVLCC2	Korean Very Large Crude Carrier, version 2
LCG	Longitudinal Centre of Gravity

LES	Large Eddy Simulation
LOA	Length Over All
M	Millions
MARG	Magnetic, Angular Rate and Gravity
MULES	Multidimensional Universal Limiter with Explicit Solution
MUSCL	Monotonic Upstream-Centred Scheme of Conservation Laws
NS	Navier-Stokes
OpenFOAM	Open source Field Operation And Manipulation
PID	Proportional-Integral-Derivative controller
PISO	Pressure Implicit Splitting of Operators
PMM	Planar Motion Mechanism
RANS(E)	Reynolds Averaged Navier-Stokes (Equations)
R&D	Research and Development
RMS	Root Mean Square
RPM	Rotations Per Minute
SIMPLE	Semi-Implicit Method for Pressure Linked Equations
SPH	Smooth Particle Hydrodynamics
SST	Shear Stress Transport
TCG	Transverse Centre of Gravity
TVD	Total Variation Diminishing
UK	United Kingdom
URANS(E)	Unsteady Reynolds Averaged Navier-Stokes (Equations)
VCG	Vertical Centre of Gravity
VLCC	Very Large Crude Carrier
VOF	Volume Of Fluid (method)
V&V	Verification and Validation
QUICK	Quadratic Upstream Interpolation for Convective Kinematics

Non dimensional representations

C_b	Block coefficient	∇/LBT
C_D	Drag coefficient	$D/\frac{1}{2}U^2c$
C_L	Lift coefficient	$L/\frac{1}{2}U^2c$
Fn	Froude number	$U/\sqrt{gL}$
F''_x	Non dimensional mean surge force	$\overline{F_x}/k\zeta_0\rho g\nabla$
F''_{xa}	Non dimensional surge force amplitude	$F_{xa}/k\zeta_0\rho g\nabla$
F''_{ya}	Non dimensional heave force amplitude	$F_{ya}/\zeta_0 C_{33}$
J	Propeller advance ratio	U/nD
K_T	Coefficient of Thrust	$\frac{T}{\rho n^2(2R)^4}$
K_Q	Coefficient of Torque	$\frac{Q}{\rho n^2(2R)^5}$

M''_{za}	Non dimensional pitch moment amplitude	$M_{za}/k\zeta_0 C_{55}$
Re	Reynolds number	UL/ν
r_s	Non dimensional propeller local radius (hub corrected)	$\frac{r-r_H}{(R-r_H)}$
t'	Non dimensional time	$t\sqrt{g/Lpp}$
x	Non dimensional propeller local radius	r/R
y^+	Non dimensional wall distance	yu_τ/ν
γ	Drag/Lift ratio	C_D/C_L
ω'_i	Non dimensional natural frequency	$\omega_i\sqrt{Lpp/g}$
σ_{AW}	Coefficient of added resistance	$\frac{R_{AW}Lpp}{\rho g\zeta_0^2 B^2}$
τ_e	Non dimensional period of encounter	$T_e\sqrt{Lpp/g}$

Operators

Δ	Difference in
∇	Gradient
$\nabla\cdot$	Divergence
δ_{ij}	Kroenecker delta
^{T}	Transpose
$\dot{()}$	Time derivative
$\cdot$	Scalar product
$\sim$	Proportional to

Symbols

Symbol	Description	SI unit
A	Face area in FV method	[m^2]
$\overline{A}$	Relative vertical velocity related to heave damping	[m/s]
A_M	Midship sectional area	[m^2]
B	Beam or breadth	[m]
B_r	Precision error	[various]
C	Courant number	[-]
	Stiffness in 6 DOF	[various]
$CD_{k\omega}$	Coefficient in $k-\omega$ SST model	[-]
C_{Hs}	Factor in estimated R_{AW} spectrum Eqn. 3.12	[-]
C_α	Interface Courant number	[-]
D	Propeller diameter	[m]
	Drag force	[N]
	Depth	[m]
	Components of added resistance	[-]

$\mathbf{D}$	Rate of strain	[1/s]
E	Constant in wall function	[-]
$\mathbf{F}$	Total force on hull	[N]
$F_{k\omega}$	Blending function in $k-\omega$ SST model	[-]
$\mathbf{F}_v/F_v$	Volume force (vector/tensor notation)	[N/m^3]
H	Freeboard	[m]
H_s	Significant wave height	[m]
I	Moment of inertia	[kg m^2]
K	Goldstein correction factor	[-]
	Coefficiant in PID regulator	[-]
L	Length (general)	[m]
	Lift force	[N]
Lpp	Length between perpendiculars	[m]
$\mathbf{M}$	Total moment on hull	[Nm]
N_r	Number of repeated tests in uncertainty analysis	[-]
$\mathbf{PN}$	Vector between two adjacent cell centres	[m]
$\mathbf{O}$	Orientation vector	[-]
P	Propeller pitch	[m]
$\mathbf{P}$	Hull displacement vector = $(x_1\ x_2\ x_3)$	[m]
P_k	Coefficient in $k-\omega$ SST model	[-]
P_r	Systematic error	[various]
Q	Torque	[Nm]
$\mathbf{Q}$	Hull rotation tensor	[-]
R	Propeller tip radius	[m]
	Total resistance in waves	[N]
R_{AW}	Mean resistance increase in waves	[N]
R_{CW}	Resistance in calm water	[N]
$\mathbf{R}$	local position relative to propeller disk	[m]
S_r	Standard deviation	[various]
S_ζ	Spectral ordinate	[m]
$S_{J\zeta}$	JONSWAP spectral ordinate	[m]
T	Thrust	[N]
	Draught	[m]
	Period	[s]
U	Speed (general)	[m/s]
U_{foil}	Blade element inflow velocity	[m/s]
$U_{\overline{r}}$	Total uncertainty	[various]
U_s	Service speed	[m/s]
U_∞	Free stream velocity	[m/s]
W	Mechanical Work	[J]
Z	Number of blades	[-]

a	Axial inflow factor	[-]
$a_{k\omega}$	Coefficient in $k-\omega$ SST model	[-]
a'	Tangential inflow factor	[-]
a_W	Defines the shape of the Wigley hull	[-]
c	Foil/blade chord	[m]
	Constant in limitedLinear TVD scheme	[-]
c_α	Interface compression coefficient	[-]
d_d	Thickness of propeller disk	[m]
$\mathbf{d}$	Position relative to propeller disk	[m]
f	Shape function	[-]
$\mathbf{f}$	Local force on surface	[N]
g	Gravitational acceleration $g = 9.81$	[m/s^2]
h_s	Distance from keel to pivot point when tuning k_{zz}	[m]
k	Wave number	[1/m]
	Radius of gyration	[m]
	Turbulence kinetic energy	[m^2/s^2]
n	Rate of rotation	[1/s]
$\mathbf{n}$	Face (unit) normal	[-]
$n_{R,C,A}$	No. of sectors (rad.,circ.,axial) in the concentric mesh	[-]
o	Flare overhang and curvature factors	[-]
p	Pressure	[N/m^2]
r	Propeller local radius	[m]
r_H	Propeller hub radius	[m]
$\mathbf{r}$	Local position relative to $\mathbf{x}_p$	[m]
$\mathbf{r}_r$	Local position relative to centre of rotation	[m]
$\mathbf{r}_v$	Propeller vertical direction	[-]
t	Thrust deduction factor	[-]
	Time	[s]
u_τ	Friction velocity	[m/s]
$\mathbf{u}/u$	Local velocity in FV method (vector/tensor notation)	[m/s]
w_T	Wake fraction	[-]
x	Long. dist. from origin (ship fixed coord. system)	[m]
	Displacements in 6 DOF for the ship	[various]
x_ϕ	Position where bow flare starts	[m]
$\mathbf{x}$	Location vector $\mathbf{x} = (x, y, z)$	[m]
y	Vertical dist. from origin (ship fixed coord. system)	[m]
	Wall distance	[m]
z	Transverse dist. from origin (ship fixed coord. system)	[m]
∇	Displaced volume	[m^3]
Δ	Displaced mass	[kg]
Φ	Transport variable	[various]

Ψ	Sweby limiter	[-]
Ψ_{lin}	BEMt inflow correction factor	[-]
Ψ_{triq}	BEMt inflow correction factor	[-]
Ω	Propeller angular frequency	[rad/s]
α	Volume fraction in VOF method	[-]
	Scale factor, model $\rightarrow$ ship	[-]
	Angle of attack	[rad]
α_i	Sharpness function for α	[-]
α_r	Inflow relaxation factor	[-]
β	Coefficient in $k-\omega$ SST model	[-]
β_i	Angle of incidence of waves	[rad]
γ	Coefficient in $k-\omega$ SST model	[-]
	Peak enhancement factor in JONSWAP spectrum	[-]
δ	Boundary layer thickness	[m]
δ^*	Boundary layer displacement thickness	[m]
ε_c	Control error	[1/s]
ε	Denotes a phase shift of the relevant variable	[rad]
ζ	Free surface elevation	[m]
η	Efficiency	[-]
	Damping coefficient	[-]
	Exponantial rate of decay/increase	[-]
θ	Momentum thickness of boundary layer	[m]
	Angle of sector in BEMt	[rad]
κ	Constant in wall function	[-]
λ	Wave length	[m]
μ	Dynamic viscosity	[kg/(s m)]
ν	Kinematic viscosity	[m^2/s]
ξ	Dimensionless longitudinal position along the hull	[-]
ρ	Density	[kg/m^3]
σ	Coefficient in $k-\omega$ SST model	[-]
τ	Stress tensor	[m^2/s^2]
ϕ	Total velocity potential	[m^2/s]
	Face flux in FV method	[various]
	Induced flow angle	[rad]
ψ	Flow angle	[rad]
ω	Angular frequency	[rad/s]
	Specific dissipation rate	[1/s]

Common subscripts

0	Amplitude of variation (force, motion, thickness etc.) **or** initial state
1–6	Component in 6 DOF 1: Surge 2: Sway 3: Heave 4: Roll 5: Pitch 6: Yaw
7	Diffraction component
G	Global coordinate system
I	Relating to cell No. I
K	Thrust
Q	Torque
a	Amplitude of variation (force, motion, thickness etc.)
b	of basin. Measurement of numerical towing tank
e	of encounter
m	Property of model scale object
p	Pressure component of forces **or** Propeller
ij	Einstein tensor notation
x	Component along (or rotating around) $x - axis$ (surge/roll)
y	Component along (or rotating around) $y - axis$ (heave/yaw)
z	Component along (or rotating around) $z - axis$ (sway/pitch)
μ	Viscous component of forces

Acknowledgements

During the three and a half years I spent at the University of Southampton I have had many opportunities to be grateful for the help and support of others.

Firstly I would like to thank my supervisors Dominic Hudson and Stephen Turnock for allowing me the opportunity to embark on this once in a lifetime adventure that is the Ph.D. I also owe them great thanks for all of their guidance, encouragement and support along the way. Thanks also go to the Lloyd's Register Foundation (previously Lloyd's Register Educational Trust) for providing the funding.

Furthermore, I would like to thank all my colleagues at the Fluid Structure Interactions Group and others who worked around me in Building 28 for creating such a socially vibrant and friendly atmosphere. I particularly enjoyed being lured away from my desk every Friday for some relaxing end of week beers. The list of people to thank can be made long but I would like to mention my office mates Aichun and Tom who started on the same day as me. We have been through a lot together.

I would also like to thank the people of the OpenFOAM community, at the university but also elsewhere. The contact with others doing similar things has benefited me on so many levels, from my first months when I knew nothing of using CFD software to my final months when discussions with my colleagues really deepened my understanding of the tools I was using.

To my parents and grandparents I owe my curiosity, my determination and my creativity. Without them I wouldn't have been able to choose such a challenging but also rewarding occupation.

Finally, I would like to thank my constant companion and best friend. My beautiful Mirjam. She agreed to stay in this foreign land when I was offered to start my studies and has been supporting me in every step of the way.

I dedicate this thesis to my parents and grandparents

Chapter 1

Introduction

The fate of ships and their crew subjected to the natural element of the open sea has been seen as being guided by chance and mysterious circumstances throughout history. This has given rise to countless legends and given seafarers status as daredevils. The benefits of transporting goods at sea have always motivated merchants and ship owners to defy the many dangers and the merchant fleet has been ever expanding. The introduction of classification societies was the first step to regulate operations at sea, in this case it was motivated by the economic interests of the owners of both ship and cargo. The Titanic disaster in 1912 sparked further concern about the safety of the crew and passengers on board. Finally, the cost of heavy oil and the necessity of speed in global trade have lead to many investigations into ship resistance and propulsion. This has been given more focus in recent years with the realisation of the effects of fossil fuel emissions as well as rising oil prices and an uncertainty of the future of combustion engines. As a result, the IMO has introduced the Energy Efficiency Design Index (EEDI) as a mandatory design constraint for new ships from 2013 (IMO, 2011).

One way to reduce the fuel consumption is to reduce the speed. So called "slow steaming" gained popularity with the recent recession and rise in fuel price. The popularity of slow steaming was largely made possible by an abundance of ships being available at low prices to maintain transporting capacity even at slower speeds (Carson, 2012). However, in a more aggressive market, this option will be less attractive. Because of this, there is great interest for novel ways to increase powering performance without negatively impacting other design factors and to accurately predict the powering performance of new designs.

Historically, two main approaches have been taken when it comes to predicting the powering performance of a given ship when it is subjected to offshore conditions. The first is to gather data from similar ships and trades and from a statistical database give predictions based on experience. The other is to scientifically explain and model the phenomena involved. Shipyards and designers have shown a tendency to rely on previously successful concepts both because it means less operational changes at the

yard but also since relying on such experience has been shown to work successfully. If one looks back at the many risks associated with shipping mentioned before, ship owners and -builders cannot be blamed for using methods that are proven to be safe and reliable. Therefore, methods of predicting performance in waves have to be reliable and ships being built solely based on such methods also have to be shown to be able to operate safely for decades. At the moment, no single method exists that can produce estimates that are proven reliable for any sea state and that can be used with confidence to govern the overall design of the hull.

1.1 Aims and objectives

The overall purpose of this work is to contribute to the improvement of ship design for better powering performance. To achieve this, the aim is to present a method able to model the powering requirement for a specific vessel in waves. Several options are discussed and their strengths and weaknesses are highlighted. Based on these discussions a number of objectives are identified regarding the capabilities of the model. The model should:

- capture the effect of waves on the flow around the hull, the boundary layer in particular.
- capture the effect of the waves and motions on the propeller performance.
- be designed with a modular approach to allow for modifications of specific parts by others in order to facilitate a broader range of future studies.
- include the ability to control the RPM.

1.2 Performance of ships in waves

When it comes to predicting the performance of a ship in a seaway, several questions have to be answered. Firstly, what is the purpose of the estimate and what is meant with “performance”? The answers can include:

- Prediction of fuel consumption to confirm economical forecasts or to estimate the emissions for the purpose of confirming compliance with standards.
- Prediction of the speed loss for a certain installed power for the purpose of confirming route timetables etc.
- Prediction of the loads on the hull, propeller and machinery etc. to estimate maintenance costs.

Each of these purposes require a holistic view of the system that is the ship travelling in waves. The factors, sequence of events and phenomena that describe the performance, in most aspects, of a ship in waves can be seen in Figure 1.1, and was drawn up by Nakamura and Naito (1981). The dashed connectors in Figure 1.1 are an addition to the original schematic representing the fact that the performance of the propeller is not only dependent on the ships speed but also its motions and the motions of the surrounding waves. Here t is the thrust deduction and w_T is the wake fraction. η_t and η_r are the efficiency of the transmission between engine and propeller and the relative rotational efficiency respectively.

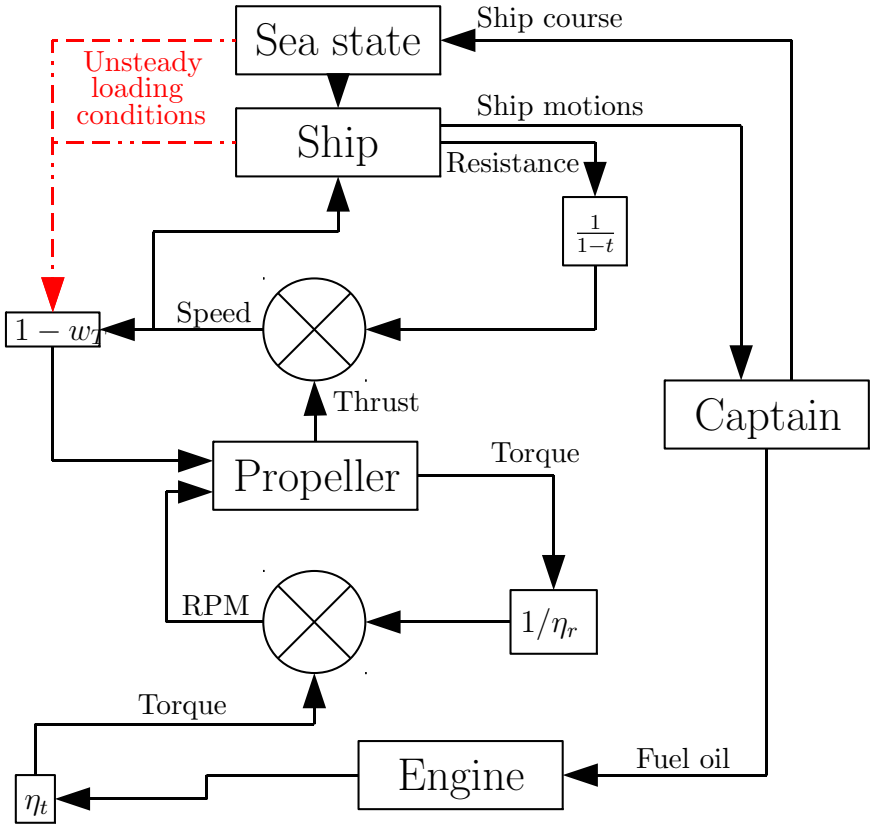

FIGURE 1.1: Schematic of interaction between different aspects of ship performance in waves (Nakamura and Naito, 1981).

Because every ship, every captain and every sea state is unique; no detailed general method to account for all of these factors can be created. The second question is therefore: what will be the focus of the prediction? For example: if the motivation is reducing fuel consumption, the focus could be on the efficiency of the engine itself, changing the behaviour of the captain through e.g. weather routing or design the ship such that resistance and/or motions are reduced. The selection should fall on the approach that is best fit for answering the first question using available resources. This thesis focuses on the hydrodynamics aspect of the problem, i.e. the interaction of the ship with the surrounding environment.

In the design spiral of a ship, performance in waves is only one of many aspects that have to be considered. Often, the driving factors for the design include safety, cargo capacity, still water performance, cargo handling etc. (Watson, 1998). A third question therefore has to be asked. Will the prediction serve to give a specific hull better performance in waves, will it be used to design a new type of hull or will it be used to compare a set of different hulls already designed based on other factors? If the answer is the latter, a crude estimate will suffice since it will quickly give an answer as to which hull is likely to perform better. If any form of new design or design improvement is to be achieved however, detailed understanding of how design changes affect all the involved phenomena is needed.

1.3 How is performance in waves best predicted?

The word prediction indicates that information about the behaviour of something is needed before it exists or when access to vital information about its state is unavailable. Hence a model is needed. To model a system as complicated as a ship travelling through a seaway it is important to outline what components need modelling before specific techniques are chosen.

Because the ideal solution would be to incorporate Figure 1.1 in its entirety in the prediction, a model allowing for as many interlinks as possible is preferable. Historically; the link between the advancing ship, the surrounding environment and the resulting powering requirement has been the most approached aspect of this problem since it is the most tangible cause of decreased performance in waves. Because of this, most of the more established methods for predicting performance in waves focus solely on this aspect. Much attention has also been given to the performance of the propeller in unsteady loading conditions. A combination of these is currently seen as the most appropriate way of assessing performance in waves (Prpić-Oršić and Faltinsen, 2012).

As was pointed out in Section 1.2, any method for predicting performance in waves should ultimately be able to deliver a prediction that fulfils its purpose. From a hydrodynamics point of view, understanding the flow around the hull and how that affects the induced forces as well as the efficiency of the propeller will give a good answer to any question posed about “performance of a ship in waves”. A diagram showing how the hydrodynamic core of ship performance relates to the different purposes for prediction is shown in Figure 1.2.

From a prediction point of view, the system in Figure 1.2 is preferable over the one in Figure 1.1 since it is focused on one problem. The problem of determining how the solid ship interacts with its fluid surroundings. It is henceforth referred to as the external system and is the focus of this thesis. The components of this system are more homogeneous in what physical phenomena they represent than the components of Figure

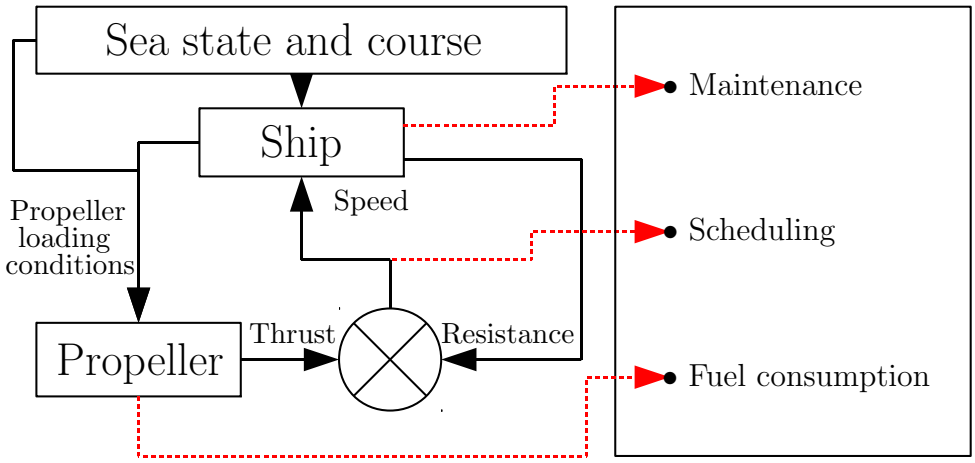

FIGURE 1.2: Hydrodynamics related to performance in waves.

1.1. This means that fewer levels of abstraction are needed to create links between the components since, for example: flow around the propeller, in the waves, and around the hull can all fall under the same modelling scope. In contrast a more empirical link is likely to be needed between for example, the hydrodynamic torque on the propeller and the fuel consumption.

A model of a system that requires only representation of mechanical and fluid motion can thus be made less uncertain than one that also requires human factors, engine physics and chemical reactions to be considered simultaneously. Such factors and any other aspects can be separated into another system representing internal factors, henceforth referred to as the internal system. The internal system influences the external system in only two ways; the ships course and the propeller RPM.

In the internal system, both the ships course and the RPM are affected indirectly by the state of the external system. Weather routing software or a captain's judgement may alter the course to avoid a certain seastate. Equally, the throttle may be changed to meet the requirements of, or to avoid a certain seastate which changes the propeller RPM. However, neither of these causes and actions are linked to the momentary state of the external system but rather to long term forecasting and planning. It is thus possible to simplify the model by separating the behaviour of the external system for a given course and sea state and the long term behaviour of the internal system in controlling which sea states to encounter.

In doing so, the external system is separate from the internal system in terms of the ships course. However, the propeller RPM is directly linked to the engine RPM (which is part of the internal system) which in turn is influenced directly by variations of hydrodynamic torque in the external system. There is therefore a momentary link between the internal and the external systems in terms of the propeller RPM. Therefore, separating them

as described above by giving a fixed RPM for a given sea state would mean more of a simplification than assuming a fixed course.

In modern ships, both the reaction to weather in terms of rudder angle and throttle as well as the reaction of the engine to torque changes are governed, to a large extent, by automatic control systems. By the above reasoning, the control system for the Engine should be taken into consideration in some way when generating an input RPM to the external system rather than giving a fixed value. Naturally, the same logic applies if focussing on the internal system. On the other hand the course could be considered fixed without too much loss of validity if this makes a working model more attainable.

This leaves the task of choosing a method to model the external system.

1.4 Modelling a ship travelling through waves

There are several options for modelling the external system for a specific ship, all have their benefits and their drawbacks.

- Construct a self propelled scale model of the ship and measure its performance experimentally in a controlled environment (towing tank.)
- Create mathematical models for the components of the system as well as the links between them.
- Gather full scale data from similar ships, use it to identify trends and from that, construct empirical relations.
- Create a model from a mixture of sources, e.g. a towing tank model but with propeller performance calculated separately using mathematical modelling or an empirical formulation.

If the target is to be as close to modelling the full system as possible, the first two approaches are preferable since they have the potential to model the entire momentary state of the system. They can thus identify any coupling effects between components that would not be taken into account if a more piecemeal approach is adopted. However, the last two approaches also hold much value in validating results and in gradually building insight into the interplay between the components of the system.

As a component in the overall design spiral of a ship, the numerical approach is more attractive since the design can be easily changed and adapted through multiple iterations of the spiral. Because of this, numerical simulation methods are used to a large extent for a variety of tasks in the shipbuilding process (Sharma et al., 2012). Furthermore, a ship design process based on numerical simulation allows for better optimisation towards

given constraints by the owner, operator and builder (Sharma et al., 2012). An experimental hydrodynamic model test is expensive and time consuming and the design can not be easily changed on demand if more iterations are needed. However, as discussed before, the numerical method must be considered reliable enough to govern the design which is one of the reasons why experimental methods are also used to a large extent in ship design. Experimental methods also remain vital for validation in the development of numerical methods.

Even though there is room for innovation in experimental methods, there is more potential for development of numerical methods. If these can be made reliable enough tools to govern the design process to a larger extent, it would provide a crucial benefit for the ship building industry in terms of improving the performance of ships in waves.

1.5 Numerical modelling

Studies focusing on pure hull/wave interaction alone using potential flow such as ones by Havelock (1942), Maruo (1957), Gerritsma and Beukelman (1972) and Faltinsen et al. (1980) have given much insight into, and means to model the hydrodynamical phenomena involved as well as the coupling effects between these. This is important since coupling between phenomena gives a significant contribution to the forces on the hull (see Maruo (1957).) Historically, the mean increase of the surge force on the hull due to waves, commonly referred to as "added resistance in waves" (R_{AW}) has been the main focus of research.

The approach of modelling added resistance with potential flow and using this prediction as a basis for predicting the powering requirement has a weakness. It cannot model individual phenomena and the links between them with enough accuracy meaning that the model becomes crude. For example, for all of the general methods that use potential flow; linearisations of the hull form, the free surface, the velocity potential itself etc. are needed to make the problem mathematically approachable. Furthermore by using potential flow, viscous and non linear effects such as wave breaking and boundary layer distortion cannot be captured. As an example of how this can have implications for ship design, the flow around the bow (and thus the shape of the bow area) has been shown to be influential for the characteristics of the boundary layer further aft (Landweber and Patel, 1979). This will affect both the propeller performance and the viscous drag of the vessel.

If detailed flow features cannot be accurately described, the linking between ship and propeller performance will also be weak. This will mean that the method will not be good enough to answer the question in the holistic way that is shown in Figure 1.2. The alternative to using potential flow is to solve the full Navier-Stokes Equations with inclusion of viscosity. This is commonly done for hydrodynamics problems using

Reynolds Averaged Navier-Stokes equations (RANS), Large Eddy Simulation (LES) or similar Navier-Stokes (NS) based methods (Molland et al., 2011, p 166-187). By doing so the entirety of Figure 1.2 could be incorporated. This however, means spending much more time and effort on setting up the model which is something that can rarely be afforded in early stages of ship design.

The choice is thus apparent. If a quick decision is needed regarding which one of a set of hulls will have the lowest added resistance in waves, the best choice is a potential flow based method since it will be accurate enough to detect differences between different hulls while not taking up any time or resources. If on the other hand a tool is needed to motivate design changes on a specific hull to achieve a lower powering requirement, a higher order methods such as RANS or LES are currently the only tools that will allow a motivation based on the holistic approach shown in Figure 1.2.

1.6 Propeller control

Using a model that allows for variations in RPM not only provides a benefit in terms of the model accuracy. It also opens the door for studies on how variations in the RPM can be used to improve performance in waves. Varying the pitch of controllable pitch propellers to suit the current operation conditions is a common way to achieve better performance across a wider range of RPM (Carlton, 2007, p 20-22). They can also be controlled more actively to give a better response to variations in inflow velocity due to surge motions and orbital velocities in waves (Ueno et al., 2013). Similar improvements could be achieved by changing the RPM. However, changes in RPM are heavily restricted by the operation of marine diesels and, for regular waves it is unlikely that the RPM could be changed fast enough to maintain optimal performance (Windén, Turnock and Hudson, 2013*a*). Nevertheless, slower variations of RPM to improve performance in an irregular seaway is a possibly novel way to achieve reduced fuel consumption. This is especially true if one considers the future of ship propulsion which is likely to include electrical motors which can better meet the EEDI requirements of future ships(Bazari and Longva, 2011). Electric motors are able to change RPM much faster than what is currently possible with marine diesels and so RPM control is likely to be an alternative to variable pitch propellers in the future. The accurate modelling of a self propelled ship with the inclusion of a control function for the RPM is of high importance if the feasibility of such systems is to be investigated.

1.7 Novel contributions

The novel contributions presented in this thesis are listed below

- The characteristics of the surge force amplitude is something which, while often mentioned is not widely studied or discussed. This thesis provides results and discussion regarding this amplitude and its relation to the wave amplitude, period of encounter, forward speed etc. This is relevant to the field of self propulsion in waves since the surge force amplitude will translate to a surge motion which is influential in the propeller performance.

- In defining the set up of the numerical towing tank some novel findings are presented. It has been shown how the wave amplitude as well as the amplitude and phase of the viscous surge force are affected by the choice of convection scheme and how these together lead to variations in the amplitude and phase of the surge force on a surface piercing object. Furthermore, it is shown how variations in the boundary layer thickness follows the waves as they travel along the length of the hull.

- The presented framework for self propulsion in waves represents a novel contribution to the science of predicting the performance of a ship. It allows for models and model specific parameters to be varied with ease which opens the door for a wider range of further studies than was previously possible. The fact that the framework is implemented in an open source CFD suite with a strong user community further increases its availability for future studies.

- The framework has been applied to study, in detail, the nature of the coupling between the BEMt and the RANS solver. This has lead to the presentation of a correction formula for correcting the discrepancies between the assumptions in both theories.

- It has been shown how different control schemes for the propeller RPM can lead to variations in the powering requirement for a self propelled ship in waves.

A number of papers have also been published, presenting the findings of this thesis to a broader audience. Papers authored by Windén et al. relate directly to the methodology presented in this thesis. Other papers have also been contributed to as a direct result of the studies presented here.

1.7.1 Journal papers

Bennett, S., Brooks, C., Windén, B., Taunton, D., Forrester, A., Turnock, S. and Hudson, D. (2014), 'Measurement of ship Hydroelastic Response using Multiple Wireless Sensor Nodes', *Ocean Engineering* **79**.

Windén, B., Turnock, S. and Hudson, D. (2014*a*), 'A RANS modelling approach for predicting powering performance of ships in waves', *International Journal of Naval Architecture and Ocean Engineering* **6**(2).

Windén, B., Turnock, S. and Hudson, D. (2014*b*), 'CFD Modelling of a Self Propelled Ship Using Body Force Propeller Models: A Framework for Creating Coupled Solvers', *Journal of Marine Science and Technology* (Pending submission).

Windén, B., Turnock, S. and Hudson, D. (2014*c*), 'Influence of waves on the computation of boundary layer development around surface piercing bodies', *Computers & Fluids* (Pending review).

1.7.2 Peer reviewed conference papers

Bennett, S., Windén, B., Brooks, C., Turnock, S., Hudson, D., Forrester, A. and Taunton, D. (2012), A Wireless sensor network for measuring ship responses in abnormal waves, *in* 'Proceedings of 29th Symposium on Naval Hydrodynamics, Gothenburg, Sweden, 26-31 August'.

Windén, B., Turnock, S. and Hudson, D. (2013*a*), A RANS modelling approach for predicting powering performance of ships in waves, *in* '12th International Symposium on Practical Design of Ships and Other Floating Structures (PRADS13), Changwon City, Korea'.

Windén, B., Turnock, S. and Hudson, D. (2013*b*), Predicting powering performance changes for ships in offshore conditions from small design modifications, *in* 'Proceedings of the 23rd International Offshore and Polar Engineering Conference (ISOPE13), June 30th - July 5th, Anchorage, Alaska'.

1.7.3 Other conference papers

Bennett, S., Windén, B., Brooks, C., Turnock, S. and Hudson, D. (2012), High speed video analysis of freak wave-ship model encounters, *in* 'Proceedings of International Conference on Violent Flows, Nantes, France, September 25-27'.

Denchfield, S., Windén, B., Brooks, C., Turnock, S., Hudson, D., Forrester, A. and Taunton, D. (2011), Wireless sensor network for determining boat motions and hydroelastic responses, *in* 'The Second International Conference on Advanced Model Measurement Technology for EU Maritime Industry', pp. 126–139.

Turnock, S., Lewis, S., Philips, A., Banks, J., Windén, B., Hudson, D. and Molland, A. (2010), Evaluating the self-propulsion of a container ship in a seastate using computational fluid dynamics, *in* 'William Froude Conference: Advances in Theoretical and Applied Hydrodynamics - Past and Future', p. 12.

Windén, B., Badoe, C., Turnock, S., Phillips, A. and Hudson, D. (2013), Self propulsion in waves using a coupled RANS-BEMt model and active RPM control, *in* 'Proceedings of the 16th Numerical Towing Tank Symposium, 2-4 September, Duisburg Germany'.

Windén, B., Turnock, S. and Hudson, D. (2012), Validating Force Calculations using OpenFOAM© on a Fixed Wigley Hull in Waves, *in* 'Proceedings of the 15th Numerical Towing Tank Symposium, 7-9 October, Cortona, Italy', pp. 170–175.

Windén, B., Turnock, S. and Hudson, D. (2014), Self propulsion modelling of the KCS container ship using an open source framework, *in* 'Proceedings of the 17th Numerical Towing Tank Symposium, Marstrand, Sweden 28-30 September'.

1.8 Outline of thesis

This thesis begins by presenting the current knowledge of what phenomena are involved in performance losses in waves in Chapter 2. Initially the focus is to describe the phenomena causing added resistance in waves. This goes hand in hand with development of potential flow methods so the first part of Chapter 2 also serves to give a review of these. The last part of Chapter 2 focuses more on self propulsion and NS based methods. Based on previous studies, it is found that among other things, the surge motion is something that has the potential to influence the propulsive performance of the ship. The surge motion will be governed by the amplitude of the surge force variations on the hull. It is also found that, while a great deal of experience exists on the mean increase of the surge force, the amplitude of the same force and how it is affected by different sea states are not well understood. Therefore, Chapter 3 presents results from a set of experiments where the surge force amplitude as well as the mean increase is studied. The experiments are designed to cover areas of particular interest identified in the literature review. It is shown that the amplitude of the surge force does not follow the same trends as the mean increase at all times. The importance of accurately modelling the surge force is established.

Drawing from the experience from both previous literature and from the new experiments, a NS based numerical modelling scheme to model all of Figure 1.2 is presented in Chapters 4 and 5. This is referred to as the numerical towing tank and is the numerical representation of the external system. Chapter 4 focuses on the basic building blocks of the numerical towing tank and how it is implemented in the open source CFD package OpenFOAM (OpenCFD and The OpenFOAM Foundation, 2010). A RANS modelling approach is chosen and the ability to predict the amplitude and phase of the surge force is investigated. The ability to predict the amplitude and phase of the heave and pitch force and moment is also discussed. Furthermore, the sensitivity of the model to the selection of numerical schemes is investigated. The impact of the waves on the boundary layer is also discussed in detail. In Chapter 5, the inclusion of propeller modelling in the numerical towing tank is discussed. A framework for coupling the flow solver to a simplified propeller model is presented. The components of the framework are presented and it is shown how these create a powerful tool for self propulsion modelling. The

implementation of a Blade Element Momentum theory (BEMt) based propeller model within the framework is also presented and it is shown how this can be coupled with the flow solver. Here, the sensitivity of the coupling to various factors is discussed and a correction to account for discrepancies in the assumptions of the flow solver and the BEMt is presented.

Recalling the statements about RPM control in previous sections, Chapter 6 deals with the proposed linkage between the modelling of the external system and the control system governing the propeller RPM. Several options for controlling the RPM are discussed and an example on how different control schemes can influence the powering performance in waves of a free to surge hull is given.

The results from applying the presented numerical model to a realistic hull form are given in Chapter 7. Here the KCS container ship is chosen for the wide range of available data. Here, it is shown how well the coupled flow solver can predict the self propulsion coefficients in calm water. This gives an indication on how well the solver is able to separate the propeller induced velocities from the total wake to yield a realistic propeller/hull interaction. The ability of the numerical model to capture the unsteady inflow to the propeller is discussed as well as the overall ability of the model to represent a self propelled ship travelling in waves. Finally, concluding remarks are given in Chapter 8 which reiterate important conclusions made in the different parts of this thesis.

Chapter 2

Performance in waves

As with most scientific problems, the development of methods to predict performance in waves goes hand in hand with discovering which phenomena are involved. This section will briefly explain, by means of selected key papers, how this process has played out over the course of the 20^{th} and 21^{st} centuries. Because of its ability to model complex problems with very limited computing power, potential flow has historically been the main choice of modelling tool. This chapter serves both to highlight which hydrodynamical phenomena are involved, but also how the problem can be modelled using potential flow and how the lessons learnt by doing so influences any NS-based method.

As stated in Chapter 1, NS-based methods allow for a more detailed study of self propulsion whereas potential flow is more suitable for faster calculations of added resistance by itself. Because of this, this chapter will first focus on added resistance only for potential flow and continue with self propulsion for NS-based methods. More detailed reviews of previous research on the relevant subjects are also given at the appropriate locations when discussing the methodology for the numerical model in Chapters 4-6.

Research on the hydrodynamic causes of added resistance could be divided into several periods. Each period can be said to have been ended thanks to one or more key publications listed below.

- A time when the extent of the problem and its causes were largely unknown.
  - Kent 1922-1935
- A time when the causes were not yet known or known only in the most basic of principles.
  - Kreitner 1939 and Havelock 1942

- A time when basic knowledge of the causes was established but when the importance of phenomena were disputed and the mathematical methods for proving arguments were deficient.
  - Maruo 1957
- A time when added resistance calculations were too mathematically advanced to get a wider picture of which physical phenomena were most influential.
  - Vossers 1961, Hanoka 1963 and Joosen 1966
- A time when the causes were known and efficient approaches to calculations existed but when researchers lacked simple enough methods to predict motions for realistic hull shapes.
  - Boese 1970, Gerritsma and Beukelman 1972
- A time when methods were established but satisfactory results could not be obtained for all types of ships in all sea states
  - Faltinsen et al. 1980

After this point the focus turned away from looking at the problem as a whole to more detailed phenomena such as wave breaking, the effects of bow shape etc. These studies were motivated by lack of accuracy in the above methods and the need for further understanding of the limitations of potential flow. Even though this has led to improvements, ultimately, the only way of reinstating the holistic approach as the mostly used method is to build more confidence in the use of NS-based methods as was argued in Chapter 1.

2.1 Quantification of the problem

By the early 20^{th} century, large scale towing tank testing had become commonplace in most developed countries looking to improve the performance of their fleet. Up until World War One, the majority of improvements shipowners sought to achieve were related to reducing weight by means of new materials and structural arrangements. At the end of the war however, registration societies had imposed such hard regulations on weight saving measures that it was no longer regarded as the way forward (Abell, 1918). Focus turned to designing ships that would be cheaper to operate without reducing the weight.

The relative ease with which the wave making resistance could be predicted using Froude's methods led to a call for investigations into other factors that influence the fuel consumption than mere still-water resistance. At a meeting of the Institution of Naval Architects in 1918, the subject of which of the factors affecting resistance should

be addressed in the future was presented (Abell, 1918) . “Power required at sea” was one factor that sparked much discussion. It was noted that: “It is not an easy task to obtain even an approximation to the loss of speed brought about in rough weather, and it is still largely a matter of opinion whether the form which is most suitable for speed in smooth water is the best form for speed-keeping under average conditions.” The conclusion was that extensive measurements should be taken on various ships to determine how they performed compared to their calculated still-water resistance.

A series of studies done by J.L Kent with both model scale (Kent, 1922) and full scale tests (Kent, 1924) in the 1920's addressed this issue and gave a first scientific approach to determining the relation between still water performance and the actual performance on the desired route. His model tests were done on a series of models in a number of different wave types. He concluded that the added resistance is mostly due to pitching motions caused by a shift in the centre of buoyancy of the ship due to the passing wave crests and troughs.

When testing different wave amplitudes, Kent concluded that the loss of speed for a given horsepower was proportional to the wave height. The tests at different wavelengths show a large variation over the tested conditions. The most important conclusion was that the maximum resistance occurs when the period of encounter is close to the ships natural frequency in pitch. It was also shown that an increase in the resistance happens when the ratio between ship length and wavelength is moderately less than one. The conclusion Kent drew from this was that the maximum resistance occurs when the ship experiences the greatest shifts in its horizontal centre of buoyancy which depends on its underwater shape.

Some further tests were presented for a ship subjected to a confused sea with varying wave heights and -lengths. From these tests, Kent concluded that the resistance in a confused sea can be estimated with reasonable accuracy using a single test with a regular wave corresponding to the average wave height and -length of the desired sea state.

In the full scale test, the required horsepower was measured over the length of a journey for three different ships and compared to their calculated still water requirements. The results of these measurements are shown in Table 2.1.

TABLE 2.1: Results of full scale tests by Kent (1924) on addition to still water required horsepower for three ships crossing the Atlantic.

Montcalm (Passenger steamer)	Liverpool, UK St.John, Canada	+22%
San Gerardo (Oil tank steamer)	Tilbury, UK Tampico, Mexico	+100%
San Tirso (Oil tank steamer)	Rotterdam, the Netherlands Tampico, Mexico	+47%

Even though much attention was given to the subject of added resistance in the 1920's the methods were not widely spread. This was mostly due to the fact that towing tank institutions worked independent of each other to a large extent and that, because of the military nature of the applications of the findings, much of it was classified. The expansion of the merchant fleet in the postwar period however, brought about a desire to share experiences. The first of many International Conference of Tank Superintendents (later known as the International Towing Tank Conference or ITTC) was held in the Hague in 1933. The conference was an attempt to standardise the art of towing tank testing and share experiences. This was the intention of most reports submitted to and discussions held at the first such conference. At the second conference in London in 1934 however, an entry was presented called "Ship Performance In Relation To Tank Results" (Payne, 1934). This report questioned the validity of results obtained by towing ship models in calm waters.

The author suggested that when moving into real weather and wave conditions, the experienced resistance could increase by more than 5%. This matter was further discussed at the third conference in 1937 where the question: "Which addition to make to the test run power to get the mean performance on a regular trade route?" was posed (Kempf, 1937). The answers provided by the participants ranges from 0 to 30% addition with a majority using about 15-20% addition for north Atlantic trades.

As an addition to this discussion, Kempf presented a report suggesting appropriate standardised additions to the drag for factors such as wind, fouling, wave interaction and more. For wave interaction, the findings by Kent in the 1920's was suggested to be used as standard. The curves in Figure 2.1, based on Kent's results were shown and the conference subsequently decided to adopt the suggestions as guidelines for resistance calculation.

2.2 Basic concepts

After the studies by Kent it became widely accepted that heaving and pitching motions were the main hydrodynamical cause of added resistance. It was clear that more sophisticated methods of describing how the ship interacted with the waves were needed. A full solution to the Navier-Stokes equations for such a complex problem was not possible in the early 20^{th} century but the simplified approach of using potential flow had been given much attention with regards to ship problems. The work of Froude had made it possible to show that the resistance of a ship stemming from the pressure distribution on the hull could be treated as separate from the resistance stemming from viscous drag. This gave more merit to the usage of potential flow to calculate the resistance of ships. Modelling a ship in the boundary between two fluids requires a solution for the potential that satisfies both the Neumann condition (no flow through the body) and

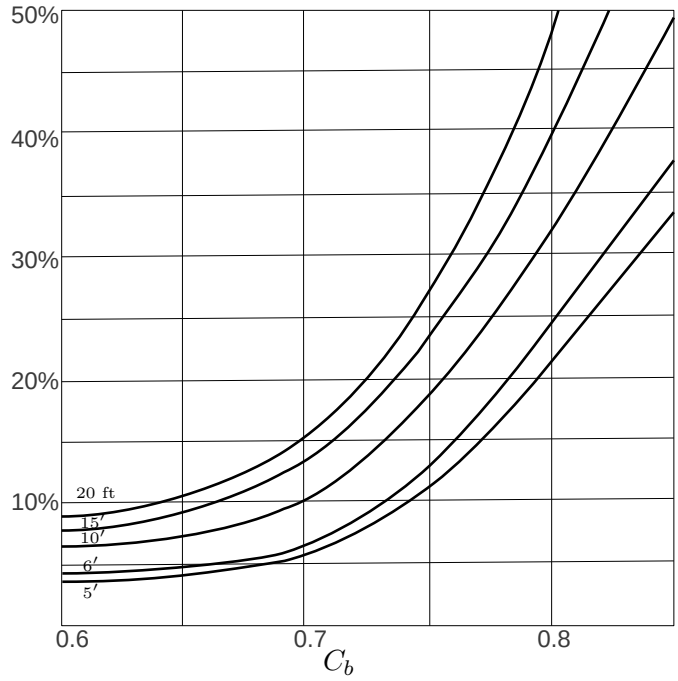

FIGURE 2.1: Percentage additions at different wave heights based on the studies by Kent, presented at ITTC3 1937.

Stokes' conditions for the potential of the waves and preservation of the free surface. The combination of these two problems is commonly referred to as the Neumann-Stokes problem. A complete solution to the Neumann-Stokes problem for a ship travelling in waves is very hard to find so several common simplifications exist.

Thin ship theory

The first substantial attempt at mathematically describing the flow around a ship by solving the Neumann-Stokes problem was by Michell (1898). Michell fully linearised both the free surface condition and the boundary condition on the body. He did this by assuming the ship was thin, i.e. that the length was much greater than the breadth. Thereby, he could assume two dimensionality along the longitudinal (x) axis and thus zero extension along the transverse (z) axis so that the boundary only existed where $z = 0$. Michell also made use of a linearised free surface condition that assumed small amplitudes compared to wavelengths which meant that the free surface could be linearised around $y = 0$. This had been proposed earlier by Kelvin and shown to be applicable for small amplitudes and sinusoidal waves (Thomson, 1886). These assumptions are the basis of thin ship theory and have been widely used since their introduction.

The Froude-Krylov hypothesis

The Froude-Krylov hypothesis states that the pressure field under a wave system can be approximated to be unaffected by the presence of a solid body within that system. This greatly simplifies the Neumann-Stokes problem since it means that the potential due to the ocean waves can be treated as separate from the waves generated by the ship. Froude (1861) introduced the idea when describing rolling motions but it was thoroughly investigated by Krylov some years later who showed that the approach was applicable to ship motions due to waves (Krylov, 1896, 1898). In other words, for the purpose of calculating wave loads on a hull, the potential can be taken as the one due to the undisturbed wave only. This eliminates the need for complex boundary conditions on the hull surface. It is then possible to calculate the pressure on a certain point of the hull by taking the pressure of the undisturbed wave train at that point thus neglecting energy put into the wave system by the hull itself. Even though this is a rather crude approximation, at the time, it opened the door to understanding the effect of surface waves on ship motions. The validity of the hypothesis will vary depending on the situation but in general it is less valid the more the waves are disturbed by the hull.

Strip theory

The Froude-Krylov hypothesis is a very useful way of simplifying the Neumann-Stokes problem when calculating wave induced loads and motions. However the problem remains very complex and a new solution has to be found for every new hull shape it is applied to. One way of significantly simplifying it is by assuming local two-dimensionality of the flow. Local two-dimensionality means that the pressure distribution on one transverse cross section of the flow is independent of the surrounding pressure field. First introduced by Lewis (1929), the idea of strip theory is that the hull can be divided into transverse sections. The boundary problem is solved in two dimensions for each such section. This is justified by the oblong shape of most hulls that yields small and smooth variations in the flow features along the length of the ship. Thus the problem can be solved in two dimensions for a large number of transverse sections (strips) of finite length and the results added together. To obtain the solution for a single strip, conformal mapping can be used where a solution to the Neumann-Stokes problem is found for a simple shape such as a cylinder and the solution mapped onto a plane so that it conforms to the shape of the hull.

Early descriptions of added resistance

Attempts at applying potential theory to arrive at a more accurate estimate of the resistance of a heaving and pitching ship in waves was made by Havelock (1937). Havelock

used the Froude-Krylov hypothesis and calculated the first order forces on a ship moving through a regular wave train. He showed that the added resistance was mostly due to the phase difference between the oscillating ship and the exciting force from the waves supporting Kent's theory.

Kreitner (1939) rejected the Froude-Krylov hypothesis as too much of a simplification in the case of calculating heave and pitch motions since it assumed the waves to be unaffected by the ship. Kreitner claimed that the average wave height at the bow could be 30% larger than the undisturbed wave and equally 30% smaller at the stern, he gave examples relating to "wave shadows" behind islands and from this he concluded that much energy must go into disturbing the wave system itself and that the majority of the additional resistance is due to reflection of the incoming waves. From this assumption he derived an expression for the added resistance of a wall-sided ship based on the energy of the reflected waves being linked to an extra "radiation pressure". The radiation pressure was suggested to be added to the one calculated by the Froude-Krylov hypothesis to give the total pressure on the hull. Thus added resistance could be calculated as the projected force in the longitudinal direction stemming from the radiation pressure. The expression suggested by Kreitner is

$$R_{AW} = \Delta \frac{B}{T} \left(0.8 \frac{2\zeta_0}{Lpp} \right)^2 \frac{U_{cbow} + U}{U_{cbow} - U} \tag{2.1}$$

where U_{cbow} is a characteristic speed depending on wavelength and angle of entrance of the bow so that $U_{cbow} = U$ would yield a resonant behaviour. He also suggested that the radiation pressure was the sole cause of added resistance. Despite this, Kreitner gave very accurate descriptions of the effects of heave and pitch damping on ships motions and the energy lost through radiating waves due to oscillations. However, he saw the energy lost in these motions not as a direct cause of added resistance. Instead he saw ship oscillations as having only a secondary effect in that it changed the attitude of the ship relative to the waves and thereby affecting the severity of the reflection. For example: a ship facing a wave with its bow up would reflect much less energy than one who faces a wave with its bow down. Thus Kreitner too realised the importance of the heave and pitch motions and their phase relative to the incident waves if only for different reasons than Havelock. Kreitner's contribution was one of the first to include almost all of the factors considered today as sources of added resistance. It also gave very elaborate explanations of the phenomena giving rise to these factors. Regrettably, his calculations contained too many assumptions and simplifications to be widely accepted as indisputably true. Havelock's theory contained a much more accurate mathematical descriptions of pressure variations in heave and pitch, albeit not with as much discussions as to what different physical phenomena were present.

In 1940, Havelock reviewed his earlier neglect of the reflection and showed that the force created from wave reflection was very small compared to forces created from heaving

and pitching (Havelock, 1940). Havelock used a quite crude potential flow approach but one that tried to explain the physics behind a body travelling through a regular wave train. This work was followed up in 1942 by a more well developed theory (Havelock, 1942).

Havelock derived the resulting force in the longitudinal direction, R_{AW} from the pressure field under the undisturbed waves. The added complexity of the ship moving within this pressure field due to heaving and pitching induced by that pressure being applied to the hull is also considered. This leads to the expression

$$R_{AW} = \frac{-k}{2}(F_y x_{30} \sin \varepsilon_3 + M_z x_{50} \sin \varepsilon_5) \tag{2.2}$$

where k is the wave number of the incident waves. F_y is the exciting force in heave, M_z is the exciting moment in pitch both calculated using the Froude-Krylov hypothesis. x_{30} and x_{50} are the amplitudes and ε_3 and ε_5 the phase lags of those motions respectively. Because $k = 2\pi/\lambda$ where λ is the wavelength, this is equivalent to

$$\frac{-R_{AW}\lambda}{\pi} = F_y x_{30} \sin \varepsilon_3 + M_z x_{50} \sin \varepsilon_5 \tag{2.3}$$

This means that the work of the resistance force over one wavelength, $R_{AW}\lambda$, is said to be proportional to the sum of the work of the heaving force and the pitching moment over one oscillation adjusted for the relative phasing between the two. Havelock admitted that this should only be used as a crude estimate since it lacked sufficiently accurate calculations of the response motions and as well as the forces and moments. Furthermore the use of the Froude-Krylov hypothesis meant that the diffraction of the incident waves by the hull was neglected. The findings by Havelock and Kreitner however made it widely accepted that added resistance is mostly due to heaving and pitching oscillations and interplay phenomena between these and the character of the incident waves. The importance of cross-coupling forces between heave and pitch has since been shown by Kashiwagi et al. (2000).

2.3 Application of advanced potential theory

After the works of Havelock and Kreitner, it was clear that accurate computation of added resistance would require a more holistic approach with methods able to capture interplay between different phenomena. A method using potential flow should model as many of the aspects of ship motions and the resulting flow as possible. Haskind (1953) tried to combine the works of Havelock and Kreitner by suggesting that added resistance was both due to reflection and ship motions and presented a potential flow

solution. This still was not enough to get a complete model since the waves created by the oscillation of the ship were neglected.

The problem of solving the Neumann-Stokes problem for an oscillating body required to predict the potential of the radiated waves had previously been addressed by Kochin (1940), Haskind (1946*a*,*b*,*c*) and John (1950). They found that the potential of the waves of an oscillating body could be described using Kochin functions; a concept introduced earlier by Kochin (1937) to solve free surface boundary problems with waves.

The application of Kochin functions to calculating wave responses due to oscillating bodies was utilised by Japanese researchers Hanoka (1957) and Maruo (1957, 1960*b*) to try and describe forces on ships in waves in more detail. Hanoka's method was based on forced oscillation which assumes that the ship will always oscillate with the same frequency as the applied force or moment. This allows for the methods developed earlier by Kochin, Haskind and John for oscillating bodies to be applied. Maruo recognised that the reason why earlier attempts of describing the phenomena physically had yielded poor and inconsistent results is that added resistance is partly due to effects that are omitted in the linear potential theory.

Maruo suggests that linear theory can still be used to describe the phenomena if certain terms are not omitted. For instance he showed that the terms Havelock omitted having to do with the disturbance of the wave system by the presence of the hull were not negligible. Maruo chose to divide the potential into three parts, the one due to the incoming wave system, the one due to diffraction of the wave system by the ship (previously omitted in added resistance problems due to the Froude-Krylov hypothesis) and the one due to to the wave system created by the oscillating ship. The total potential is thus described as

$$\phi = \phi_w + \phi_i + \phi_e \tag{2.4}$$

Where ϕ_w is the potential due to the incident wave system, ϕ_i is the potential due to the singularities which represent the ship and ϕ_e is the potential due to the wave system created by the oscillation of these singularities representing the heaving and pitching of the ship. Maruo applied a Green's function to find the distribution and strength of the singularities representing the hull giving ϕ_i where sources placed on the centreline was chosen as a way to represent the hull. Kochin functions for waves generated by oscillating bodies were used to calculate ϕ_e. This was obtained by letting this distribution oscillate with the encounter frequency similar to the approach by Hanoka. Maruo then set up the equations of motion of the ship by considering its motion as a small oscillation around the point of equilibrium and used Lagallys theorem (Lagally, 1922) to extract the mean forces acting on the body. Unfortunately, this theorem only holds for a fixed body which, together with the small amplitude oscillation assumption makes the theory unsuitable for large motions. Linear strip theory was then used to relate the forces to motions

which in turn can be used to create a new estimate of the potential as shown in Figure 2.2.

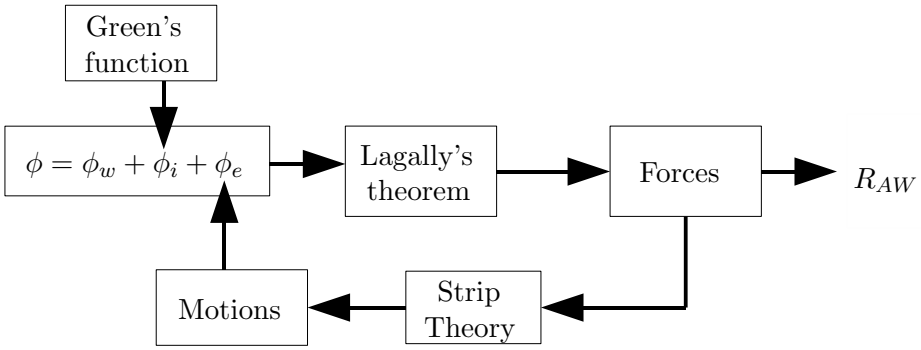

FIGURE 2.2: Flow chart of the method proposed by Maruo (1957).

Maruo identified two parts that were dominant, pure heaving and pure pitching. These two together with the diffracted wave are thus identified as the source of added resistance. Maruo also identified three other phenomena that affected the result namely; coupling between heave and pitch, coupling between heave and the reflected wave and coupling between pitch and the reflected wave. The influence of these factors at different Froude numbers can be seen in Figure 2.3 where D_{55} represents pure pitch, D_{33} pure heave, D_{77} pure diffraction. The remaining coefficients are combinations of these three. These are normalised with the amplitude and phase of the respective oscillation.

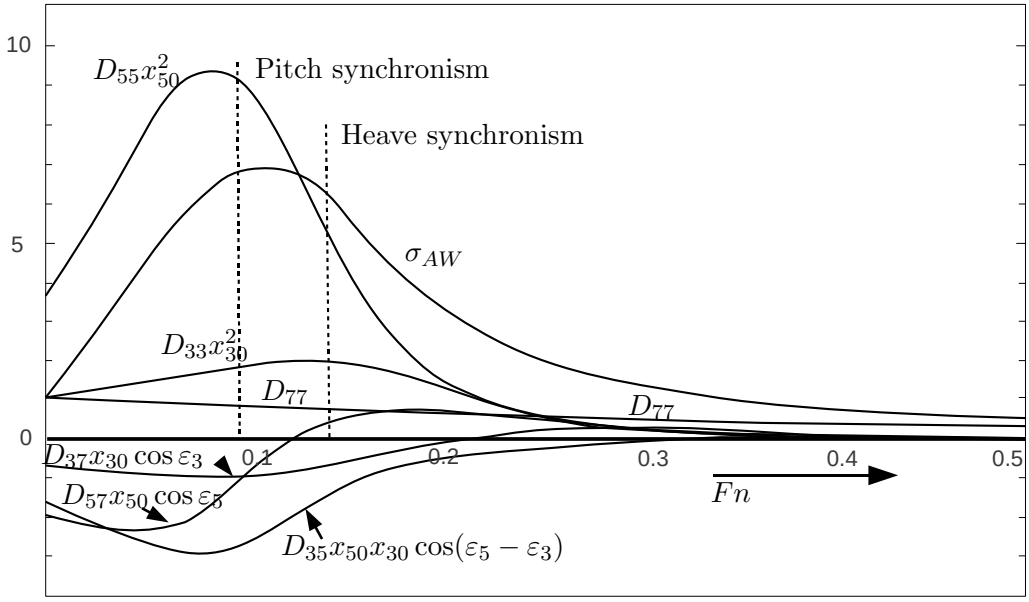

FIGURE 2.3: Influence of different factors on added resistance (σ_{AW}) found by Maruo (1957) .

The total added resistance is described as

$$R_{AW} = \frac{\sigma_{AW}\rho g\zeta_0^2 B^2}{Lpp} \tag{2.5}$$

where ζ_0 is the wave amplitude and σ_{AW} can be seen in Figure 2.3. Using this method, Maruo also showed that the increase in the resistance is proportional to the square of the wave height. This is somewhat similar with the findings of Kent that the speed loss is proportional to the wave height if one assumes that the resistance is proportional to the square of the velocity.

Maruo's original method assumes head seas which is why it can be written in a relatively simple form. Hosoda (1974) performed a full derivation of Maruo's approach which is valid for oblique waves. This derivation however, is very complex and requires complicated algorithms if it is to be used for computations. Hosoda (1973) also presented a simplified method valid for oblique waves by assuming that the effect of lateral motions on added resistance was negligible. A further simplification of the method is to assume a relatively high frequency of encounter (Maruo and Ishii, 1976). This assumption was previously implied by the validity of the used strip theory and the poor results obtained for lower frequencies but not used to simplify calculations.

2.4 Energy methods

Maruo's method has been improved with a control volume approach replacing the direct integration of pressure (Maruo, 1960*a*, 1963). In this approach the forces on the hull are related to the momentum difference over a control volume containing the near- and far fields which can be calculated using the same separation of the potential as in Eqn. 2.5.

A further attempt at simplifying Maruo's method is by Joosen (1966) who was able to arrive at a simplified expression of the Kochin function by assuming a small value of the slenderness parameter; thus

$$\frac{\sqrt{A_M}}{Lpp} \ll 1 \tag{2.6}$$

where A_M is the sectional area amidships. Joosen also assumed that the wave number would be in the order of 1 and that second order terms could be neglected. In doing so he was able to show that the expression for the force in the direction of travel derived by Maruo and Newman can be reduced to

$$R_{AW} = \frac{Lpp\cos(\beta_i)}{8\sqrt{A_M}} \int_{-1}^{1} |x_{30\xi}|^2 \overline{A}^2(k,\xi) d\xi \tag{2.7}$$

where ξ is the dimensionless position along the length of the ship so that $\xi = 2x/L$. $\overline{A}^2(k,\xi)$ is related to local two dimensional damping of vertical motions $\eta_{33\xi}$ as

$$\overline{A}^2(k,\xi) = \frac{\sqrt{gk^3}\eta_{33\xi}}{\rho} \tag{2.8}$$

$x_{30\xi}$ is defined as the dimensionless amplitude of the ship vertical motion at any point ξ and β_i is the angle of the incoming waves. Joosen also showed that this could be written as a coupled heave and pitch expression

$$R_{AW} = \frac{\omega^3}{2g}(\eta_{33}x_{30}^2 + \eta_{55}x_{50}^2) \tag{2.9}$$

where η_{33} and η_{55} are the damping coefficients for heave and pitch respectively. This is quite similar to Havelock's expression (Eqn. 2.3), only instead of relating resistance to the exciting force in pitch and heave, it relates it to the magnitude of the energy lost in damping of these motions. This is compliant with suggestions by Vossers (1961) and Hanoka (1963) that added resistance is due to three factors:

- The drifting force, or force associated with the ship interacting with the wave system.
- Reflection of the incident waves.
- Energy lost through damping of the ships motions.

Each of these are naturally interlinked, without wave interaction and pressure variations there would be no energy lost in damping the resulting motions. Upon seeing separations of the causes of added resistance as the one above; it may seem strange that methods aiming at describing only one of these have reached surprisingly similar results as methods trying to describe another. In reality, the whole problem is one of understanding what happens to the energy within the system that is the ship. Whether one tries to describe the forces acting on the hull or trying to understand how the energy those forces induced is lost trough damping of the motion; it does not matter as long as the different steps in the energy flux is captured correctly. A common problem for all methods has been that even though they can describe one stage of the energy flux correctly, they neglect that energy can be lost or gained in other stages as well.

The benefit of using damping of motions as a measurement of the total energy that is lost is that it is the last step of the energy flux, where the energy leaves the ship. If one assumes that the ship is able to sustain its speed relatively well and that motions do not grow significantly over a small period of time, one can assume that the majority of the energy that is induced by wind and waves has to leave the ship somehow. One can also

assume that most of the energy will leave the ship as kinetic energy induced into the water, thus neglecting heat transfer and all kinetic energy induced into the air. With these assumptions one could say that all of the induced energy, no matter what complex and interlinked phenomena caused it, can be equated to the energy lost through wave making due to ship oscillations.

2.5 Simplified approaches for realistic hull shapes

Methods such as the ones described in section 2.3 are very useful to highlight general trends and phenomena and, as Figure 2.3 shows, gives the opportunity to study the influence of separate flow features. The use of thin ship theory and the many simplifications needed to make them suitable for computation however, make them hard to apply to specific hull forms of more complex shape. The improved accuracy of strip theory in the later part of the 20^{th} century lead to Havelock's approach of using the Froude-Krylov hypothesis getting revisited by Boese (1970). The coordinate system used by Boese is shown in figure 2.4.

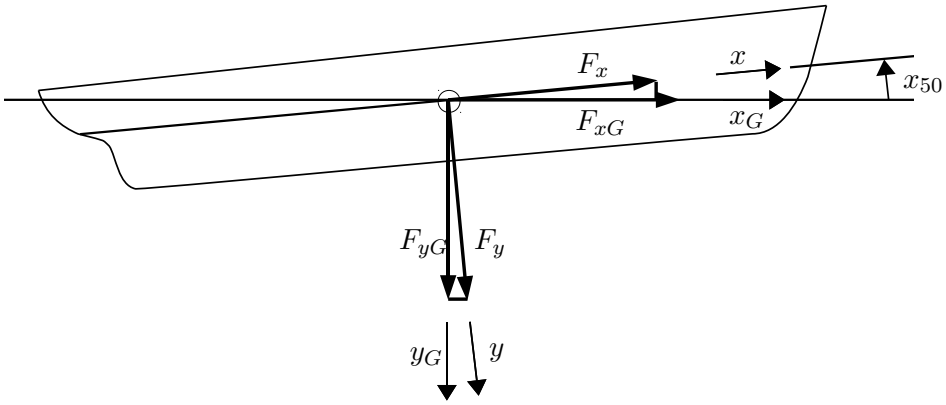

FIGURE 2.4: Coordinate system used by Boese (1970).

Boese used strip theory to calculate the wave induced forces in the longitudinal x and the vertical y-direction. These are then related to the total force in the direction of travel x_G. The mean value of this force over one period of encounter is said to be the added resistance due to waves R_{AW}

$$R_{AW} = \overline{F_{xG}} = \overline{F_x(t)\cos x_{50}(t) + F_y(t)\sin x_{50}(t)} \tag{2.10}$$

If x_{50} is small this can be linearised to

$$R_{AW} = \overline{F_{xG}} \approx \overline{F_x(t) + x_{50}(t)F_y(t)} \tag{2.11}$$

The forces $F_x(t)$ and $F_z(t)$ were divided by Boese into one part due to buoyancy and one part due to the pressure variations resulting from the movement of the free surface relative to the hull.

Gerritsma and Beukelman (1972) elaborated on Joosen's findings and assumed that added resistance in waves could be entirely related to energy dissipated from damping of the ships motions due to these waves. They used strip theory to relate the dissipated energy to the damping of the relative vertical motion between each strip and the free surface. The relative vertical motion is due to pitching, heaving and movement of the surface. The linking of added resistance to the relative vertical motions is a way of explaining why pitching and heaving is so dominant. It also explains why synchronisation between the surface movements and these motions yield large values of resistance.

If sections are small, the hull surface and the waves can be assumed to be two dimensional along each strip. In a surface fixed system the situation can be equated to a 2D section moving up and down with a certain velocity, see Figure 8. Energy will be dissipated as waves radiating out from the section, the magnitude of which depends on the damping coefficient of the section in question.

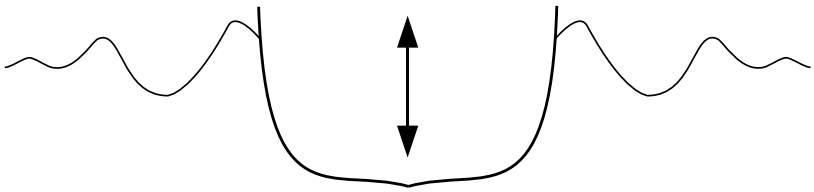

FIGURE 2.5: Waves generated by a hull section moving relative to a fixed surface.

The energy dissipated for the whole ship due to relative vertical velocity during one period of encounter can be written as

$$W = \int_0^{T_e} \int_0^{Lpp} \eta_{33x} \dot{y}_{3r}^2 dx dt \tag{2.12}$$

where η_{33x} is the local damping coefficient, $\dot{y}_{3r}$ is the relative vertical velocity of a strip. The integral over dx represents summation of influences from each strip over the total length Lpp and T_e is the period of encounter. A modified strip theory developed earlier (Gerritsma and Beukelman, 1967) was used to calculate the velocity. In this, a modified Froude-Krylov hypothesis to correct for changes in wave amplitude due to the presence of the ship was applied. This reduces Eqn. 2.12 to

$$W = \frac{\pi}{\omega_e} \int_0^{Lpp} \eta_{33x} \dot{y}_{3ra}^2 dx \tag{2.13}$$

Where $\dot{y}_{3ra}$ is the *amplitude* of the relative motion which is assumed to oscillate with ω_e, the frequency of encounter. Gerritsma and Beukelman defined the added resistance force R_{AW} as the force acting on the hull, the work of which over one wave length must be equal to the energy dissipated during one period of encounter hence, using Eqn. 2.13

$$W = R_{AW}\lambda \rightarrow R_{AW} = \frac{k}{2\omega_e} \int_0^{Lpp} \eta_{33x} \dot{y}_{3ra}^2 dx \tag{2.14}$$

By assuming that the effects of lateral motions were negligible, Gerritsma and Journée (1978) generalised the theory to be valid for oblique waves. A version of the theory extended to include damping of lateral motions was developed by (Loukakis and Sclavounos, 1978). It must be noted that if potential theory is used to estimate the energy lost through radiating waves, the energy lost through viscous damping is neglected. This has an impact on the accuracy of the method close to the resonance frequency for fuller hull forms (Beukelman, 1983). Motion based methods have also proven to have difficulties predicting the added resistance in following or quartering seas especially when the period of encounter approaches zero (Journée, 1976*a*).

2.6 Added resistance in short waves

Because of the increase in demand for VLCCs that the end of the 1970's oil crisis brought about; a large number of studies of the effects of smaller waves on ships with blunt bows were conducted in the 1980's and 1990's. Modelling resistance as energy lost through damping of motions neglects the relatively overwhelming inertia of large ships compared to the energy of smaller waves and the lack of induced motions at short wavelengths. Using models which assume ship oscillations at the same frequency as the waves will therefore fail in short waves. In such waves, energy can be lost without any motions happening as a result. The energy flux is thereby different in that it goes almost directly from incident wave to reflected wave without inducing any considerable motions. This is the case of reflection for smaller waves by large ships where energy is lost not through motions but through pure diffraction of the waves.

Added resistance for ships with blunt bows at moderate speeds should therefore be divided into one part relating to pure motions and one part relating to reflection of incident waves (Fujii and Takahashi, 1975). Because of coupling effects, this division is only valid if one of the terms could be considered negligible (Faltinsen et al., 1980). This would be true at encounter frequencies close to the heave or pitch resonance or at very short waves not inducing any motions.

Following from this conclusion, (Faltinsen et al., 1980) proposed a pressure integration using strip theory (similar to the approach by Boese (1970)) to get the added resistance

for a ship in waves large enough to induce motions. For the special case of short waves they proposed an asymptotic formula based on the force induced by waves modelled with potential theory on a vertical wall. In this case, Faltinsen et al. uses the same idea of a wave shadow that Kreitner (1939) used to consolidate his theory (see Figure 2.6.) Added resistance is obtained by integrating the force on the non-shadow side of the hull.

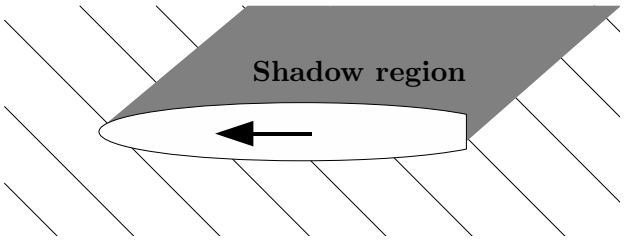

FIGURE 2.6: Shadow region of a ship travelling in a system of short waves with small amplitude.

The ship is assumed to be wall sided but corrections are made for finite draught. This is motivated with the exponential decline of the energy of the waves with increasing depth. An experimental study by Ogiwara and Yamashita (1996) supports this by showing that the resistance in short waves of small amplitude is due to a pressure increase on a very narrow strip of the hull surface corresponding to the vertical range of the wave profile. This also means that the theory is only proven valid for waves of moderate amplitudes. The theory by (Faltinsen et al., 1980) includes a constant current which allows for predictions of the added resistance at forward speed. Even though the importance of wave reflection is most apparent for slow ships with blunt bows and large block coefficients, it is significant for ships with slender bows and waves with a wave length down to 1% of the length of the ship (Steen and Faltinsen, 1998).

The usage of the wall sided approach gives higher discrepancies for slender ships at higher Froude numbers ($Fn > 0.25$) because of non-linear effects at the bow (Fujii and Takahashi, 1975). Faltinsen (1983) has addressed this problem by deriving a special slender ship theory for the bow region that better captures the reflections off slender bows at high speeds. The improved method shows better agreement with experimental values for slender bows at higher speeds but the improvement is not significant. Similar discrepancies, even for lower speeds and blunt bows, have been experienced when calculating added resistance due to pure reflection using the far field diffracted wave pattern (Ohkusu, 1980, 1984, 1986).

It was suggested by Nakamura et al. (1983) that this is due to the breaking of diffraction waves which will not be captured by analysing the wave energy in the far field. Naito et al. (1985) conducted experiments to study the behaviour of the reflected waves and concluded that waves reflected off certain parts of the studied bow did indeed break and that the contribution of these would be excluded from the methods of both Ohkusu and Faltinsen et al. The importance of the breaking of the diffracted wave was shown

analytically by Naito et al. (1987*a*). They showed a strong interaction between the hull generated flow field and the incident waves near the bow. This creates breaking waves which explains discrepancies between previous theories and experimental data. An improved wave pattern analysis technique was developed by Ohkusu (1998) that is more efficient at capturing all the waves associated with diffraction in small sea states and thus gives a better prediction of the added resistance.

2.7 Added resistance in irregular waves

Kent (1922) had shown at an early stage that the resistance in a confused sea was somehow connected to the resistance of the regular waves making up that sea state. However, his theory that the resistance in irregular waves was the same as the resistance in the regular wave of the average period and height of that sea is not true. This is partly due to the interaction of frequency components as shown by Newman (1974) but mostly due to the fact that short and long waves contribute to different parts of the added resistance (induced motions and diffraction). To accurately predict the resistance in irregular seas, all frequency components must thus be considered.

If it is assumed that there is a linear relation between the height and frequency of a regular wave and the resistance of a ship being subjected to that wave, the theory of linear superposition could be applied to find the resistance in a combination of regular waves. Pierson and St. Denis (1953) were the first to mathematically apply the principle of superposition to the added resistance problem even though Maruo (1957) was the first to suggest it while presenting a comprehensive approach to calculating the individual components. The validity of superposition for the purpose of estimating resistance in irregular seas was confirmed experimentally by Gerritsma et al. (1961) This discovery, according to the ITTC, opened the door to predicting the propulsion power required in rough seas, but also re-established the importance of tests made in regular head waves as the results of these can be superimposed to yield the performance in an irregular sea (Lewis et al., 1963).

Further investigations of the validity of the superposition theorem is by Sibul (1966) and Vassilopoulos (1967). Vassilopoulos showed that the superposition theorem was mathematically valid by using non linear system theory. Sibul's experiments show that for large waves and motions, the superposition theorem underestimates the added resistance of the composite wave but that it is valid for waves of smaller amplitude. Experiments with the purpose of validating the superposition theorem have also been conducted by Moor and Murdey (1968, 1970) with similar results.

When applying Maruo's method to ships in irregular waves by superimposing results from regular waves, a discrepancy has been noted and is due to interactions between different frequency components in the incident waves giving rise to a slowly varying

force adding to the total force and creating more oscillations (Newman, 1974). To fully resolve this force that contributes to the added resistance, one needs to solve the complete second order velocity potential. However, Newman suggests that the slowly varying force may be replaced by the mean drift force in the regular wave that would yield the same oscillations. This greatly simplifies the problem and the assumption is widely used. The validity of this assumption has been investigated by Faltinsen and Løken (1979) among others and it has been shown to give satisfactory results when applied to Maruo's method.

2.8 Verification of and comparison between different methods

The different components of added resistance, as shown in Figure 2.3, calculated using the methods of Gerritsma and Beukelman and Maruo have been compared to experimental values by Kim (1987). Kim obtained the separate components of added resistance by keeping the model fixed or forcing oscillations in the relevant degrees of freedom. For example, to get R_{33} the hull was undergoing forced heave oscillations at forward speed with other degrees of freedom fixed. To get the coupled component between heave and diffraction, the hull was free to heave in regular head waves but fixed in pitch etc. The study shows good agreement for some of the the coupled and individual components compared to the ones calculated using Gerritsma and Beukelman's method. However, both analytical methods show large discrepancies with experimental values for other components. The results by Kim (1987) are shown in Figure 2.7.

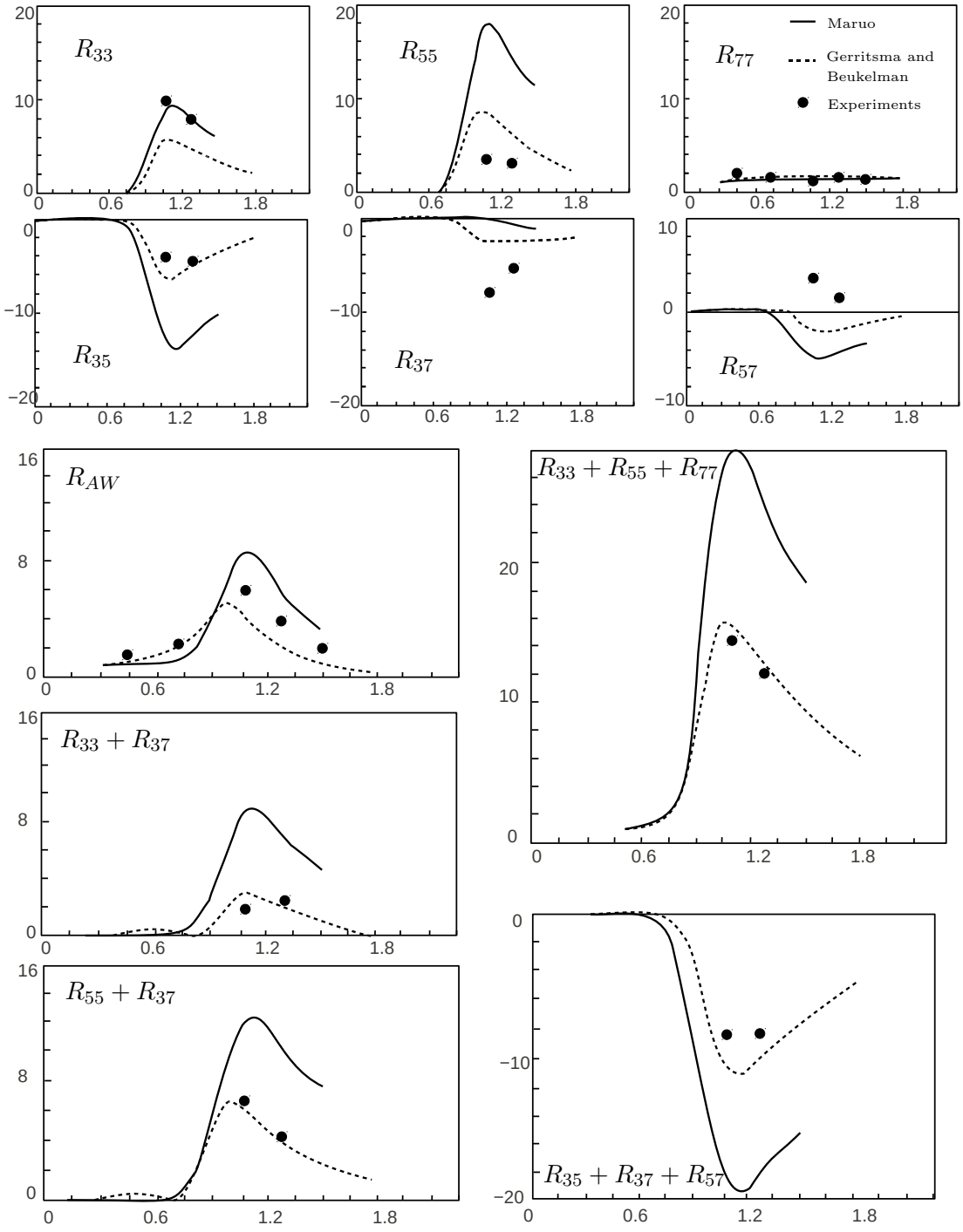

FIGURE 2.7: Results of comparative study (Kim, 1987) for individual and coupled components of added resistance.

Here, the components R_{**} have the same definition as in Figure 2.3 but representing the force components rather than the nondimensionalised components.

2.9 Effect of bow shape

While the overall shape of the hull is usually not subject to large changes to improve performance in waves, the shape of the bow is a parameter that, with smaller impact on the general arrangement of the ship, can affect the added resistance significantly. Blok (1987) discussed the importance of above water bow shape in rough seas and showed that the added force on the bow is almost synonymous with the total added resistance for some wavelengths. The results by Blok (1987) show a large spread of values although the general trend suggests that the force on the bow is of great importance when determining the added resistance. Similar results showing the importance of the forces acting on the bow have been presented by Naito et al. (1987*b*). Naito and Ueda (1992) also showed the importance of bow shape in short waves in a comparative study of several bows.

A simplified method relating the added resistance in short waves to the waterline bow shape was presented by Naito and Takagishi (1995, 1996). Based on previous research on the relevance of bow shape Naito et al. (1996) proposed new above-water bow shapes to be applied.

Shibata et al. (1983) showed that added resistance for tankers could be decreased by about 30% by adding a domed forecastle allowing waves to run over the deck rather than having to be deflected by the bow. Similar reductions were achieved by the "Beak-Bow" shape proposed by Matsumoto et al. (1998) which also deals with the water transport above the waterline. Further concepts for dealing with the above waterline transport of water are the sharpened "Ax-Bow" and the "Leadge-bow" developed by Hirota et al. (2005). The importance of the bow flare for reducing added resistance has been shown by Kihara et al. (2005). Kihara shows a decrease in added resistance with increasing flare while Hirota shows that a bow with an almost vertical stem (Leadge-bow) can be successful in reducing the added resistance. There is thus no unison consensus on how to design the above-water bow shape for minimal added resistance. Different methods may be more applicable to individual sea states and less applicable to others.

Corporate R&D departments have also developed their own designs claiming to be efficient in reducing the added resistance. Such is the case of the "X-bow" developed by Ulstein Group (2011) which has a tumblehome flare for increased performance in large waves as well as a bow developed by STX Europe (2011) where different sections of the bow are optimised for increased performance in both large, medium and small waves. Another bow concept developed with the purpose of reducing added resistance is the Oshima "Seaworthy bow" claiming a 5% reduction in fuel consumption on the North Atlantic trade (Anon., 2011).

2.10 Self propulsion in waves

Self propelled model tests in calm water is a common method to estimate the true powering performance of a ship (Molland et al., 2011, p 151-152), these can also be replicated using various numerical methods. NS simulations of self propelled ships have appeared in recent years for example by Lübke (2005) and Carrica et al. (2010) but also coupled with simplified propeller models for example by Fu et al. (2010); Phillips et al. (2008); Simonssen and Stern (2005); Turnock et al. (2010). However, when considering modelling self propulsion in waves, the model inevitably becomes more complex and more sensitive to errors.

2.10.1 The unsteady wake

Ueno et al. (2013) gives an overview of previous research regarding the effects of waves on the propeller performance. It has been shown that the average open water performance of a propeller working under regular waves is very close to the calm water case (Nakamura, Naito and Inoue, 1975). When considering the presence of the ship, Tsukada et al. (1997) showed that the average wake behind a ship without propeller varies depending on the wavelength. However, the average wake in irregular waves is similar to the one in calm water (Nakamura, Hosoda, Naito and Inoue, 1975). Furthermore, linear superposition of the thrust and torque fluctuations measured in regular waves agree well when compared to those measured in a composite irregular seaway (Aalbers and van Gent, 1984; van Sluijs, 1972).

Nakamura and Naito (1977) showed experimentally that the pitch motion has a large impact on the wake velocities, in particular close to the pitch natural frequency. Faltinsen et al. (1980) also argued that the pitch motions has a large impact on the wake due to pressure changes from the oscillatory vertical motion. According to Faltinsen et al. (1980), the pressure changes create a pressure gradient along the hull which changes the nature of the boundary layer and accelerates the flow towards the stern, affecting not only the propeller inflow but also the viscous resistance and stern separation of the ship. Recently, Ueno et al. (2013) argued that even though there is an influence of heave and pitch motions, the main influence on the wake comes from surge motions. The unsteadiness of the wake not only affects the actual delivered thrust but also the efficiency (Johnsson, 1968; Moor and Murdey, 1970; Nakamura and Naito, 1977), this is likely to be due to a change in the radial distribution of the inflow (Yamzsaki, 1966). Finally, the proximity of the propeller to the surface and the possibility of partial ventilation is something that can prevent the use of open water performance charts when considering a propeller working behind a ship heaving and pitching in waves (Faltinsen et al., 1980; Nakatake, 1976).

It is clear that the inflow to the propeller will be influenced by the nature of the viscous flow around the hull. How the viscous flow is disturbed by the passing waves is therefore of interest for propeller performance. Villeger and Alessandrini (1992) showed that there is a significant difference in the integral quantities of the boundary layer along the hull when using a double hull model and when using a surface piercing model. When considering a ship advancing in waves, the free surface effects should be stronger due to increased amplitudes and unsteadiness. Stern et al. (1987) showed a significant effect of waves of varying steepness on the boundary layer of a flat plate. Recently, Bingjie et al. (2012) pointed out the effect of waves on the wake of the KVLCC2 tanker using CFD. The effects of the free surface on the wake have been obtained experimentally by Seol et al. (2013). These studies show that the boundary layer and its separation are affected by the waves. This will have implications both for the viscous forces on the hull but also for the wake in which the propeller is operating.

Even though these studies have given good insight into the average performance of the propeller in waves, real time prediction of the inflow and propeller performance is still lacking (Ueno et al., 2013). Furthermore, it is not clear what role propeller/hull interaction plays in the interplay with waves. Improvements in real time predictions of the propeller performance behind a hull in waves will thus serve to more accurately predict the true performance of a ship in a seaway. This is particularly true when considering variable pitch propellers which have the ability to adapt to the performance to the instantaneous conditions in real time (Ueno et al., 2013). Relating to the discussions about control in Section 1.6, this may also have implication for the RPM control system.

2.10.2 Propeller modelling

Currently a relatively high level of accuracy in predicting the local flow around the propeller can be achieved by directly incorporating the propeller geometry in the NS solution (Stern et al., 2013). Rotation can be achieved using for example an Arbitrary Mesh Interface (AMI) between a rotating and a static region of the mesh or using an overset grid method (Carlton, 2007, p 200-201). Promising results compared to EFD for the flow around rotating propellers behind a hull have been demonstrated, see for example Muscari and Di Mascio (2011). For highly detailed studies of local flow around the blades, vortex shedding and cavitation, incorporating the propeller in the NS solution is currently the only option. The drawback to this approach is mainly the computational effort required due to the addition of cells to resolve the complex propeller geometry. This is partly due to the need to include boundary layer refinement around the blades and the hub. A high refinement level is also needed in the wake since the accuracy of the predicted performance is particularly sensitive to capturing of the wake and the tip vortices (Turnock et al., 2006).

When using RANS-based methods to consider the flow around the hull and around the propeller in the same scope, issues also arise with turbulence closure. Because the viscous flow regimes around the slender hull and the fast rotating propeller are different it will be difficult to adapt standard turbulence models to accurately suit them both. Even with a fine mesh, models assuming fully turbulent flow such as the $k-\omega$ SST model are not well suited for capturing aspects such as vortex shedding and the strength of the tip vortex. This gives a significant disadvantage to using them when predicting the performance of propellers, especially in off design conditions compared to more advanced transition sensitive models (Wang and Walters, 2012). Furthermore, the turbulence in the vortex core is likely to be anisotropic which means that standard models will again be lacking (Molland et al., 2011, p 343). Using more advanced turbulence models is also beneficial for predicting the flow around the hull to correctly predict stern separation and bilge vortices. Anisotropic models will give better predictions of resistance and manoeuvring performance (Ismail et al., 2010; Xing et al., 2012). Hybrid URANS-LES methods can also be used to better predict the development of the unsteady flow at the stern (Kornev et al., 2011). Separation and bilge vortices affect not only the forces on the hull but can also affect the propeller inflow. Correctly predicting them is therefore important to achieve high accuracy for self propulsion simulations. There is therefore a motivation for using more advanced models both in terms of capturing the propeller flow but also the flow around the hull.

However, the Reynolds number and the local length scales of the propeller and the hull are still different and so the problem of finding a model suitable to predict them both remains. Separating the modelling of the propeller flow and the flow around the hull thus provides a practical advantage since it allows for each part of the simulation to be carried out using methods better tuned to the local flow regime (Molland et al., 2011, p 340). An example of how a separate modelling method for the propeller can be coupled with a RANS solver is given in Chapter 5.

2.11 Conclusions

This chapter discusses the capabilities of potential flow methods in predicting the added resistance in waves. Overall, the average performance can be predicted with acceptable accuracy with current methods if care is taken which method is applied at what sea state. The asymptotic formulation using pure diffraction by Faltinsen et al. (1980) together with the motion damping based method by Gerritsma and Beukelman (1972) together provide good predictions for most wavelengths. However, these methods are not able to predict local flow features with sufficient accuracy to be able to accurately model the self propelled ship. This requires the viscous wake as well as detailed local flow features to be represented. To achieve this, a NS based solver needs to be used.

The discussions about the dominance of the bow force distribution as well as the non linear interaction of the bow wave and the incoming waves lead to the conclusion that the numerical model must pay special attention to resolving the flow at, and in front of the bow area. Furthermore, the presence of motions and the unsteady flow variations due to waves have an impact on the boundary layer. When developing the numerical method, these effects should be studied in order to capture their effect on both the unsteady wake and the viscous resistance of the hull. Finally, for the true powering performance to be obtained using a numerical model it must be able to capture the unsteady interaction between the wake and the propeller.

Apart from the conclusions drawn in this section from previous studies, new experiments are needed to highlight some effects that will further influence the selection of modelling technique. As stated before, the surge motion will have an impact on the propeller performance and thus the overall powering performance. It is therefore important to establish how the surge force amplitude is affected by different sea states. Most previous studies have solely focused on the mean increase in surge force which does not leave much data from which to draw conclusions about the surge motion. The experimental study, presented in the next chapter therefore presents both the mean added resistance and the amplitude of the surge force. Based on the subjects discussed in this chapter, the experimental study is designed to be directly related to four areas of interest for this thesis.

- How does the forward speed influence the surge force. If linear theory holds well, the speed should mainly influence the results in terms of changing the period of encounter. However, if non linear or viscous effects are present, this will not be true.
- How does superposition in irregular seas hold up at different wave heights and when are non linear effects prominent.
- When does the added resistance stop following a predictable quadratic increase and is the surge force amplitude equally predictable?
- How much does the forward speed affect the heave damping? This chapter has established that the damping of heave (and pitch) motions is very closely connected to the added resistance. It is therefore important to establish if this is affected by the forward speed, something that would not be predicted by linear theory.

Chapter 3

Surge force variations in waves

This chapter concerns the experimental study conducted to gather data related to performance losses in waves. The mean surge force increase as well as the amplitude of the oscillation is recorded and discussed. All the cases tested in this experiment include phenomena that are identified as having a possibility to affect the validity of potential flow for modelling added resistance in waves. The conclusions drawn from the results of this study are related both to their importance for potential flow but also how they affect the choice between potential flow and NS-based methods. Furthermore, the gathered data will be useful for future validation studies regarding how well certain non linear phenomena can be predicted with numerical methods.

3.1 Setup

Estimates of performance of ships in waves using model testing can be obtained in two ways (ITTC, 2011).

- A model propelled with a constant force using a sub-carriage (or with a free model fitted with propulsion equipment), measuring the speed loss.
- A carriage mounted model running at a constant speed, measuring the resulting resistance.

In terms of the calculated performance in waves, these two methods have been shown to be equivalent (Journée, 1976*b*). Using constant speed results in much higher variations of the resistance force (due to the fact that the model is not free to surge) as well as other motions which may lead to lower accuracy due to a higher range of operation for the force gauges and potentiometers (ITTC, 2011). However, to successfully conduct experiments with constant thrust, a much more complex towing apparatus is needed

(ITTC, 2011). For the experiments in this thesis, the constant speed method is chosen to avoid complications arising from installing self propulsion equipment in the model or modifications to the carriage.

All experiments are performed using the Leander class frigate hull form, the particulars of which are given in Table 3.1 where U_s is the service speed of the full scale ship for reference.

TABLE 3.1: Particulars of Leander frigate model.

	Full scale	Model scale
Scale factor	1 : 1	1 : 43.62
Lpp (m)	109.72	2.52
B (m)	12.36	0.29
T (m)	4.50	0.10
Δ	2440 tonnes	29.4 kg
U_s (m/s)	9.3 (18 kts, $Fn = 0.28$)	1.4
LCG aft of amidships (m)	3.96	0.09*
VCG above keel (m)	4.27	0.098*
TCG from centreline (m)	0	0
Pitch radius of gyration (% of LOA)	25.26	25.66**

The experiments were performed in the Southampton Solent University towing tank between the 12^{th} and the 14^{th} of April 2011. The particulars of the tank are given in Table 3.2.

TABLE 3.2: Particulars of the Southampton Solent University towing tank.

Length (m)	60
Width (m)	3.7
Water depth (m)	1.86
Max. carriage speed (m/s)	4.6
Water temperature during tests (°C)	15.4
Wave maker	Computer controlled electromechanical flap type

3.1.1 Measurement equipment

Forces and displacements are measured using conventional strain gauges and potentiometers. As a part of a study on the applicability of wireless sensors to the capturing of motions in towing tank experiments (Bennett et al., 2014; Bennett, Windén, Brooks, Turnock and Hudson, 2012; Bennett, Windén, Brooks, Turnock, Hudson, Forrester and

*Estimate, see section 3.1.2, **Best achieved representation, see section 3.1.2

Taunton, 2012; Denchfield et al., 2011), the model is also fitted with three wireless MARG (Magnetic, Angular Rate and Gravity) sensors in some tests.

To record the wave elevation, a sword shaped resistance probe suitable for forward speed is used. This is mounted 1.27 m to starboard of the centreline and 0.62 m aft of the forward perpendicular. This location can safely be considered to be undisturbed by the hull since; if one assumes that the bow wave forms a 19.50 degree angle with the centreline, the last hull generated wave crest would form at 23.4 cm to starboard of the centreline at the chosen longitudinal location.

3.1.2 Weight distribution

The pitch radius of gyration k_{55} for the model is tuned by swinging the model according to Lloyd (1998). The model is swung about a fixed point $h_s = 1.350$ m above the keel (with the vertical line from this point passing through the centre of gravity) and the time for ten oscillations T_{s10} is measured. The pitch radius of gyration is then calculated as

$$k_{55} = \sqrt{\left(\frac{T_s}{2\pi}\right)^2 g(h_s - VCG) - (h_s - VCG)^2} \tag{3.1}$$

where

$$T_s = \frac{T_{s10}}{10} \tag{3.2}$$

Weights are redistributed until the radius of gyration matches the one of the full scale ship as closely as possible. The results of the measurements after tuning are shown in Table 3.3. Three measurements are taken and T_{s10} calculated as the mean value.

TABLE 3.3: Tuning of model pitch inertia in experiments.

T_{s101}	25.50 s
T_{s102}	25.20 s
T_{s103}	25.60 s
T_{s10}	25.43 s
k_{55}	0.667 m (25.66% of LOA)

The correct LCG and TCG are obtained by shifting weights with the model afloat and ensuring 0° trim and heel using a spirit level. This changes the k_55 obtained as explained above. The model was re-tuned for k_{55} two times until both satisfactory values of trim and radius of gyration were obtained. No direct tuning of VCG is done other than from experience of previous use of the same model.

3.1.3 Data collection and processing

The experimental data in this chapter regarding resistance in regular waves is presented using both the mean increase in resistance R_{AW} and the amplitude of the force variations R_{AWa}. Both of these quantities are defined in Figure 3.1. R_{AW} is obtained by taking the mean of the signal and subtracting the calm water resistance R_{CW} at the current speed. The amplitude R_{AWa}, the amplitudes of heave and pitch oscillations x_{30} and x_{50} and the wave amplitude ζ_0 are calculated by taking the RMS of the signal around the mean value and multiplying this with $\sqrt{2}$ so that, in the case of resistance

$$R_{AWa} = \sqrt{2}\, RMS\langle R(t) - R_{AW} - R_{CW}\rangle \tag{3.3}$$

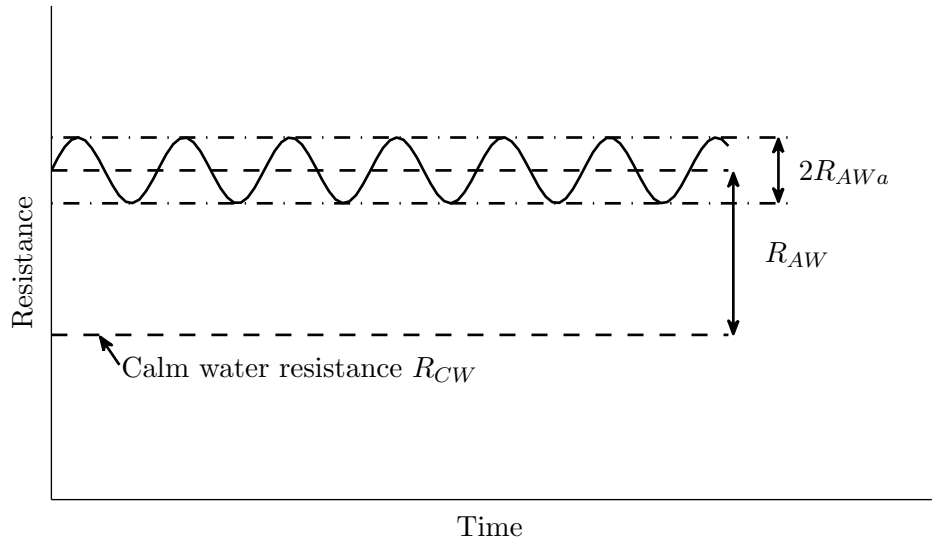

FIGURE 3.1: Definition of measured quantities of added resistance.

To obtain R_{CW}, a set of experiments are conducted in calm water at all speeds presented in the experimental study. For comparison, the results are shown in Figure 3.2 together with results from earlier experiments with the same model and hull form by Denchfield (2011). This comparison shows good correlation with previous results except for a slightly steeper increase with speed.

For tests in regular waves, at least 20 encountered waves are ensured for the majority of tests in accordance with ITTC recommended procedures which states that 20-25 encounters is enough for resistance tests (ITTC, 2011). The ITTC also recommends a timespan corresponding to 20-30 minutes in full scale for tests in irregular waves (ITTC, 2011). In accordance with this, around 20 minutes of full scale time is measured in this case. This is accomplished by three separate runs in each sea state. However, because of the many non-linear effects on added resistance it has been suggested that, to get a properly converged resistance estimate in irregular waves, a time span of 1-1.5 hours in

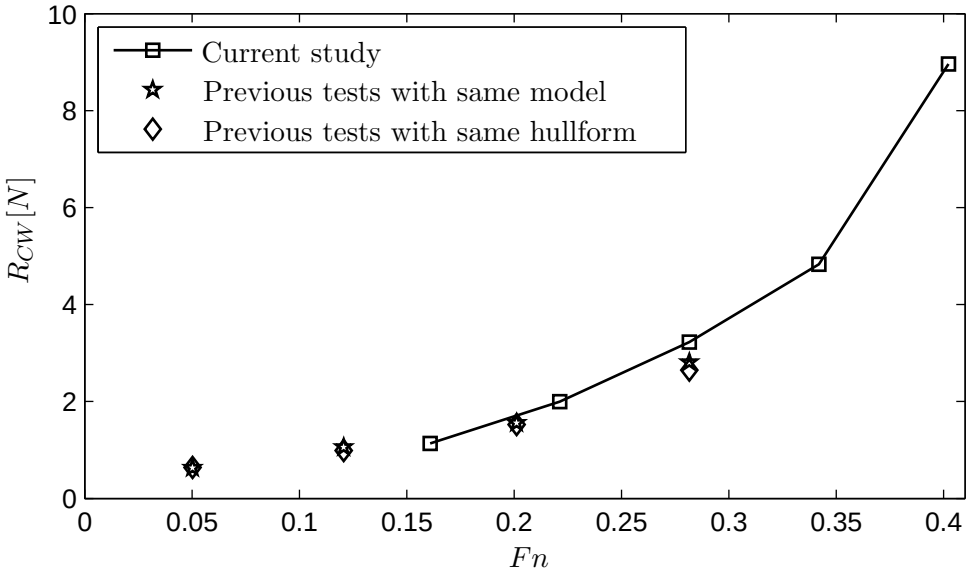

FIGURE 3.2: Comparison of calm water resistance for this setup with previous experiments.

full scale is needed (Kim and Kim, 2010; Naito and Kihara, 1993). This may influence the quality of the resistance spectra obtained from these tests.

In cases where a non dimensional added resistance coefficient is presented, for the mean increase this is defined in Eqn. 2.5 and for amplitude, it is defined as

$$\sigma_{AWa} = \frac{R_{AWa} Lpp}{\rho g \zeta_0^2 B^2} \tag{3.4}$$

3.2 Uncertainty analysis

A separate analysis of the uncertainties regarding measurements obtained using an identical setup is conducted. This is based on a set of repeated tests in regular waves at different wavelengths and -heights conducted by Bennett, Windén, Brooks, Turnock, Hudson, Forrester and Taunton (2012). The uncertainty is obtained from these tests using the method of Coleman and Steele (1999) and assuming 95% confidence in the results. The overall uncertainty for a measured dataset is assumed to be a combination of systematic and precision errors and is calculated as

$$U_{\bar{r}} = \sqrt{B_{\bar{r}}^2 + P_{\bar{r}}^2} \tag{3.5}$$

The systematic error B_r is assumed based on the range and precision of the measurement equipment and is given in Table 3.4. The precision error is given by the standard deviation S_r of the repeated tests and the number of repeats N_r as

$$P_{\overline{r}} = \frac{2S_r}{\sqrt{N_r}} \tag{3.6}$$

TABLE 3.4: Estimates of systematic errors in measurements.

Quantity	B_r
Resistance	0.2 N
Wave elevation	0.5 mm
Heave displacement	0.5 mm
Pitch angle	0.05^o

Three different wave amplitudes are considered; 25.2 mm, 50.3 mm and 62.9 mm with 3-5 wavelengths for each one. Two speeds are considered, zero speed and service speed. For most of the wave conditions, three repeats are performed. The results of the uncertainty analysis are presented in Figure 3.3 in terms of a percentage of the average value for the measured quantity over the repeated tests.

A level of uncertainty of less than 10% of the measured values is shown for all cases except for low wave heights at zero speed. All measurements at the lowest wave amplitude ($\zeta_0 = 25.2$ mm) also show a higher level of uncertainty. This stems from the low quality of these waves as seen in the increase in uncertainty for the wave elevation at $\zeta_0 = 25.2$ mm compared to that of higher amplitude waves.

No accurate way of monitoring the carriage speed is available, however; in tests where the period of encounter is kept constant a standard deviation of the recorded wave encounter period of 2.7% is experienced. This leads to the conclusion that the interplay of carriage speed and wave maker is satisfactory. In tests with zero speed the encountered period shows a standard deviation of 2.5% which indicates that the wave maker provides the greatest source of error in this interplay. As a consequence of this conclusion, the uncertainty of the recorded wavelengths is assumed to be <3%.

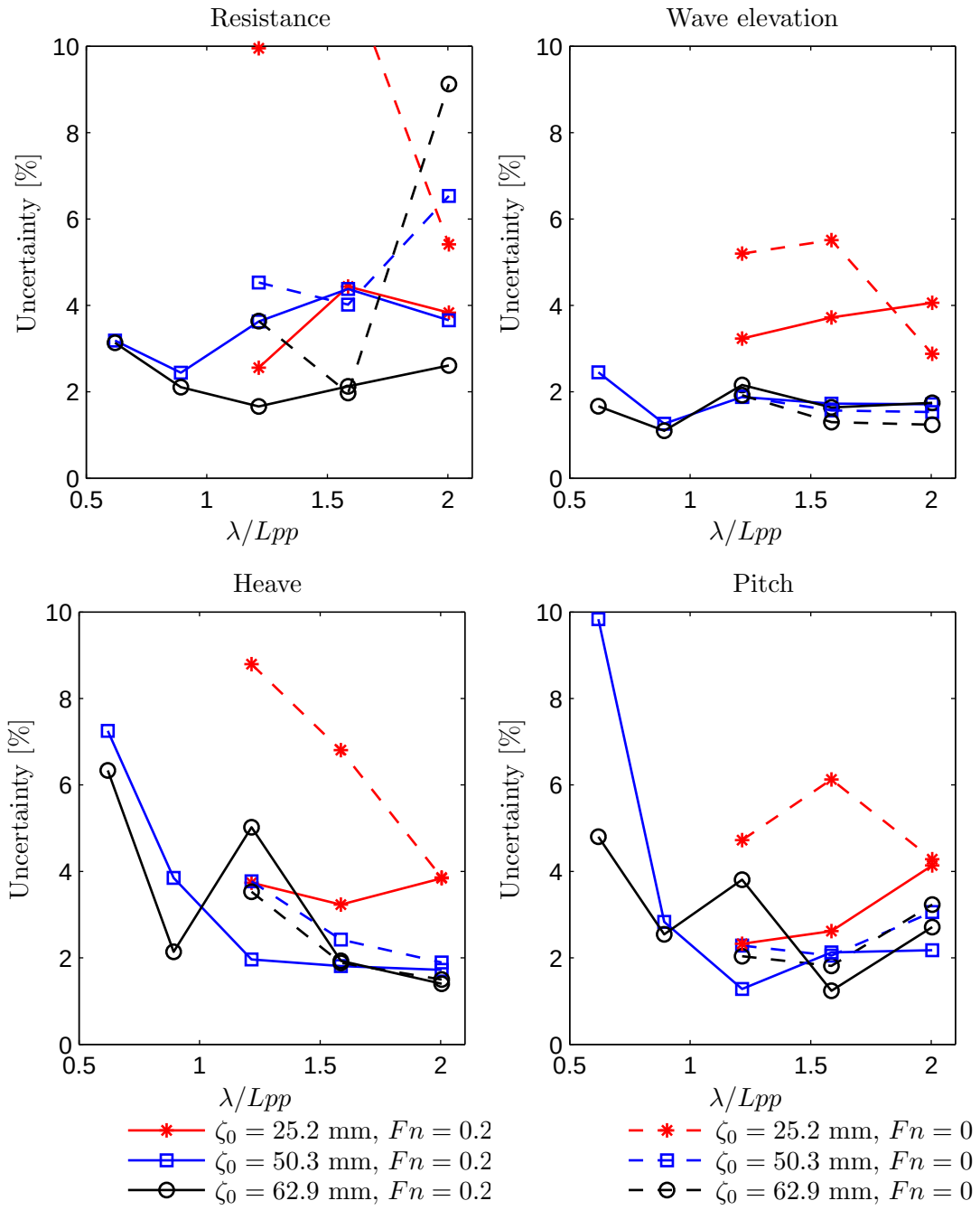

FIGURE 3.3: Results of uncertainty analysis for the experimental setup.

The results of Figure 3.3 are translated to representative values for this setup to be used to estimate uncertainties in the following studies. These representative values are shown in Table 3.5. Wherever data for shorter waves is missing, 10% is set as an estimate for waves shorter than $\lambda/Lpp < 1$.

Since the tests are carried out over the course of several days, the measurement equipment is tested for variations in recorded values. This is done by testing against known displacements at the end of the experiment. The potentiometers measuring heave and pitch show a deviation of approximately 0.9% from the original rate. The resistance

TABLE 3.5: Representative values of $U_{\overline{r}}$ for the experimental setup.

		$\zeta_0 < 50mm$	$50mm < \zeta_0 < 63mm$	$\zeta_0 > 63mm$
Resistance	$\lambda/Lpp < 1$	10%	8%	8%
	$\lambda/Lpp > 1$	10%	5%	3%
Wave elevation	$\lambda/Lpp < 1$	10%	2.5%	2.5%
	$\lambda/Lpp > 1$	6%	2.5%	2.5%
Heave displacement	$\lambda/Lpp < 1$	10%	8%	8%
	$\lambda/Lpp > 1$	9%	3%	3%
Pitch angle	$\lambda/Lpp < 1$	10%	10%	6%
	$\lambda/Lpp > 1$	6%	2.5%	3%

gauge shows a deviation of >0.1% as does the side force gauge. The wave probe is the largest source of error and is tested and recalibrated three times. The wave probe shows a constant slip in its rate of 4.3% for each day of testing which may also influence the error of the recorded wave amplitudes.

The values in table 3.5 are comparable to example values given by the ITTC (2005) where 2 - 3.5% error across the frequency range for pitch and 3.5 - 6% error for heave is quoted. This shows that the used experimental rig should produce reasonably accurate results with international standards.

Sources of error that are hard to give exact values to regarding their contribution to the final results include

- The model is not free to surge.
- The model VCG is not explicitly tuned.
- The clamp fixing the model in yaw is not rigid enough causing some oscillations.
- The correct model pitch radius of gyration is very hard to achieve with crude methods.
- Water immersion and shifting of weights during seakeeping tests may influence the balancing of the model.
- Water immersion may influence the on-board pitch potentiometer.
- The hull surface has imperfections giving an overestimation of the bare-hull resistance.
- The model features a replaceable bow section which forms a narrow vertical gap possibly influencing the resistance.
- The model draught is not controlled other than by ensuring the correct displacement.

3.3 Speed dependency tests

A series of tests aimed at gathering data regarding how the surge force is influenced by forward speed are conducted. This is relevant both in terms of discussing non linear effects but also; possibly the influence of viscous effects since nature of the boundary layer varies with the forward speed. In these tests, the period of encounter and wave height are kept constant and the forward speed varied from 0 to 2 m/s corresponding to a Froude number range of 0 to 0.40. The period of encounter T_e is made non dimensional here as

$$\tau_e = T_e \left(\frac{Lpp}{g} \right)^{-0.5} \tag{3.7}$$

Three series are recorded, one where $\tau_e = 1.38$, one where $\tau_e = 1.97$ and one where $\tau_e = 2.37$. The full list of conducted tests is shown in Table 3.6.

TABLE 3.6: Tested wave conditions in speed dependency tests.

$\tau_e = 1.38$			$\tau_e = 1.97$			$\tau_e = 2.37$		
Fn	λ/Lpp	ζ_0	Fn	λ/Lpp	ζ_0	Fn	λ/Lpp	ζ_0
0.16	0.67	0.025 m	0.16	1.16	0.025 m	0.16	1.57	0.025 m
0.22	0.79	0.025 m	0.22	1.36	0.025 m	0.22	1.79	0.025 m
0.28	0.92	0.025 m	0.28	1.53	0.025 m	0.28	2.03	0.025 m
0.34	1.03	0.025 m	0.34	1.71	0.025 m	0.34	2.26	0.025 m
0.40	1.15	0.025 m	0.4	1.90	0.025 m	0.40	2.48	0.025 m

3.3.1 Results of speed dependency tests

The results of the speed dependency study are shown in Figure 3.4 and 3.5. Since added resistance is known to be much influenced by the nature of the heave and pitch oscillations, a representation of these motions at different speeds is shown in Figure 3.6 for the three different periods of encounter.

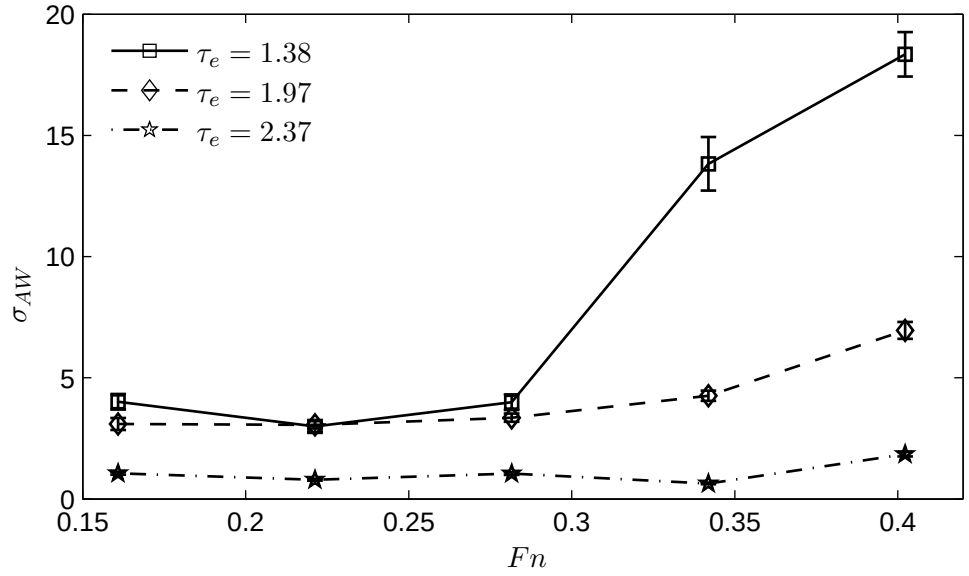

FIGURE 3.4: Measurements of mean added resistance at different speeds with the period of encounter kept constant.

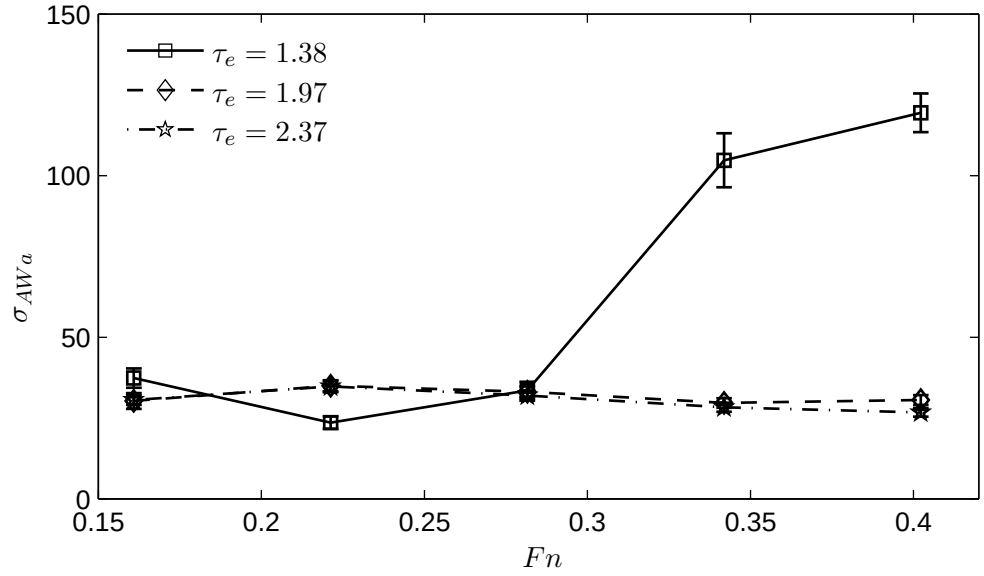

FIGURE 3.5: Measurements of added resistance amplitude at different speeds with the period of encounter kept constant.

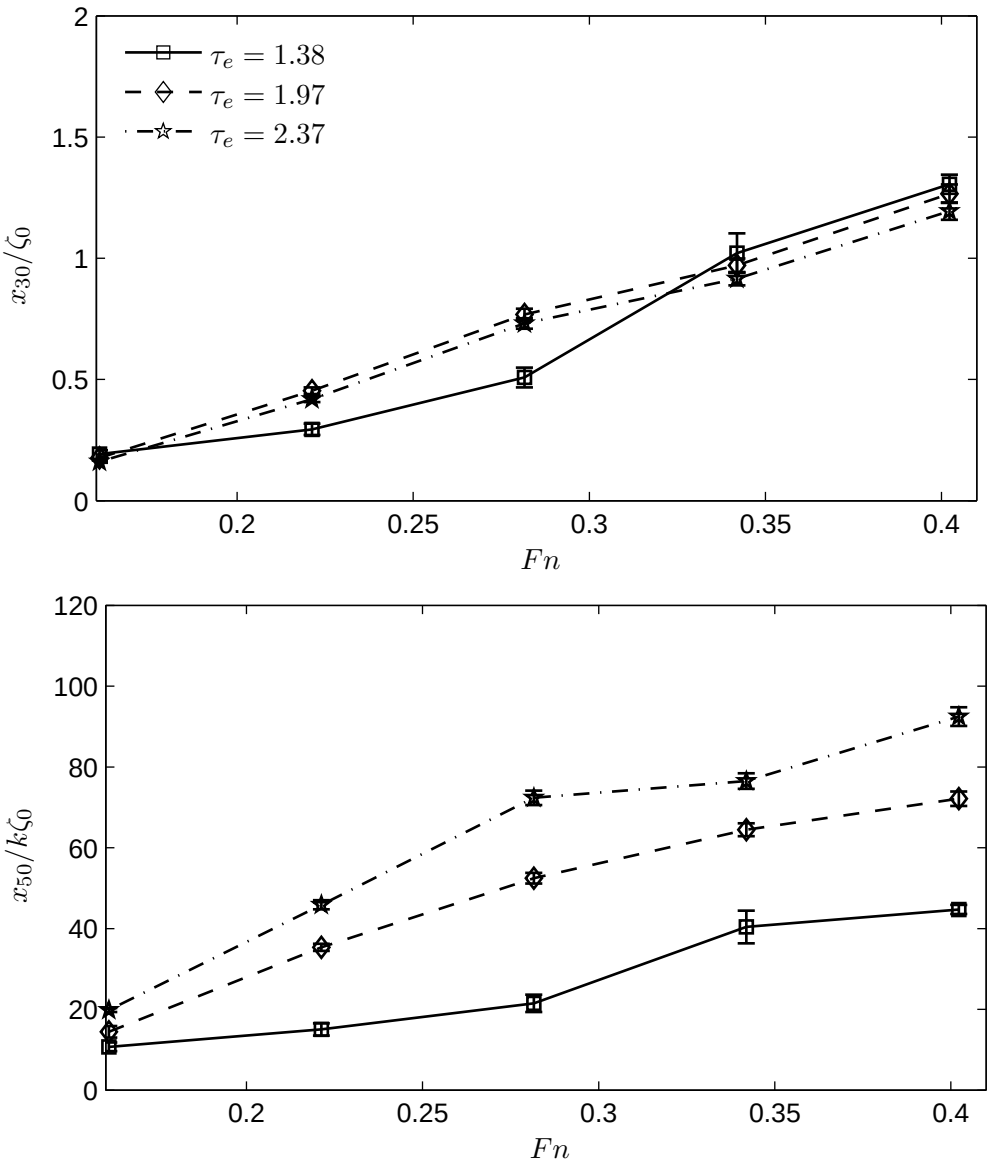

FIGURE 3.6: Heave and pitch responses different speeds with the period of encounter kept constant.

3.3.2 Conclusions of speed dependency tests

In Figure 3.4, the variation of R_{AW} with speed is shown to be dependent on the period of encounter. The impact of speed is highest for $\tau_e = 1.38$ and decreasing with increasing τ_e. Looking at Figures 3.6 and 3.4, the variations of σ_{AW} with speed at particular τ_e appears to be strongly related to the trend of increasing heave- and possibly pitch motions with speed at that period. This increase is likely to stem from the increase in wavelength (due to the fact that the period of encounter is kept constant.) This is to be expected since the transfer function for heave is at its maximum for lower frequencies. The variations in R_{AW} between different periods of encounter come from the relative synchronism of heave, pitch and the natural frequencies of the hull. This is know as the added resistance transfer function and it is not studied here but has a well defined general shape (see e.g. Strøm-Tejsen and Yeh (1973).)

The amplitude of the resistance variations σ_{AWa} does not follow the same pattern as σ_{AW}. Here, the magnitude decreases slightly with increased speed except for $\tau_e = 1.38$. Since both pitch and heave motions are increasing, this decrease cannot be explained with linear theory. The influence of the period of encounter is also much more pronounced for the amplitude variations with $\tau_e = 1.97$ and $\tau_e = 2.37$ giving very similar results and results for $\tau_e = 1.38$ standing out more.

These tests show how the surge force can be presented as a function of speed. This presentation however, is not entirely fit for purpose due to the fact that the varying wavelength used to keep the period of encounter constant has an effect on the results through the heave and pitch responses. This means that conclusions as to what effect the actual speed has are hard to draw. It would be possible to suppress the effect of wavelength by normalising the response with the response in the same wavelength at zero speed. The complete set of wavelengths used in this section are not tested at zero speed so no such normalisation can be made.

3.4 Irregular wave tests

To gather data regarding the limitations of the superposition principle for added resistance in irregular waves, test in two irregular sea states are conducted. Both sea states are generated according to a JONSWAP spectrum with a peak period of 1.45 s and $\gamma = 3.3$. The significant wave heights of the two systems are 0.08 m and 0.12 m. The quality of the resulting waves is shown in Figure 3.7 as the spectral ordinate S_ζ generated from analysis of the wave probe signal compared to the JONSWAP input $S_{J\zeta}$ fed to the wave maker.

If the wave elevation ζ of the irregular wave is separated into its components by Fourier analysis so that

$$\zeta(t) = \sum \zeta_{0n} \cos(\omega_n t + \varepsilon_{\zeta n}) \tag{3.8}$$

S_ζ can be calculated as

$$S_\zeta(\omega_n) = \frac{\zeta_{0n}^2}{2\Delta\omega} \tag{3.9}$$

where $\Delta\omega$ is the spacing between frequencies used in the Fourier analysis.

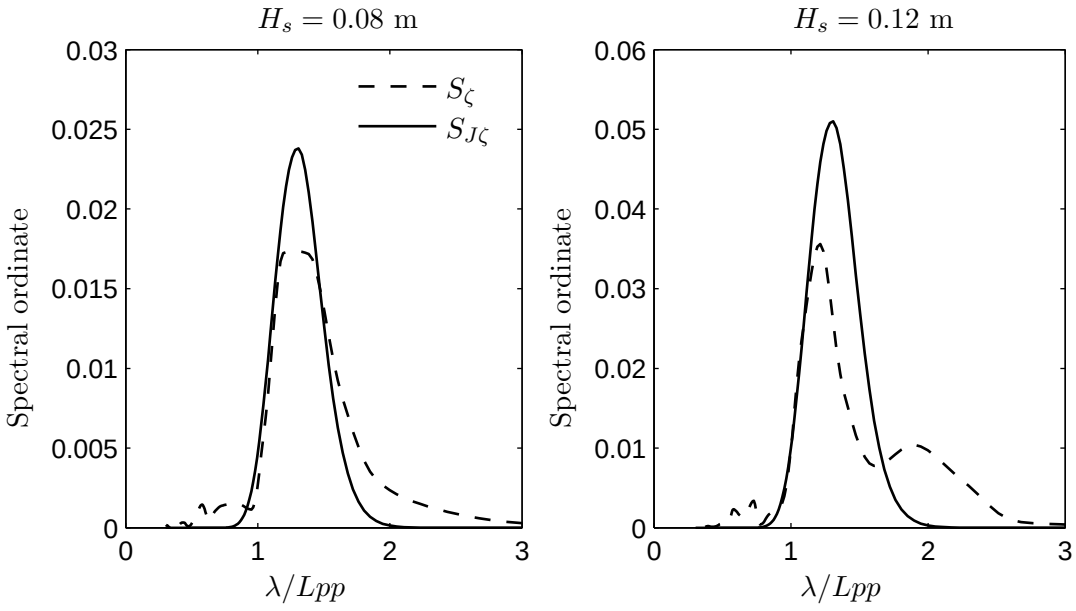

FIGURE 3.7: Spectral ordinate generated by wave probe data compared to input JONSWAP spectrum.

From the amplitudes $\zeta_{0n}(\omega_n)$ making up the irregular wave system, four are chosen for each significant wave height to be tested separately as regular waves. This is done so that the frequency and amplitude of the regular wave correspond to a point on the amplitude spectrum as shown in Figure 3.8*. The components were selected to cover the peak region and to avoid wave components that were poorly represented by the wave maker. The selected regular wave components are presented in Table 3.7.

*Slight discrepancy due to different algorithms used for Fourier analysis during experiments and in later analysis

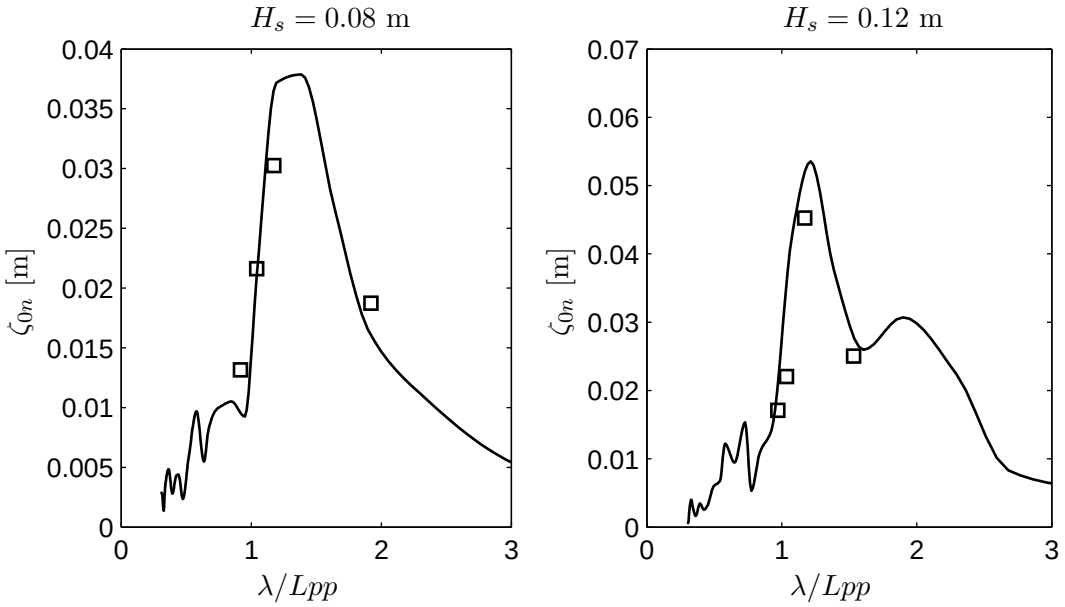

FIGURE 3.8: Amplitude spectrum of waves from wave probe analysis with selected waves for retesting as regular waves.

TABLE 3.7: Selected regular wave components from irregular wave spectrum to be tested separately.

$H_s = 0.08$		$H_s = 0.12$	
ζ_0	λ/Lpp	ζ_0	λ/Lpp
0.0134 m	0.9163	0.0171 m	0.9705
0.0216 m	1.0419	0.0220 m	1.0355
0.0302 m	1.1735	0.0453 m	1.1702
0.0186 m	1.9209	0.0252 m	1.5329

3.4.1 Results of irregular wave tests

The amplitude spectrum of surge force R_{AWan} is defined so that

$$R(t) = R_{CW} + R_{AWi} + \sum R_{AWan} \cos(\omega_n t + \varepsilon_{Rn}) \tag{3.10}$$

when $R(t)$ is the resistance measured during the experiments and R_{AWi} is the mean added resistance in the irregular waves. As was shown in section 3.2, the quality of the produced waves decreases with decreasing wave height. To avoid noise and bad quality waves influencing the results when presenting the nondimensionalised added resistance, the amplitude resistance signal is passed through a band-pass filter before the analysis. The filter is set to allow frequencies between $0.8 < \lambda/Lpp < 2.5$ to pass with unaltered amplitude.

If R_{AWan} at each frequency ω_n is plotted against the corresponding wave amplitude ζ_{0n} at that frequency, it is possible to present the results as a variation of surge force with wave amplitude. This is shown in Figure 3.9. This presentation assumes that a component of force at ω_n stems from the wave component of the same frequency.

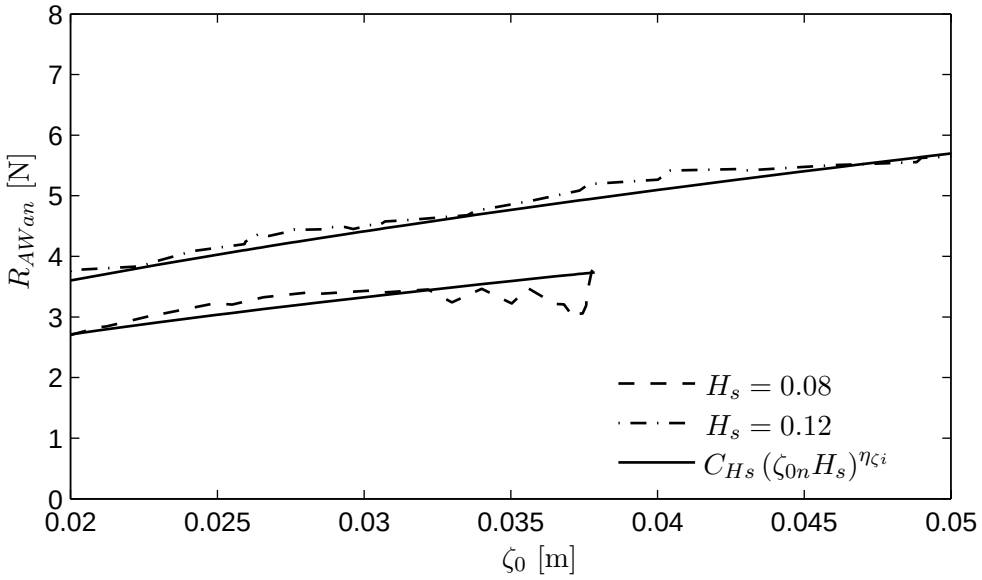

FIGURE 3.9: Added resistance as a function of wave amplitude in irregular waves.

For this case, the surge force amplitude corresponding to a specific wave height in an irregular sea is found to be proportional to

$$R_{AWa}(\omega_n) \sim C_{Hs}\,(\zeta_{0n}H_s)^{\eta_{\zeta i}} \tag{3.11}$$

where C_{Hs}=70 and $\eta_{\zeta i}$=0.5. This relation can be used to show an estimate of the added resistance in irregular waves based on the wave amplitude spectrum. The estimate R_{AWne} is defined as

$$R_{AWne}(\omega_n) = C_{Hs}\,(H_s\zeta_{0n}(\omega_n))^{\eta_{\zeta i}} \tag{3.12}$$

This estimate together with the resistance in the chosen regular waves (shown in Figure 3.8) and the measured amplitude spectrum R_{AWan} are shown in Figure 3.10. It should be noted that, since Eqn. 3.12 represents a curve fit and not a direct description of force components, the units are not consistent. If data from more experiments were available, it would be possible to perform a dimension analysis for this expression to find possible physical meaning of the coefficients.

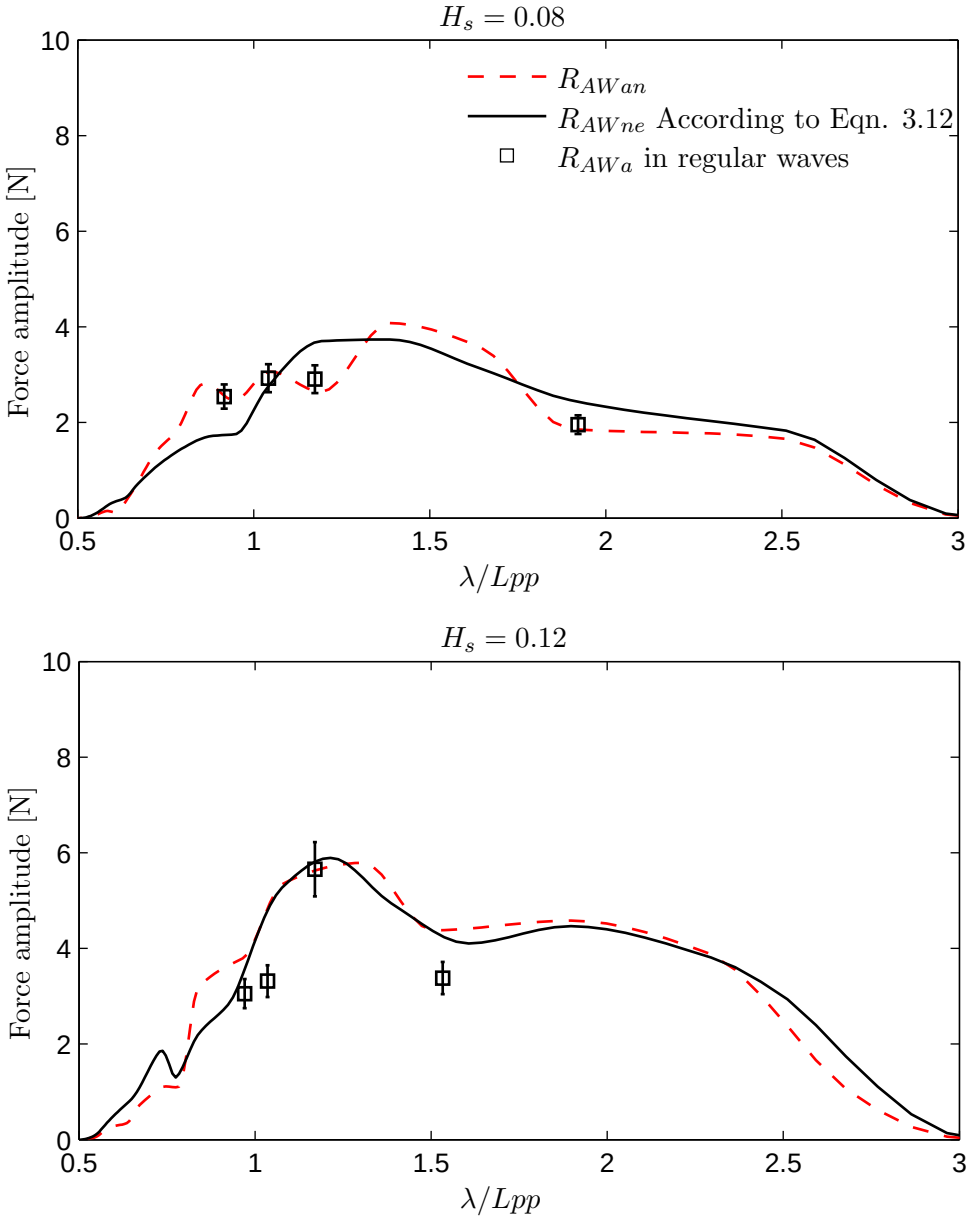

FIGURE 3.10: Measured amplitude spectrum of added resistance in irregular waves compared with estimates based on wave spectra and tests in regular waves.

3.4.2 Conclusions of irregular waves tests

For waves of lower amplitude, the regular wave analysis of added resistance conforms better to the irregular wave amplitude spectrum of force. For higher amplitude waves, the correlation is worse suggesting reduced validity of the superposition principle. This is consistent with previous literature as was discussed in Section 2.7. On the other hand, the estimate based on the wave spectrum and Eqn. 3.12 works best for the larger wave height. As shown before, large errors in the frequency analysis stem from the poor quality of the waves and the high levels of noise. The quality is improved with increased

wave height which is probably why the R_{AWne}-estimate is better for $H_s = 0.12m$ in Figure 3.10.

The estimate R_{AWne} is unlikely to hold as it is presented in Egn. 3.12 for sea states and hullforms other than the one tested here. The coefficients C_{Hs} and $\eta_{\zeta i}$ are based solely on results from this study and are likely to be different in other cases. The estimate is useful however, for showing the strong relation between the wave amplitude spectrum and the resistance amplitude spectrum. This is shown to be stronger than the correlation between regular wave tests and tests in irregular seas for waves of higher amplitude pointing to strong non-linear coupling effects between frequencies for such waves.

These results suggest problems with using potential flow methods based on addition of regular wave components for prediction of performance in irregular seas with larger significant wave heights. There is a problem with drawing definite conclusions from these tests for two reasons. Firstly, the quality of the waves generated are not high enough to distinguish in detail between the energy content of the signal at different frequencies, especially away from the peaks. The measured wave spectrum does not conform well to the JONSWAP input as seen in Figure 3.7 which shows that the quality of the waves is not well controlled. Secondly, the sample lengths might be too short to capture all effects that influence the added resistance as discussed in Section 3.1.3.

3.5 Wave height linearity tests

To gather data regarding the range of validity of the assumption that $R_{AW} \sim \zeta_0^2$ and if this holds true also for the surge force amplitude, a series of tests with varying wave amplitude are conducted. The tests are carried out at zero speed and at service speed ($Fn = 0.28$.) The full set of tested wave amplitudes is presented in Table 3.8. The wave length is chosen as to give the same encounter frequency at both Froude numbers and that gives as little uncertainty as possible.

TABLE 3.8: Tested wave amplitudes in wave height linearity tests.

$Fn = 0.28$			$Fn = 0$		
τ_e	λ/Lpp	ζ_0	τ_e	λ/Lpp	ζ_0
2.37 s	2	0.030 m	2.37 s	0.795	0.030 m
2.37 s	2	0.035 m	2.37 s	0.795	0.035 m
2.37 s	2	0.045 m	2.37 s	0.795	0.045 m
2.37 s	2	0.060 m	2.37 s	0.795	0.060 m
2.37 s	2	0.075 m	2.37 s	0.795	0.075 m
2.37 s	2	0.090 m	2.37 s	0.795	0.090 m

3.5.1 Results of wave height linearity tests

The results are presented in terms of absolute force in Figures 3.11 and 3.12. To illustrate any deviation from a quadratic increase, the nondimensionalised added resistance coefficients are shown in Figures 3.13 and 3.14. Because added resistance is normalised with ζ_0^2, if the trend was completely quadratic σ_{AW} and σ_{AWa} would show constant values with varying amplitude.

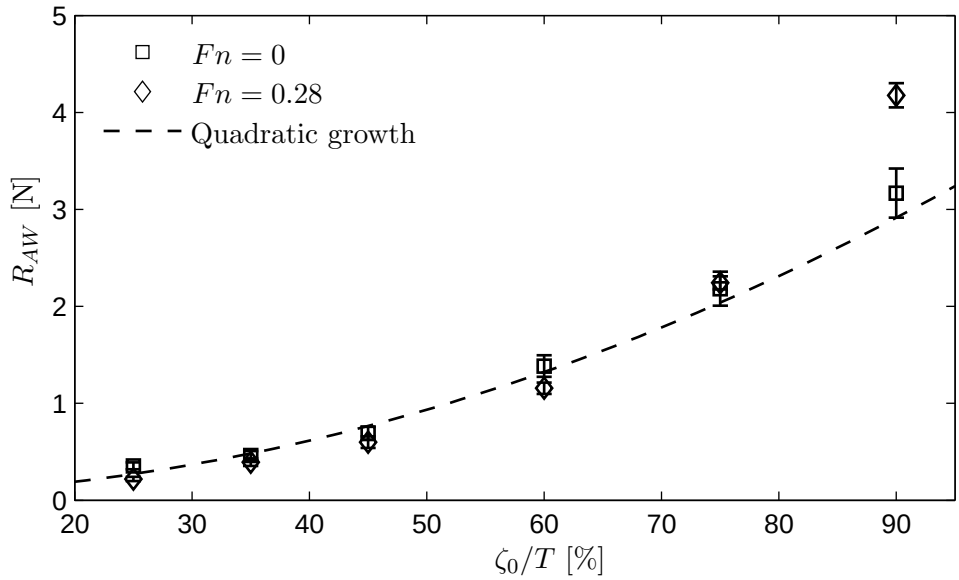

FIGURE 3.11: Measured variation of mean added resistance with wave amplitude for $Fn = 0$ and $Fn = 0.28$.

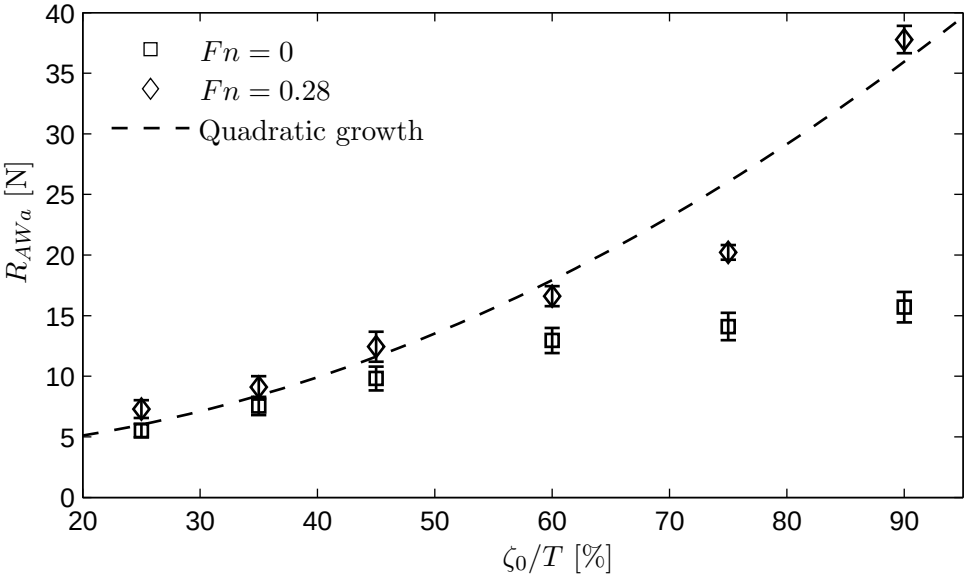

FIGURE 3.12: Measured variation of added resistance amplitude with wave amplitude for $Fn = 0$ and $Fn = 0.28$.

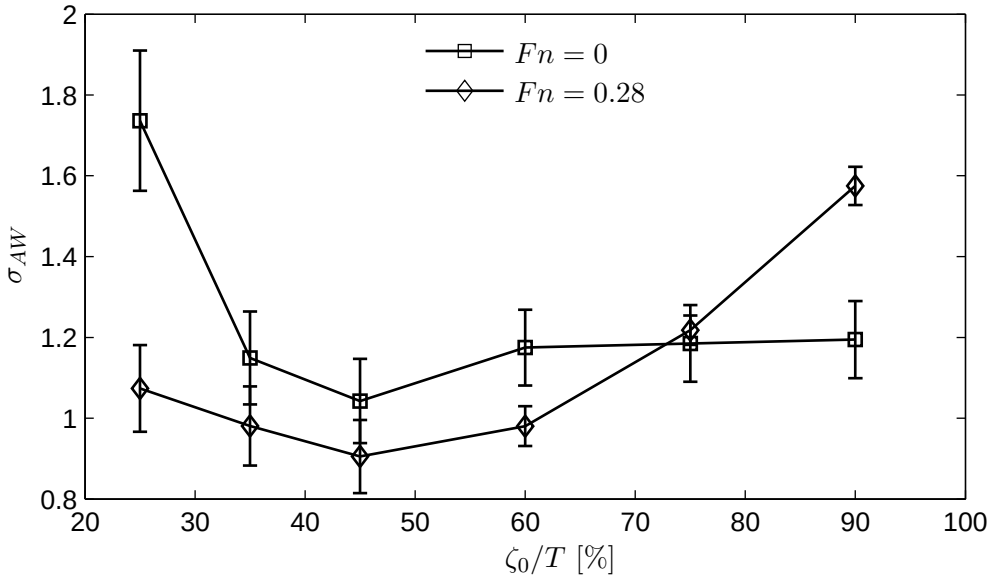

FIGURE 3.13: Measured variation of mean added resistance coefficient with wave amplitude for $Fn = 0$ and $Fn = 0.28$.

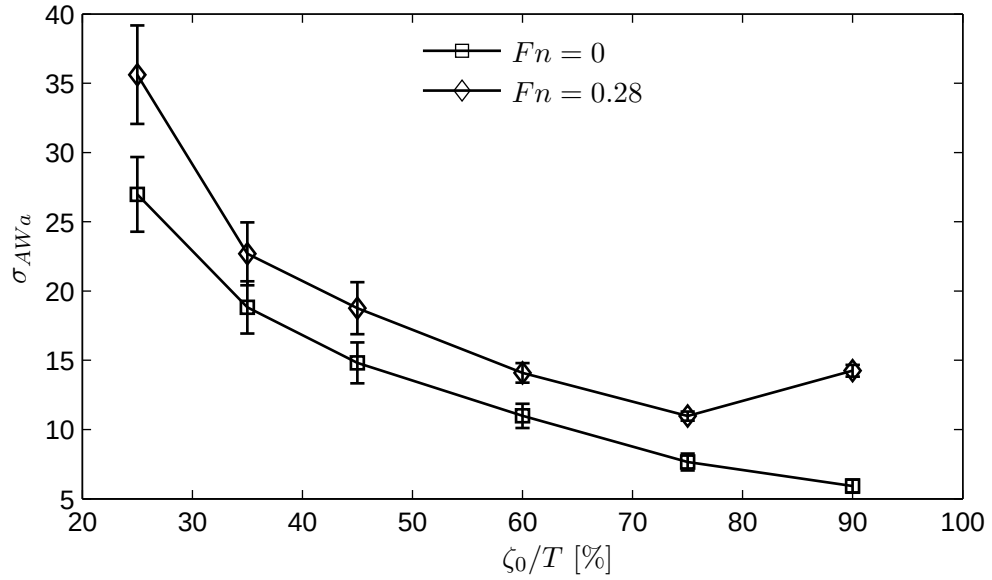

FIGURE 3.14: Measured variation of added resistance coefficient amplitude with wave amplitude for $Fn = 0$ and $Fn = 0.28$.

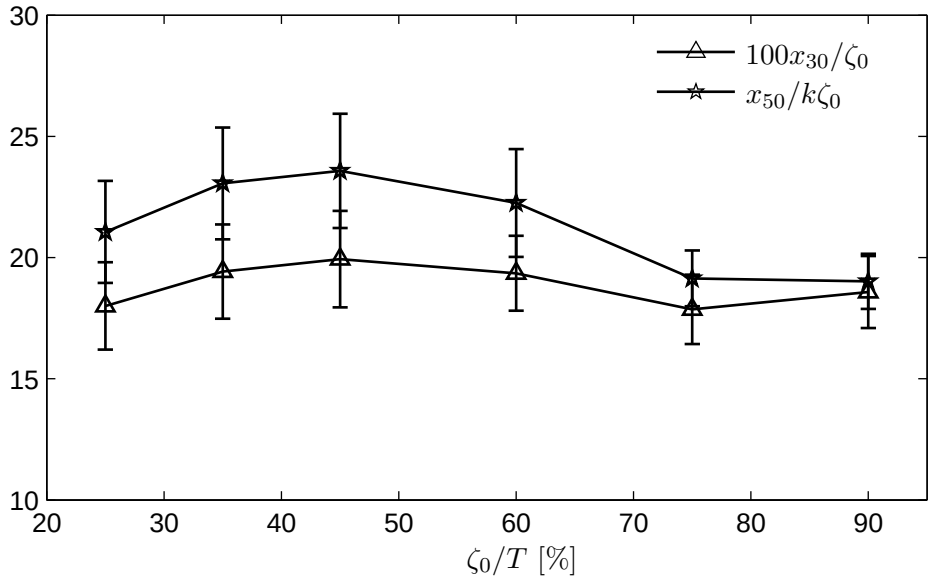

FIGURE 3.15: Measured variation of heave and pitch with wave amplitude for $Fn = 0$.

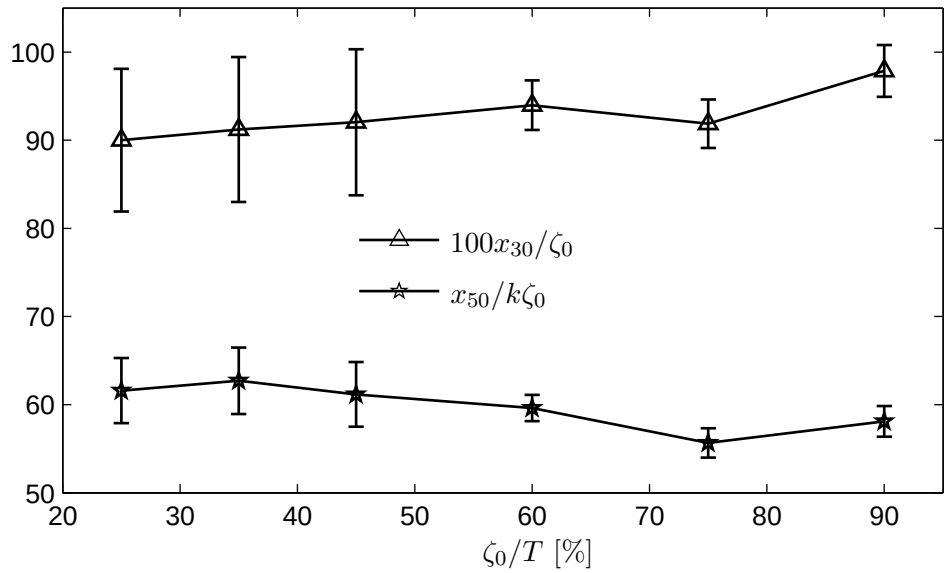

FIGURE 3.16: Measured variation of heave and pitch with wave amplitude for $Fn = 0.28$.

3.5.2 Conclusions of wave height linearity tests

Figure 3.11 shows that R_{AW} for both speeds approximately follows a quadratic increase although deviation is seen at $\zeta_0/T = 0.9$. Very violent motions are experienced at this wave amplitude and both the resistance gauge and the heave potentiometer are occasionally topped out. For this reason no conclusion can be drawn about the trend for $\zeta_0/T > 0.75$. Despite appearing to conform well to the quadratic trend in Figure 3.11, the added resistance coefficient in Figure 3.13 shows, that there is a deviation from a quadratic trend that is more distinct than what would come from mere noise at $Fn = 0.28$. The trend for $Fn = 0$ seems to be relatively constant at $\sigma_{AW} \approx 1.15$ taking the large uncertainty into account. A deviation from this trend is seen at low wave amplitudes which, again, may be due to poor quality waves.

The results in Figure 3.12 show that R_{AWa} does not appear to follow a distinct quadratic increase with wave height for any of the speeds, this is supported by a distinct variation of σ_{AWa} with wave amplitude as seen in Figure 3.14. Even though R_{AWa} is not following a quadratic trend, it is still showing a steady increase with wave height. The heave and pitch responses in Figures 3.15 and 3.16 show an initial increase or relatively constant amplitude relative to the wave amplitude followed by a decrease with increasing wave amplitudes. More energy is thus consumed in damping the heave and pitch motions for higher amplitude waves which may be attributed to effects such as wave breaking and non-linear damping. These effects also appear to change with forward speed. The increase in heave and pitch response before $\zeta_0/T = 0.5$ and decrease at $\zeta_0/T > 0.5$ could explain why R_{AWa} increases faster before and levels off after $\zeta_0/T = 0.5$.

By changing the exponent on wave height used to normalise* the surge force amplitude, a more suitable trend than ζ_0^2 can be found. This is shown in Figure 3.17. Here, $\eta_\zeta = 0.8$ is found to give the best result. Note that this variation of surge force amplitude with wave amplitude is different than the one found for irregular waves ($\eta_{\zeta i} = 0.5$.)

The conclusion is that the assumption that $R_{AW} \sim \zeta_0^2$ holds well but that the increase in amplitude is more closely connected to variations in heave and pitch motions with increasing wave amplitude. These seem to be influenced by non linear effects which makes the amplitude R_{AWa} harder to predict than the mean added resistance R_{AW}.

As was the conclusion from the speed dependency tests (see Section 3.3.2), the static difference in added resistance between different Froude numbers is mostly due to the fact that the heave response is greater for the longer waves needed to keep the period of encounter constant at higher speeds. This should not however, affect the difference in the rate of increase with increasing wave height which is seen in Figure 3.12.

*Normalisation is only for illustration of trends, if the exponent is $\neq 2$, σ_{AW} no longer represents a non dimensionalisation of force.

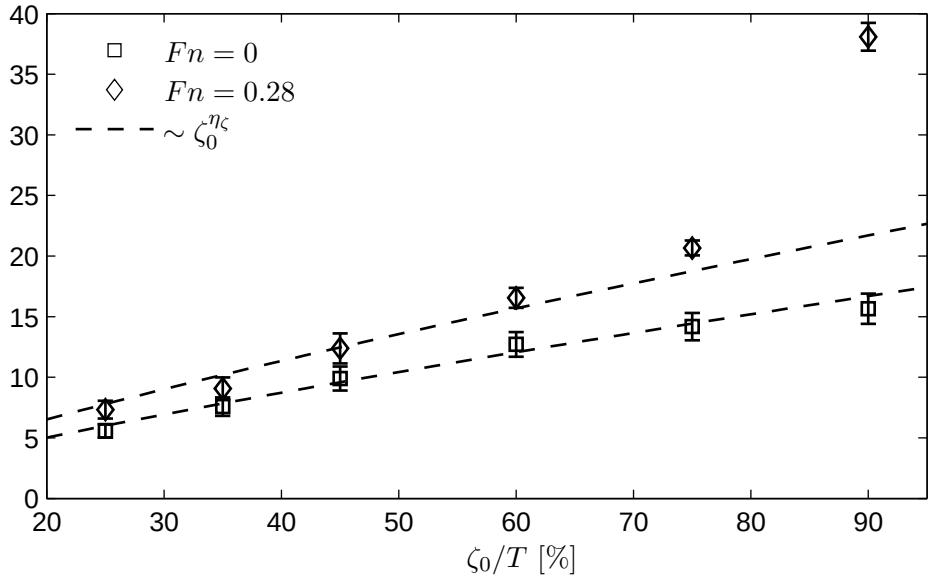

FIGURE 3.17: Apparent trend for increasing added resistance amplitude with wave amplitude.

3.6 Damping tests

Following discussions around non linear effects on the damping of motions and the effect of forward speed on added resistance, a set of tests are conducted to investigate the effect of forward speed on heave damping. Seven tests are performed in a speed range of 0 to 2.5 m/s. In each test the displacement is increased by 30.9%, corresponding to a draught increase of 17.5% at zero forward speed. Upon reaching the desired velocity, the displacement is then instantaneously reduced to its original value resulting in heave oscillations. It must be noted that the model experiences increased sinkage with increased speed and thus oscillations occur around different points of equilibrium, this must be taken into consideration when comparing the results. The shape of the used hull above the waterline is relatively wall-sided and the sinkage should therefore have a smaller impact on the damping than if large flares had been present. The model is locked in pitch for these tests.

Speeds below 1 m/s are excluded from the analysis due to reflections from the tank wall interfering with the heave oscillations. This leaves four tests that this analysis is based on. The conditions of these tests are shown in Table 3.9

If the heave oscillations are assumed to have the form

$$x_3 = x_{30} e^{\eta_U t} cos(\omega_i t) \tag{3.13}$$

TABLE 3.9: Test conditions for damping tests.

Fn	Steady sinkage at release [% of T] (includes 17.5% increased draught)	∇_i [% of ∇]
0.202	19.38	130.9
0.282	21.76	130.9
0.403	30.77	130.9
0.504	34.42	130.9

the decay rate η_U and the oscillation frequency ω_i can be found through fitting of Eqn. 3.13 to the measured heave displacement. Results are normalised by normalising time and frequency before the fitting of curves so that

$$t' = t\sqrt{\frac{g}{Lpp}} \tag{3.14}$$

$$\omega_i' = \omega_i\sqrt{\frac{Lpp}{g}} \tag{3.15}$$

An example of a fitted curve for $Fn = 0.2015$ is shown in Figure 3.18

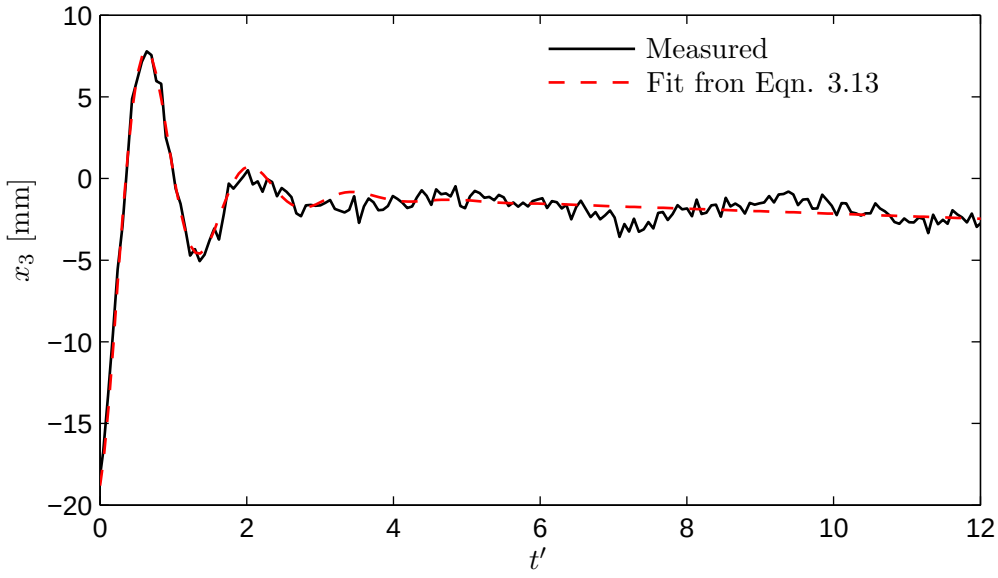

FIGURE 3.18: Example of fitting an exponential decay curve to the measured heave decay ($Fn = 0.2015$).

3.6.1 Results of damping tests

Results are compared with previous decay experiments in forward speed using the same hull form by Crossland et al. (1992) in Figure 3.19. Different combinations of the coefficients in Eqn. 3.13 can produce fits to the data of seemingly equal quality. For this reason, several fits are used and the variation in the coefficients η_{33} and ω_i' are shown as error bars around the mean value.

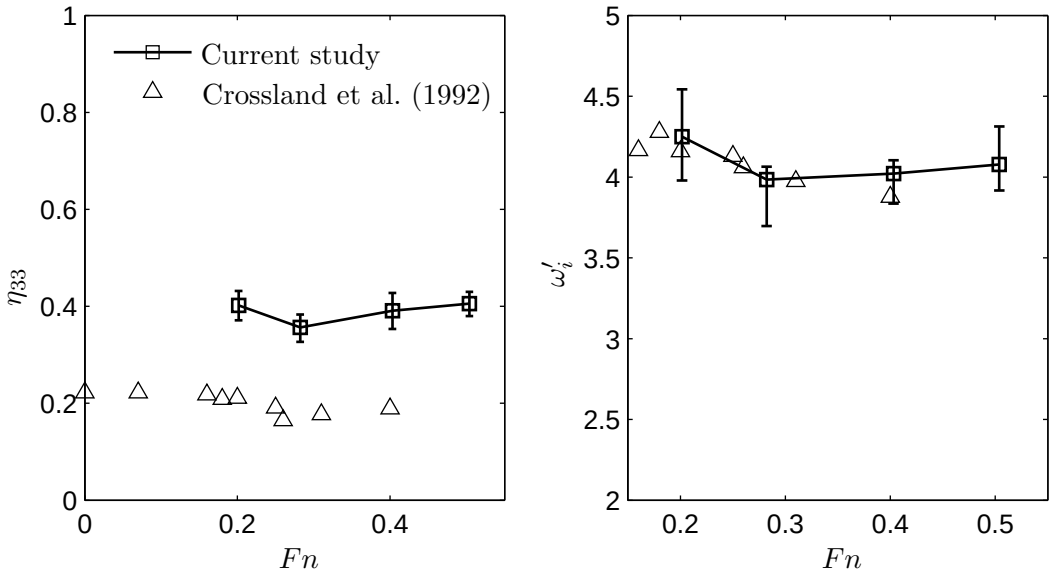

FIGURE 3.19: Measured heave damping coefficients and natural frequencies at different speeds.

The heave damping coefficient η_{33} is defined here as

$$\eta_{33} = \frac{\eta_U}{\sqrt{\eta_U^2 + \omega_i'^2}} \tag{3.16}$$

3.6.2 Conclusions of damping tests

The results differ form those of Crossland et al. (1992) with higher values of η_{33} being obtained. However, their experiments were carried out slightly differently in that the model was induced with both pitch and heave oscillations. Since only heave oscillations are performed in this case, it is to be expected that more energy is lost through pure heave damping. The measured natural frequency of heave and the general trend of the curves are still in good agreement.

Crossland et al. (1992) showed that their results differed slightly from heave damping predicted using linear strip theory but that this had little effect on the heave transfer functions away from heave resonance. They argued however, that the change in η_{33} had

more effect on the pitch response of the ship across the frequency range because of the coupled nature of these motions. Crossland et al. (1992) attributes these discrepancies to non linear effects that are ignored when calculating the forcing terms in linear strip theory but it cannot be excluded that some of it is due to viscous effects on the damping. Added resistance is strongly coupled to heave and pitch motions, especially around their resonance frequencies which means that effects of forward speed on heave and pitch damping have to be considered.

3.7 Overall conclusions of experimental study

The experimental study provides a broad set of data to support the development of the numerical model as well as highlighting important phenomena. The results have shown some of the weaknesses and strengths of linear theory with regards to resistance in waves. One particular outcome from this study is to demonstrate the difficulty of predicting the amplitude of force variations around the mean R_{AW}. This has been shown to depend more on non linear effects than R_{AW} itself in both the speed dependency and the wave height linearity tests. It is also indicated that forward speed means that non linear and/or viscous damping effects will influence the surge force through heave and pitch motions.

In this series of tests the model is not free to surge. This is one of the reasons why the amplitude variations R_{AWa} and σ_{AWa} reach high values compared to the mean increases in R_{AW} and σ_{AW}. In a realistic case with a self propelled hull, some of these large variations in resistance would be translated into surging motions. A surging hull in turn would have an effect on the effective wake and the performance of the propeller. Studying the amplitude variations, even if they would not be present for a self propelled ship, can therefore give some indication of the magnitude of the influence of surge on the performance of the ship in waves.

From the previous literature and the conducted experiments, it is concluded that to satisfy the objectives set up in Section 1.1 the numerical model needs to be able to

- resolve local flow phenomena.
- capture the effect of waves and motions on the boundary layer.
- facilitate a model that is free to surge and be able to capture non linear effects on the exciting surge force amplitude.
- have the ability to model the propeller, either directly in the same scope as the flow around the hull or as a separate model. If the later is chosen, the model must be able to separate the propeller induced velocities from the unsteady wake.

- include easily modifiable modules for propeller modelling and -control to facilitate a broader range of future studies.

This requires the use of NS based modelling. Several software options exist for this purpose, both commercial and open source. It is clear that the chosen software suite requires additional custom made plug ins apart from actual flow modelling. Furthermore, the modular approach will be most attractive if the code is modifiable by anyone. With these requirements in mind, the open source CFD package OpenFOAM (OpenCFD and The OpenFOAM Foundation, 2010) is chosen to provide the base for NS modelling of the self propelled ship. This will allow for custom modifications to the code to fulfil the previously discussed requirements. It will also allow for communication and dissemination of the developed methods to the open source CFD community. The outcome of such communication is hoped to be future studies based on this work, improving it by giving more focus to subjects that are not covered by this thesis.

The following chapters are devoted to implementing many of the features discussed so far into OpenFOAM. Here unsteady RANS modelling is used due to its superior speed compared to other NS methods. For brevity, the basics of this modelling approach are given in Appendix B rather than being presented in the text. Due to the limited scope of this thesis, not every aspect can be thoroughly studied. However, with a modular approach taken and with an open source philosophy, the hope is that more aspects can be covered in the future. Initially, simpler geometries are used to build confidence in the model. However, to fulfil the aims of being able to model ships with realistic hull forms, the KCS container ship is chosen as a benchmark case. The KCS is a well known hull shape used for CFD validation. The hull shape was created in Korea in the 1990's as a benchmark model representative of a modern container ship. Several sets of experimental data exists, for example by Van et al. (1998) and Kim et al. (2001). Because of the availability of experimental data, the KCS has been used as a benchmark case in several international CFD workshops such as the Gothenburg 2010 CFD workshop (Larsson et al., 2014).

Chapter 4

Numerical towing tank

This chapter concerns the development of a numerical model for studying ship performance in waves. The phrase "numerical towing tank" refers to an application of CFD to studying marine problems in model scale, much like an experimental towing tank. Most of this chapter is also included in a current paper by Windén et al. (2014*c*). Because this chapter is devoted to studying how the basic set up is to be approached, it uses simple geometries. The following chapters apply the recommendations found from this set up to the more advanced KCS hull form.

Prediction of ship performance in waves by means of Computational Fluid Dynamics (CFD) is an increasingly popular complement to towing tank testing. Recent CFD workshops have shown encouraging results for the applicability of CFD to many aspects of ship hydrodynamics (Hino, 2005; Larsson et al., 2003, 2014) but also deficiencies in certain aspects such as accurately predicting the phase lag of the wave induced forces and moments using conventional approaches. This is likely to be partly due to unresolved local flow features since an improvement was shown to be obtainable for very fine grids (Larsson et al., 2014). Even so, most conventional approaches to predicting forces and moments on ships in waves still show issues with the phase lag (Larsson et al., 2010, p 245-267). Despite the relative maturity of many of the methods used, Verification and Validation (V&V) of marine CFD is still lacking in many areas (Stern et al., 2006).

Conventionally, CFD is applied to ship performance problems in a piecemeal manner. Good accuracy can be achieved on still water performance with methods capturing, in high detail, viscous phenomena in the boundary layer and at the stern separation region. Seakeeping predictions using CFD is generally approached with the presumption that the viscous forces are negligible. Good accuracy on the motions can thus be achieved without much attention being paid to how well the boundary layer is captured. Finally, good prediction of propeller performance can be obtained using Large Eddy Simulation (LES) on large rotating grids (Carlton, 2012). All the three aspects mentioned above are

inherently coupled and considering them as a single problem will give a closer numerical representation of a ship travelling in a seaway.

For the model to be able to capture the effects of ship motions, a mesh motion scheme is needed. This can involve either a sliding grid approach such as an Arbitrary Mesh Interface (AMI), a deforming mesh method, adaptive mesh refinement or an overset grid method. Furthermore, for self propulsion to be achieved, either the geometry of the rotating propeller must be incorporated within this moving environment or the propeller must be approximated by momentum sources. In all of these methods some form of interpolation and/or remapping of the solution is needed which introduces errors.

The more complexity is added, the higher the computational cost. The computational cost required for a calm water resistance calculation, an added resistance calculation and a simulation of a self propelled ship travelling in waves will therefore be widely different. Assuming that both propulsion and motions need to be included to some degree, more advanced methods for representing these necessitate more computing power. Therefore simplified methods are preferred if resources are limited. However, simplified schemes introduce more errors. These errors are not related to physical modelling but to the numerical implementation itself. The numerical implementation lies much closer to the final CFD solution than the physical approximation of the fluid in terms of abstraction from the true flow (Molland et al., 2011, p 173-174). Errors relating to numerical schemes can therefore be more easily quantified since the equations governing them are well defined and methods exist to reduce them (Lipnikov and Shashkov, 2006). However, if too many different numerical approximations are present, it will be difficult to quantify the impact of each one. When looking to reduce errors in viscous simulations of ships in waves, it is therefore preferable to focus the simulation such that only a few physical phenomena are studied at once. In that way, the true impact of certain numerical approximations in predicting those particular phenomena can be studied. When more certainty is established, the focus can be broadened until the full problem can be studied with confidence.

As was pointed out in Section 2.10, capturing the effects of the waves on the boundary layer is important to better represent the propeller inflow. This is an aspect of ship performance which has received limited attention (Turnock et al., 2010). Furthermore, the ability of the model to predict the amplitude and phase of the surge force needs to be established as discussed in the previous chapter. With these requirements in mind, this chapter will demonstrate how the viscous flow around a ship in waves can be approached numerically. It will also be discussed how different numerical schemes can influence the quality of the prediction. In the validation phase, a Wigley hull is chosen for its simplicity, allowing for easier distinction of phenomena relating to wave-boundary layer interaction. The Wigley hull shape has previously been argued to give a better focus when studying interaction between the viscous flow and the free surface around surface piercing bodies by Seol et al. (2013). This was due to the lack of stern separation

and a small bow wave. For the same reason and to be able to more clearly focus the study on the numerical model rather than geometry, the hull is fixed in all degrees of freedom. Forward speed diffraction for a Wigley hull is a well established reference problem for gathering understanding of the physics of ships travelling in waves. It is also used as a stepping stone in the development of numerical methods for calculating ship flows such as Unsteady Reynolds Averaged Navier Stokes (URANS) equations (Rhee and Stern, 2001; Söding et al., 2014; Weymouth et al., 2005), Potential flow (Kjellberg, 2011; Seo et al., 2013) and Smooth Particle Hydrodynamics (SPH) (Pearce et al., 2012).

Having established confidence in the presented set up, it will subsequently be used to study self propulsion for realistic hull shapes in the following chapters.

4.1 Scale effects

Model scale is used here to reduce the computational effort. Castro et al. (2011) confirmed that there are significant differences in the boundary layer thickness and the wake around a ship between simulations in model scale and in full scale. These results were validated against experimental data for the model scale case using the benchmark test case from the 2005 Tokyo CFD workshop (Hino, 2005). For the full scale case, reliable data is difficult to obtain. Exceptions are e.g. full scale measurements of the boundary layer by Lewthwaite et al. (1985) and stern wave measurements by Wyatt et al. (2008). However, such measurements are difficult to obtain and often relate to only one parameter (e.g. wave pattern or boundary layer.) The results by Castro et al. (2011) show that, it is not yet clear whether or not computational results for viscous flow around ships in waves will be scalable.

In waves, as in calm water, the effect of the Reynolds number is evident primarily for the viscous component of resistance and does not affect the motions notably (Bhushan et al., 2007). To know the effect of scaling fully, model- and full scale flow features must be compared. If the general flow features look similar, scaling should be straight forward requiring only corrections for the different boundary layer thickness. If however the flow features look different (e.g. bow sheet spray instead of intact waves) the scaling process is not straight forward and full scale measurements may be necessary (Rood, 1996).

Furthermore, when considering self propulsion, scaling effects have been shown to affect the wake fraction due to the thinner boundary layer at full scale (Bulten and Nijland, 2011). The fact that the boundary layer will be disturbed under waves means that this effect may be larger when considering self propulsion and waves combined.

However, the drawback to carrying out simulations in full scale is the increased computational cost due to the Reynolds number being higher in full scale. The higher Reynolds number means that the turbulent flow features are smaller relative to the hull than in

model scale. Correctly resolving the viscous flow around the hull therefore requires much finer meshes near the wall and lower time steps in full scale. Because of this, developing good practice and understanding of physical phenomena by comparing CFD simulations in model scale to experiments is currently the most practical option in the field of marine CFD.

4.2 Set up of the Numerical towing tank

A numerical towing tank set up is created here with the purpose of studying ships travelling in waves. The set up described in this section is initially applied in four separate studies to address specific issues regarding the ability of the model to represent the flow. In each of these studies, a different flow obstacle is used. The same set up is then used in later chapters to study self propulsion in waves for realistic hull shapes. The set up is summarised in Table 4.1.

TABLE 4.1: Summary of numerical towing tank set up.

Geometry	Rectangular region, half air and half water, hull placed on centreline a set distance downstream. See Figure 4.1.			
Meshing	Free surface and body refinement using iterative procedure described in Figures 4.2 and 4.3.			
Flow model	URANS with PISO pressure velocity coupling			
Multiphase model	VOF with MULES cycle for sharp resolution.			
Wave generation	Relaxation towards analytical Stokes first order wave in prescribed relaxation regions as described by Jacobsen et al. (2012).			
Boundary conditions	Top/bottom		:	Slip
	Sides		:	Symmetry plane
	Inlet	p	:	Neumann
		k,ω	:	Fixed value
		u,α	:	Following waves and freestream
	Outlet	k,ω,α	:	Neumann
		p	:	Fixed $p - \rho g h = 0$
		u	:	Neumann/Dirichlet
	Hull	p,α	:	Neumann
		k,ω	:	Wall function
		u	:	Fixed value of zero
Convection schemes	u,k,ω	:	Limited TVD	
	α	:	MUSCL	

Firstly, the set up is used with a surface piercing flat plate. This is done to be able to discuss the influence of the choice of convection scheme on the viscous forces on a

surface piercing object. A flat plate is chosen to focus the study on the viscous force component. Secondly, an empty domain is used to show how the choice of convection scheme influences the quality of free wave propagation using this set up. The studies regarding the choice of convection scheme serve to give new insight about the impact of numerical approximations on the quality of the computed viscous flow. Furthermore they serve to provide the convection scheme to be used in the following sections where the Wigley hull is used.

The forces and moments on the Wigley hull are validated against experimental data before the hull is used to study the influence of the waves on the boundary layer as they move aft. Apart from the studied object and specific modifications which are all stated clearly in the beginning of each study, the set up described in this section is used for all the studies conducted in this thesis.

4.2.1 Flow modelling

The flow is modelled using the URANS equations

$$\frac{\partial \overline{u}_i}{\partial t} + \overline{u}_j \frac{\partial \overline{u}_i}{\partial x_j} = \frac{1}{\rho}\left(\mu \frac{\partial^2 \overline{u}_i}{\partial x_j^2} - \frac{\partial \tau_{ij}}{\partial x_i} - \frac{\partial \overline{p}}{\partial x_i} + F_v\right) \tag{4.1}$$

The equations are discretised using the Finite Volume (FV) method and solved using OpneFOAM v.1.7.1 on the computing cluster Iridis3 at the University of Southampton using 10 computing nodes. Each node consists of 12 CPUs divided into two 6-core 2.4 GHz processors. The PISO algorithm (Issa, 1986) is used for pressure-velocity coupling. The time step is adapted in run time based on a specified Courant number limit. For details on the specific implementations used in this thesis regarding the use of Eqn. 4.1 to model the flow, see Appendix B.

4.2.2 Multiphase model

The free surface is captured using the Volume Of Fluid (VOF) method where the volume fraction α is governed by

$$\frac{\partial \alpha}{\partial t} + \nabla \cdot (\alpha u_i) = 0 \tag{4.2}$$

Furthermore, the Multidimensional Universal Limiter with Explicit Solution (MULES) algorithm (Ubbink and Issa, 1999) is used to ensure a sharp resolution of the surface. The interface flow in the cases studied here is expected to be smooth and without sudden entry or re-entry of the bow. For more violent flows, where slamming or similar

phenomena are present, it is advisable to instead use a multiphase model that takes compressibility into account as this will give a better prediction of pressure peaks and entrapped air (Godderidge, Turnock, Earl and Tan, 2009; Godderidge, Turnock, Tan and Earl, 2009).

Since multiphase simulations are particularly sensitive to the time step used, a second constraint is set on the adaptive time stepping to limit the movement of the interface in each step.

The interface Courant number C_α is defined for each face as

$$C_\alpha = \frac{U_i}{\Delta x}\Delta t \tag{4.3}$$

where Δt is the time step, Δx is the local grid spacing. The movement of the interface U_i is defined as

$$U_i = \alpha_i \frac{|\phi|}{A} \tag{4.4}$$

where ϕ is the local flux and the function α_i is 1 when $0.01 <= \alpha <= 0.99$ (i.e. near the interface) and 0 otherwise.

This definition is equivalent to the normal Courant number definition but allows for a stricter limit to be set near the interface which is more sensitive to diffusion and distortion. In all simulations in this thesis the time step, in addition to being controlled by a set limit on the Courant number, is limited by enforcing $C_\alpha < 0.7$.

4.2.3 Geometry

For validation purposes the geometry of the domain is created to match, as closely as possible, the conditions in which experimental data by Journée (1992) on fixed Wigley hulls in waves was obtained. The Delft University of Technology Ship Hydrodynamics Laboratory towing tank measures 142 m by 4.22 m with a nominal water depth of 2.5 m. With the hull particulars given in Table 4.9, this gives a cross sectional blockage of 0.45%. Normally for estimates of ship performance using RANS, the lack of geometrical constraints means that a lower blockage can be achieved compared to towing tank testing. This is one of the advantages of the numerical towing tank. However, a recommended maximum blockage of 0.5% for towing tank tests (Comstock, 1967) suggests that blockage effects should be relatively small and the importance of replicating the wave systems as they would have appeared in the experiments is deemed more important in this case.

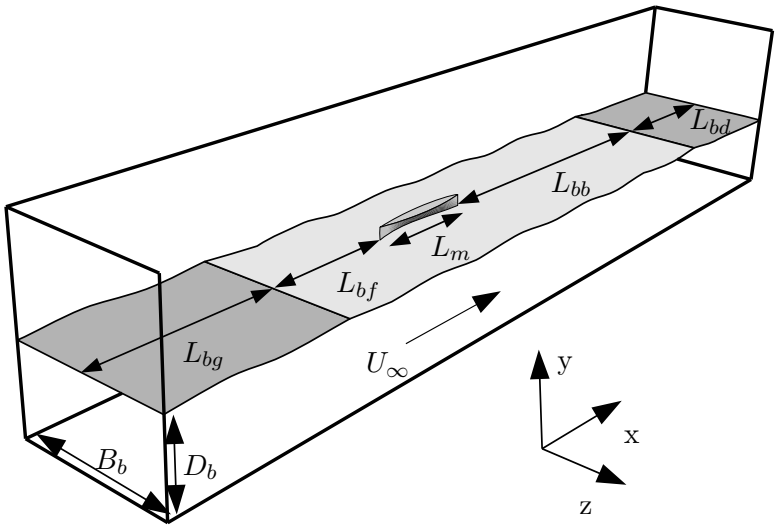

FIGURE 4.1: Geometry of the numerical towing tank.

An air column of equal height as the water depth is added to create a domain with a cross section of 4.22 x 5 meters. Since the forward speed of the model is represented by a current rather than mesh motion, the length of the domain is chosen to be just long enough to capture the interesting parts of the wave system. One model length L_m is allowed forward of the forward perpendicular to allow the bow wave to develop. To ensure that the following wave system, the interaction with the regular waves and the viscous wake are captured, the length of the domain after the aft perpendicular is set to $3L_m$. Furthermore, two relaxation zones are added to generate and dissipate waves. The length of these are set to the longest wavelength in the validation case, 6m. The particulars of the domain and their values are shown in Figure 4.1 and Table 4.2. $L_m = 3m$ for both the Wigley hull and the flat plate.

TABLE 4.2: Domain particulars for the numerical towing tank.

D_b	=	2.5 m	B_b	=	4.22 m
L_{bg}	=	6 m	L_{bd}	=	6 m
L_{bf}	=	L_m	L_{bb}	=	$3L_m$

4.2.4 Wave generation

Waves are generated and dissipated using the wave generation toolbox waves2Foam for OpenFOAM (Jacobsen et al., 2012) where relaxation is applied to the velocity and volume fraction fields. A first order Stoke's wave is used as the relaxation target. Because a constant current is used to simulate forward speed, the generated waves are corrected by Doppler shifting the frequency as

$$\omega_d = \omega + kU_\infty \tag{4.5}$$

where ω is the frequency of the regular wave without current and k is the wave number calculated using the dispersion relation for shallow water

$$\omega^2 = gk \tanh(kD_b) \tag{4.6}$$

The benefit of linking the numerical towing tank to the waves2Foam toolbox is that it includes a wide range of tools for modelling waves. This includes the ability to generate irregular waves and oblique waves which will improve the applicability of the developed model for future studies.

4.2.5 Turbulence model

The $k-\omega$ Shear Stress Transport (SST) model (Menter et al., 2003) is used to achieve good modelling of both near-field turbulence (inside boundary layer) and far-field turbulence (wake and ambient turbulence.) A small fixed value corresponding to 3% of U_∞ is set on the inbound turbulence intensity to model the presence of some initial turbulence in the tank. This is in line with commonly used values of 1-5% for towing tank and wind tunnel simulations. Furthermore a value of the specific dissipation rate ω is given as 2/s at the inlet.

4.2.6 Meshing

Several factors have to be considered when creating the mesh for the numerical towing tank.

- Mesh density in the free surface region is chosen to mitigate the effects of numerical damping.
- Mesh density increased close to the hull to capture the boundary layer.
- Mesh density aft of the hull to capture the viscous wake.
- Smooth transitions between these areas.
- Minimising number of cells to speed up calculation time.

To smoothly blend the near-hull refinement with the free surface refinement, a stepwise refinement algorithm is used. The method uses three different zones; the free surface region, the near-hull region and the wake region. Based on an original uniform background mesh, cells are stepwise selected and split in the vertical or horizontal direction in these regions. After each refinement level step, the extent of each zone is reduced so that, in

the final step, they correspond to the region which is to have the finest refinement level. This ensures smooth transitions between areas of different mesh densities. The process is defined for an arbitrary hull geometry and is shown in Figure 4.2. This process is applied to generate the mesh for both the Wigley hull and the flat plate.

For selecting and splitting cells, the OpenFOAM utilities cellSet and refineMesh are used respectively. For snapping the generated mesh to the hull and to generate the boundary layer mesh, the utility snappyHexMesh is used. To implement the process shown in Figure 4.2, a shell script is created to call these utilities and to control their input data. To illustrate the procedure, a schematic of the refinement evolution after a number of iterations is shown in Figure 4.3. Here, d_0 is the distance from the hull, within which the finest refinement level will be applied and ζ_{0ref} is the elevation above $y_G = 0$ that will have the finest level of vertical free surface refinement. γ and γ_ζ are expansion ratios determining how quickly the refinement zones are decreased in size and N is the highest refinement level. This gives the current distance from the hull ($\mathbf{d}$) and from $y_G = 0$ (ζ_{ref}) to refine within for each level.

Figure 4.3 serves only to illustrate the procedure and is not necessarily related to the mesh used for calculations. In Figure 4.3, the horizontal refinment level on the free surface is zero which is why only cells near the hull are marked for refinement in the horizontal direction. As opposed to what is shown in Figure 4.3, it is desirable to make larger steps when shrinking the refinement regions so that there is a buffer region of cells of equal size between each layer of refinement. This serves to further decrease the changes in cell volume and aspect ratio over small distances and helps maintain accuracy.

Mesh independence

The uncertainty relating to the mesh resolution is usually established by systematically refining and coarsening the whole mesh. This is beneficial to be able to directly relate the error to a single parameter, the level of refinement. However, for the forward speed diffraction problem and for ships advancing in waves in general, it is difficult to establish the grid uncertainty because of the non - convergent nature of many of the parameters (Hänninen et al., 2012).

Even though a systematic approach should be employed in discussing the uncertainty of future studies a piecemeal approach to mesh uncertainty is taken here. Three test are conducted to ensure that:

1. The mesh in the free surface region is fine enough to be able to capture the propagation of surface waves.
2. The mesh near the hull is fine enough to resolve the development of the boundary layer.

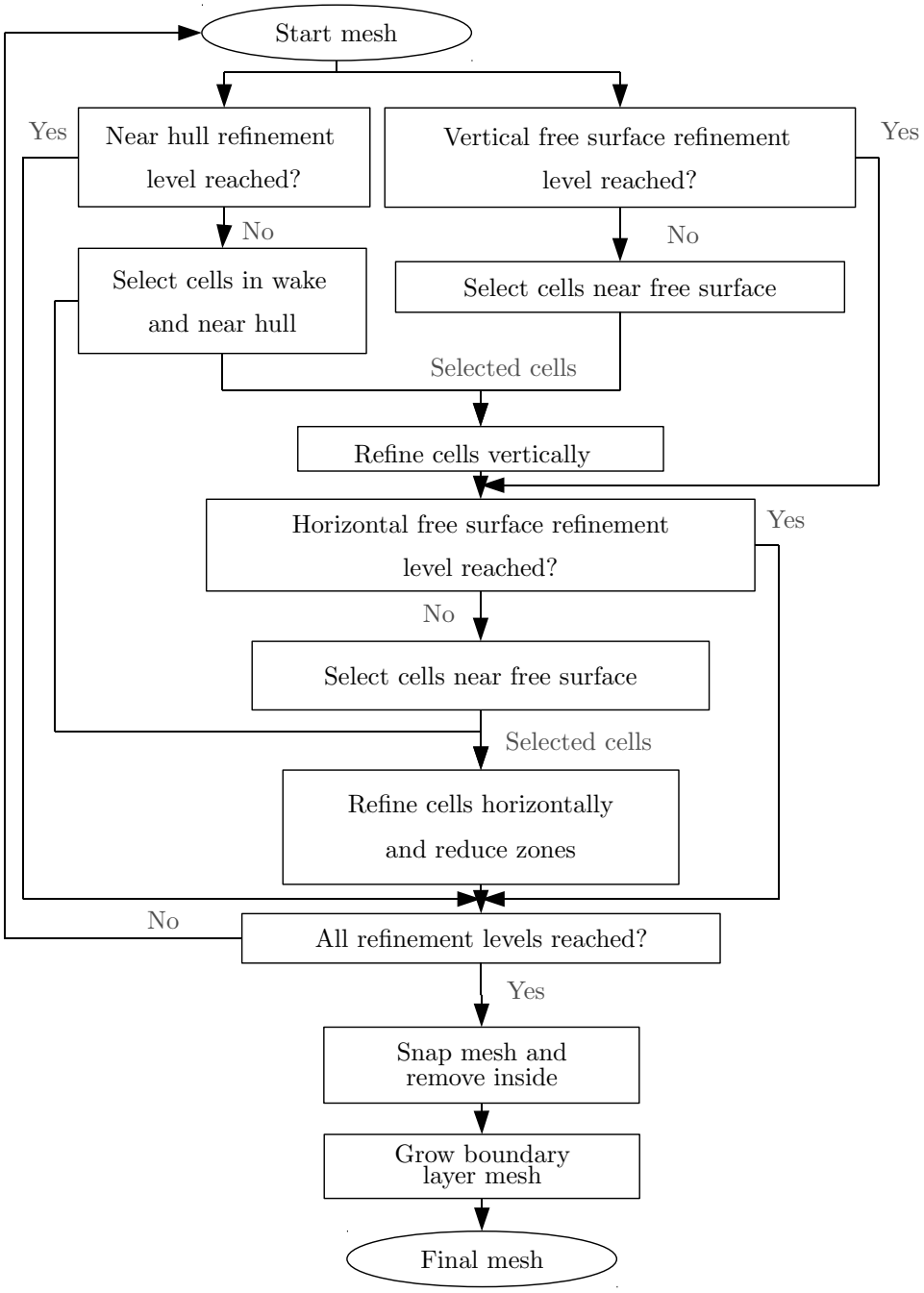

FIGURE 4.2: Mesh refinement algorithm.

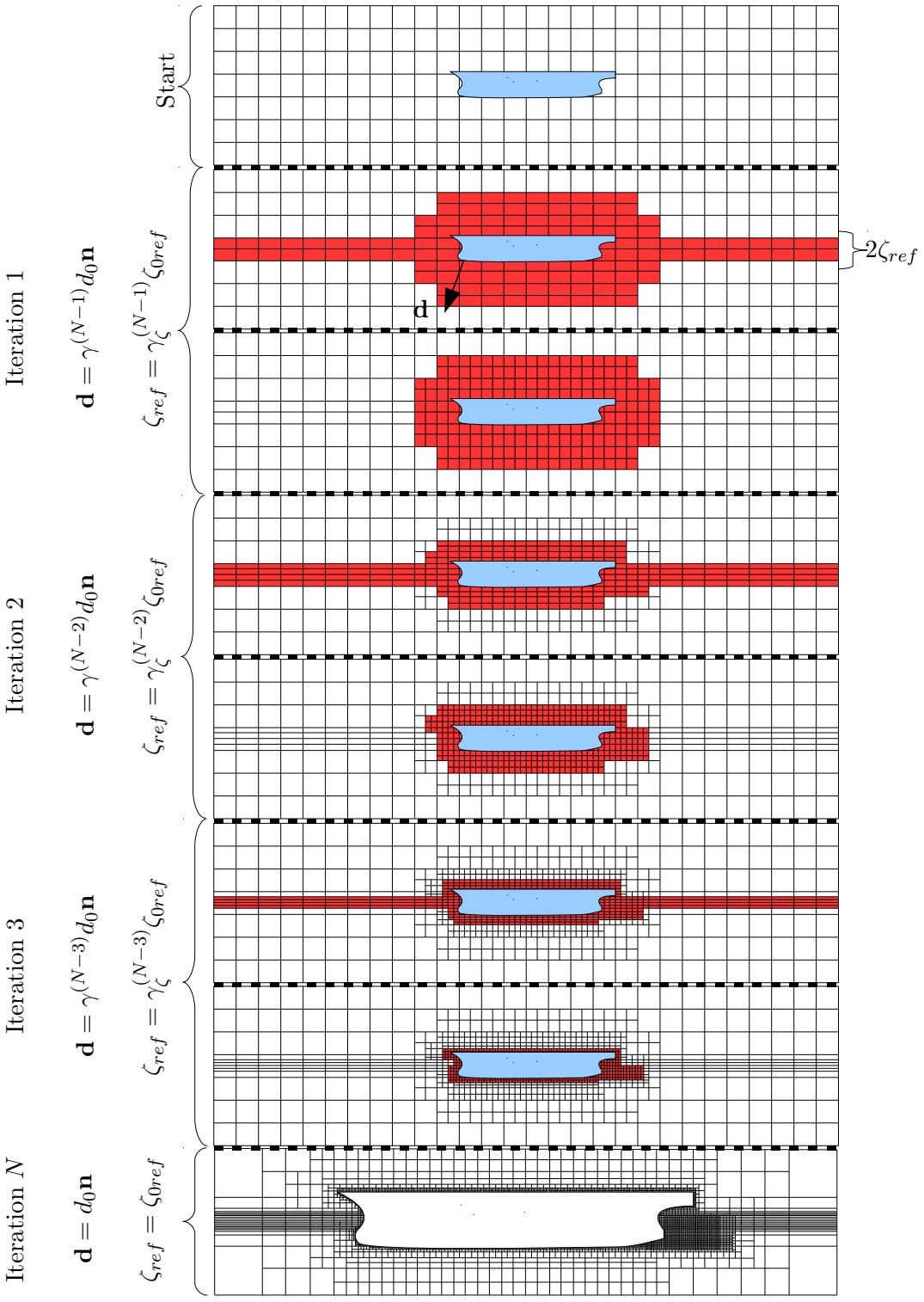

FIGURE 4.3: Schematic of mesh generation, illustrating iterations of the procedure in Figure 4.3 (Iteration N shows a zoomed in view.)

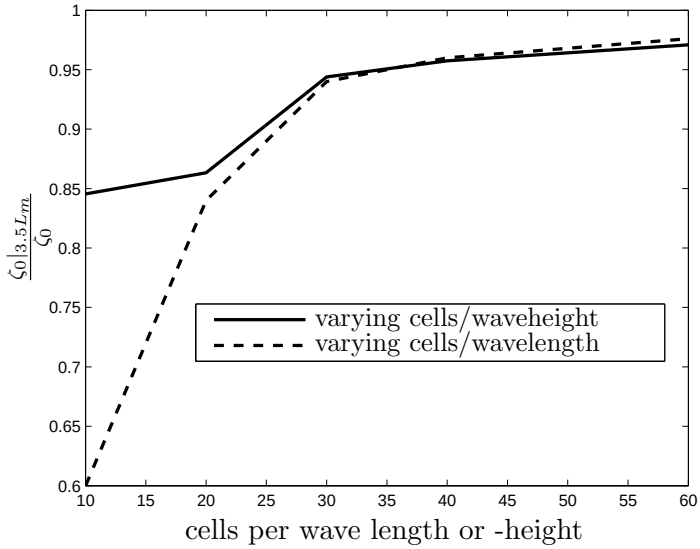

FIGURE 4.4: Effect of mesh independence on wave propagation, wave amplitude at $3.5L_m$ compared to generated wave.

3. The overall cell count is within appropriate limits for free surface computations for ships.

By separately establishing the suitability of the mesh to fulfil these parameters, a smaller number of cells can be achieved than if the whole mesh is refined at once to a certain level.

The mesh cell density in the free surface region needed to accurately model surface waves has been found to lie somewhere in the order of 30-50 cells per wavelength (Larsson et al., 1998; Vaz et al., 2009) and around 30 cells per waveheight (Vaz et al., 2009). The exact number of cells required in the vertical direction is dependent on the wave slope as well as the wave height with steeper waves requiring a finer resolution. Because these conclusions were drawn from different solver algorithms than the one used, a study is carried out on mesh independence of the wave propagation using OpenFOAM. The density of the mesh in the free surface region is varied in the vertical and horizontal directions. The amplitude of a wave generated with amplitude $\zeta_0 = 0.023$m and wavelength $\lambda = L_m$ is recorded at 3.5 L_m downstream of the end of the inlet relaxation zone. This wave has a relatively low steepness of $\zeta_0/\lambda = 7.6\ 10^{-4}$.

Figure 4.4 shows the results of this study for 10-60 cells in each direction. When varying the number of cells per wave height, the number of cell per wave length is kept constant at its maximum of 60 and vice versa. No ship model is present in the tank in this study. Based on these results at least 30 cells per wave height and 40 cells per wave length are used throughout the calculations.

It should be noted that even at 60 cells per wave length and -height, there is still a loss of 3% of the total wave amplitude at $3.5L_m$ downstream. These results can be put in relation to physical dissipation due to viscosity. The energy W of a gravity wave dissipates along the axis of propagation x as (Behroozi, 2004)

$$\frac{dW}{dx} + W\frac{8\mu k^3}{\rho\omega} = 0 \tag{4.7}$$

For the set up in this chapter this would give a loss of 0.02% of the energy in the wave over 3.5λ of propagation. This should give <0.01% reduction in the wave amplitude if $E \sim \zeta_0^2$. There is thus a fair amount of numerical dissipation still present. The domain used here is relatively short and the hull is located relatively close to the inlet. For longer domains, for example when studying multiple objects in tandem this could impact the result and the cell density is likely to have to be increased to achieve the same accuracy on the wave amplitude. An alternative to mesh refinement is to generate a higher amplitude wave at the inlet in order to have the model encounter waves at the correct amplitude.

The chosen turbulence model is designed to resolve the flow down to the wall and to accurately resolve the turbulent boundary layer. To do this without further wall treatment the required nondimensional wall distance of the first cell is considered to be less than 2. However, the $k-\omega$ SST model has been shown to give accurate results at even coarser meshes (Salim and Cheah, 2009). Here, a y_1^+-value of 1 is used as a target. The thickness of the boundary layer mesh is set to 12 cells with an expansion ratio of 1.2. The target is achieved in most areas (99.4% of near wall cells) except near sharp corners where layers need to be collapsed to reduce skewness and non-orthogonality of the mesh.

The findings of the 2010 Gothenburg workshop on marine CFD(Larsson et al., 2014) pointed towards the overall grid resolution required to resolve the forward speed diffraction problem as being in the order of 100s of Millions of cells if using Large Eddy Simulation (LES) or Detached Eddy Simulation (DES) but that this could equally be resolved in URANS using more accurate turbulence models. Regardless of the set up, the grid resolution should be finer than 3M cells to model this type of problem (Larsson et al., 2014). In this study there is no complex vortex shedding which should reduce the need for anisotropic turbulence models and the grid size for the Wigley hull case is >6M. This is a factor two finer than the quoted resolutions from the workshop so the general grid resolution is seen as appropriate.

Several other factors will impact the quality of the result. For example as was discussed in Chapter 2, one of the weaknesses of linear potential flow in predicting the force variations comes from the inability to capture non linear interaction between the bow wave and the incoming waves. A high resolution in front of, and around the bow area is

therefore preferred to achieve an advantage over such methods. Hänninen et al. (2014) showed that the local pressures and wave profiles on the bow area of a ship advancing in short waves can be predicted with good accuracy with the VOF method using a similar size mesh (6.5M.)

Based on these figures, the meshes used in this study are seen as appropriate to capture the discussed phenomena. However, for computations using more complex hull shapes a more systematic approach to verify the mesh independence of the solution would be needed. Furthermore, even though the average quantities can be predicted with good accuracy, local features can show a much higher sensitivity to the grid resolution (Hänninen et al., 2012). Accurately predicting the local flow, especially on the aft body is important for hull/propeller interaction. While detailed studies of local flow around realistic hull shapes is outside the scope for this thesis, this is something that will have to receive more attention in the future.

Final mesh

The resulting mesh around the aft half of the Wigley hull, including the wake refinement, can be seen in Figure 4.5. A closer view showing the boundary layer mesh near the free surface can be seen in Figure 4.6. The mesh sizes for each of the simulations conducted in this chapter are given in Table 4.3

4.2.7 Boundary conditions

To replicate forward motion of a hull in a stationary tank, slip conditions are put on the tank bottom and roof while the sides are defined as symmetry planes as this gave a slightly faster computational time.

Even though the expected situation at the outlet boundary is a constant flux, the outlet boundary condition on velocity is set to be adaptive to avoid instabilities. The outlet varies between a Neumann type boundary condition (zero gradient) for the velocity if the velocity vector points into the domain and a Dirichlet type (with a fixed value on the flux representative of the freestream) if the velocity vector points out of the domain.

TABLE 4.3: Mesh sizes for different flow obstacles in the numerical towing tank.

Study	Mesh size
Free wave propagation	660 000
Flat plate	6.5 M
Wigley Hull	6.6 M

The inlet boundary condition is set so that the volume fraction and velocity follow those of the waves being generated in the adjacent relaxation region ensuring that all the

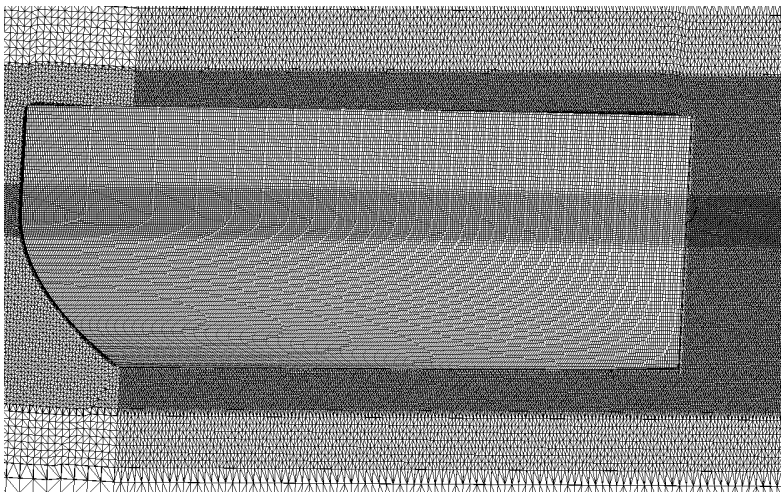

FIGURE 4.5: Mesh on the aft part of the Wigley hull obtained using the described method; shown in the xy and yz planes, both centred amidships.

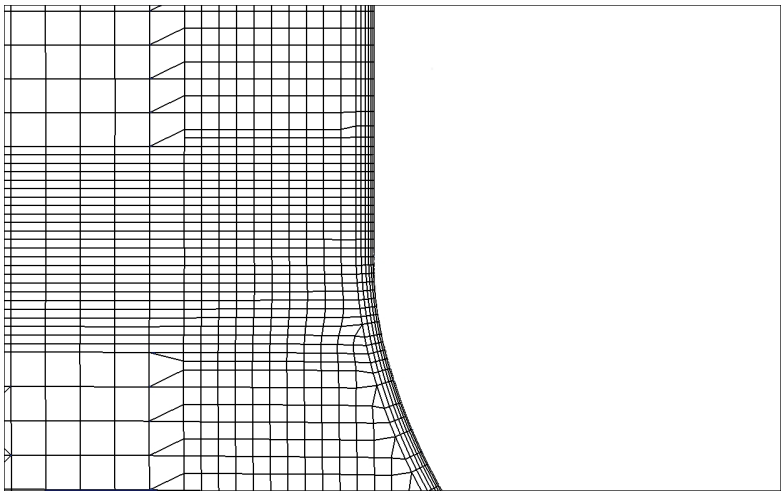

FIGURE 4.6: Detail of boundary layer refinement near the free surface, shown in the yz plane amidships.

gradients over the inlet boundary equal zero. On the hull, the velocity is set to zero. The flow at the wall is resolved in most areas. However, in some places the mesh is coarser to be able to capture the sharp corners present both on the flat plate and on the Wigley hull. Therefore the viscous effect of the wall is modelled using a wall function where needed adding to the eddy viscosity in the first cell ν_{t1} according to

$$\nu_{t1} = \nu_t + \nu_{wall} \tag{4.8}$$

where

$$\nu_{wall} = \nu \left(\frac{y_1^+ \kappa}{\ln(E y_1^+)} - 1 \right) \tag{4.9}$$

Here, $\kappa = 0.41$ and $E = 9.8$. The non dimensional first cell distance y_1^+ is calculated from the first cell height y_1 and the turbulence kinetic energy k as

$$y_1^+ = 0.09^{\frac{1}{4}} \left(\frac{y_1 \sqrt{k}}{\nu} \right); \tag{4.10}$$

The wall function is activated if $y_1^+ > 11.5$ and otherwise $\nu_{wall} = 0$ and the viscous effect at the wall is considered as resolved. Wall functions are also used for the near wall treatment of the turbulence kinetic energy k and the specific dissipation ω. The viscous force dependence on y^+ for the OpenFOAM implementation of these wall functions has been studied by Haase et al. (2012) using the $k - \omega$ SST model. They found that for $y^+ \leq 10$, the forces are almost independent of the grid size and between $30 < y^+ < 125$, the forces did not vary much. If not otherwise stated, the boundary condition for volume fraction and pressure is set to a Neumann type for all boundaries except for the outlet where the pressure is fixed to $p - \rho g h = 0$.

4.2.8 Data recording

The viscous force on each face i on the hull boundary is calculated from the inner product of the local viscous stress tensor and the face normal as

$$\mathbf{f}_{vi} = \boldsymbol{\tau}_i \cdot \mathbf{n}_i \tag{4.11}$$

where the viscous stress is calculated from the effective viscosity ν_e (as calculated by the turbulence model), the local density $\rho(\alpha) = (1-\alpha)\rho_{air} + \alpha\rho_{water}$ and the strain rate tensor $\boldsymbol{D}$ as

$$\boldsymbol{\tau} = 2\rho(\alpha)\nu_e \boldsymbol{D} \tag{4.12}$$

with

$$\boldsymbol{D} = \frac{1}{2} dev \left(\nabla \boldsymbol{u} + \nabla \boldsymbol{u}^T \right) \tag{4.13}$$

where *dev* indicates the deviatoric part and $\boldsymbol{u}$ is the velocity vector field.

Note that $\boldsymbol{f}_{vi}$ is normalized with the face area in this case so to get the viscous force on each face $\boldsymbol{f}_{vi}$ is multiplied with the face area A_i. The pressure force per face area is calculated from the pressure field p as

$$\boldsymbol{f}_{pi} = p_i \boldsymbol{n}_i \tag{4.14}$$

This gives the total pressure and viscous force on the hull $\boldsymbol{F}_p$ and $\boldsymbol{F}_\mu$ and the total force $\boldsymbol{F} = \boldsymbol{F}_p + \boldsymbol{F}_\mu$ as

$$\boldsymbol{F}_p = \sum_{Hull} A_i \boldsymbol{f}_{pi} \tag{4.15}$$

$$\boldsymbol{F}_\mu = \sum_{Hull} A_i \boldsymbol{f}_{vi} \tag{4.16}$$

and the total moment $\boldsymbol{M} = \boldsymbol{M}_p + \boldsymbol{M}_\mu$ as

$$\boldsymbol{M}_\mu = \sum_{Hull} A_i \left(\boldsymbol{f}_{vi} \times \boldsymbol{r}_{ri}\right) \tag{4.17}$$

$$\boldsymbol{M}_p = \sum_{Hull} A_i \left(\boldsymbol{f}_{pi} \times \boldsymbol{r}_{ri}\right) \tag{4.18}$$

with $\boldsymbol{r}_{ri}$ being the vector from each face centre to the centre of rotation. The centre of rotation is taken here as the centre of gravity for the object in question. In all force calculations, both the forces stemming from the water phase and the air phase are recorded. However, the force stemming from the air phase is generally less than 0.5% of the total force at any given time during the simulation. This definition of forces has a potential to yield erroneous results if the interface is not sharp. A smeared interface may give an incorrect distribution of forces from the two fluids. In these simulations, the mesh is fine enough to keep a sharp interface (generally the layer where $1 > \alpha > 0$ is one cell thick or less.)

The wave elevation is calculated by probing the volume fraction α over a set of points uniformly distributed over the length of a straight line set to represent a wave probe. The two adjacent points i and $i-1$ where $\alpha_i <= 0.5$ and $\alpha_{i-1} >= 0.5$ (or vice versa depending on the direction of travel along the probe) are located and the point where $\alpha = 0.5$ interpolated as

$$\zeta = y_{Gi-1} + \frac{\alpha_{i-1} - 0.5}{\alpha_{i-1} - \alpha_i} \left(y_G i - y_{Gi-1}\right) \tag{4.19}$$

where y_G is the global vertical coordinate.

4.3 Effect of convection scheme

The numerical representation of the convective terms of the RANS equations often requires corrections to cope with stability problems due to the inability of the central differencing algorithm to identify the flow direction. Various upwind schemes have been

proposed to cope with this, all representing a trade-off between accuracy and stability. One of the major disadvantages of diverting from the central differencing scheme in terms of accuracy is the increase in the discretisation error or numerical diffusion (Zhou et al., 2008; Zurigat and Ghajar, 1990). The numerical diffusion due to discretisation schemes has been shown to be significant in relation to physical dissipation (Huh et al., 1986). In marine applications, a large amount of numerical diffusion leads to non physical damping of waves and thus to a more significant change in the flow regime than diffusion in each separate phase. Ismail et al. (2010) highlighted the importance of the convection scheme when performing single phase calculations on the KVLCC2 tanker model. They found that the choice of convection scheme in combination with the choice of turbulence model can greatly influence both the integral quantities of forces and moments on the hull but also the local flow features at the stern. The general recommendation by Ismail et al. (2010) is to use a limited Total Variation Diminishing (TVD) scheme.

To quantify the effects of the chosen convection scheme on the multiphase simulations shown in this chapter, four different schemes are tested for their ability to predict free (non-diffusive) wave propagation as well as oscillations of viscous drag due to waves on a semi-submerged flat plate. Both these abilities are seen as important to establish confidence in the presented results. The tested schemes are implementations in OpenFOAM of the central differencing scheme, an upwind scheme, and two limited TVD schemes. The central differencing scheme is unlikely to be used in many ship flow calculations. However, it is presented here out of interest in how different numerical schemes perform in terms of accuracy and computational effort.

In general, limited TVD schemes are constructed by blending a higher and a lower order scheme based on the local flux gradients and making sure that the flux is locally bounded based on the findings by Sweby (1984). These schemes are derived for an arbitrary mesh by Jasak (1996). The flux on a certain face is blended between a higher and a lower order scheme as

$$\phi_f = \phi_f^{UD} + \Psi \left(\phi_f^{CD} - \phi_f^{UD} \right) \tag{4.20}$$

where ϕ_f^{CD} is the flux calculated using a higher order scheme (in this case central differencing.) ϕ_f^{UD} is the flux calculated using a lower order scheme (in this case upwind differencing) and Ψ is the blending function. The blending function is regulated based on the gradient of the flux as

$$r = \frac{\phi_C - \phi_U}{\phi_D - \phi_C} \tag{4.21}$$

where $\phi_{C,U,D}$ is the flux from the owner cell, the upwind cell, and the downwind cell for a face respectively. How these cells are identified is dependent on the local flow direction.

The **limitedLinear** scheme in OpenFOAM (Jasak, 1996) uses a limiter similar to the one proposed by Sweby (1984) that satisfies the TVD condition

$$\Psi = 2r/c \tag{4.22}$$

This limiter varies the weighting between central and upwind differencing using a constant multiplicator c (see Table 4.4.) The limiter is restricted between 0 and 1 (full upwind and full central differencing.) It is therefore also similar to the minmod limiter (Roe, 1986) in that it follows a constant value after the initial slope of $\Psi(r)$. However, as with the Sweby limiter, the initial slope can be changed.

The **filteredLinear** scheme uses an alternative control on the limiter Ψ to more efficiently apply upwinding where it is needed. The scheme uses the difference in flux between the current cell P and its neighbours N as

$$\Delta\phi = \phi_N - \phi_P \tag{4.23}$$

and the gradients of ϕ_N and ϕ_P along the direction vector between the two cell centres P and N as

$$\phi_P^G = (P - N) \cdot grad(\phi_P) \tag{4.24}$$

$$\phi_N^G = (P - N) \cdot grad(\phi_N) \tag{4.25}$$

$$\Psi = 2 - 0.5 \frac{min\left(|\Delta\phi - \phi_P^G|, |\Delta\phi - \phi_N^G|\right)}{max\left(|\phi_P^G|, |\phi_N^G|\right)} \tag{4.26}$$

The limiter is constrained between 1 and 0.8 (0-20% upwind.)

The tested schemes in this study are presented in Table 4.4. The schemes mentioned here are applied to the interpolation of the divergence of the variables u_{1-3}, k and ω in all cases. Table 4.4 also shows the Courant number limit required to keep the simulation using the different schemes from diverging as well as the formal accuracy for each scheme.

4.3.1 Convection of α

This study concerns only convection of the continuum variables. The choice of schemes to control convection of the volume fraction α will have an impact on the accuracy, especially on the wave propagation. However, to limit the scope of this study, the scheme is fixed in all cases. Here, the MUSCL scheme (van Leer, 1979) is used to resolve the convective term. In addition, a compression scheme is used to ensure a sharper interface. To this end, the flux of α is defined as

$$\phi_\alpha = \phi_{MUSCL}(\phi, \alpha) + \phi_{cpr}(\phi_{cpr}(-\phi_r, 1-\alpha), \alpha) \tag{4.27}$$

TABLE 4.4: Tested divergence schemes.

Scheme	Order of accuracy	Ψ	C
Upwind	1^{st}	-	> 1
lL	$1^{st}/2^{nd}$	$2r/1$	> 1
lL	$1^{st}/2^{nd}$	$2r/0.8$	1
lL	$1^{st}/2^{nd}$	$2r/0.6$	1
lL	$1^{st}/2^{nd}$	$2r/0.4$	0.9
lL	$1^{st}/2^{nd}$	$2r/0.2$	0.5
lL	$1^{st}/2^{nd}$	$2r/0.05$	0.2
fL	$1^{st}/2^{nd}$	Eqn. 4.26	$0.25 - 0.5$
Central	2^{nd}	-	0.1

where ϕ_{MUSCL} is the flux of α calculated using the MUSCL scheme and ϕ_{cpr} is the correction for interface normal flux of α. ϕ_r is the interface normal flux which is defined as

$$\phi_r = (\hat{\mathbf{n}}_i \cdot \mathbf{n}) min\left(c_\alpha \left|\frac{\phi}{A}\right|, max\left(\left|\frac{\phi}{A}\right|\right)\right) \tag{4.28}$$

where $\hat{n}$ and A are the face normal and area respectively. The compression coefficient c_α is set to one and the local interface normal $\hat{n}_i$ is estimated from the local gradient of α. In Eqn. 4.28 the max operator refers to the global maximum of ϕ/A whereas the min operator is a local comparison between two scalars.

This is equivalent with the addition of another term in the transport equation for α so that Eqn. 4.2 becomes

$$\frac{\partial \alpha}{\partial t} + \nabla \cdot (\alpha u_i) + \nabla \cdot (\alpha(1-\alpha)u_r) = 0 \tag{4.29}$$

where u_r is only non-zero near the interface. The extra term increases the local gradient of α normal to the interface to ensure a sharper resolution. The compression scheme also limits ϕ_r using the fourth order limiter Ψ_α. This limits the flux normal to the interface as to reduce diffusion of the volume fraction. Ψ_α is defined as

$$\Psi_\alpha = min(max(1 - max(\Psi_{\alpha P}, \Psi_{\alpha N}), 0), 1) \tag{4.30}$$

where

$$\Psi_{\alpha P} = (1 - 4\phi_{rP}(1 - \phi_{rP}))^2 \tag{4.31}$$

$$\Psi_{\alpha N} = (1 - 4\phi_{rN}(1 - \phi_{rN}))^2 \tag{4.32}$$

4.3.2 Effect on wave propagation

An empty basin of the same dimensions as in Table 4.2 is used to study the effects of the chosen schemes on free wave propagation. Waves of $\lambda = 3$m and $\zeta_0 = 0.023$ m are generated. Wave probes are positioned at x =-1.5 , 0 ,1.5, 3 and 6 m. This represents locations at λ, 1.5λ, 2λ, 2.5λ and 3.5λ downstream of the end of the relaxation region. The mesh size for this study is considerably smaller than for all the other conducted studies since no object refinement is needed. The mesh size is 660 000 so a smaller number of CPUs can thus be used for this study than what was mentioned in Section 4.2. Here, 4 cores at 2.67 GHz each are used and the total time to complete 25 s of simulation time is presented for each scheme in Table 4.5. Since the time step is different for different schemes (as shown in Table 4.4), the average time to complete a time step is also shown. Finally, the total number of iterations on average spent on the momentum predictor and pressure corrector steps in the PISO loop are presented. For the momentum equation, the convergence criterion is a residual smaller than 10^-9 and for the pressure, a residual smaller than 10^-7.

TABLE 4.5: Computational time when using different convection schemes to study free wave propagation.

Scheme	Total comput. time	Time per step	Momen. predict. iter.	Pressure correct. iter.
Upwind	20 h	0.5s	8	10
lL(1)	25 h	0.7 s	8	24
lL(0.8)	26 h	0.7 s	9	25
lL(0.6)	26 h	0.7 s	9	24
lL(0.4)	26 h	0.7 s	8	24
lL(0.2)	27 h	0.7 s	9	26
lL(0.05)	27 h	0.75 s	11	29
fL	26 h	0.7 s	8	26
Central	30 h	0.8 s	14	31

The results are presented in Figure 4.7 as the recorded wave heights at these locations as a fraction of the wave height at the end of the relaxation region ($\zeta_0 = 0.023$ m.) The results in Figure 4.7(a) are based on the steady amplitudes averaged between $t = 10T_e$ and $t = 14T_e$. Figure 4.7(b) represents the same distribution after a longer simulation time and the results here show the average amplitudes between $t = 22T_e$ and $t = 26T_e$.

It is seen here that the choice of upwinding limit for the limitedLinear scheme makes very little difference ($\approx 0.7\%$ of ζ_0) for the recorded amplitudes at any location. As expected, the limitedLinear scheme performs much better than a pure upwind scheme but also significantly worse than the central scheme in early stages of the simulation.

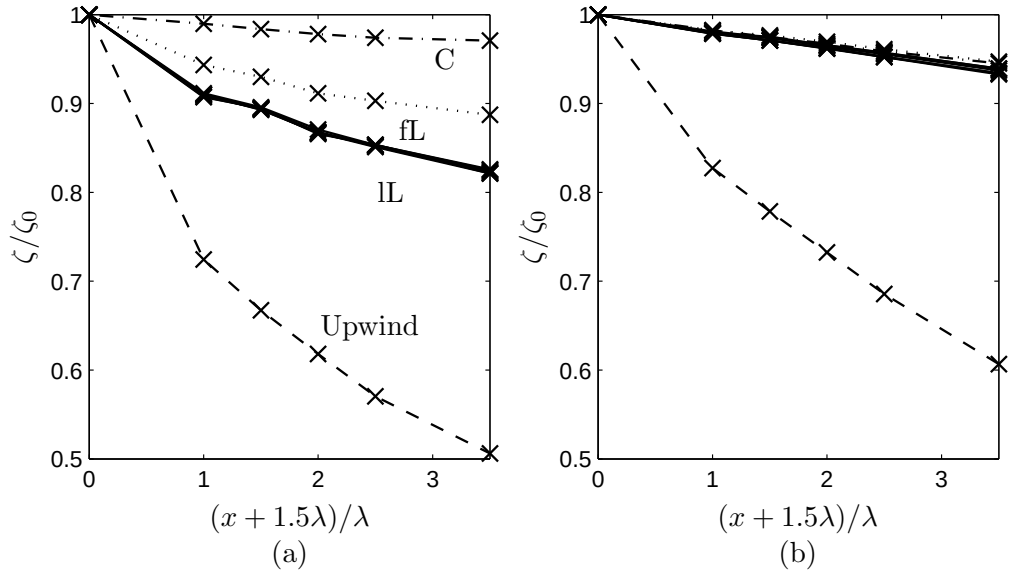

FIGURE 4.7: Measured wave amplitudes between (a) $t = 10T_e$ and $t = 14T_e$ and (b) $t = 22T_e$ and $t = 26T_e$ at different probe locations with different divergence schemes. The x-coordinate i shifted by 1.5λ to give the distance from the relaxation region rather than the absolute location.

The filteredLinear scheme performs slightly better than limitedLinear in early stages of the simulation but equally well after a sufficient amount of time has been allowed to pass. The wave profiles at $t = 10T_e$ are shown in Figure 4.8.

The amplitude losses at each position at the early and late recording scopes are shown in Table 4.6.

Even though this study shows that central differencing or filteredLinear is preferable to ensure free wave propagation, in reality, the limitedLinear scheme is superior in this case. Firstly, the loss where the hull is located does not differ much between filteredLinear and limitedLinear. Furthermore the stability of both the central differencing and filteredLinear is much lower than for limitedLinear leading to a major reduction in the time step to keep the respective simulations stable as shown in Table 4.4.

TABLE 4.6: Loss of amplitude for different convection schemes.

Scheme	Averaging span: $10T_e \rightarrow 14T_e$		Averaging span: $22T_e \rightarrow 26T_e$	
	1.5λ	3.5λ	1.5λ	3.5λ
Upwind	32.3%	49.3%	21.9%	38.6%
limitedLinear	5.7%	6.3%	2.7%	6.5%
filteredLinear	5.4%	6.1%	2.3%	5.5%
Central	1.6%	2.3%	2.3%	5.5%

The final consideration from this study is the importance of simulation length. All schemes except central differencing improve significantly with increased simulation time. This may be due to the steadiness of the wave pattern and the fact that, numerically

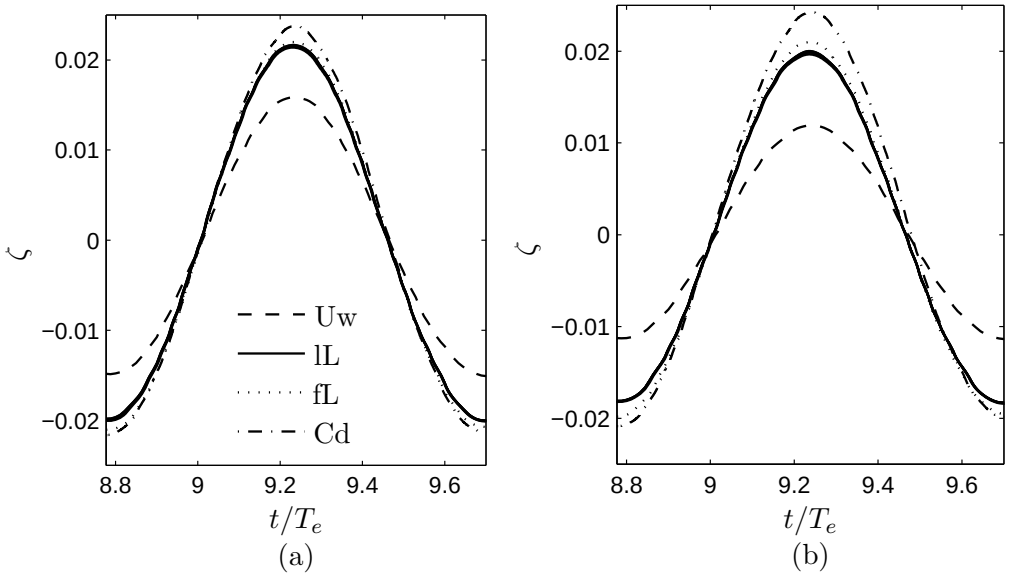

FIGURE 4.8: Wave profiles at $x = 0$ (a) and $x = 2\lambda$ (b).

each wave introduced at the inlet contributes to more energy in the pattern. The dissipation will thus be less and less significant as time passes. This would mean that the convection scheme alters how the wave energy propagates (as opposed to propagating with the group velocity as would be expected physically.) Figure 4.7(b) represents a time where a steady state is reached, i.e. when the amplitude no longer increases with time. When considering a quasi-steady situation with constant forward speed and regular waves, it is therefore worth using a limitedLinear scheme and a longer simulation time. When considering irregular waves and variable forward speed, the wave pattern is not as steady meaning that it cannot accumulate energy over time. In such a case it would be preferable to use a higher order convection scheme. The extra computational time required to do so must however be put in relation to the available resources and the number of analyses to be conducted.

4.3.3 Effect on viscous drag

A surface piercing flat plate of the same length and draught as the Wigley hull is used to represent a wave/body interaction situation where the viscous force variation is dominant in the added drag due to waves. It was suggested by Dugan (1969) that the boundary layer of a flat plate moving near a free surface might interact with the surface waves to alter the viscous drag compared to a plate travelling in an infinite fluid. However, because of the simplicity of the method used by Dugan (1969), no conclusion could be drawn if this would also happen for less slender bodies moving closer to, or piercing, the free surface. Even though the instantaneous viscous contribution to the added resistance and motions of a ship is small, modelling errors in forces, and thereby motions are cumulative since they are intrinsically linked. Therefore, even a small amplitude- or phase change could have an impact when looking at the time history of motions.

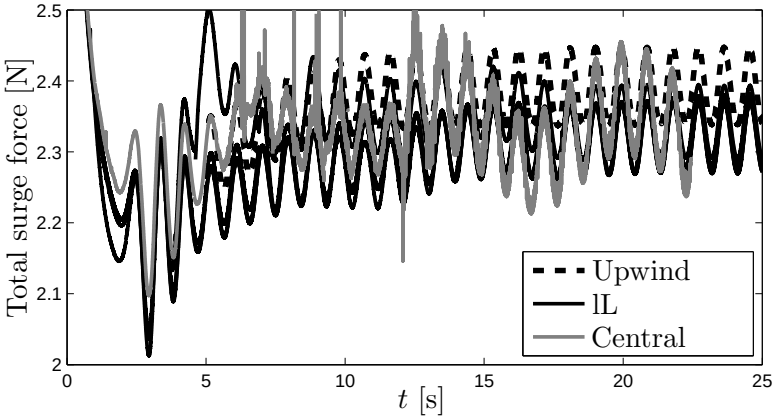

FIGURE 4.9: Development of total surge force over time for different schemes.

To create the mesh, the same strategy as described in Section 4.2.6, with the same levels of refinement as was used for the Wigley hull is employed. A mesh size of 6.5M is achieved and the total time to complete 25 s of simulation time is presented for each scheme in Table 4.7. Since the time step is different for different schemes (as shown in Table 4.4), the average time to complete a time step is also shown. Finally, the total number of iterations on average spent on the momentum predictor and pressure corrector steps in the PISO loop are presented. For the momentum equation, the convergence criterion is a residual smaller than 10^-9 and for the pressure, a residual smaller than 10^-7. In this case, limitedLinear with $\Psi = 2r/0.05$ as well as filteredLinear are unstable and have been excluded.

TABLE 4.7: Computational time when using different convection schemes to study viscous forces on a flat plate.

Scheme	Total comput. time	Time per step	Momen. predict. iter.	Pressure correct. iter.
Upwind	22 h	3.5 s	13	14
lL(1)	27 h	6.5 s	15	46
lL(0.8)	31 h	7 s	14	50
lL(0.6)	31 h	7 s	15	54
lL(0.4)	35 h	7 s	12	53
lL(0.2)	38 h	7.5 s	12	56
Central	44 h	7.5 s	23	65

As shown in Figure 4.9, the solution for all remaining schemes except central differencing reaches a steady oscillation amplitude around a fixed mean value. The solution using central differencing, displays a noisy and volatile behaviour.

Figure 4.10 shows the amplitude and mean value while Figure 4.11 shows the phase of the surge force.

The amplitude and mean values of surge force show similar trends when varying the convection scheme. The amplitude varies with less than 1% between the different values

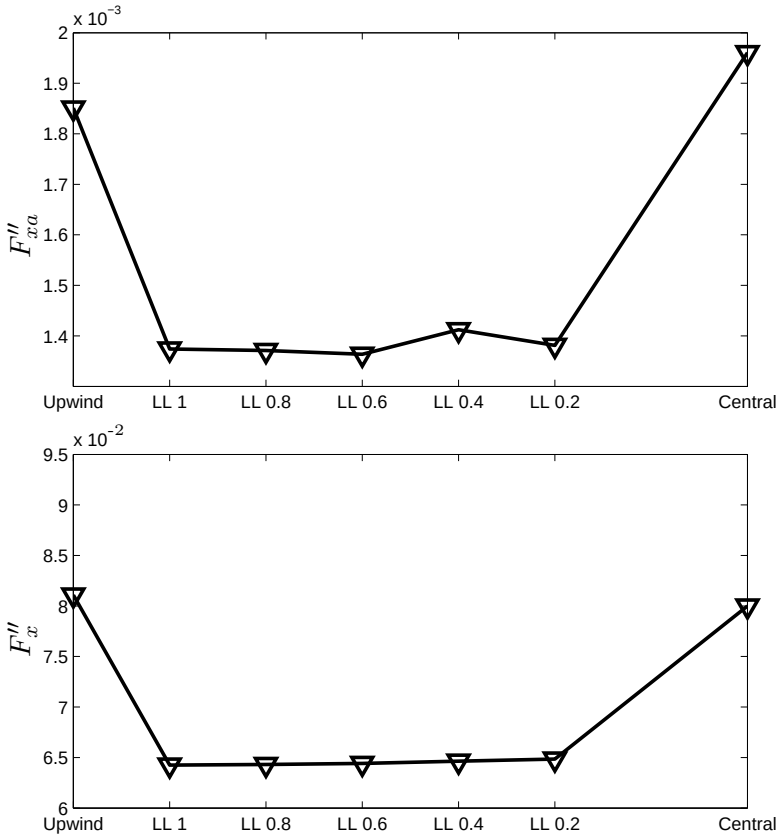

FIGURE 4.10: Amplitude and mean value of surge force on plate.

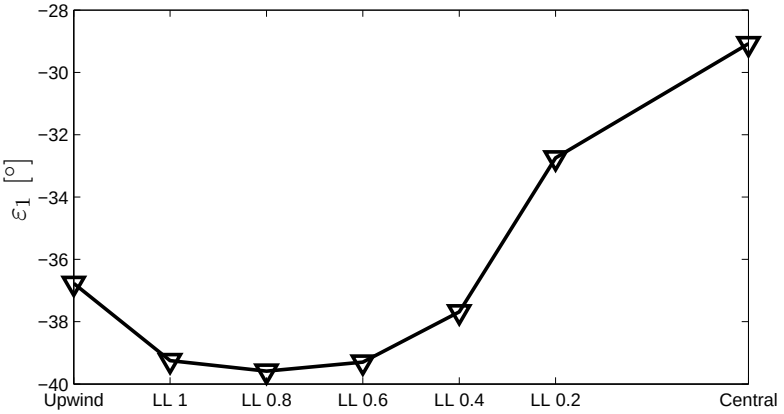

FIGURE 4.11: Phase of surge force on plate relative to mid-plate wave elevation.

of c in the limitedLinear scheme with the exception of $\Psi = 2r/0.4$ which is about 3.5% larger than the others. There is no explanation for this relating to the equations so it is likely to be due to a local deviation or instability. The surge force amplitude calculated using the pure upwind scheme is 36% larger than for the limitedLinear schemes. Central differencing gives an amplitude of the surge force which is 44% larger than limitedLinear. However, as shown in Figure 4.9, the solution is not steady so the value is likely not to be representative. Note that the wave amplitude will be slightly different between the cases. This is taken into account by using the non dimensional form of the amplitude F''_{xa} and the mean F''_x in Figure 4.10 (see Eqns. 4.36 and 4.39). Here, the measured amplitude of the waves at the mid point of the length of the plate is used as the value of ζ_0. The fact that the upwind scheme has over predicted the viscous force variation for a certain wave height but under predicted the wave height itself (as shown in Figure 4.7) means that the actual difference in the predicted surge force amplitude between upwind and limitedLinear is only about 10%.

The phase is affected more by the selection of scheme with a variation of about 8° between the different limitedLinear schemes, generally increasing with increasing values of the constant c in Eqn. 4.22. The upwind scheme gives a similar phase to mid-range limitedLinear. limitedLinear with $\Psi = 2r/0.2$ and central differencing show a distinctly lower phase lag than the others.

Based on the results in this section the limitedLinear convection scheme with $\Psi = 2r/0.6$ is used throughout the Wigley hull study in the following sections. As shown in the previous sections, this represents a good compromise between speed and stability while performing well in comparison to other schemes in terms of numerical damping of the waves. In this case, there seems to be little motivation for using a lower value of c in Eqn. 4.22 and both upwind and central differencing have large disadvantages in terms of accuracy and stability.

4.4 Validation of the predicted surge force

The forces and moments on a fixed Wigley hull in waves are validated against experiments by Journée (1992) as well as compared to results from a non-linear Boundary Element Method (BEM) (Kjellberg, 2011). This is done for a range of wavelengths between $\lambda/L_m = 0.5$ and $\lambda/L_m = 2$. Here, the mesh size is 6.6M and the time step is limited by $C < 0.9$. The total computational time for 25 s of simulation time and time per time step are presented in Table 4.8. For the momentum equation, the convergence criterion is a residual smaller than 10^-9 and for the pressure, a residual smaller than 10^-7. This validation was previously presented by Windén et al. (2012).

TABLE 4.8: Computational time for simulation of a Wigley hull in waves.

λ/L_m	Fn	Total comput. time	Time per step	Momen. predict. iter.	Press. correct. iter.
0.50	0.2	60 h	18 s	18	83
0.75	0.2	57 h	17 s	17	79
1.00	0.2	57 h	17 s	17	78
1.25	0.2	56 h	16.5 s	17	76
1.50	0.2	53 h	16 s	16	72
1.75	0.2	50 h	15 s	16	68
2.00	0.2	45 h	13.5 s	14	62

The validation comparison is made in terms of the amplitudes and phases of the force variations F_x, F_y and M_z representing the surge force, the heave force and the pitching moment.

$$F_x = F_{xa} \sin\left(t\sqrt{gk} + \varepsilon_1\right) \tag{4.33}$$

$$F_y = F_{ya} \sin\left(t\sqrt{gk} + \varepsilon_3\right) \tag{4.34}$$

$$M_z = M_{za} \sin\left(t\sqrt{gk} + \varepsilon_5\right) \tag{4.35}$$

The amplitudes are nondimensionalised as

$$F''_{xa} = \frac{F_{xa}}{k\zeta_0 \rho g \nabla} \tag{4.36}$$

$$F''_{ya} = \frac{F_{ya}}{\zeta_0 C_{33}} \tag{4.37}$$

$$M''_{za} = \frac{M_{za}}{k\zeta_0 C_{55}} \tag{4.38}$$

and the mean value of the surge force is nondimensionalised as

$$F''_x = \frac{\overline{F_x}}{k\zeta_0 \rho g \nabla} \tag{4.39}$$

with C_{33} and C_{55} being the stiffness terms in the equations of motion for heave and pitch respectively given by the geometry. k and ζ_0 are the wave number and -amplitude of the incident waves and ∇ is the volume displacement of the hull. The phase shifts $\varepsilon_{1,3,5}$ are relative to the wave elevation amidships.

TABLE 4.9: Particulars of Wigley hull used for validation.

L_m	=	3 m	B_m	=	0.3 m
T_m	=	0.1875 m	∇	=	0.0780 m^2
C_{33}	=	6119	C_{55}	=	2874
a_W	=	0.2	KG	=	0.17 m

4.4.1 Validation setup

The used hull is the one labeled "Wigley III" by Journée (1992), the particulars of which are shown in Table 4.9 where a_W gives the shape of the hull as:

$$z = \frac{B_m}{2}\left[1 - \left(\frac{y}{T_m}\right)^2\right]\left[1 - \left(\frac{2x}{L_m}\right)^2\right]\left[1 + a_W\left(\frac{2x}{L_m}\right)^2\right] \tag{4.40}$$

Above the waterline, the cross section is fixed at the one when $y = 0$.

Based on the results of the mesh independence study given in Figure 4.2, the mesh density in the free surface region is set to 30 cells per waveheight. Since the wavelength is varied but the mesh kept constant, the density is set to 40 cells per wavelength for the shortest wave (and thus achieving 160 cells per wavelength for the longest wave.) The waveheight is very small compared to the wavelength so a higher density is set in the horizontal direction to achieve a lower aspect ratio.

Good correlation with both experimental values and with the BEM is demonstrated in Figure 4.12 for most quantities, however, both numerical methods have a discrepancy from the experimental values of surge force at $\lambda/L_m = 1$ which is unexplained. The total relative errors compared to the experimental values are given in Table 4.10. For heave, the errors in phase are very high. This is due to the use of relative error and the fact that the absolute phase is close to 0 for heave. The general shapes of the curves are very close to the experiment in all cases.

4.5 Viscous effects on forces

As shown in Figure 4.13, the viscous contribution to F''_{ya} and M''_{za} in the validation case is small but for F''_{xa}, an increasing viscous contribution with increasing λ/L_m is noted. Here, the amplitudes of the viscous force and moment variations as a fraction of the total amplitudes are shown.

A more prominent viscous effect can be seen when comparing the mean values of the force variations rather than the amplitudes. This is demonstrated in Figure 4.14 which shows the viscous contribution to the increase in the mean of each of the force components due to the waves.

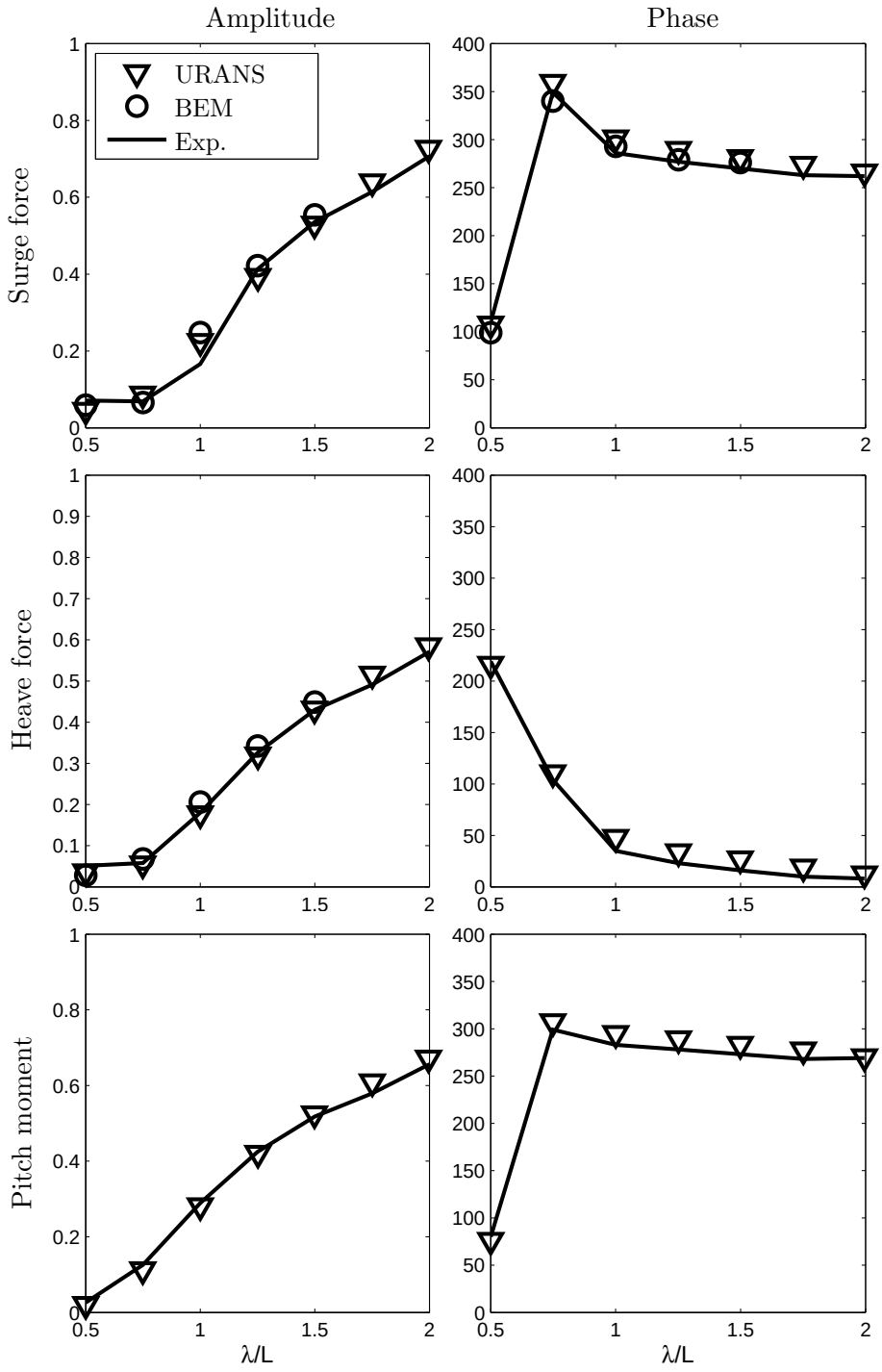

FIGURE 4.12: Results of validation case, experimental data by Journée (1992).

TABLE 4.10: Relative errors compared to experimental values by Journée (1992).

DOF	$\frac{\lambda}{L_m}$	Amplitude		Phase	
		URANS	BEM	URANS	BEM
Surge	0.5	-35.9%	-16.9%	-1.9%	-10.0%
	0.75	27.2%	-37.8%	3.0%	-2.6%
	1	35.3%	49.4%	5.5%	2.4%
	1.25	-4.7%	2.2%	4.6%	0.7%
	1.5	-1.1%	3.4%	4.1%	2.2%
	1.75	4.2%		4.3%	
	2	2.9%		1.6%	
Heave	0.5	-28.7%	-45.1%	-1.3%	
	0.75	-37.6%	-23.8%	6.5%	
	1	-1.5%	14.4%	37.4%	
	1.25	-1.8%	4.9%	48.1%	
	1.5	0.4%	4.4%	69.7%	
	1.75	5.2%		91.4%	
	2	2.5%		57.2%	
Pitch	0.5	-19.6%		-4.9%	
	0.75	-41.8%		2.8%	
	1	-2.5%		4.2%	
	1.25	-1.0%		4.1%	
	1.5	1.3%		3.8%	
	1.75	5.2%		3.6%	
	2	2.5%		0.5%	

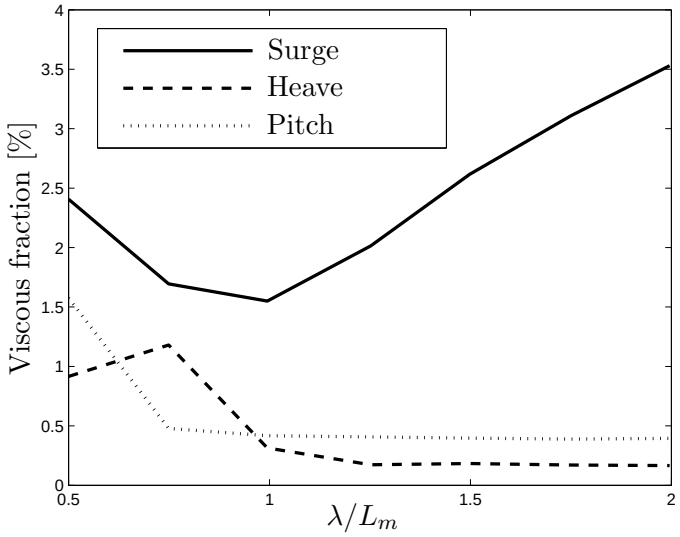

FIGURE 4.13: Viscous contribution to the total amplitudes F''_{xa}, F''_{ya} and M''_{za} in Figure 4.12.

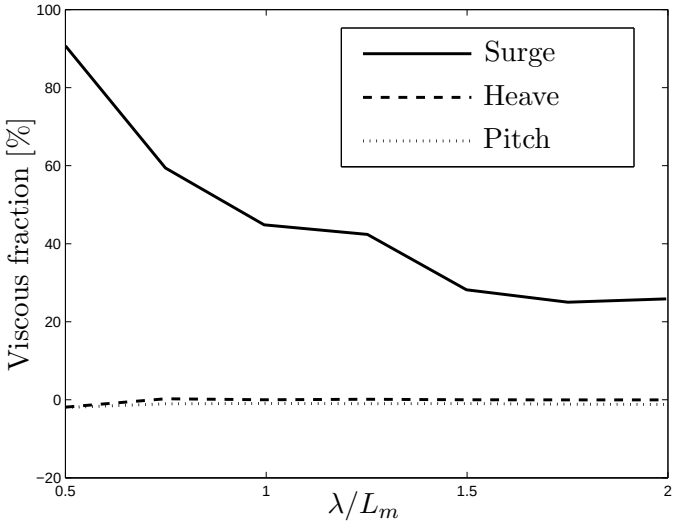

FIGURE 4.14: Viscous contribution to the increase in mean values of force/moment.

Even though the viscous contribution is significant in the fixed hull-case; in a free case, the induced motions from the heave and pitch forces would lead to an increase in the pressure component due to unfavourable attitudes of the hull to the incident waves. Furthermore, large increases in mean values of surge would not occur in an unrestrained case since the hull would obtain a new location relative to the wave due to the surge motion. However, the results from the fixed-hull case have demonstrated that there is likely to be an effect of the passing waves on the boundary layer.

4.6 Effect of above water shape

Previous studies have shown that modifying the above water shape of the Wigley hull described in Table 4.9 and Eqn. 4.40 has an effect on the total added resistance (Masuya, 2009) and that this can be predicted with good accuracy using the non linear slender body theory by Kihara et al. (2005). These studies relate to the added resistance due to the pressure distribution but, as was stated earlier, understanding how the viscous force distribution and thus the boundary layer behaves due to interaction with waves also has implications for the total performance of the ship in a seaway. To investigate how the above water bow shape affects the viscous forces, a parametric study is conducted using a modified Wigley hull with changing flare angles.

4.6.1 Modified Wigley hull

The modified Wigley hull has the same definition of shape under the waterline as in section 4.4.1 but rather than being wall sided above the waterline, the hull is distorted

to create a flare. If x_o, y_o and z_o are coordinates giving the shape of the original hull, the modified hull is defined as:

$$x_{mm} = \left\{ \begin{array}{llllll} x_o & if & x_o \geq x_\phi & or & y_o \leq 0 \\ \\ x_o + \phi_x & if & x_o < x_\phi & \& & y_o > 0 \end{array} \right\} \tag{4.41}$$

$$z_{mm} = \left\{ \begin{array}{llllll} z_o & if & x_o \geq x_\phi & or & y_o \leq 0 \\ \\ z_o \pm \phi_z & if & x_o < x_\phi & \& & y_o > 0 \end{array} \right\} \tag{4.42}$$

where

$$\phi_x = o_{xmax} \left(\frac{y_o}{H_m} \right)^{o_x} \frac{(x_o - x_\phi)}{(0.5L + x_\phi)} \tag{4.43}$$

$$\phi_z = \left(\frac{B}{2} - |z_o| \right) \left(\frac{y_o}{H_m} \right)^{o_{z1}} \left(\frac{x_o + 0.5L}{x_\phi + 0.5L} \right)^{\frac{1}{o_{z2}}} \tag{4.44}$$

and with $y_{mm} = y_o$. H_m is the freeboard, o_{xmax} the maximum overhang in the x direction, and x_ϕ the start of the flare region. The exponents o_x and o_{z1} determine the curvature of the flare. The exponent o_{z2} determines the curvature and extent of the deck. All parameters relating to the flare are defined in Figure 4.15.

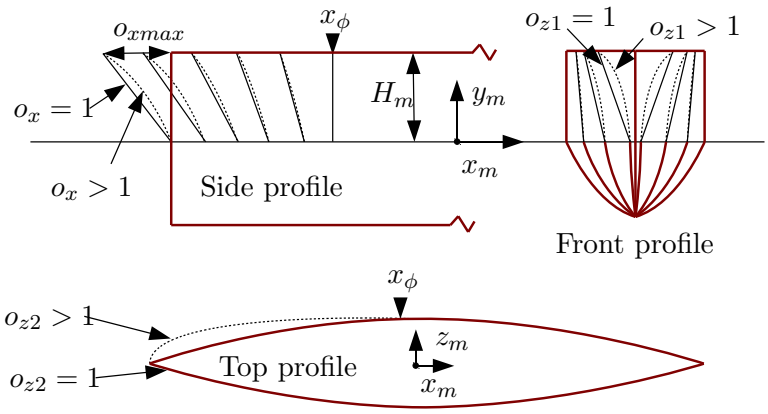

FIGURE 4.15: Definition of flare parameters on modified Wigley hull.

As seen in Eqns. 4.41 and 4.42, the waterline profile is undistorted so the waterline length L_m is kept constant.

4.6.2 Effect of flare angle

Six hulls are tested, the parameters $o_x = o_{z1} = o_{z2} = 3$ and $x_\phi = 0$ are fixed and the overhang o_{xmax} is varied according to Table 4.11. The resulting hulls are shown in Figure 4.16.

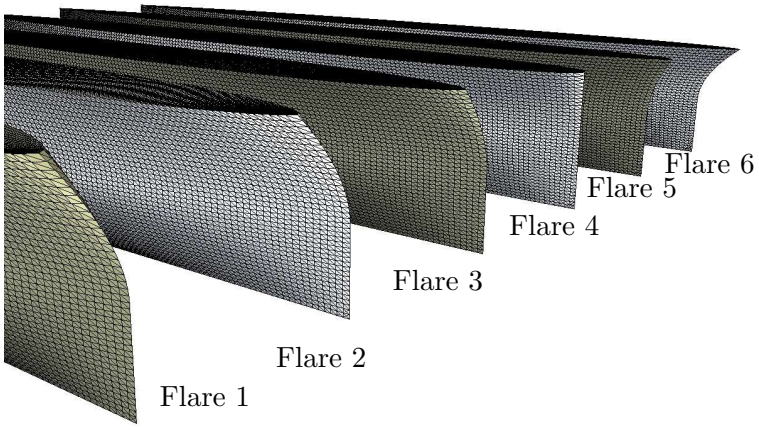

FIGURE 4.16: Visualisation of tested bow sections.

TABLE 4.11: Description of flared hull series.

Hull #	o_{xmax}
1	-6.3 % of *Lpp*
2	-4.2 % of *Lpp*
3	-2.1 % of *Lpp*
4	0
5	2.1 % of *Lpp*
6	4.2 % of *Lpp*

For these hull shapes, very little or no change in the amplitude and phase of the resistance variations is noted. There is however an effect on the mean increase of resistance across the range of the flare overhangs. The variation in mean increase of forces and moments for the different flare overhangs is shown in Figure 4.17. Windén, Turnock and Hudson (2013*b*) also showed that while there are differences in the turbulence kinetic energy in the wake behind these six hulls, the velocity profile (and thus the propeller inflow) is unaffected by the flare change. When moving to a more realistic hull form, this result will have to be revisited.

4.7 Effects of waves on the boundary layer

Using the simulation conducted in Section 4.4, the behaviour of the boundary layer around the Wigley hull in regular waves at $\lambda/L_m = 1$ is analysed. This is done to shed more light on the influence of the waves on the viscous flow around a ship.

To probe the near-hull velocities and turbulence intensity, 26 points on the hull surface along the streamwise direction are chosen. From each one of these, 100 points are picked along a line following the local normal to the surface. These are spaced between $y = 0$

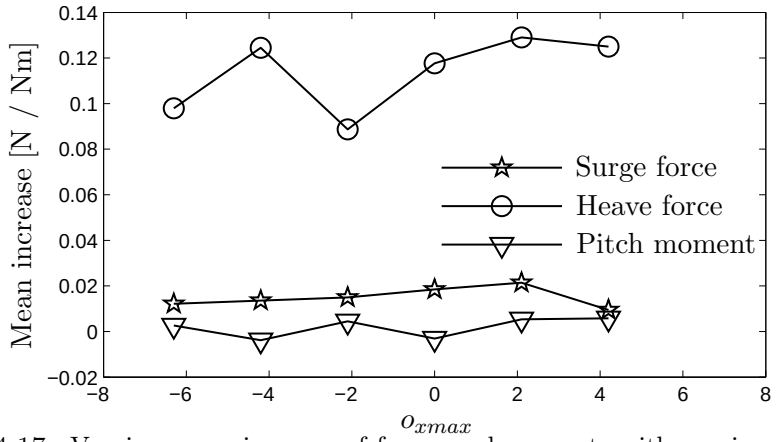

FIGURE 4.17: Varying mean increase of forces and moments with varying flare overhang.

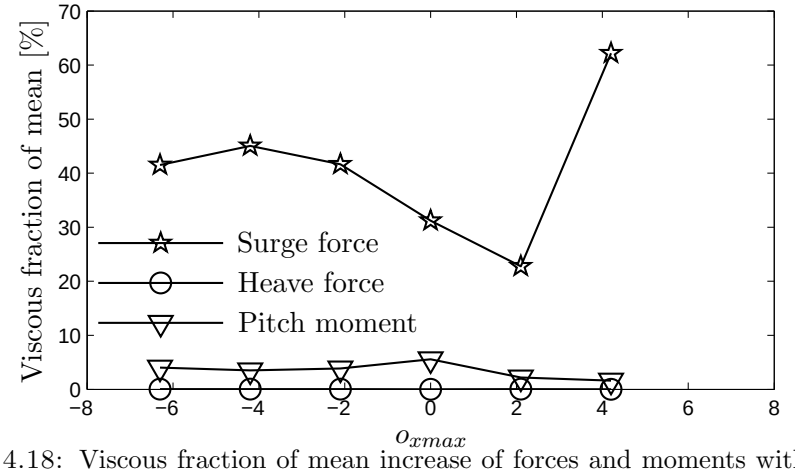

FIGURE 4.18: Viscous fraction of mean increase of forces and moments with varying flare overhang.

and $y = \delta$ where y is the distance from the wall. δ is an estimate of the thickness of the boundary layer given by

$$\delta = \frac{0.16 L_m}{Re^{1/7}} \tag{4.45}$$

The points are located at 35% of the draught which is enough to ensure that none of the probe locations are intersected by the free surface at any point during the simulation. The velocity profiles at selected points along the hull are shown when a wave crest passes amidships in Figure 4.19 and when a wave trough passes amidships in Figure 4.20. Here, the horizontal lines on the right indicate the resolution of computational cells in the boundary layer. The distance from the wall is given as the non-dimensional distance y^+ which is defined as

$$y^+ = \frac{y u_\tau}{\nu} \tag{4.46}$$

where the friction velocity u_τ is estimated as

$$u_\tau \approx U_\infty \sqrt{\frac{0.027}{4Re^{1/7}}} \tag{4.47}$$

and ν being the kinematic viscosity of water. The estimates in Eqns. 4.45 (for the distribution of probes) and 4.46 (for the non dimensional wall distance) are used to give a smoother and more consistent layout of the presented figures. The actual values of y^+ as calculated in the simulation vary slightly along different parts of the hull but; apart from at the bow, the stern and the keel, they are within 5% of the estimated value. The same applies for δ where the maximum extent of the boundary layer in the simulation is within 5% of the estimated value.

As a reference, the momentum thickness θ is also shown which gives an indication of the momentum distribution in the boundary layer along the hull. The momentum thickness is defined as

$$\theta = \int_0^\infty \frac{U}{U_\infty}\left(1 - \frac{U}{U_\infty}\right) dy \tag{4.48}$$

However, because of the wave orbital velocities, U will not necessarily approach U_∞ as $y \to \infty$ so the integral in Eqn. 4.48 will be infinite. Because of this the local U_∞ is approximated as the value of U at the probe farthest from the wall. This correction is used only in Eqn. 4.48 and is not present in Figures 4.19 and 4.20 where the true U_∞ is used.

The distribution of the turbulence intensity k is shown when a wave crest passes amidships in Figure 4.21 and when a wave trough passes amidships in Figure 4.22. The horizontal lines represent the distribution of cells in the boundary layer. Here, the turbulence intensity is presented as a fraction of the ambient value k_∞, taken at the outermost probe point. All curves show a variation of k/k_∞ between 1 and 2 except near the bow when, in the case of a trough passing, the value is less than 1.

4.7.1 Variation of momentum thickness with time

Figures 4.19 to 4.22 represent instantaneous states of the boundary layer. By studying the quasi-steady situation of a wave system travelling at the same speed as a flat plate,Stern et al. (1987) showed large oscillations of displacement thickness δ^* along the hull when waves are present. In the case studied here, the wave profile is not steady relative to the hull. To get a better idea of what happens to the flow near the hull as the waves move past, the momentum thickness is recorded at all locations over several periods of encounter. Figure 4.23 shows the difference between θ in waves and θ_c in calm water over one period of encounter. Here, the position of the wave crest is marked

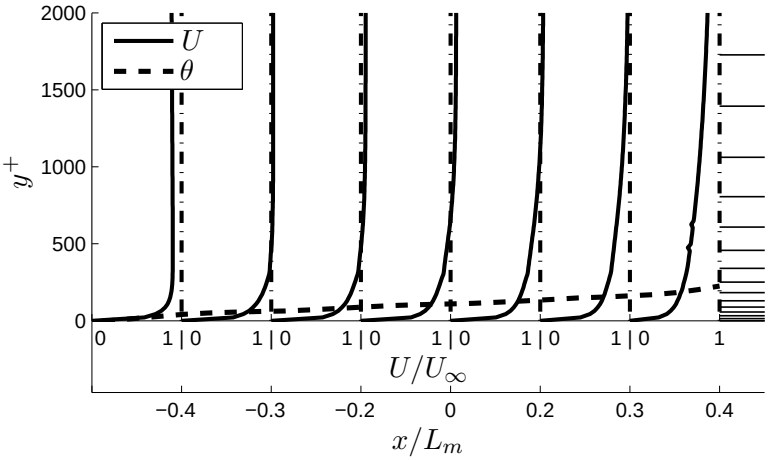

FIGURE 4.19: Profiles of U along the hull (wave crest amidships, trough at bow and stern.)

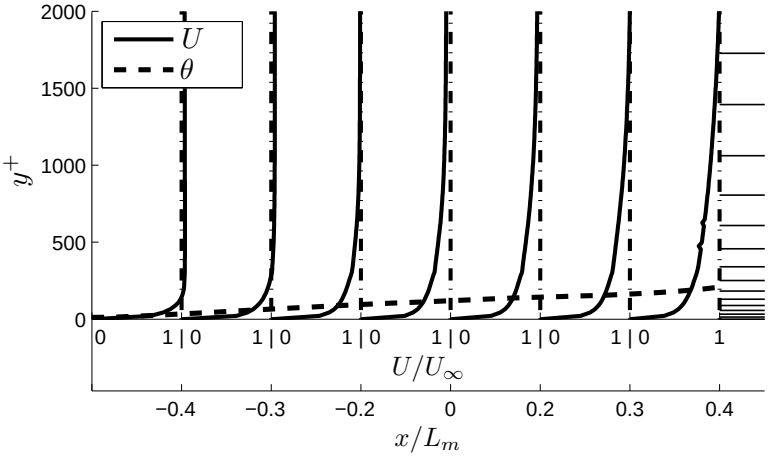

FIGURE 4.20: Profiles of U along the hull (wave trough amidships, crest at bow and stern.)

with a vertical dashed line. Wave troughs are marked with a vertical dotted line. To be able to see the evolution of Figure 4.23 with time more easily, the difference in the mean value of θ compared to calm water is also shown as a dashed line. This is constant throughout the time series.

A trend can be seen in Figure 4.23 where an increase in θ compared to calm water starts slightly ahead of the passing wave crest and lingers for about $T_e/4$ before a decrease induced by a passing wave trough is initiated. Figure 4.24 shows the mean value of θ at each x-location and Figure 4.25 shows how much the thickness is varying due to the waves. The local amplitude of variation θ_a is defined as

$$\theta_a = \frac{\theta_{max} - \theta_{min}}{2} \tag{4.49}$$

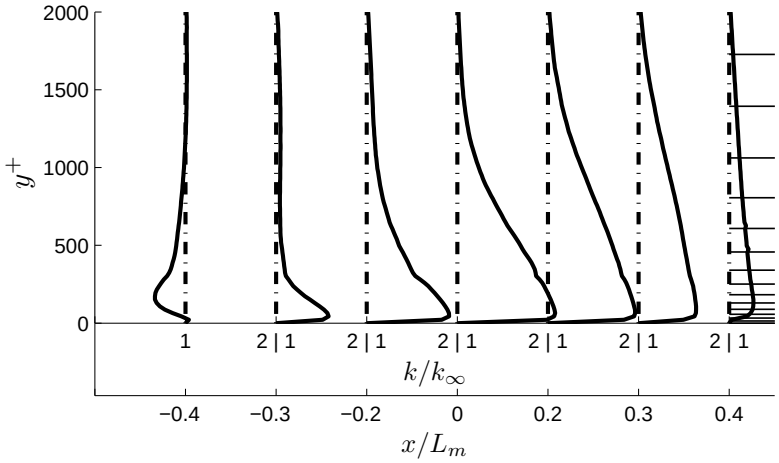

FIGURE 4.21: Profiles of k along the hull (wave crest amidships, trough at bow and stern.)

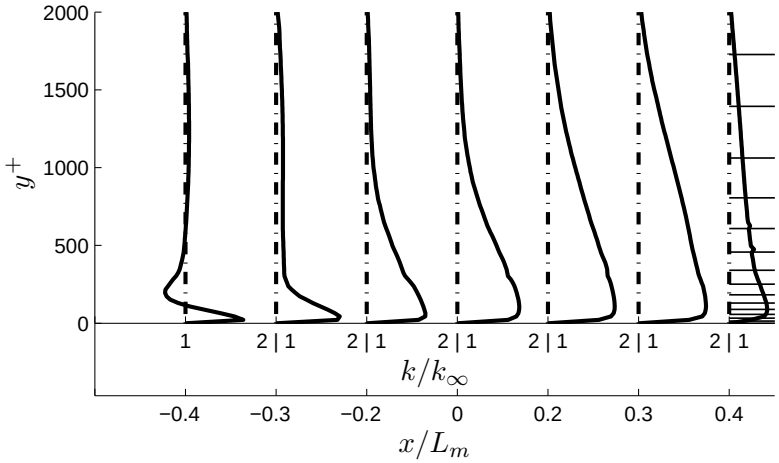

FIGURE 4.22: Profiles of k along the hull (wave trough amidships, crest at bow and stern.)

The results shown in Figure 4.24 are similar to those obtained by Stern et al. (1987) on a flat plate with the thickness varying between positive and negative relative to the calm water conditions. However, the trend near the stern seems to be reversed with reduced θ_m recorded at the stern in this study compared to an increased δ^* recorded by Stern et al. (1987). This indicates that apart from disturbing the boundary layer locally, waves make the disturbance travel downstream in head waves. Stern et al. (1987) also showed that the trends in decrease/increase of momentum thickness remain very similar with increasing depth but that the actual magnitude of the discrepancy from calm water reduces further away from the free surface.

Figure 4.25 shows that the momentum thickness varies between ± 15-20% of the mean value near the bow and between ± 5% of the mean value further aft. The mean momentum thickness in waves is very similar to the calm water value on the forward part of the hull but is reduced aft of amidships to a minimum of 85% of the calm water θ at

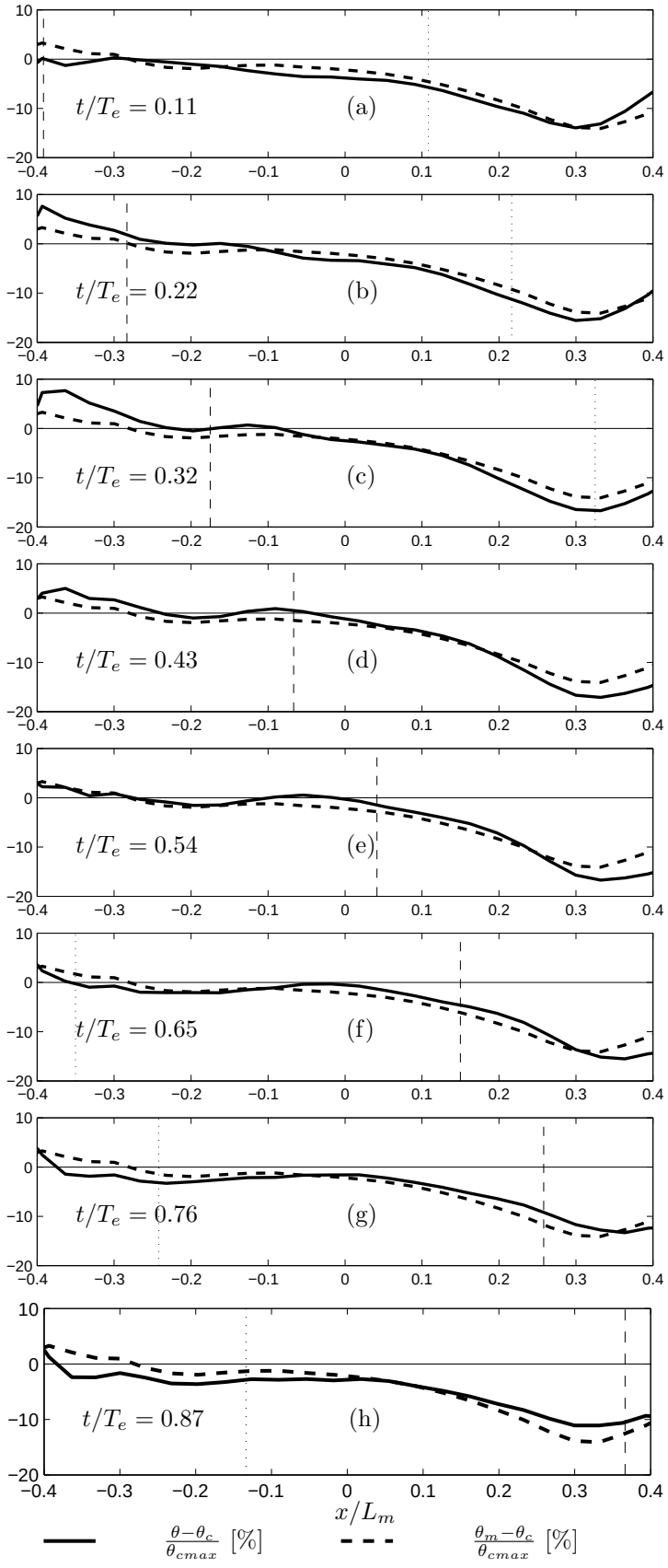

FIGURE 4.23: Variation of θ-θ_{calm} over period of encounter along hull.

$x/L_m = 0.3$. Aft of $x/L_m = 0.3$, the momentum thickness increases faster to again be roughly equivalent to the calm water value at $x/L_m = 0.4$.

To give an idea what causes values of θ_a at different locations along the hull to be different, the variation in velocity U_a, defined as

$$U_a = \frac{U_{max} - U_{min}}{2} \tag{4.50}$$

is shown as a contour plot representing slice through the boundary layer in Figure 4.26. In Figure 4.26, the variation of θ and θ_a are overlain for easier comparison. Furthermore, the approximate locations of the crests and troughs of the ship generated wave pattern are shown for reference.

Looking at Figure 4.26, a conclusion can be drawn that on the front of the hull, the interaction between the regular waves and the ship generated waves near the hull is strong enough to oscillate the lengthwise velocity deep within the boundary layer. This can be clearly seen in the contour plot of U_a. Further back, lower values of U_a indicate that the interaction between the regular wave and the ship wave system near the hull is less strong. This is possibly due to deflection of the regular wave by the hull meaning that the near-hull steady wave pattern is less disturbed further aft. On the front part of the hull there is no clear correlation between peaks in θ_a and wave crests/troughs. Aft of $x/L_m \approx -0.2$ however, peaks and troughs in θ_a seem to roughly correspond to crests and troughs in the steady wave pattern respectively.

There is a slight bias in the probe point distribution where points towards the bow and stern are slightly closer to the free surface than points nearer to amidships. This is likely to be the reason why the values of θ_a are higher near the bow and stern. The conclusion from Figure 4.26 is therefore that θ_a varies along the hull in an oscillatory manner with the mean approximately constant (if one disregards the rise towards bow and stern.) The oscillation is loosely connected to the wave crests and troughs of the steady wave pattern.

Another area of large oscillations in lengthwise velocity is found at the stern region. These oscillations are likely stemming from the interaction between the stern wave and the regular wave system. This will have an impact on the the propeller inflow velocity.

4.8 Conclusions

This chapter has provided the basic set up for a RANS based numerical towing tank. To be able to build confidence in the model gradually, it has used a simple geometry to focus on the importance of modelling the interaction between the near wall flow and incident waves. When studying the effect of waves on the near-wall flow around the Wigley hull

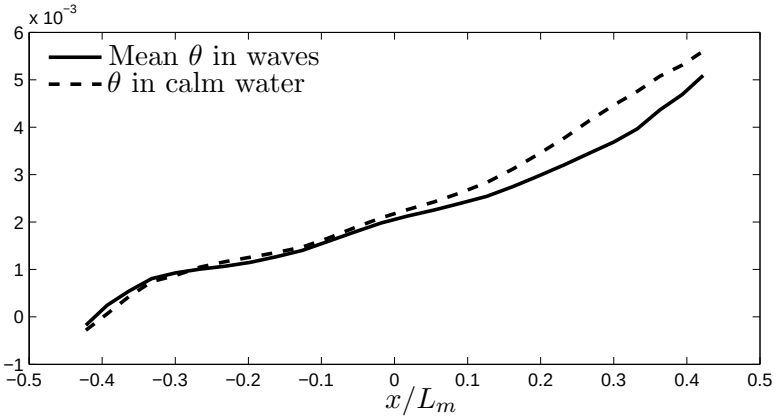

FIGURE 4.24: Mean θ in waves compared to calm water at different lengthwise locations.

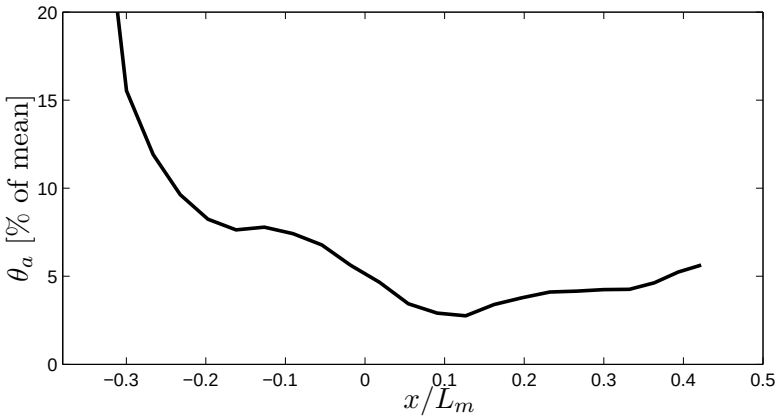

FIGURE 4.25: Variation of θ around mean value due to waves at different lengthwise locations.

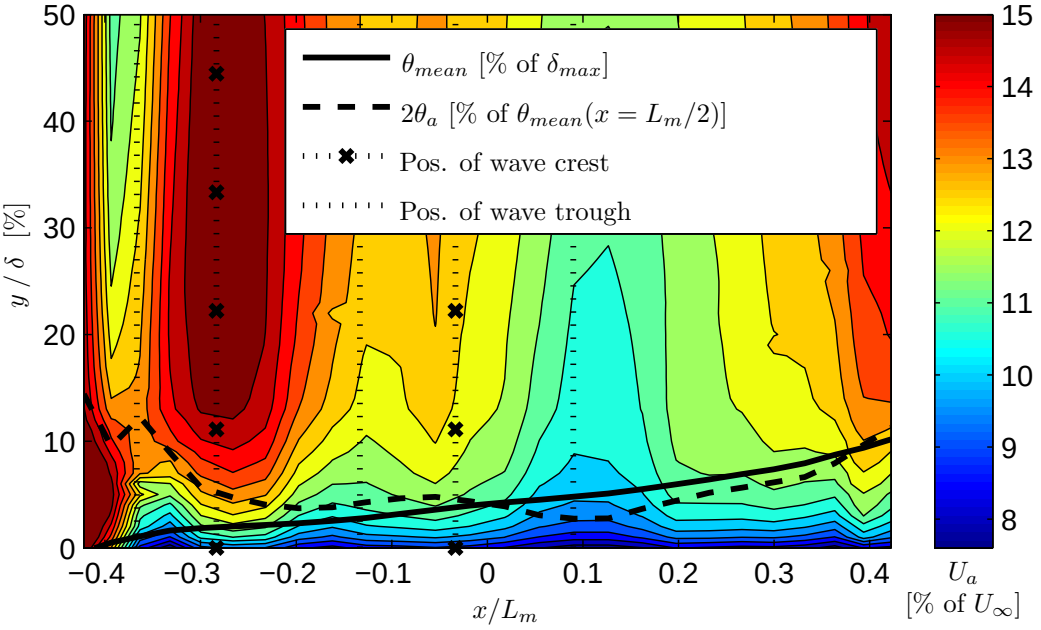

FIGURE 4.26: Variation amplitude of axial velocity inside boundary layer, mean value and variation amplitude of θ are overlain.

using this setup, it can be concluded that a passing wave crest is accompanied by a local increase in the momentum thickness followed by a decrease at the following wave trough. The amplitude of oscillation of θ between crest and trough varies along the length of the hull. Furthermore, the mean momentum thickness is shown to be lower than in calm water on large parts of the aft hull. Variations in the mean momentum thickness in waves will also mean a change in the mean viscous resistance something that is not considered if using traditional methods. The results in this chapter serve to indicate the basic effect of the waves on the boundary layer, for this reason the hull has been fixed. The actual profiles and integral quantities when considering a hull that is free to move in the waves are likely to be altered.

Since the effects discussed here are characterised by small variations and small spatial scales, the quality of the modelling will have a large impact on the results. To quantify some of this impact, the effects of chosen numerical schemes are demonstrated. The choice of convection scheme is shown to greatly influence the free wave propagation, especially when using shorter simulation times. It is also shown to affect the phase of the viscous drag force on a flat plate in waves with up to 10°. It is concluded that the limitedLinear and filteredLinear TVD schemes produce satisfactory results at relatively high Courant numbers. However, to get a better idea of the true quality of modelling detailed measurements of the near-hull flow around ships in waves are needed. Only the quality of modelling of the continuum variables has been investigated. For accurate predictions of viscous flow around a ship in waves, the representation of the free surface and its interaction with the near-hull flow should also be addressed. The $k-\omega$ SST model, as well as any common turbulence model has been shown to not accurately represent the turbulent flow close to the free surface when using a VOF method (Shirani et al., 2006). This is something that should be addressed in future studies.

The conclusions drawn about the influence of waves on the boundary layer and conclusions regarding the effect of numerical schemes on the phase of the viscous forces relate strongly to the deficiencies in predicting ship performance in waves mentioned by Turnock et al. (2010). There is clearly an effect of the waves on the boundary layer and thus the viscous wake, the performance of the propeller and the ship motions. In the cases studied in this here, there is very little separation present due to the shape of the Wigley hull. Furthermore, the waves used here have low steepness. Steeper waves, even on a very slender body can lead to wave induced separation regions near the free surface (Stern et al., 1987). When considering more realistic hull forms in steeper waves, it is therefore likely that the waves will have an even larger effect on the viscous flow around the hull by altering the stern separation pattern.

Reduction of errors in the viscous forces as well as the viscous wake would be important improvements in the accuracy of free running unsteady simulations of e.g. seakeeping and manoeuvring since errors in these types of simulations will be cumulative. In general

it can be concluded that more attention should be given to the near-hull flow when considering ship performance in waves.

Chapter 5

Self propulsion model

Recalling the schematic of the desired numerical approach shown in Figure 1.2, the numerical towing tank should include the ability to model the ship and its propulsor in interplay. This chapter discusses different options for this as well as the implementation of a general framework for propeller modelling in OpenFOAM. Furthermore, the details of a coupling between the RANS model and the preferred propeller model is presented.

As was discussed in Section 2.10, several options exist for including the propeller in the numerical towing tank and, as with most modelling techniques they all represent a different ratio between accuracy and computational effort. The target here is to be able to accurately represent the KCS propeller working behind the hull in unsteady conditions.

In this chapter, four important parameters will be used to represent the performance of the propeller. The advance ratio J relates the rotation of the propeller to the inflow speed as

$$J = \frac{U_\infty}{n2R} \tag{5.1}$$

where n is the rotation frequency. The non dimensional thrust and torque coefficients K_T and K_Q are defined as

$$K_T = \frac{T}{\rho n^2 \left(2R\right)^4} \tag{5.2}$$

$$K_Q = \frac{Q}{\rho n^2 \left(2R\right)^5} \tag{5.3}$$

where T is the thrust and Q is the torque. Finally, the efficiency of the propeller is defined as the work done to the fluid by the thrust compared to the work needed to produce the corresponding torque so that

$$\eta = \frac{U_\infty T}{\Omega Q} \tag{5.4}$$

where Ω is the angular frequency defined as $\Omega = 2\pi n$. Eqns. 5.1 and 5.4 are based on the free stream velocity U_∞ and are thus valid in open water. How local variations in the inflow velocity affect these quantities will be discussed later.

5.1 Body force approach

As was discussed in Section 2.10 separating the modelling schemes of the propeller and the ship provides a practical advantage. A separated approach is preferred here to avoid excessive computational time and to simplify grid generation. If the flow around the propeller and the hull are considered using separate methods, a regime for linking the state of one to the state of the other must be decided.

A common and fast way to achieve such a regime is to consider the action of the propeller as a momentum source. The advantage of this is that no modifications to the RANS approach are needed other than the addition of an extra source term in the momentum equation. The role of the propeller model then becomes to calculate the strength and distribution of the extra source term throughout the RANS domain. The disadvantage is that it is problematic to separate the propeller induced velocities from the total wake if the coupling is not based directly on the velocity fields of the two models. Gao et al. (2012) stated an large over prediction of the propeller induced velocities when using a momentum theory based body force approach compared to modelling the propeller geometry directly in the RANS solution.

Several approaches to calculating the momentum source distribution and approaches to finding the wake exist. Two prominent types can be mentioned.

- Models which calculate the body force directly from the pressure on the blade surface by solving the velocity field around the propeller using e.g. a panel code.
- Models that reduce the complex geometry to a force distribution governing the flow through a zero thickness actuator disk.

The actuator disk usually infers an averaged or smeared distribution of thrust and torque since the instantaneous locations of the blades are not modelled. This allows for a very fast handling of the propeller modelling. In contrast, models solving the full velocity field for the specific geometry can achieve higher accuracy but at a higher computational cost.

Choi and Kinnas (2000) presented a momentum source distribution based on a panel based potential flow method. This was coupled with an Euler flow solver. By arguing that, even though viscosity has a role in the development of the wake, it does not do much for the interaction between the wake and the propeller induced velocities, Choi and Kinnas (2000) could separate the propeller induced velocities from the total wake. This was done by stating that the propeller induced velocities could be found directly from the perturbation potential in the potential flow solver.

For models not explicitly solving the velocity field, the undisturbed wake must be determined prior to invoking the propeller model. This presents further issues. If the propeller induced velocities are not computed by the model with sufficient accuracy, a cumulative error will be introduced in the coupling since an erroneous wake will be used in the next iteration. This will lead to errors in computing the next set of induced velocities etc.

If considering the case of the steady flow around a self propelled hull at constant forward speed, the RANS-body force model coupling is usually done in an iterative manner (Phillips et al., 2008; Molland et al., 2011, p 180; Tahara et al., 2006 Simonssen and Stern, 2005). First, a steady RANS solution is obtained. Second, the probed wake is input into the propeller model which calculates the distribution of thrust and torque in the fluid. The RANS solution is restarted with the additional momentum added. The process can be repeated until convergence of the flow field and the integral thrust and torque values between iterations is reached (when using a fixed RPM) . A further criteria can also be added to say that the RPM should be varied until the integral value of thrust matches the ships resistance. However, this approach is not practical in a case where the wake is unsteady. Achieving this type of iterative convergence, would involve multiple iterations through the pressure-velocity coupling algorithm in each time step and so would increase the computational effort.

The approach to modelling the momentum induced by the blades depends on the amount of information needed about the instantaneous effect of the blades on the surrounding fluid. This must be put in relation to the time scales of other phenomena around the propeller such as vortices separating from the stern area and how well the interaction of these with the propeller are to be modelled. The most prominent causes of changes in the propeller inflow due to waves are surge motions and wave orbital velocities. While heave and pitch motions also contribute they have a smaller impact on the effective wake (Ueno et al., 2013). Other sources of unsteadiness at the ship stern include unsteady flow separation.

In this case the frequency of the waves passing and thus the variations in resistance and surge are deemed most important. The relation between the passing period of wave crests T_e at different λ/L in relation to different rotational frequencies $1/Tr$ for the propeller are shown in Figure 5.1. The rotational frequency is given as the full scale

RPM found as $RPM_{full} = \alpha^{-0.5} RPM_{model}$ where α is taken as an example scale factor of 40 (Lpp of full scale ship = 120m when using the model described in Table 4.9.)

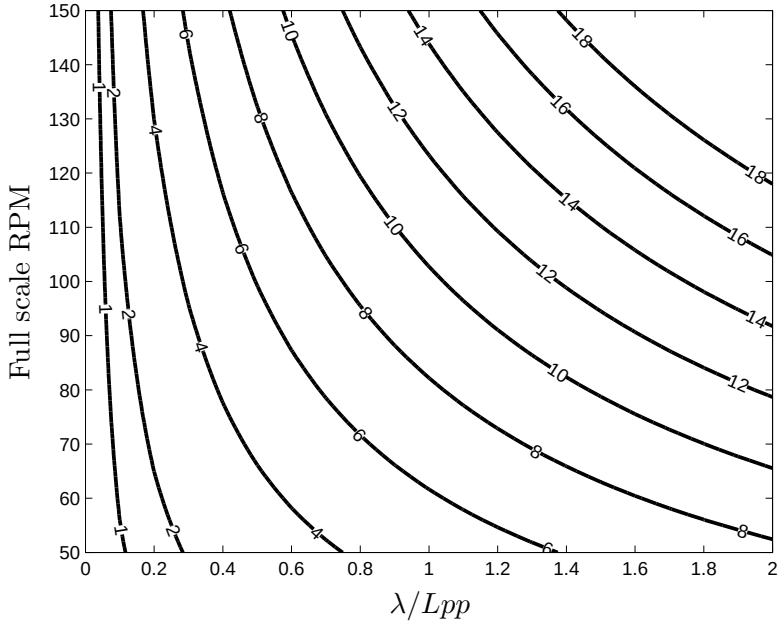

FIGURE 5.1: Contours of the ratio T_e/T_r.

As seen in Figure 5.1, there will be more than 4 rotations of the propeller for every wave encounter in most situations. For low values of λ/L, the wave encounter frequency is significant.

Using a smeared approach will still capture the periodic variations of thrust and torque due to the waves by probing the velocity in run time. However, rather than giving the instantaneous loading condition on the blades, this variation would represent an oscillation of average performance of the propeller. For the purposes of this study, the smeared approach is seen as suitable and an actuator disk type propeller model can be used to save computational time.

Because of the unsteady nature of the inflow, predicting propeller-hull interaction in this case requires a model that handles coupling between flow and propeller models automatically in runtime. A framework for coupling the flow solver with any momentum source based propeller model has been developed for this purpose.

5.2 Framework for self propulsion modelling

The framework has three main purposes

- To determine/control the propeller RPM.

- To handle information exchange between the flow solver, the propeller model and the dynamic mesh solver.
- To have a modular definition of the propeller model and control function.

Controlling the propeller RPM in real time allows for the self propulsion point to be found (Carrica et al., 2010) but also allows for possible performance improvements in waves as discussed in Section 1.6. Furthermore, to handle the information exchange as efficiently as possible is important to reduce the computational time used for other things than flow modelling.

The last purpose is added in the spirit of the open source community and to fulfil the set up objectives. The framework provides all the basic building blocks of a propeller model such as access to the relevant flow variables, global variables, functions for identifying cells in the propeller region and more. For a user to create a new model, all that is needed is the addition of the specific equations or schemes for calculating the thrust and torque distribution. The user then gives the new propeller model a name and it becomes a selectable option for propeller modelling within the framework. The framework supports an unlimited amount of selectable options for propeller modelling and so it is well suited for comparing the accuracy and efficiency of different types of models. As with the propeller model itself, the scheme for controlling the propeller RPM is also a selectable option with a simple template for creating new ones (see Appendix A.)

One of the basic building blocks is the definition of the region where the propeller operates. This is labelled the propeller disk and, if ship motions are present, it must be made to follow the rigid body motion of the hull.

5.2.1 Defining the propeller disk

The framework includes pre defined functions for calculating the extent, position and orientation of the propeller disk. The propeller disk is defined as a cylinder, with a height d_d, and a radius R centred around the propeller centroid $\mathbf{x_p}$. The unit normal to the disk $\mathbf{O}$ is parallel to the propeller axis (oriented from forward to stern.) Here R is set to the tip radius of the propeller blades and d_d should be chosen to suit the chosen theory (see Section 5.5.5.) Despite what is shown in Figure 5.2, this does not necessarily mean that the disk completely envelops the extent of the propeller to be modelled. The central plane of this disk (i.e. the circular cross section at $d_d/2$) is henceforth referred to as the propeller plane or the propeller centre plane. The propeller disk is used for all propeller models to determine which cells should have an active body force. The other primary purpose of the disk is to provide a reference frame for propeller calculations. For simpler propeller models, the strength of the momentum source term for cells within it is given directly by their location relative to the disk. For more complicated models,

calculations can be performed separately in the disk reference frame. This is considered as fixed and ship motions can thus be excluded from the equations governing the thrust and torque distribution. Ship motions are instead considered as further additions to the unsteady flow field through the disk and can be incorporated into the wake fraction.

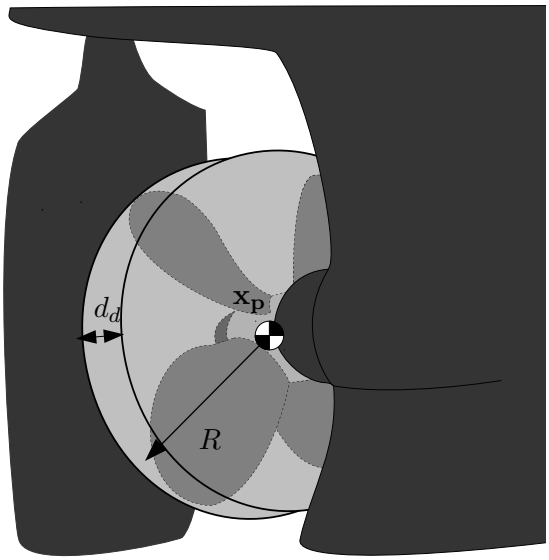

FIGURE 5.2: Definition of propeller disk (light grey.)

The position of the propeller centroid $\mathbf{x}_p$, the orientation of the propeller disk $\mathbf{O} = (O_1, O_2, O_3)$ for an arbitrary ship orientation (defined by the global ship rotation tensor $\mathbf{Q}$ and the offset $\mathbf{P}$) are shown in Figure 5.3. These are calculated using the original centre of gravity $\mathbf{CG}_0$ and the original orientation vector $\mathbf{O}_0$ as

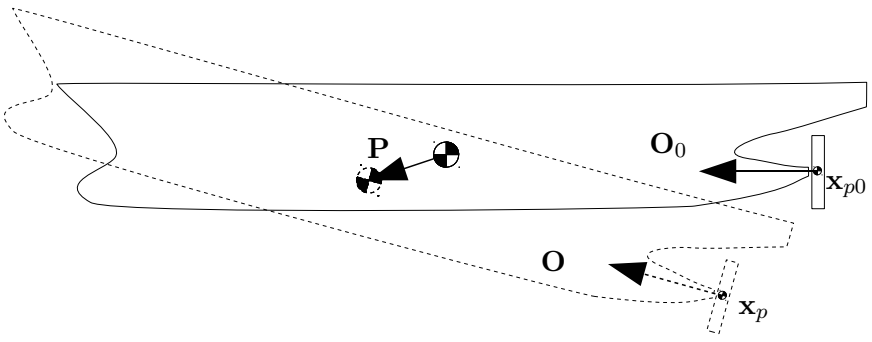

FIGURE 5.3: Movement of propeller disk due to arbitrary ship motions.

$$\mathbf{x_p} = \mathbf{CG}_0 + \mathbf{P} + \mathbf{Q} \cdot (\mathbf{x}_{p0} - \mathbf{CG}_0) \tag{5.5}$$

$$\mathbf{O} = \mathbf{Q} \cdot \mathbf{O}_0 \tag{5.6}$$

With these definitions, cells can be identified as active or passive based on their location relative to the propeller disk. Let $\mathbf{r}_I$ be the vector from the propeller centroid $\mathbf{x}_p$ to the centroid of cell I, the relative position of a cell I is then given by the projection of $\mathbf{x}_I$ onto the propeller plane as

$$\mathbf{R}_I = \begin{bmatrix} O_2^2 + O_3^2 & -O_1O_2 & -O_1O_3 \\ -O_1O_2 & O_1^2 + O_3^2 & -O_2O_3 \\ -O_1O_3 & O_2O_3 & O_1^2 + O_2^2 \end{bmatrix} \mathbf{r}_I \tag{5.7}$$

$$\mathbf{d}_I = \mathbf{O}\left(\mathbf{r}_I \cdot \mathbf{O}\right) \tag{5.8}$$

The vector $\mathbf{R}_I$ describes the radius from $\mathbf{x}_I$ to the propeller axis in the propeller plane and $\mathbf{d}_I$ is the distance from $\mathbf{x}_I$ to the propeller plane. Using this definition, active cells can be identified as fulfilling $r_H < |\mathbf{R}_I| < R$ and $|\mathbf{d}_I| < d_d/2$ where r_H is the hub radius. For some propeller models using simple radial distributions of thrust and torque, $|\mathbf{R}_I|$ will also directly determine the momentum source strength added in cell I.

For more advanced models, a routine for calculating the angular position of cell I is available in the framework. Let $\mathbf{r}_V$ be a unit vector that is orthogonal to $\mathbf{O}$ and that is vertical in the initial state. $\mathbf{r}_V$ then defines the vertical direction of the propeller and follows the movement of the hull in the same way as $\mathbf{O}$ (i.e $\mathbf{r}_V = \mathbf{Q} \cdot \mathbf{r}_{V0}$.) The angle θ_I of cell I relative to this vertical direction is then found as

$$\theta_I = \begin{cases} if\ \ (\mathbf{O} \times \mathbf{R}_I) \cdot \mathbf{r}_V >= 0 & : \quad cos^{-1}\left(\frac{\mathbf{R}_I}{|\mathbf{R}_I|} \cdot \mathbf{r}_V\right) \\ if\ \ (\mathbf{O} \times \mathbf{R}_I) \cdot \mathbf{r}_V < 0 & : \quad 2\pi - cos^{-1}\left(\frac{\mathbf{R}_I}{|\mathbf{R}_I|} \cdot \mathbf{r}_V\right) \end{cases} \tag{5.9}$$

The projection of $\mathbf{x}_I$ on the propeller plane in order to obtain $\mathbf{R}_I$,$\mathbf{d}_I$ and θ_I is shown in Figure 5.4.

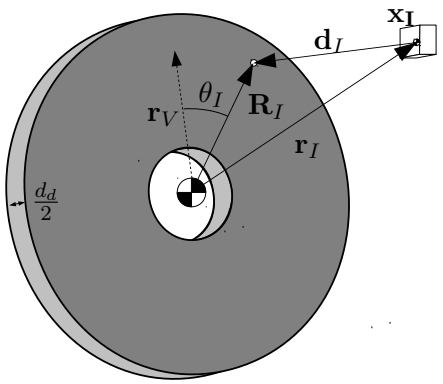

FIGURE 5.4: Definition of $\mathbf{R}_I$,$\mathbf{d}_I$ and θ_I by projection of $\mathbf{x}_I$ onto propeller plane (dark grey.)

With these definitions, the propeller advance coefficient J is given as

$$J = \frac{\left(\mathbf{U}_0 + \frac{\partial \mathbf{x_P}}{\partial t}\right) \cdot \mathbf{O}}{n\ 2R} \tag{5.10}$$

In Equation 5.10, care must be taken with the signs of $\mathbf{U}_0$ and $\frac{\partial \mathbf{x}_p}{\partial t}$ so that they, with the coordinate system used, have the same definition of positive speed.

5.2.2 Concentric mesh for propeller calculations

For more advanced models it is convenient to perform calculations on a separate mesh. The main motivation for this is that the structure of the RANS mesh within the propeller disk does not have to be adapted to fit the needs of the propeller model. Creating a suitable mesh to capture the flow around a complex hullform is a challenging task in itself without considering the requirements of a separate modelling scheme. Furthermore, more comprehensive and focused verification studies of the propeller model can be performed if the RANS mesh can be kept constant. The framework includes the possibility to define a concentric mesh with a given number of axial, radial and circumferential sectors on which calculations of the thrust and torque distribution can be performed.

For the separation to be possible, interpolation algorithms between the two meshes must be defined. Interpolation of u from the RANS mesh onto the concentric mesh to define the local wake fraction and interpolation of the resulting $\mathbf{F}_v$ back to the RANS mesh are the most likely candidates for interpolation in a standard model. However, the framework also supports interpolation of e.g. the turbulence kinetic energy k or any other flow variable onto the concentric mesh if a propeller model requires it.

Interpolation from the RANS mesh to the concentric mesh is handled using any of the stock interpolation functions for a finite volume mesh available in OpenFOAM. In addition to the coordinates of the point where information is sought (concentric mesh node), these also require the ID of the cell containing that point in order to create an interpolation stencil of neighbouring cells. This requirement comes from the arbitrary structure of the RANS mesh. For interpolation from the concentric mesh to the RANS mesh the calculated values of $\mathbf{R}_I$,$\mathbf{d}_I$ and θ_I are used. Because of the known structure of the concentric mesh it is then inherently known which 4 (2D mesh) or 8 (3D mesh) donor nodes would form the base for the interpolation stencil. A schematic of the interpolation between RANS and concentric meshes is shown in Figure 5.5.

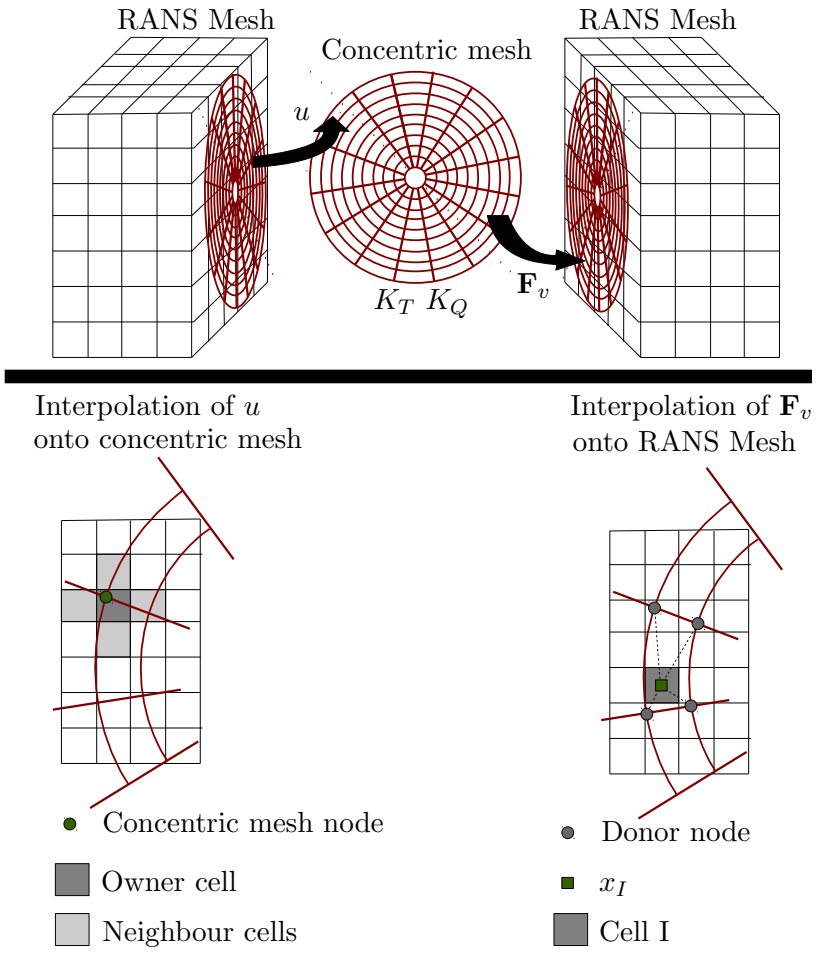

FIGURE 5.5: Mapping of u and $\mathbf{F}_v$ between RANS and concentric meshes.

Cell linking

The requirement of the cell ID to be known in interpolation from the RANS mesh onto a concentric mesh node provides a possible weakness in terms of computational effort for this approach. With a well designed mesh motion scheme, the cells inside the propeller disk are expected to remain relatively stationary since mesh motion close to the hull should be following, as closely as possible the rigid body motion. The propeller disk also follows the rigid body motion and so, in the moving propeller disk reference frame, the RANS mesh should be constant. However, to be able to truly handle interpolation between an arbitrary RANS mesh and a concentric mesh at an arbitrary location, the owner cell for each concentric mesh node must be updated in each time step. This is important to ensure the stability of the model. Since the RANS mesh is considered arbitrary, there is no relationship between cell ID and spatial location and thus the mesh must be searched until the cell containing each node is found. Using standard search algorithms for cell IDs in OpenFOAM would yield an unacceptable computational effort devoted to this task.

Because of this, the framework also includes a custom search algorithm. The basic idea of the search algorithm is to travel between cells based on shared faces. Given a cell I, if this does not contain the sought point, the search should move to one of its neighbours. Cell I has N faces, each of these faces has a centroid. The algorithm would focus the search towards the face which has its centroid closest to the search target. If this face is not a boundary face or if the algorithm has not crossed it previously, the search moves to the cell which shares this face with cell I. This gives a fast way of searching in arbitrary meshes since the algorithm usually ignores cells which are not directly on the trajectory from the start guess towards the target point. A flow chart for the search algorithm is shown in Figure 5.6.

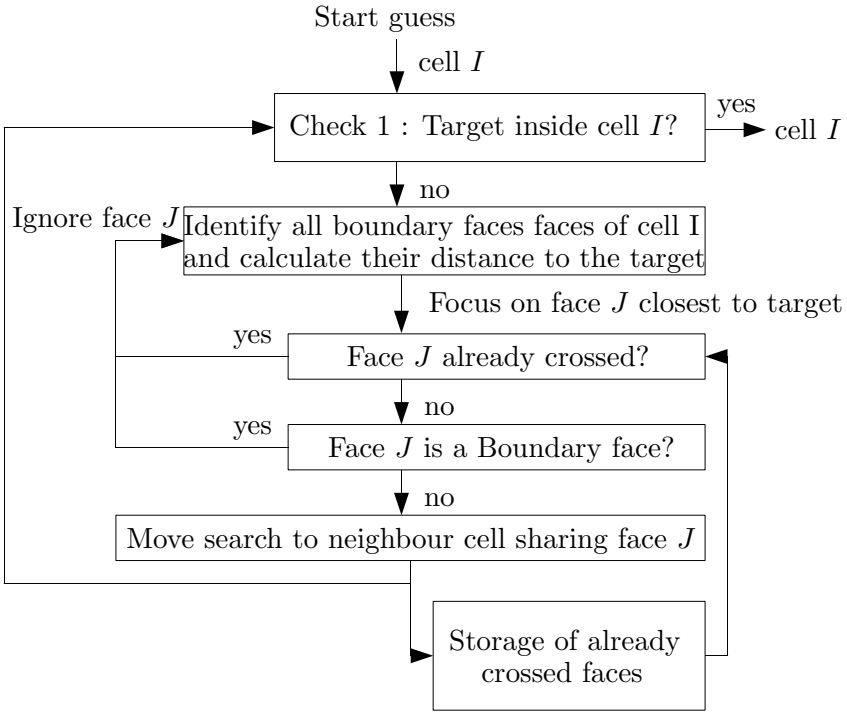

FIGURE 5.6: Search algorithm for cell IDs.

The cell ID associated with each concentric mesh node is saved between each time step to be used as start guesses in the next. If no nodes have changed owner cells, the first check will yield true and no searching is performed. If one or more nodes have changed owner, they are likely to be found in the neighbouring cells to where they were in the last time step and the algorithm will find them very fast. In the first time step, the cell ID from the previous concentric mesh node is used as a start guess except for the first node for which cell ID 0 is used as a start guess.

5.2.3 Overview of framework

A rough overview of the framework and the connectivity in terms of variable exchange between different parts is shown in Figure 5.7. As shown in Figure 5.7, the controller part of the framework also acts as a central hub of information. Apart from the fluid mesh, the velocity field and the body force distribution, all information is passed through the control block to be distributed where it is needed in the framework. This simplifies the process of accessing information since every part only has to have access to the control block, however it also has a benefit from a control point of view. Since the control block has direct contact with both the flow solver, the dynamic mesh solver and the propeller model, it can control the RPM based on any criteria.

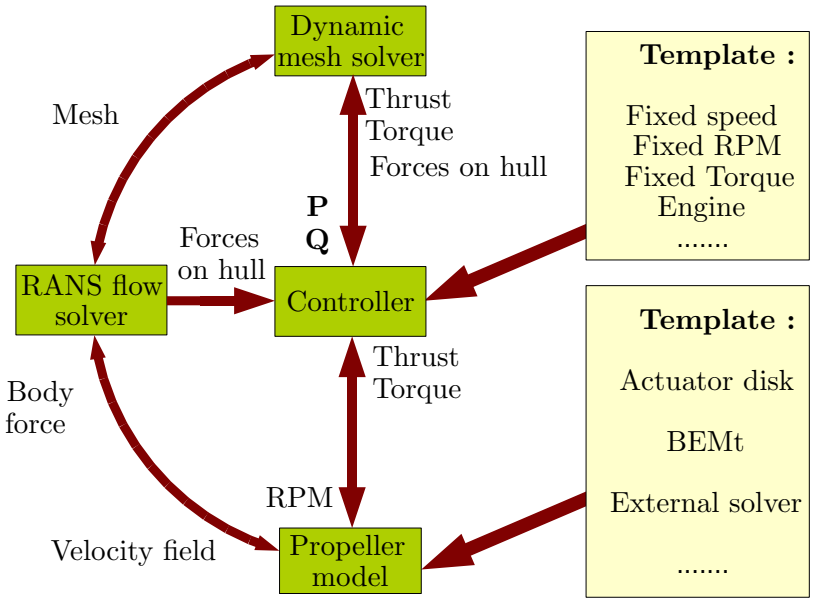

FIGURE 5.7: Self propulsion framework for OpenFOAM.

Both the control block and the propeller modelling block in Figure 5.7 are templates. As discussed before, this allows for great flexibility in how the framework can be applied. The template definition means that a great deal of functionality exists automatically whenever a new propeller control function or propeller model is created. Rough overviews of the functionality available in the two templates (grey blocks) and where user specified algorithms fit in (white blocks) are given in Figures 5.8 and 5.9 for a propeller controller and a propeller model respectively.

To give an idea how the functionality of the templates would manifest itself in actual code, an example propeller controller attempting to adjust the RPM to keep a fixed torque is shown in Appendix A, Figure A.1. Furthermore, an example propeller model using the concentric mesh approach is given in Figure A.2. As with all OpenFOAM software, the framework is controlled using C++ dictionaries in which the user specifies

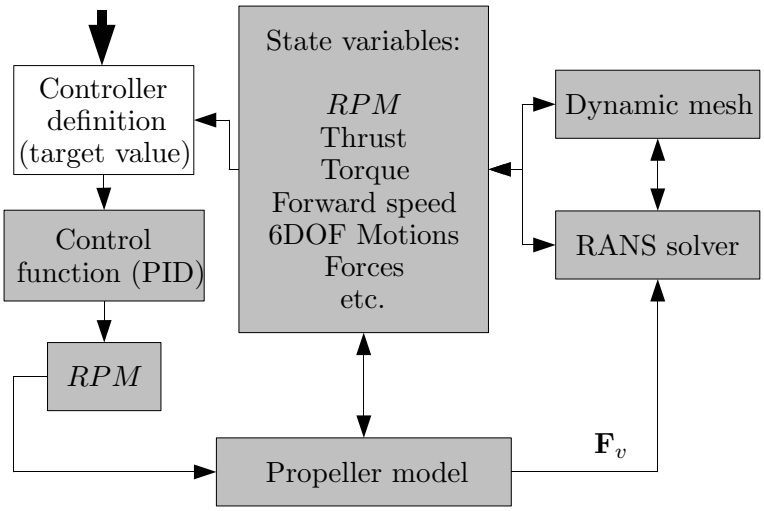

FIGURE 5.8: Template for a propeller controller where grey boxes indicate processes handled by the framework and white boxes indicate user defined processes.

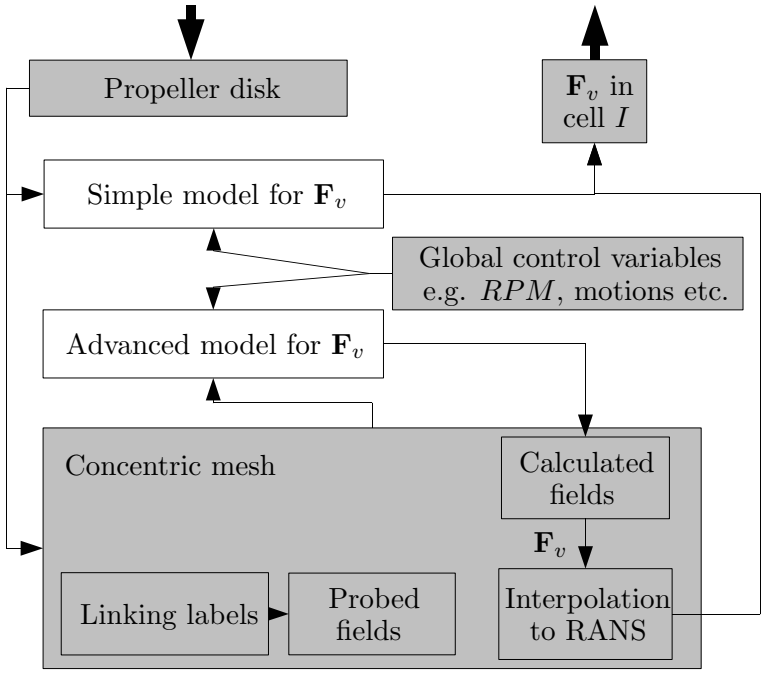

FIGURE 5.9: Template for a propeller model where grey boxes indicate processes handled by the framework and white boxes indicate user defined processes.

the parameters to be used. In this case two dictionaries are used, one to give parameters relating to the propeller (propellerDict) and one to give parameters relating to the hull (hullDict), examples of both are shown in Figures A.3 and A.4 respectively.

The framework provides a large step towards the fulfilment of the aims and objectives of this thesis. It allows for easy modification of a wide range of parameters and for easy implementation of new propeller models and control schemes. It therefore facilitates a wider range of present and future studies on self propulsion in waves.

The details and code structure of the framework is presented by Windén et al. (2014*b*).It was tested using both a Wigley hull with simple radial distributions of thrust and torque by Windén, Turnock and Hudson (2013*a*); Windén et al. (2014*a*) and for the KCS using Blade Element Momentum theory (BEMt) to model the propeller by Windén, Badoe, Turnock, Phillips and Hudson (2013) and Windén et al. (2014*d*). The implementation of the BEMt is discussed below.

5.3 Blade Element Momentum theory

The selection of propeller model in the framework is free for the user to decide based on the specific requirements of the problem at hand. The BEMt is chosen here for its ability to model propeller-hull interaction for specific propeller geometries.

2D blade element theory provides a fast way to evaluate the forces and moments on a propeller blade. However, it provides no coupling between the forces and moments on the blade and the induced velocities in the fluid. Therefore, it is unsuitable where interaction between the propeller and its environment is to be studied. On the other hand axial momentum theory relates the thrust and torque to the momentum induced in the fluid by the propeller over the propeller plane. The weakness of axial momentum theory comes from the fact that the distribution of thrust and torque cannot be directly related to the flow around the propeller geometry. Typically, empirical radial distributions of thrust and torque are used. By combining these two theories as first suggested by Burrill (1944), a calculation method suitable for predicting the mean flow due to the propeller can be created. Blade Element Momentum theory is a combination of 2D blade element theory and axial momentum theory that is suitable for calculations on marine propellers close to the design working condition (Benini, 2004) and allows for studies of propeller/hull interaction for more specific propeller geometries (Molland et al., 2011, p 338-339).

The implementation of the BEMt used here follows the procedure by Molland et al. (2011, p 343-361) but is explained here for better readability. This implementation of the BEMt was successfully coupled with a RANS solver using an iterative approach to study manoeuvring coefficients of a self propelled ship by Phillips et al. (2009). To be able to use it for unsteady performance calculations, the theory is implemented in OpenFOAM and the self propulsion framework. The radial distance from the centreline is normalised with the propeller radius R so that $r = xR$ where r is the local radius and x is the non dimensional radius.

5.3.1 Momentum theory

The flow in a stream tube passing through the propeller disk is considered as shown in Figure 5.10. The main assumptions are that

- the propeller works in an ideal fluid so no frictional losses or mixing will occur in the stream tube.
- all the power generated by the engine can be transferred to the fluid via a discrete pressure jump at the propeller plane.

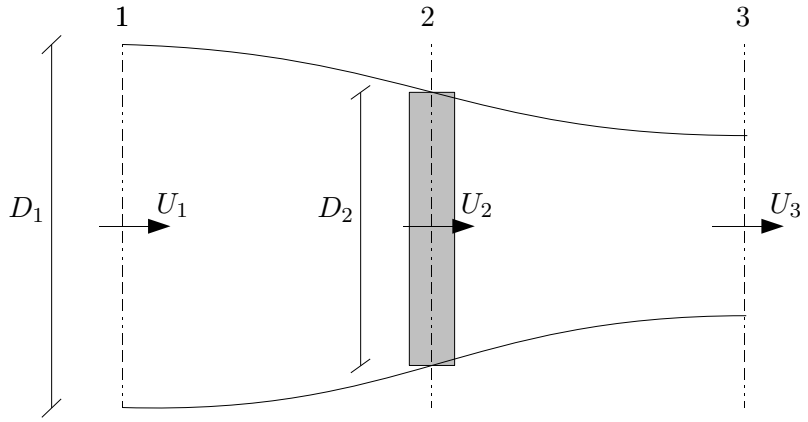

FIGURE 5.10: Momentum generated by pressure jump over the propeller plane (plane 2.)

If the flow through an annulus of radius r and span dr in the stream tube is considered, the mass flow rate through the corresponding section of the propeller plane is

$$\dot{m} = 2\pi r dr \rho U_2 \tag{5.11}$$

and the axial rate of momentum change in the annulus is $\dot{m}\,(U_3 - U_1)$. If the pressure jump at the propeller plane is considered discrete, this can be equated to a thrust force acting only on the annulus part of the propeller plane so that

$$dT = \dot{m}\,(U_3 - U_1) \tag{5.12}$$

The velocities U_2 and U_3 are related to the velocity far upstream with the axial inflow factors

$$U_2 = U_1(1 + a_{2\infty}) \tag{5.13}$$

$$U_3 = U_1(1 + a_{3\infty}) \tag{5.14}$$

In open water flow, it can be shown that the velocity at the propeller plane is the average of the values far upstream and downstream (Carlton, 2007) so that

$$a_{3\infty} = 2a_{2\infty} \tag{5.15}$$

Combining Eqns. 5.11, 5.12, 5.14 and 5.15 gives the thrust acting on the annulus part of the propeller plane as

$$dT = 4\pi r \rho U_1^2 a_{2\infty}(1 + a_{2\infty})dr \tag{5.16}$$

This expression is only valid if the interference between blades is neglected, i.e. for an infinite number of blades. With a finite number of blades, each blade will be operating in the wake behind other blades. This means that the effective inflow factors will change. The thrust and torque expressions can be corrected for this by using the Goldstein correction. This was introduced by Goldstein (1929) to relate the local flow around a finite set of blades to the mean flow for an infinite number of blades. Here a curve fit to the experimentally established correction factor K, presented by Molland et al. (2011, p 346) is used where

$$K = \frac{2}{\pi}\cos^{-1}\left(\frac{\cosh\left[x\left(\frac{Z}{2x\tan\phi} - 0.5\right)\right]}{\cosh\left[\frac{Z}{2x\tan\phi} - 0.5\right]}\right) \tag{5.17}$$

where ϕ is the hydrodynamic pitch (see Fig. 5.11) and Z is the number of blades. Finally, using the non dimensional radial position, an expression for the thrust coefficient contribution from each annulus dK_T is defined as

$$dK_T = \pi x J^2 K a(1 + a)dx \tag{5.18}$$

where a is now the inflow factor at the blade at plane 2. A similar reasoning as is applied to the thrust can be applied to derive an expression for the torque

$$dK_Q = \frac{1}{2}\pi^2 x^3 J K a'(1 + a)dx \tag{5.19}$$

where a' is the circumferential inflow factor at the blade at plane 2. This relates to the Goldstein correction in the same manner as a and $a_{2\infty}$ between Eqns. 5.16 and 5.18. Here, $a'_{2\infty}$ is the circumferential inflow factor relating the angular velocity (in plane) at plane 1 to the one at plane 2 as

$$\omega_2 = 2a'_\infty \omega_1 \tag{5.20}$$

Finally, the local efficiency is obtained as

$$\eta = \frac{dTU_1}{\Omega dQ} = \left(\frac{U_1}{r\Omega}\right)^2 \frac{a}{a'} \tag{5.21}$$

5.3.2 Blade element theory

Blade element theory is based on the assumption that the lift and drag of the propeller blades can be obtained by means of 2D foil sections. Here, a number (n_R) of 2D sections are said to make up the geometry of the blade with the lift and drag of each section contributing to the total force. The lift and drag for all blades are summed up and the total force in the axial direction (thrust) and the moment around the propeller axis (torque) can be determined. The lift contribution dL and drag contribution dD for a section with span dr are determined from the angle of attack and the inflow speed as

$$dL = \frac{1}{2}\rho Z c(r) U_{foil}^2 C_L(\alpha) dr \tag{5.22}$$

$$dD = \frac{1}{2}\rho Z c(r) U_{foil}^2 C_D(\alpha) dr \tag{5.23}$$

where $c(r)$ is the local chord of the blade and Z is the number of blades. It now remains to determine the angle of attack α and the local inflow velocity U_{foil}. The velocities contributing to the inflow conditions for each foil are given by the 2D representation of the rotating propeller as shown in Figure 5.11. As shown here, the orientation of the foil is determined by the blade design through the local section pitch angle. How the inflow angle relates to this orientation depends on the rate of rotation Ω, the inflow speed U_1 (wake) and the propeller induced velocities.

From this geometry, the angle of attack is defined as the difference between the local section pitch and the induced flow angle so that

$$\tan(\phi + \alpha) = \frac{P}{2\pi r} = \frac{P/D}{\pi x} \tag{5.24}$$

The lift and drag are converted into thrust and torque as

$$dT = dL\cos\phi - dD\sin\phi = dL\cos\phi\,(1 - \tan\phi\tan\gamma) \tag{5.25}$$

$$dQ = r\left(dL\sin\phi + dD\cos\phi\right) = rdL\cos\phi\left(\tan\phi + \tan\gamma\right) \tag{5.26}$$

where

$$\tan\gamma = \frac{dD}{dL} = \frac{C_D(\alpha)}{C_L(\alpha)} \tag{5.27}$$

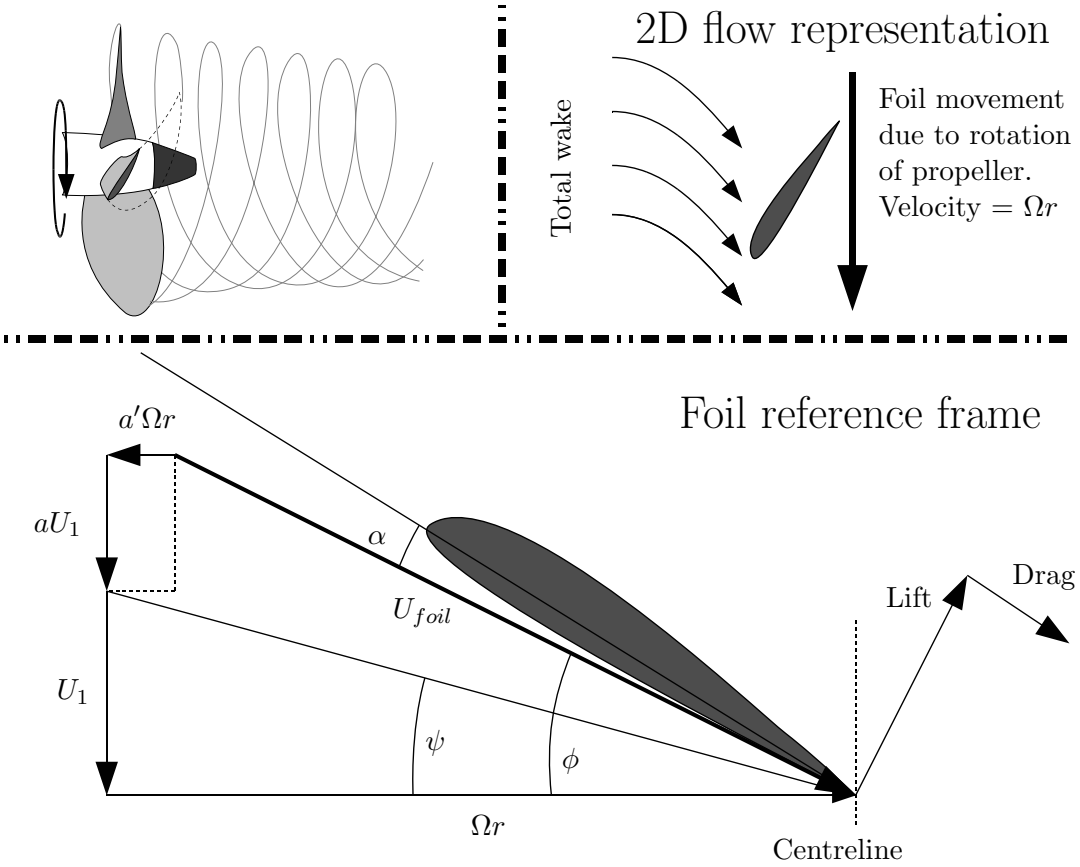

FIGURE 5.11: Representation of propeller blades as 2D airfoil sections.

Finally the local efficiency of the section is given as

$$\eta = \frac{U_1 dT}{\Omega dQ} = \frac{U_1}{\Omega r}\frac{1}{\tan\left(\phi+\gamma\right)} \tag{5.28}$$

Due to the geometry it is found that

$$\tan\psi = \frac{U_1}{\Omega r} \tag{5.29}$$

$$\tan\phi = \frac{U_1(1+a)}{\Omega r(1-a')} \tag{5.30}$$

also

$$\tan\phi = \tan\psi \frac{1+a}{1-a'} \tag{5.31}$$

Eqn. 5.28 then reduces to

$$\eta = \frac{\tan\psi}{\tan(\phi+\gamma)} \tag{5.32}$$

5.3.3 Coupling of Blade element and momentum theories

By combining the two independent equations for local efficiency, blade element theory is coupled to momentum theory. By combining Eqns. 5.21 and 5.29 and recalling Eqn. 5.32

$$\begin{aligned} \textit{Momentum theory} \quad &: \quad \eta = \tan^2\psi \frac{a}{a'} \\ \textit{Blade element theory} \quad &: \quad \eta = \frac{\tan\psi}{\tan(\phi+\gamma)} \end{aligned} \tag{5.33}$$

a coupling is achieved between the flow in the stream tube and the local loading of the propeller blades. However, a method is still required to find a suitable combination of a and a' to fulfil this. This is done by utilising the ideal efficiency in blade element theory η_i which is found if $C_D = 0 \rightarrow \gamma = 0$ hence

$$\eta_i = \frac{\tan\psi}{\tan\phi} \tag{5.34}$$

Combining Eqns. 5.31 and 5.34

$$\eta_i = \frac{1-a'}{1+a} \tag{5.35}$$

Combining Eqns. 5.33 and 5.35 gives

$$a' = \frac{a\tan^2\psi}{\eta} = 1 - \eta_i(1+a) \tag{5.36}$$

from which it follows that

$$a = \frac{1-\eta_i}{\eta_i + \frac{\tan^2\psi}{\eta}} \tag{5.37}$$

The BEMt equations are solved here in an iterative manner. The process is illustrated by Molland et al. (2011, p 351). The general procedure to finding convergence in terms of η is to obtain a from a start guess of η. In the first iteration the start guess is that $\eta = \eta_i$. This can then be used to obtain dK_T/dx from Eqn. 5.18, followed by C_L from combining Eqns. 5.22 and 5.25 and by recalling the conversion between dT and dK_T. C_D is then obtained from a curve fit to an experimentally measured $C_D(\alpha)$ curve which yields γ and the actual efficiency which is recycled as a new start guess. The process is repeated until the start guess matches the final η to within a set tolerance. The $C_D(\alpha)$ curve was interpolated to data from Burrill (1944) and Hill (1949) by Tang (1985).

To find the angle of attack, a start guess is compared with one obtained from the calculated C_L after convergence of the efficiency loop. The angle of attack (and thus the start guess η_i for the inner loop on η) is then recycled in an outer convergence loop on α until the start guess matches the final value. The process also includes a camber correction to account for the fact that, despite what is shown in Figure 5.11, the flow will curve around the foil section reducing the effective angle of attack as well as the lift. Here, the angle of attack is corrected at the end of the efficiency loop to account for this using a curve fit to data obtained from Eckhardt and Morgan (1955).

The process does not use directly measured values of C_L. Instead it assumes a constant slope of the $C_L(\alpha)$ curve determined by empirical relations for common foils. This together with the thrust from the previous iteration gives an estimate of C_L. This means that the model will not be able to capture the point where the foil stalls i.e. when C_L rapidly drops due to increased flow separation. The described method will continue to yield increased thrust for decreasing J. Care must therefore be taken that it is not applied outside of a reasonable loading condition. If this is necessary, the method can be easily improved by including a table lookup or curve fit to experimental $C_L(\alpha)$ curves.

As an input to the BEMt, the parameters in Table 5.1 are used. In the case where the number of radial sectors does not match the given number of pitch and chord values, cubic interpolation from the values in Table 5.1 is used to obtain these. The framework also supports curve fitting from any other reference distributions.

A correction to this theory to account for the effects of the tangential wake is given by Molland et al. (2011, p 359-361) but is not used in this analysis. To capture the effects of a non uniform wake, the solution can be divided into circumferential sectors, each with their own radial distribution of J. The process described above is then conducted for each sector. The process to arrive at a converged BEMt solution is shown in Figure 5.12. Here θ is the angle of each sector.

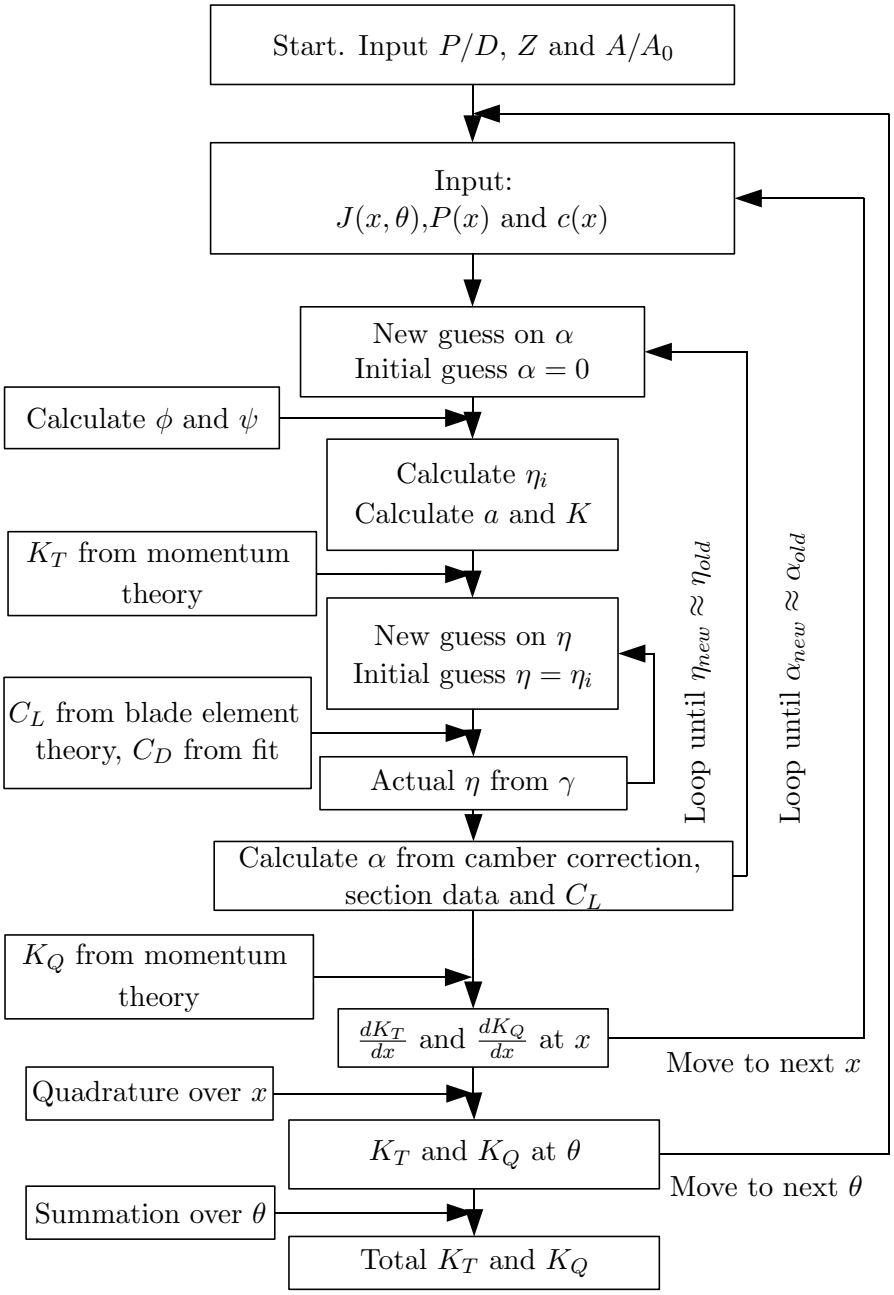

FIGURE 5.12: Steps of the BEMt algorithm.

5.3.4 Validation of BEMt code for the KCS propeller

The BEMt code is first applied separately (without RANS coupling) to verify that it can predict the open water performance of the KCS propeller with sufficient accuracy. The particulars of the KCS propeller are given in Table 5.1. Here the pitch and chord distributions are given relative to the value at $0.7R$.

The calculated values of K_T K_Q and η are compared with experimental data by SVA (2008). The comparison is made for a range of $0.3 < J < 0.9$ using ten radial sectors in

TABLE 5.1: Particulars of the KCS propeller.

P/D	1				
A/A_0	0.7				
Z	5				
r/R	0.2	0.3	0.4	0.5	0.6
c	0.7752	0.8778	0.9562	1.0038	1.0202
P	1.0082	1.0439	1.0483	1.0387	1.0216
r/R	0.7	0.8	0.9	0.95	1
c	1.0000	0.9189	0.7379	0.5553	0.0444
P	1.0000	0.9755	0.9491	0.9353	0.9213

the BEMt. The results are shown in Figure 5.13.

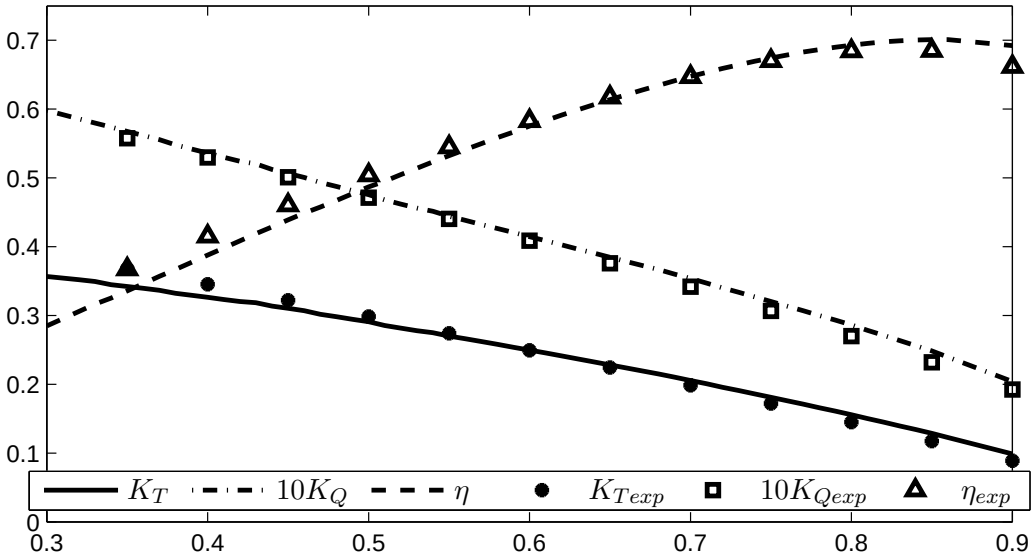

FIGURE 5.13: Open water data for the KCS propeller calculated using the BEMt and compared with experimental data.

Overall, the open water curves are well predicted. A slight variation in the incline of the thrust and torque curve compared to the experiments can be seen where the values at higher advance ratios are slightly over predicted and values at lower advance ratios are slightly under predicted. The best agreement is found where $0.6 < J < 0.8$ which is close to the design condition of the propeller. This is consistent with previous studies concluding that the BEMt approach works best close to the design condition and that its accuracy is decreased the further away form the design condition it is applied.

5.4 RANS-BEMt coupling

The BEMt is coupled with the RANS solver using a two way coupling. Firstly, the velocity in the RANS solution is used to provide a wake field which affects the thrust and

torque distribution in the propeller code. Secondly, the thrust and torque distribution is mapped back onto the RANS domain to represent velocity and pressure variations due to the presence of the propeller.

5.4.1 Correction for propeller induced velocities

To represent the effects of variations in the wake on the propeller performance, U_1 needs to be found for every sector to estimate the local wake fraction. If a correction for the tangential wake is implemented, ω_1 must also be known. This presents a problem for the coupling since U_1 and ω_1 are defined as the velocities far upstream. For a case when the propeller is working in open water, these can be probed directly from the RANS solution. However, with a hull present, an alternative strategy to estimate them is needed. Given the available places to probe the velocity in the RANS solution, the propeller disk centre plane (plane 2 in Figure 5.10) is the most attractive for several reasons.

- It will always be entirely inside the fluid domain (i.e it will never intersect the hull or the rudder.)
- The coupling will be less sensitive to diffusion due to poor mesh design up- or downstream of the propeller.
- Equations in momentum theory can be used to relate the velocity here to velocities upstream.

The first statement also applies to any plane offset from the centre plane by less than $d_d/2$.

Probing at plane 2 would yield the velocity U_2 and the angular velocity ω_2. According to momentum theory this relates to the sought velocities U_1 and ω_1 as shown in Eqns. 5.13 and 5.20. Here the term $a_\infty U_1$ represents the increase in axial velocity in the stream tube between planes 1 and 2 due to the propeller action for an infinite number of blades. Here, another problem with coupling the BEMt to the RANS solver arises. The axial and circumferential inflow factors are corrected for a finite number of blades using the Goldstein correction factor K. The lift and drag, and hence the thrust and torque distributions are therefore corrected for interference between the blades. However, since the local blade locations are not resolved, thrust and torque distributions are mapped onto the RANS mesh as the swept mean over one rotation as explained in Section 5.4.2. This means that while the axial and circumferential inflow factors a a' as seen by the blades are known from the blade element solution, the propeller induced velocity in the RANS solution will be closer to a_∞. The Goldstein correction can be used to relate the mean flow for an infinite number of blades to the flow with a finite number of blades. However, it is not designed to determine the local mean flow from local values of a and

a' in a converged blade element solution which has been mapped as a smeared force distribution. It should also be noted that the Goldstein correction is based on a steady inflow. How the interference between blades is affected by an unsteady inflow is currently unknown (Abels, 2013).

Despite these limitations, reasonable approximations of a_∞ a'_∞ are given by reverse applying the Goldstein correction. By equating the thrust and torque distributions with and without the correction

$$\frac{dT}{dr} = 4\pi r\rho U_1^2 a_\infty(1+a_\infty) = 4\pi r\rho U_1^2 Ka(1+a) \tag{5.38}$$

$$\frac{dQ}{dr} = 4\pi r^3\rho\Omega U_1 a'_\infty(1+a_\infty) = 4\pi r^3\rho\Omega U_1 Ka'(1+a) \tag{5.39}$$

a_∞ a'_∞ can be obtained as

$$a_\infty = \sqrt{\frac{1}{4} + Ka\,(1+a)} - \frac{1}{2} \tag{5.40}$$

$$a'_\infty = \frac{Ka'(1+a)}{1+a_\infty} \tag{5.41}$$

The inflow conditions far upstream can thus be estimated as

$$U_1 = \frac{U_2}{1+a_\infty} \tag{5.42}$$

$$\omega_1 = \frac{\omega_2}{2a'_\infty} \tag{5.43}$$

5.4.2 RANS-BEMt coupling procedure

The BEMt equations are solved on a concentric mesh with n_R radial sectors, n_C circumferential sectors and n_A axial sectors. In these calculations $n_A = 1$ in all cases. U_2 and ω_2 from the RANS solution are obtained on the concentric mesh using the mapping procedure described in Section 5.2.2. This yields distributions of dK_T/dx and dK_Q/dx from the BEMt solution. The total thrust and torque are obtained by integrating these distributions by quadrature.

These distributions (one value per radial and circumferential sector) represent the mean thrust and torque exerted on that section by the sweeping blades. Since the blade location is not locally resolved, these values should be divided by the circumference to represent the mean value over one rotation. dK_T/dx and dK_Q/dx should therefore be

divided by $2\pi|\mathbf{R}_I|$ to obtain the local averaged axial and tangential force distributions. These are defined in each cell I of the RANS mesh as

$$f_{aI} = \frac{\frac{dK_T}{dx}\Big|_{map} \rho n^2 D^4 dx}{2\pi|\mathbf{R}_I|} \tag{5.44}$$

$$f_{\theta I} = \frac{\frac{dK_Q}{dx}\Big|_{map} \rho n^2 D^5 dx}{2\pi|\mathbf{R}_I|^2} \tag{5.45}$$

where $|_{map}$ indicates that the value has been mapped from the concentric mesh onto cell I using the procedure described in Section 5.2.2.

The volume force term in cell I is obtained by multiplying these with the disk orientation $\mathbf{O}$ and the local tangential direction $\mathbf{O}_\theta$. Furthermore, Eqns. 5.44 and 5.45 are normalised so that the sum of the body force in all cells, multiplied by their volume V_I equal the thrust and torque calculated by the BEMt. This requires that

$$\sum \mathbf{O} \cdot \mathbf{F}_{vI} V_I = T \tag{5.46}$$

$$\sum \mathbf{O}_\theta \cdot \mathbf{F}_{vI} V_I |\mathbf{R}_I| = Q \tag{5.47}$$

To satisfy Eqns. 5.46 and 5.47, the volume force in cell I of the RANS mesh inside the propeller disk is defined as

$$\mathbf{F}_{vI} = \mathbf{O} f_{aI} \frac{T}{\sum f_{aI} V_I} + \mathbf{O}_\theta f_{\theta I} \frac{Q}{\sum f_{\theta I} |\mathbf{R}_I| V_I} \tag{5.48}$$

where the local tangential direction is given by

$$\mathbf{O}_\theta = \pm \frac{\mathbf{O} \times \mathbf{R}_I}{|\mathbf{O} \times \mathbf{R}_I|} \tag{5.49}$$

In Eqn. 5.49, the sign can be changed to yield the tangential force for a clockwise or counter-clockwise rotating propeller. Which sign corresponds to which direction of rotation depends on the coordinate system. For the setup of the numerical towing tank used here, a positive sign yields a counter-clockwise rotating propeller (as seen from astern.)

5.5 Verification of coupling algorithm

To verify that the induced velocities can be predicted with sufficient accuracy using the described procedure, it is applied to a propeller working in open water. A uniform inflow is provided far upstream in the RANS solution. No deduction of propeller induced velocities is conducted and U_1 in the BEMt code is fixed to the far upstream value U_∞. The velocity at the propeller plane in the RANS solution is recorded as well as a_∞ and a'_∞ in the BEMt solution. If the coupling is ideal, the recorded axial velocity will equal $U_1(1+a_\infty)$ and the tangential velocity will equal $2\Omega a'_\infty$. If that is the case Eqns 5.42 and 5.43 are valid for estimating the undisturbed wake. However, a number of discrepancies between the assumptions of the BEMt theory and the realisation of the flow using the prescribed RANS solver means that there will be a mismatch between the recorded and expected velocities. Some of these can be avoided by carefully designing the setup. However, as will be shown below, it is not possible to achieve an ideal coupling with the methods used here unless additional corrections are introduced.

Some of the main assumptions in the BEMt theory that the flow in the RANS solution fails to satisfy are listed below

- There are no viscous losses and there is no mixing between the flow in the separate annuli in momentum theory (this stems from the ideal fluid assumption.)
- The pressure jump at the propeller plane is discrete and the thrust and torque is applied on a zero thickness disk.
- The Goldstein correction factor assumes constant hydrodynamic pitch (locally) and zero hub radius. Any distortion of the slipstream due to the presence of the hub or from other sources will reduce the validity of the correction.
- The present theory only utilises a single Goldstein correction factor to account for the hydrodynamic pitch at both plane 2 and 3. In reality, the pitch will increase downstream due to contraction of the slipstream.
- The change of angular velocity from Ω to $\Omega + \omega_1$ happens very rapidly across the thin disk.
- The camber correction is based on open water loading so it is not clear how well it works away from this condition (i.e in a non converged RANS solution or with an unsteady inflow.)

The domain used for the RANS simulations is shown in Figure 5.14. No hull is present so the propeller is working in open water. A radius of $R = 0.5m$ and a hub radius of $r_H = 0.1m$ are used and the propeller plane is set at $60R$ downstream of the inlet. The hub is represented by a cylindrical boundary extending all the way between inlet and

outlet, the impact of this geometry will be discussed later. Slip conditions are placed on the velocity at the outer radial boundary as well as the hub. The simulation is run for at least two flowthroughs of the domain.

The mesh is created in 6 blocks. In the flow direction, one set of blocks towards the inlet, one set of blocks within $\pm 0.3R$ of the propeller plane and one set of blocks towards the outlet are used. Each set contains a block below $r = R$ and one block towards the outer radial boundary. The cell spacing within each of these blocks is defined in Table 5.2.

TABLE 5.2: Description of mesh for coupling verification study.

	Direction	Cells inside propeller radius			Cells outside propeller radius		
		Towards inlet	Within $\pm 0.3R$	Towards outlet	Towards inlet	Within $\pm 0.3R$	Towards outlet
number	axial	100	20	100	100	20	100
	tangential	120	120	120	120	120	120
	radial	25	25	25	30	30	30
gradient	axial	1/10	1	1/10	1/10	1	1/10
	tangential	1	1	1	1	1	1
	radial	1	1	1	1/20	1/20	1/20

120 cells around the circumference are used. 20 uniformly spaced cells in the flow direction are used within $\pm 0.3R$, after this another 200 cells are added with a gradient of 1/10 towards the outlet and inlets.

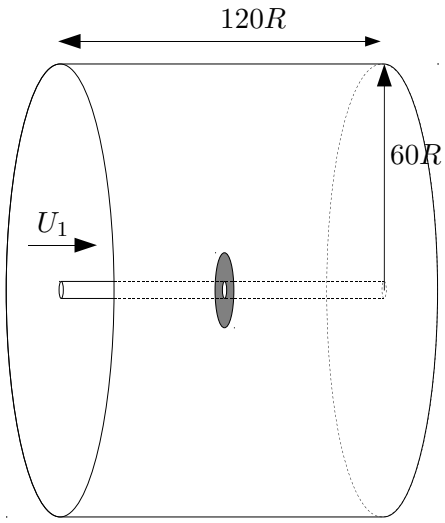

FIGURE 5.14: Domain for coupling verification study.

Figure 5.15(a) shows the agreement between U_2 and $U_\infty(1 + a_\infty)$ and Figure 5.15(b) between ω_2 and $\Omega a'_\infty$ for the basic setup with no corrections and with the mesh defined in Table 5.2. For reference, the non-corrected (through Eqns. 5.41 and 5.41) inflow factors a and a' are also shown. It is clear that the probed axial velocity profile is shifted towards the hub compared to the one expected from momentum theory but that

the angular velocity matches well with the expected value. A distorted profile could be caused by a discrepancy in the amount of slipstream contraction due to the pressure jump not being discrete. The slipstream contraction at the propeller plane in momentum theory can be calculated according to Carlton (2007, p 170) as

$$\frac{R_1}{R} = \sqrt{\frac{1}{2}\left(1 + \sqrt{1 + 4\frac{T}{\rho\pi R U_1^2}}\right)} \tag{5.50}$$

where R_1 is the radius of the undisturbed stream tube far upstream. For the verification case this yields a slipstream contraction of 11.5 %, this can be compared to a measured contraction in the RANS solution of 11.1 % indicating that the shape of the stream tube is well captured in the coupling.

Figure 5.16 shows that the distribution of axial volume force $\mathbf{F}_v \cdot \mathbf{O}$ matches well with the expected distribution of thrust given by K_T/r indicating that the interpolation between the BEMt and RANS meshes is able to represent these distributions with good precision. However, there is a discrepancy between the volume force distribution and the resulting velocity field. This is partly due to the presence of the tangential body force. As mentioned, in momentum theory the angular and axial momentum are said to be induced over a zero thickness disk, in the RANS solution the development of axial and angular momentum is governed by the momentum and continuity equations. This means that they will relate to each other differently in the RANS solution and in momentum theory. As shown in Figures 5.15 and 5.16, if no tangential body force is applied ($Q = 0$), the axial velocity distribution matches the expected values better for low values of r although a discrepancy remains away from the hub. In Figure 5.16 C represents a constant multiplicator to be able to compare the shape of the curves.

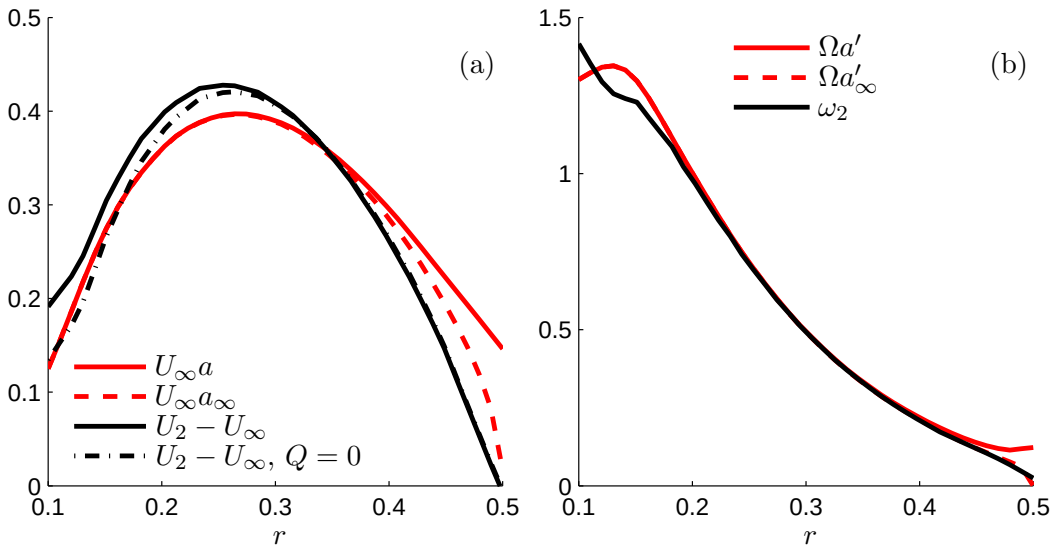

FIGURE 5.15: Comparison of the predicted and probed propeller induced velocities.

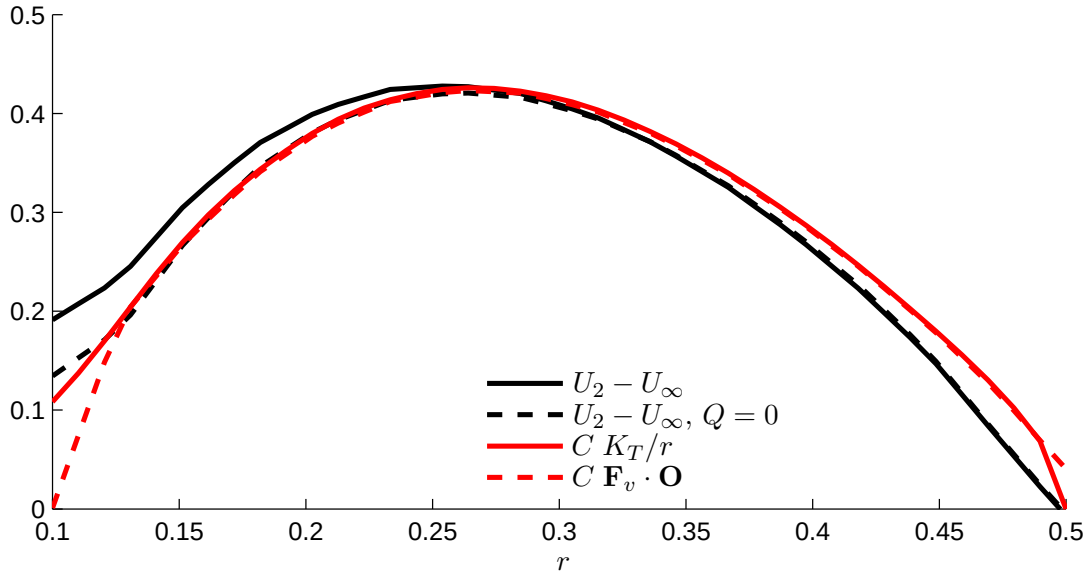

FIGURE 5.16: Comparison of the variation of various quantities along the propeller radius.

Finally, Figure 5.17 shows how these discrepancies influence the prediction of the wake using Eqns. 5.42 and 5.43. Both the axial and angular wakes are correctly predicted at $r = 0.35$ which corresponds to $r/R = 0.7$. Away from this radius, the axial momentum is over-predicted towards the hub and under-predicted towards the tip. The angular momentum is under-predicted near the hub as well as near the tip. It should be noted that values closest to the hub and tip have been excluded in Figure 5.17 since the absolute values are low and thus the relative error is subject to a high level of noise.

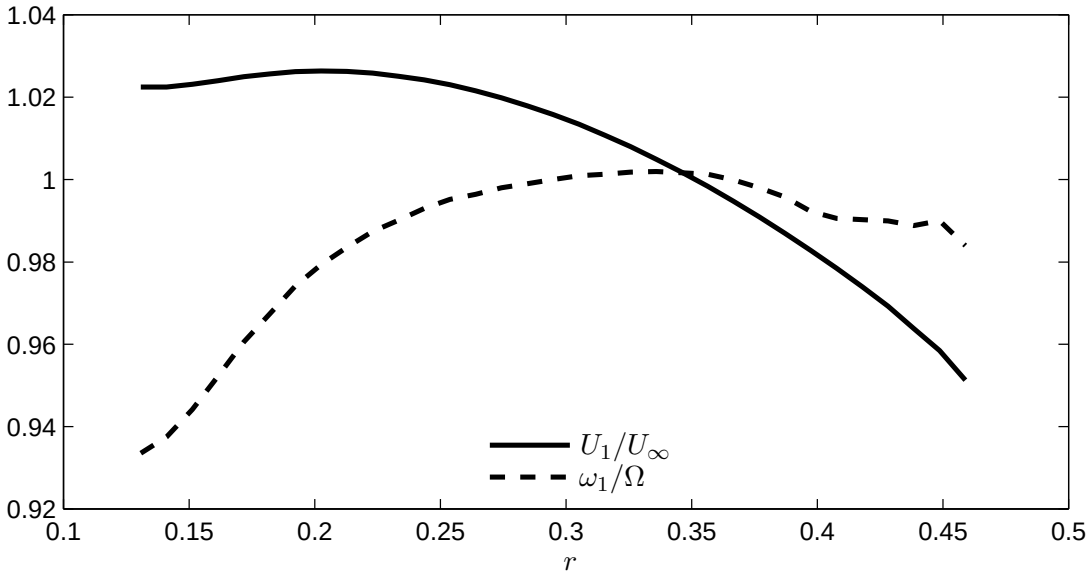

FIGURE 5.17: Discrepancy in the estimated wake due to incorrectly predicted propeller induced velocities using the described RANS-BEMt coupling.

The sensitivity of the coupling to various parameters is assessed in the following sections. Even though the relative discrepancy of the angular momentum is higher as shown in Figure 5.17, the absolute value is better matched to the expected value as shown in Figure 5.15. Therefore, for brevity, only the impact on axial momentum is considered in the following sections.

5.5.1 Influence of hub type

As the Goldstein correction could be sensitive to the presence of the hub as stated earlier, the influence of different hub types is investigated. Three different hub types are tested, the base case with the hub extending from inlet to outlet, a case where the hub ends after the propeller disk with a cone shaped hub cap of length $1r_H$ and finally a case with no hub present. For the case with no hub present, the BEMt is applied both with the original hub radius of $0.2R$ enforced and with the hub radius ≈ 0. The results are shown in Figure 5.18.

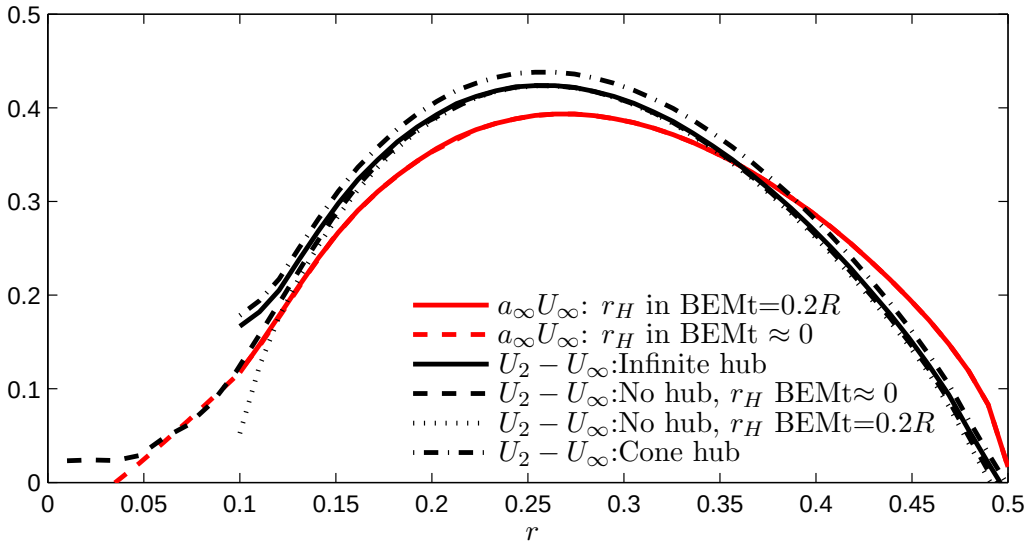

FIGURE 5.18: Influence of hub types on RANS-BEMt coupling.

The present theory uses a curve fit equation to the original Goldstein relations for K. These assume zero hub radius and may thus be less suitable here since the slipstream and thus the hydrodynamic pitch will contract differently if a hub is present. Tachmindij and Milan (1957) provided a corrected relation for propellers with 3-6 blades with a non-zero hub radius. To assess the sensitivity of the coupling to the chosen Goldstein correction with regards to the hub, the results using the present method for obtaining K are also compared to those when using Tachmindji-corrected factors (available only for $r_H = 0.167R$) provided by Carlton (2007, p 174). The results using the hub corrected Goldstein factors for the infinite hub are shown in Figure 5.19.

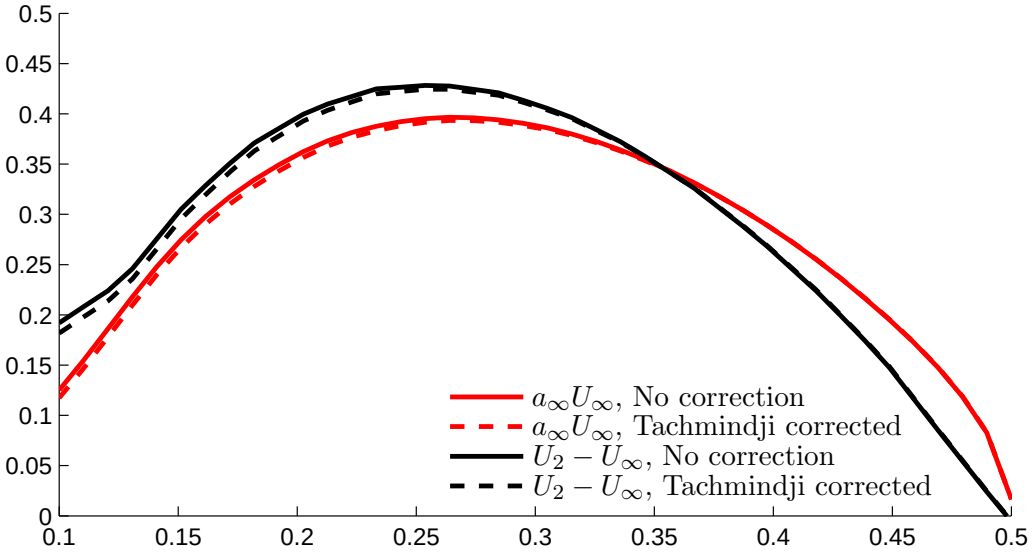

FIGURE 5.19: Influence of Tachmindji correction for finite hub thickness on RANS-BEMt coupling.

From Figures 5.18 and 5.19, it can be seen that the influence of the hub on the coupling is limited to a small area close to the hub and even there, the effect is very small. The overall mismatch between a_∞ and U_2 remains regardless of the hub setup and/or correction.

5.5.2 Influence of RANS mesh density

The accurate representation of the flow field in the RANS solution depends on having a suitable grid density near and within the propeller disk to resolve the flow gradients. In order to establish how this effects the coupling, a set of meshes with different density are used. In this section, the BEMt mesh is fixed as having $n_R = 40$ and $n_C = 10$. The tested meshes are defined in Table 5.3, if not otherwise stated, values of cell spacings are the same as the base case shown in Table 5.2.

TABLE 5.3: Definitions of mesh refinement variations in verification study, i and o denote if the number concerns cell spacing inside or outside $x = \pm 0.3R$ and $r = R$.

Mesh	Cells			
	Radial	Circumferential	Axial	Total cells inside disk
Fine $r\theta$	100 i	200 i&o	20 i	120000
Fine x	25 i	80 i&o	60 i 150 o	40000
Medium $r\theta$		Base case		18000
Coarse $r\theta$	15 i	60 i&o	10 i 50 o	3600

The results are shown in Figure 5.20 where it can be seen that the changes in resolution for the RANS mesh make little difference for the agreement. It should be noted that,

changing the rate of cell size expansion to be $\neq 1$ in the radial direction inside the propeller disk has no impact on the results in Figure 5.20.

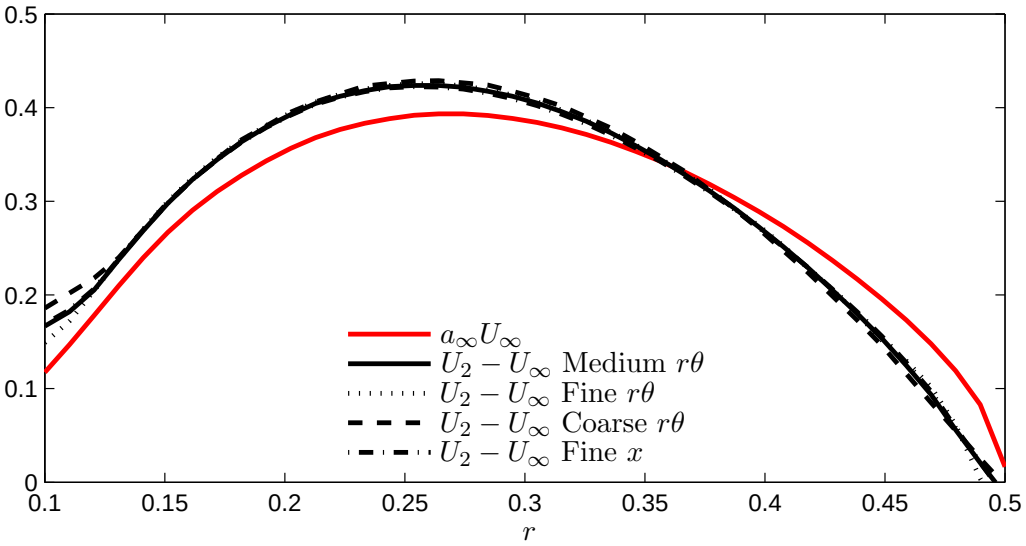

FIGURE 5.20: Results of mesh independence study for the RANS-BEMt coupling algorithm.

5.5.3 Influence of BEMt mesh density

The density of the concentric mesh is varied to assess its impact on the coupling. Varying the circumferential discretisation has no effect since the flow field is rotationally symmetric. The calculated a_∞ and the probed U_2 are shown for a range of radial discretisations in Figure 5.21. As demonstrated here, the radial dicretisation does not affect the distributions notably. A slightly lower velocity is obtained for $n_R = 10$ since the lack of discretisation points near the tip means the curve is less full and thus the integral value of thrust is slightly lower.

5.5.4 Influence of viscosity

To asses how the ideal fluid assumption of momentum theory affects the coupling, the simulation is run with $\mu = 0$ and $\mu = 10^{-6}$ as well as with the turbulence model switched on and off. All of these combinations yield identical velocity distributions.

5.5.5 Influence of propeller disk thickness

Four different values of d_d were used with the standard set up to assess the impact of disk thickness on the coupling. The resulting velocity profiles are shown in Figure 5.22.

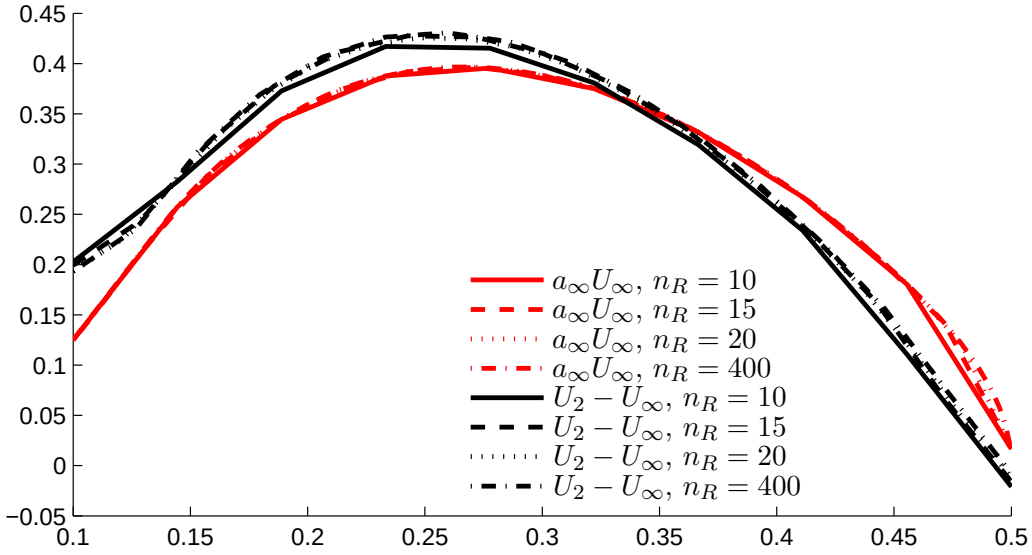

FIGURE 5.21: Impact of number of BEMt radial sectors on RANS-BEMt coupling.

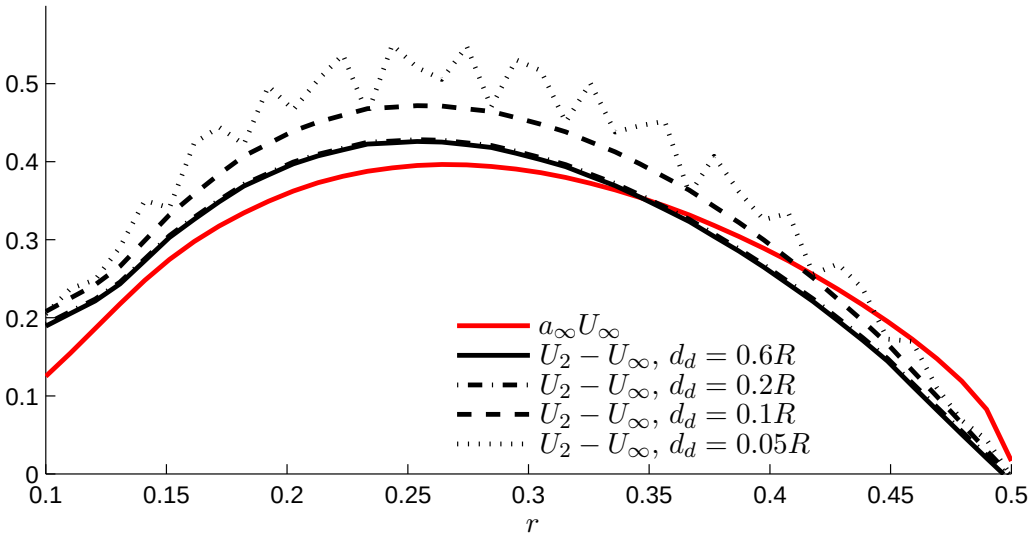

FIGURE 5.22: Impact of disk thickness on the RANS-BEMt coupling.

The thickness of the disk influences how the body force is distributed in the domain. A thinner disk means a more abrupt increase and decrease of the force but any thickness will mean a discrete change in $\mathbf{F}_v$ between the outside and inside of the disk. The abrupt changes in $\mathbf{F}_v$ in turn lead to very steep pressure gradients near the disk which in turn are a smeared representation of the discrete pressure jump in momentum theory.

The PISO pressure velocity coupling scheme is used here with a collocated grid meaning that the pressure has to be interpolated onto the cell faces. Instabilities caused by this interpolation are resolved using a correction similar to the Rhie-Chow algorithm (Rhie and Chow, 1983). However, this algorithm is not designed to work with flows

which have large body forces (Andersson et al., 2012), especially not if the body force has large gradients (Mencinger and Žun, 2007) as is the case here. Using the standard PISO formulation can thus be problematic when using it in conjunction with body force modelling of propellers and turbines which feature a thin actuator disk (Réthoré and Sørensen, 2008). The instability in the pressure velocity coupling is visible in Figure 5.22 where the velocity field is noisy for the thinnest disk since this yields the strongest discontinuity.

To assess if the discontinuity effect in the pressure velocity coupling also causes an overall error in the velocity profile inside the disk, an alternative body force distribution is used where $\mathbf{F}_v$ is smoothly varied in the axial direction but where the integral value is maintained. A disk of $d_d = 0.6R$ is used to give a maximum amount of diffusion of $\mathbf{F}_v$. The resulting velocity profile is identical to the one for the same thickness in Figure 5.22. However, since the body force is large and, since a discontinuity in the radial direction remains, using standard pressure velocity coupling can still cause problems. A corrected pressure interpolation algorithm was proposed by Réthoré and Sørensen (2008) to improve body force modelling of wind turbines. They also argued that by improving the pressure velocity coupling with consideration to the actuator disk, the number of cells in the axial direction could be greatly reduced. While this correction is not used here, it is suggested that a similar correction should be employed in future studies to improve the RANS-BEMt coupling.

The pressure field when $d = 0.2R$ is shown in Figure 5.23. It can be seen that the areas of highest and lowest pressure are not aligned on either side of the disk. The low pressure region is shifted slightly towards the hub and the high pressure region is shifted slightly towards the tip. As a consequence the zero pressure line is not centred on the propeller centre plane. A small asymmetry is expected since the slipstream contraction manifests itself as a small radial velocity. However, the asymmetry shown here, while not affecting the slipstream contraction notably, causes an increase in the axial velocity near the hub and a reduced axial velocity near the tip. It is unclear if this is due to pressure velocity coupling errors as stated before but asymmetric over- and undershoots of pressure near the body force discontinuity as demonstrated by Réthoré and Sørensen (2008) has the potential to cause a similar shift.

Whatever the cause, this phenomenon prevents an ideal coupling via the inflow factors and the probed velocity at plane 2. The difference in pressure at the front and back ends of the propeller disk along the radius is shown in Figure 5.24 as Δp. As an indication of the expected magnitude of the pressure jump from momentum theory, the relation between Δp and the angular velocity just behind the disk given by Carlton (2007, p 170) is also shown in Figure 5.24. Here, the shift in the pressure jump is confirmed to not follow the expected distribution.

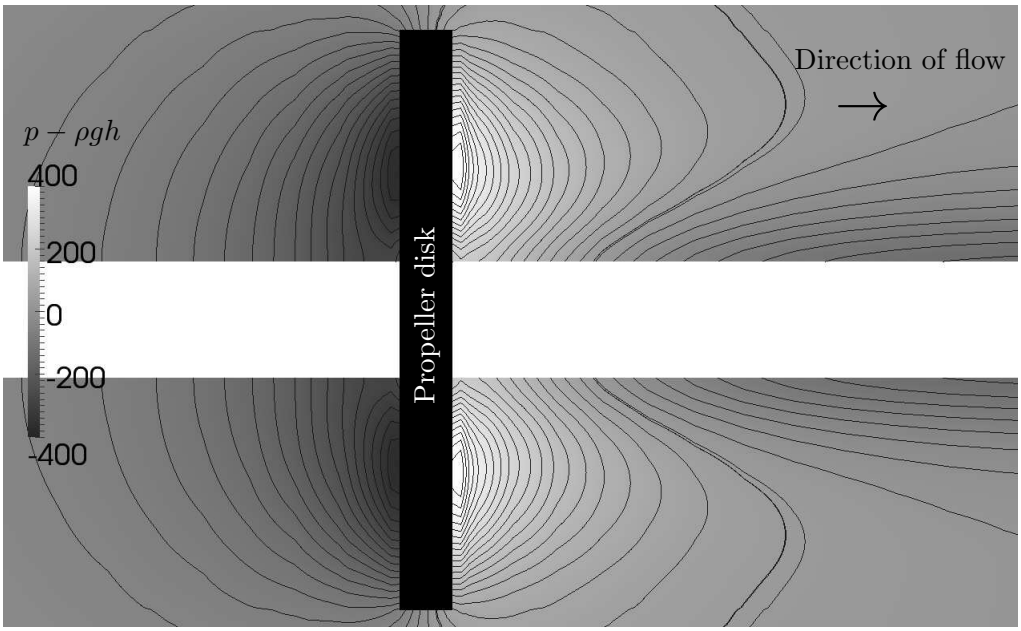

FIGURE 5.23: Pressure distribution around propeller disk.

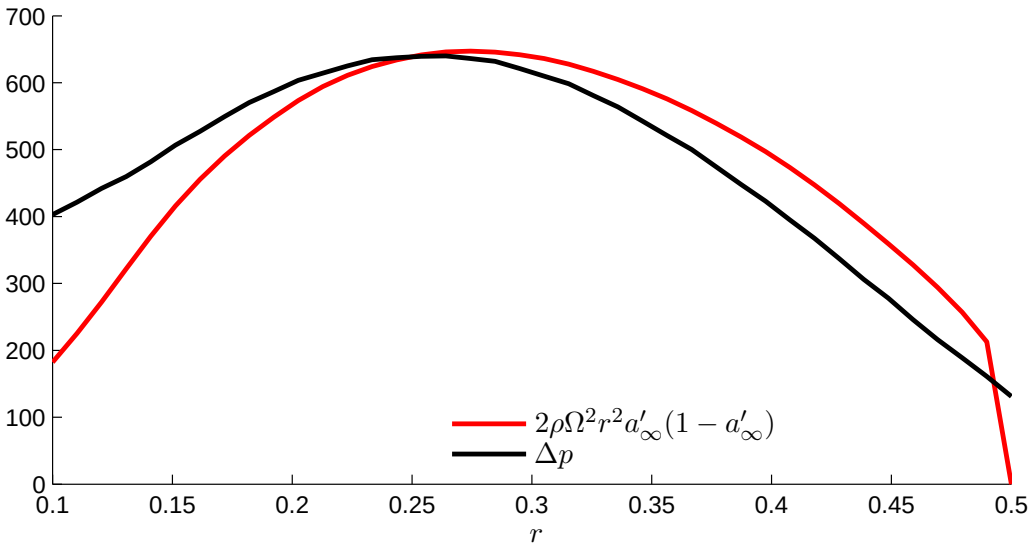

FIGURE 5.24: Discrepancy in the measured pressure jump over propeller plane.

5.5.6 Influence of scale

To assess the scalability of the coupling, the simulation is run with various combinations of U_∞ and the propeller RPM, all yielding the same advance coefficient. it is found that there is no difference in the discrepancy between the expected and recorded velocity profiles over a range from $U_\infty = 10$, $1500RPM$ to $U_\infty = 0.1$, $15RPM$. There is also no notable effect on the coupling if the radius of the propeller is changed in a range from $R = 0.05m$ to $R = 5m$. This means that any conclusions drawn here should be applicable to the same propeller regardless of the scale.

5.5.7 Influence of propeller geometry

The previous sections have discussed the impact of various aspects of the simulation on the coupling for a specific propeller. However, the single most influential factor on the discrepancy between a_∞ and U_2 is the propeller geometry itself which is defined as an input to the BEMt. For example, varying the blade area ratio changes the alignment of the velocity profiles significantly. The same applies for changing the pitch and chord distributions. Generally, the agreement is better for lower values of A/A_0.

5.6 Inflow correction factor

Figure 5.25 shows the predicted value of U_1 for all the variations discussed in Section 5.5. It can be seen that they (apart from some deviations which are highlighted) all have a similar deviation from the expected value of $U_\infty = 1$. For the purposes of this thesis, this deviation is corrected for using an empirical correction ensuring that, for the open water case $U_1 = U_\infty \; \forall \; r$. However, there is no guarantee that this will yield the correct wake field when $U_1 \neq U_\infty$. Future studies should therefore aim to improve the RANS-BEMt coupling to better account for the weaknesses mentioned in previous sections.

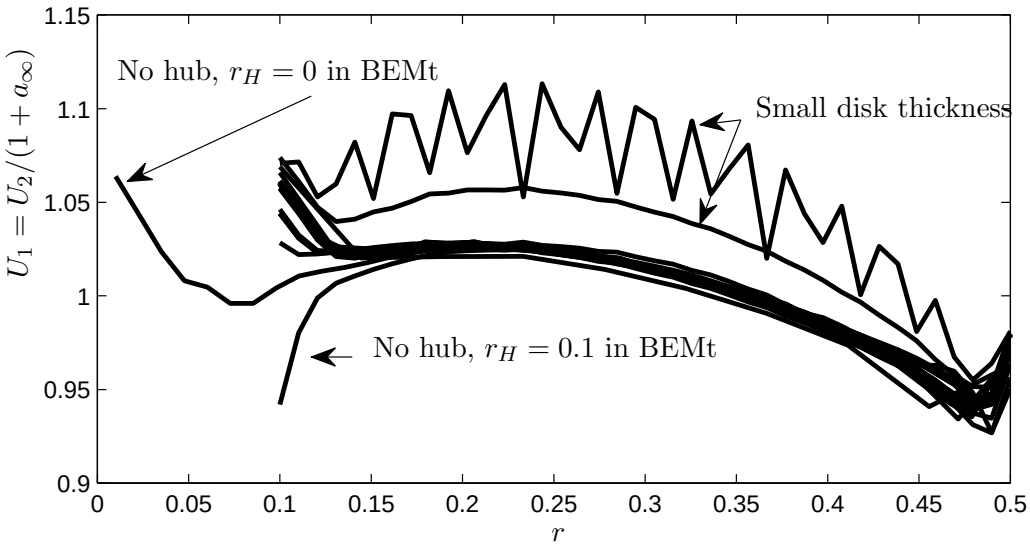

FIGURE 5.25: Predicted wake velocity for all variations of the RANS-BEMt coupling.

Several options exist to achieve an empirical correction. These all require the discrepancy in open water to be determined first.

- Correct the probed value of U_2 to match the estimated a_∞.
- Correct the estimate of a_∞ to match the generated velocity profile.

- Correct the thrust and torque distribution to match the generated velocity with a_∞.

Since the integral values of the thrust and torque distributions already give satisfactory results compared to experiments as shown in Figure 5.13, these are not altered. Having eliminated this option, the two remaining options are identical in principle since neither affect any other part of the solution than the calculation of the wake. Here, a correction is applied to a_∞ to better match the generated velocity in the RANS domain.

A suitable correction to achieve this is given in Eqn. 5.51.

$$U_1 = \frac{U_2}{U_\infty(1+a_\infty)} - (\Psi_{lin} + \Psi_{triq}) + U_\infty \tag{5.51}$$

where

$$\Psi_{lin} = 1.6790 - 1.3744J + 0.7424J^2 + \frac{r}{R}\left(-0.7606 + 1.3864J - 0.6705J^2\right) \tag{5.52}$$

$$\Psi_{triq} = -J^{-2.7048}\left(0.7370\left(\frac{r}{R} - 0.5587\right)^5 + 0.0694\left(\frac{r}{R} - 0.5582\right)^3\right) \tag{5.53}$$

Eqn. 5.51 should not be seen as an attempt to describe components of velocity but rather as a curve fit to the correct distribution. This is why the dimensions are not consistent. With this correction

$$U_\infty(\Psi_{lin} + \Psi_{triq})(1+a_\infty) \approx U_2 \tag{5.54}$$

since $U_1 = U_\infty$ in open water conditions.

Figure 5.26 shows the agreement between the velocity profiles for a range of J between 0.3 and 0.8 with and without the correction applied. The expected induced velocity when the correction is applied matches well with the recorded velocity profiles. Figure 5.27(a) shows how well the correction can reproduce the desired value of $U_1 = U_\infty$ using Eqn. 5.51. The original estimate of U_1 without the correction is also shown. U_∞ is well reproduced for most of the span, some noise occurs close to the hub and tip. This is of less importance since most of the thrust and torque is delivered away from the extreme values of r/R. Figure 5.27(b) shows how the correction performs when a non-uniform inflow is applied. Here, the expected profile is a simple sinusoidal variation of U_1 defined as $U_1 = U_\infty + 0.05U_\infty \sin(3\pi r/R)$. Again, the obtained values of U_1 represent a substantial improvement from the original estimate without any correction. The shape of the wake is well captured although the predicted amplitude is slightly smaller than the expected value.

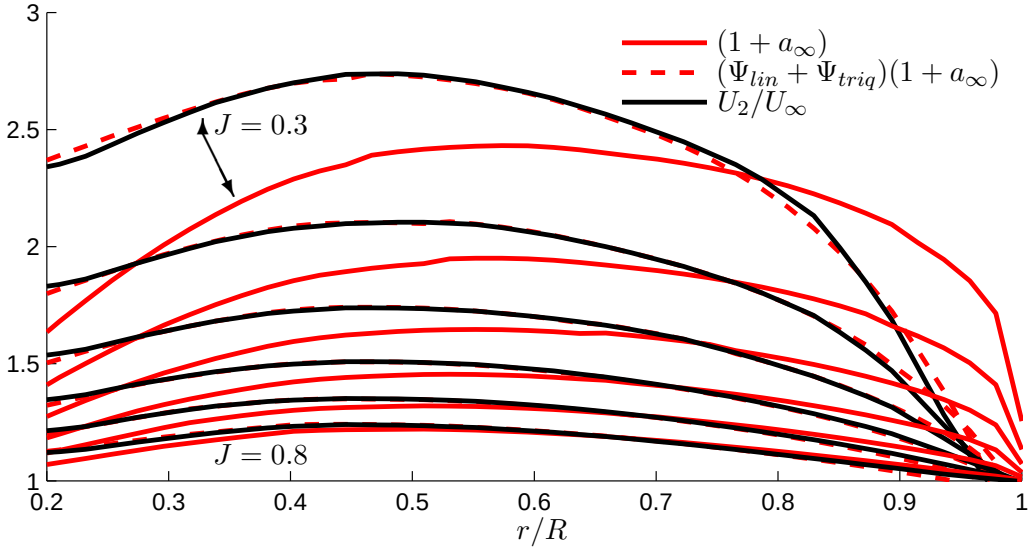

FIGURE 5.26: Agreement between expected and recorded velocity profiles using the inflow correction.

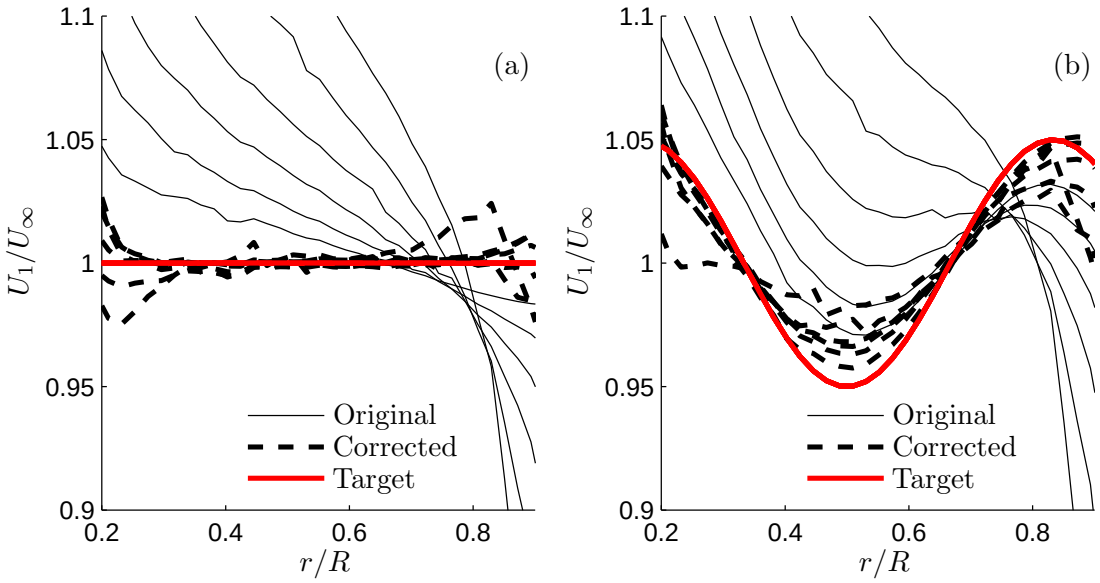

FIGURE 5.27: Agreement between expected and estimated wake profiles with and without the inflow correction.

Finally, Figure 5.28 shows the scalability of the correction where the predicted wake when $U_\infty = 1$ at 150 RPM is shown together with the one for $U_\infty = 10$ at 1500 RPM as well as when $R = 0.5$ and $R = 0.075$. All cases show less than 1% deviation from U_∞ in the calculated wake.

With these definitions the local advance ratio, used to calculate the thrust and torque distributions for a non uniform wake is given as

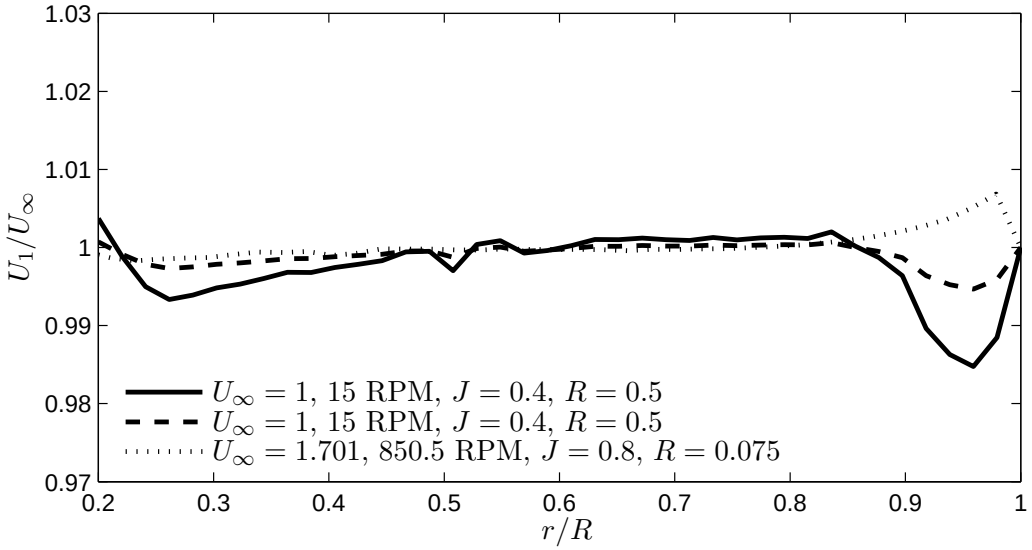

FIGURE 5.28: Scalability of inflow correction.

$$J_{local} = J(1 - w_T) \tag{5.55}$$

with w_T given by the corrected value of U_1 as

$$w_T = \frac{U_\infty - U_1}{U_\infty} \tag{5.56}$$

5.7 Inflow relaxation factor

The momentum theory based induced velocities a_∞ and a'_∞ represent the converged solution. Using these together with velocities probed from the RANS solution to find the undisturbed wake as described in the previous section will therefore only yield the correct wake if the velocity field due to the body force has converged. In the initial start-up process, the BEMt will yield the final induced velocity while the probing of the RANS solution will only yield a small fraction due to inertia. To prevent this from causing an incorrect wake in the initial start-up which might cause an error in the converged solution, relaxation can be applied to the calculated value of U_1.

The application of the relaxation is based on the rate of change of U_1 and U_2. If U_1 changes faster than U_2 between two time steps, changes in a_∞ will be driving changes in the wake. This is not desirable since changes in the wake should lead to a different loading condition for the propeller and hence in turn lead to a change in the induced velocities. Therefore a relaxation can be applied so that U_2 always changes faster than

U_1. If the subscript indices $_i$ and $_{i-1}$ indicate values in the current and previous time steps, the relaxed value of U_1 can be obtained as

$$U_{1irelax} = \begin{cases} if\ |U_{1i} - U_{1i-1}| > |U_{2i} - U_{2i-1}|\ :\ U_{1i-1} + \alpha_r(U_{1i} - U_{1i-1}) \\ else\ :\ U_{1i} \end{cases} \tag{5.57}$$

where α_r is a relaxation factor. Figure 5.29 shows the development of the average value of J from an initial value of 0.8 with different values of α. The simulation time is normalised to show the number of rotations of the propeller at the current RPM. The results show that J for all relaxation factors returns to the expected value after 1.5 - 2 rotations of the propeller with a slight over prediction. All relaxation factors reach the same predicted J after convergence, the only difference is the severity of the under prediction of J in the initial start up phases. Since this is of less concern, a relaxation factor of $\alpha = 1$ (no relaxation) is preferred here since it will not interfere with the variations in the unsteady wake in any way.

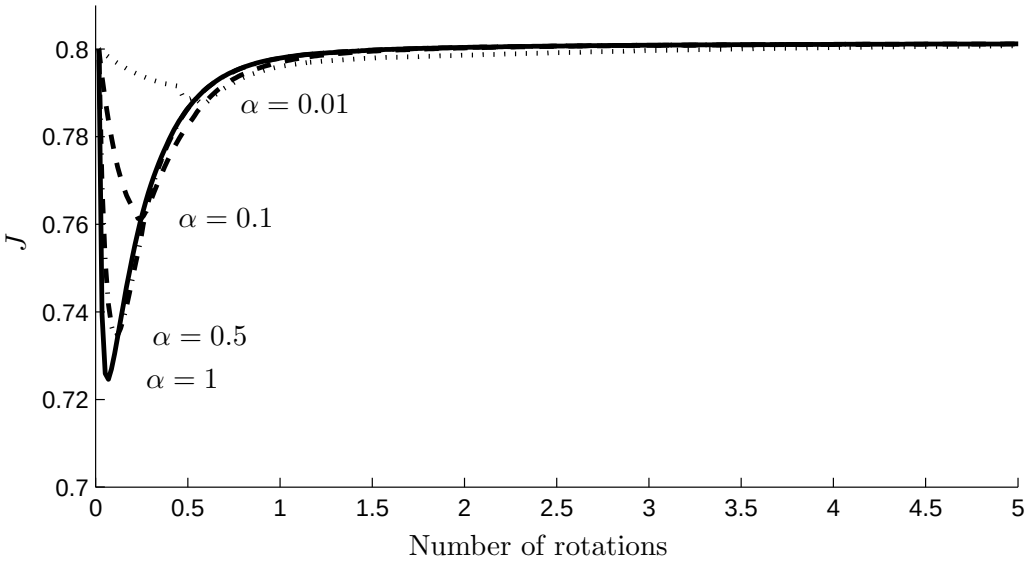

FIGURE 5.29: Development of J in open water when correcting for propeller induced velocities using different relaxation factors.

From Figure 5.29 it can be noted that the highest relaxation factors make J reach the converged value faster. This is because the higher thrust that comes with a larger drop in J helps to make the RANS solution converge faster by increasing the acceleration over the propeller plane. The lower relaxation factors make J converge much slower since a lower level of thrust is maintained throughout the process.

The obtained value of J after convergence is over predicted with only 0.15 % indicating that the coupling procedure is able to account for the propeller induced velocities with

satisfactory results. The results shown here for open water are encouraging. In Chapter 7 the correction will be used to assess the influence on the propulsive performance when the wake is non-uniform and unsteady.

5.8 Computational cost

One of the main arguments for using a simplified propeller model such as the BEMt is the computational cost required to include self propulsion in the modelling. The total computational time taken up by running the framework with a BEMt propeller model versus the total computational time for the complete RANS-BEMt simulation is shown in Table 5.4. Here all mapping, data handling as well as solving the BEMt equations is taken into account in the time taken up by the framework. The domain described in Section 5.5 is used. In these simulations, the RANS solution is obtained using a decomposed domain. An average of around 50 000 cells is handled by each processor in all cases. Using fewer processors will yield a more favourable performance of the framework relative to the RANS solution. However, the framework performance is also affected by the decomposition since different processors can handle the probing of inflow variables if the propeller disk is located in separate processors.

TABLE 5.4: Computational time required by the framework compared to total simulation time.

RANS cells total	RANS cells inside disk	n_R	n_C	Time spent on framework per time step	Time spent on framework (% of total time)
7M	96 000	10	10	1.6s	0.7%
7M	96 000	40	10	1.6s	0.7%
7M	96 000	40	1000	2.0s	0.8%
1.2M	11 000	10	10	0.25s	1.0%
1.2M	11 000	40	10	0.26s	1.0%
1.2M	11 000	40	1000	0.5s	1.2%
300 000	4000	10	10	0.07s	1.5%
300 000	4000	40	10	0.07s	1.5%
300 000	4000	40	1000	0.09s	1.6%

All configurations of the RANS and concentric meshes yield around 1% of the computational time being devoted to the framework. Most of the change occurs when varying the number of cells in the RANS mesh. This is likely to be caused by the fact that the framework accesses the memory where the mesh is stored and even though it does not need to search through it, a larger mesh means slower performance of the tasks such as probing etc. Varying the number of nodes in the concentric mesh therefore has less influence. This also indicates that less time is spent on solving the actual BEMt equations than on data handling.

The values in Table 5.4 can be put into perspective with the typical computational effort required to facilitate a discretised propeller and rotating geometry using an AMI. Windén, Badoe, Turnock, Phillips and Hudson (2013) reported a total simulation time which was five times longer when comparing the performance of an AMI to the one for the BEMt for a similar case. It should be noted that the AMI suffers both from an increase in the computational time per time step (because of the larger mesh and interpolation algorithm) but also from a longer overall simulation time. The performance of the BEMt converges quickly since momentum theory assumes a converged flow field and thus a high initial thrust. The AMI requires the actual flow field around the propeller to converge in the RANS solution which leads to a longer simulation time.

It is demonstrated here that the data handling and mapping provided by the framework can be achieved with little computational effort (approximately 1% of the total simulation time.) This would not have been possible using previously available methods in OpenFOAM. Furthermore the solving of the blade element and momentum equations only take up a small fraction of the total computational time.

Chapter 6

RPM control for a self propelled ship

As was discussed in Section 1.3, the numerical towing tank should include the ability to control the propeller RPM in run time. The development of the self propulsion framework presented in Section 5.2 has provided the necessary interface between the RANS model, the propeller model and the control scheme. However, the choice of control scheme still needs to be addressed. This thesis does not aim at presenting a detailed study on how various controllers can be implemented in the framework, such studies are left as future work. However, a list of possible controllers is presented in Table 6.1. Only some of these are implemented in the current version of the framework which is also indicated. The *Fixed speed* controller was used to investigate the influence of propeller controlling on the powering requirement in head seas by Windén, Turnock and Hudson (2013*a*) and Windén et al. (2014*a*).

6.1 Control function

Most controllers in Table 6.1 can be implemented by defining the discrepancy between the desired value and the current value as the error ε_c and use a standard Proportional-Integral-Derivative (PID) controller to make the system respond in order to minimise ε_c. The controller can then be defined as

$$RPM(t) = RPM(t - \Delta t) + K_s \varepsilon_c(t) + K_i \int_{\tau=0}^{\tau=t} \varepsilon_c(\tau) d\tau + K_d \frac{d\varepsilon_c(t)}{dt} \tag{6.1}$$

The standard PID controller has been implemented as a selectable control function in the self propulsion framework. The framework thus provides support for any control

TABLE 6.1: Examples of propeller control schemes for the self propulsion framework.

Name	Description	Currently implemented
Fixed RPM	A dummy controller which allows for a fixed RPM value to be set	YES
Fixed speed	Attempts to keep constant forward speed (zero surge variation)	YES
Fixed torque	Attempts to keep the generated torque constant at a pre-set value	YES
Fixed thrust	Attempts to keep the generated thrust constant at a pre-set value	YES
Self propulsion point finder	In calm water, varies the RPM until force balance in the surge direction is found	YES
Engine	Attempts to mimic the RPM variations a specific engine/engine control system would produce	NO
Wave adaptive	Attempts to anticipate changes in inflow conditions due to waves and adapt the RPM to keep the propeller operating at higher efficiency	NO

function which is based on the discrepancy of a single variable from a pre-set value. More advanced controllers can also be devised by defining a ε_c as a multivariate function. For more advanced controllers see for example Xiros (2002). The *Wave adaptive* controller could be realised by anticipating the effects of the waves from motions and orbital velocities as described by Ueno et al. (2013).

6.2 Limiters

In addition to the PID-controller governing the RPM, some restrictions must be applied to make the simulation more realistic. The RPM should not be allowed to exceed a certain value since that would mean a great risk of cavitation and damage to machinery in a real propulsion system. Large acceleration of the propeller rotation rate should also be disallowed since the torque needed to achieve such acceleration lies beyond the capability of both engines and propeller shafts. Furthermore, RPM increases are usually limited in marine engines to avoid large heat gradients etc.

A typical maximum value at full scale for how fast the propeller rotation is allowed to change is around 1 RPM per minute. If an example scale factor of 40 is applied in this case, this is equivalent to a maximum increase of 0.67 RPM/s in model scale. Furthermore typical working shaft-RPM for most large merchant vessels lie between 40

and 100 RPM. This corresponds to between 250 and 630 RPM in the example model scale.

6.3 Results for a Wigley hull

The methodology and results presented by Windén, Turnock and Hudson (2013*a*) and Windén et al. (2014*a*) for a self propelled Wigley hull in waves are shown here. This is mainly done to highlight important findings regarding the use of the framework for RPM control but also to show the ability of the framework to facilitate a free to surge model. In particular, conclusions drawn about initial conditions are of use for the final application of the numerical towing tank. This section also serves to illustrate how simple radial functions for the thrust and torque distributions can be used with the framework.

The same Wigley hull as was used in Chapter 4 is used. This is subjected to waves of $\lambda/L = 1$ and $\zeta_0 = 0.023m$ at $Fn = 0.2$.

An error function is used based on the current and integral values of acceleration to try and achieve constant forward speed for a self propelled Wigley hull. The error is defined as

$$\varepsilon_c = -\rho\nabla\frac{\partial^2 x_1}{\partial t^2} - 1000\int\frac{\partial^2 x_1}{\partial t^2}\,dt \tag{6.2}$$

Even though the controller has access to both the current forward speed and the surge displacement, the acceleration in the surge direction $\partial^2 x_1/\partial t^2$ is chosen here since this is something that could be measured on a real ship using a simple accelerometer. Windén et al. (2014*a*) found that this controller is not able to keep constant speed in waves of $\lambda/L = 1$ at realistic RPM change rates. If a higher rate of change is allowed, the speed can be kept relatively constant albeit at a displaced value of surge. Furthermore, keeping constant speed using this controller greatly increased the delivered power. This controller is only meant as an example of how the framework can be used and more advanced controllers are likely to perform better.

The setup is identical to the one described in previous chapters. For this example, the thrust and torque distribution inside the propeller disk is determined by a radial shape function which is zero at the hub and tip and approximately follows the Goldstein (1929) optimum distribution. A non-dimensional radius r_s is defined as

$$r_s = \frac{|\mathbf{R}_I| - r_H}{R - r_H} \tag{6.3}$$

A shape function describing the thrust distribution is given as

$$f_K = r_s\sqrt{1-r_s}; \tag{6.4}$$

and equally for the torque

$$f_Q = \frac{r_s\sqrt{1-r_s}}{r_s(1-r_H)+r_H} \tag{6.5}$$

The shape functions f_K and f_Q are shown in Figure 6.1.

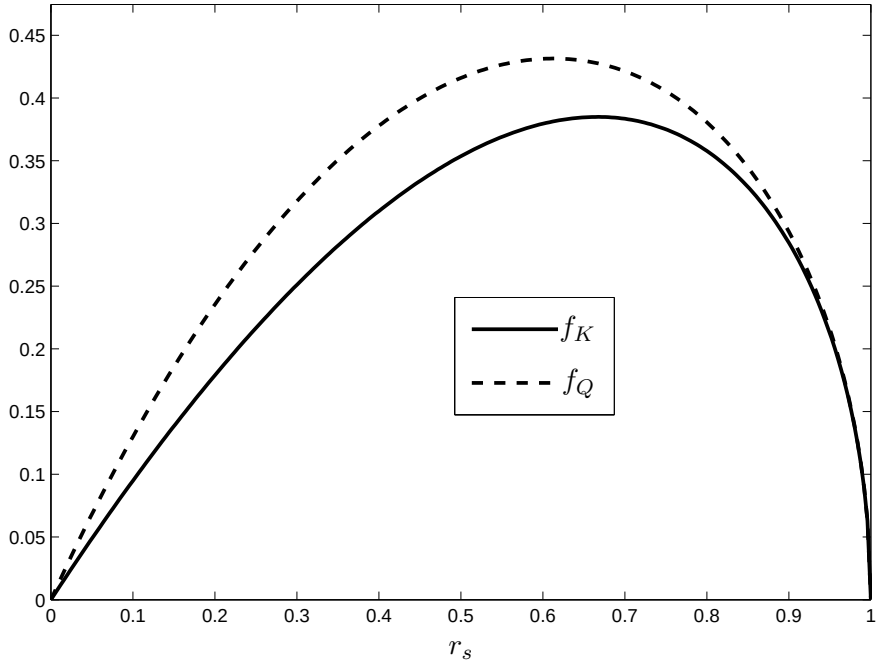

FIGURE 6.1: Thrust and torque shape functions f_K and f_Q.

The shape functions are normalised so that the summation value over the entire disk corresponds to the desired thrust and torque.

$$f_{KN} = T\frac{f_K}{\sum\limits_{Disk} V_I f_K} \tag{6.6}$$

$$f_{QN} = Q\frac{f_Q}{\sum\limits_{Disk} V_I|\mathbf{R_I}|f_Q} \tag{6.7}$$

The body force for a cell I is now given as

$$\mathbf{F}_{vI} = \mathbf{O}f_{KN} + \mathbf{O}_\theta f_{QN} \tag{6.8}$$

TABLE 6.2: PID coefficients and initial RPM value.

K_s	1.2	K_d	0
K_i	0.5	Start RPM	496.4

The thrust and torque are decided by the K_T and K_Q as well as the current working RPM.

$$T = K_T \rho \left(\frac{RPM}{60}\right)^2 (2R)^4 \tag{6.9}$$

$$Q = K_Q \rho \left(\frac{RPM}{60}\right)^2 (2R)^5 \tag{6.10}$$

Since the propeller blades are not explicitly modelled in this case, the variation of K_T and K_Q with the RPM is not known. For stock propellers such as the Wageningen B-series, these can be found by interpolation of tabulated values based on experimental data for example from Bernitsas et al. (1981). Here, a 5^{th} order polynomial fit to the open water characteristics of a MARIN 7967 propeller as described by Carrica et al. (2013) is used where

$$\begin{aligned} K_T &= 0.398399 - 0.067794J - 1.286040J^2 \\ &+2.286960J^3 - 2.039820J^4 + 0.676134J^5 \end{aligned} \tag{6.11}$$

$$\begin{aligned} K_Q &= 0.051144 - 0.000390J - 0.171650J^2 \\ &+0.330060J^3 - 0.327865J^4 + 0.119477J^5 \end{aligned} \tag{6.12}$$

In contrast to the BEMt described in the previous chapter, equations 6.9 and 6.10 as well as the shape functions (Equations 6.4 and 6.5) assume that the flow into the propeller is uniform. This means that the advance ratio is constant over the disk. Furthermore, the periodic variation of thrust and torque is not considered other than through the surging motion changing the overall J. By applying a BEMt method post run-time to estimate the thrust and torque variations behind the Wigley hull in this study, Windén, Turnock and Hudson (2013*b*) found a thrust variation of 16% around the mean value because of the unsteady wake.

Simulations are started from an initialised solution where the steady wave pattern of the hull is allowed to develop. At the initial state, the resistance is recorded and the starting RPM is set as to match this resistance with a corresponding thrust. The hull is then subjected to regular waves with the first crest reaching the hull at about $t/T_e = 3$.

All the information about the propeller extent and position are shown in Table 6.3 the hull is the same one used in the validation case in Chapter 4. Nine different values on

TABLE 6.3: Positioning and extent of propeller.

R	0.0796875 m	$\mathbf{O}_0$	(1 , 0 , 0)
d_d	0.0159375 m	$\mathbf{x}_{p0}$	(1.53 , -0.1078125 , 0)
r_H	0.00796875 m	$\mathbf{CG}_0$	(0 , -0.0175 , 0)

TABLE 6.4: RPM constraints.

#	max $\partial RPM/\partial t$	#	max $\partial RPM/\partial t$
1	0.65	6	0.9
2	0.60	7	1
3	0.70	8	∞
4	0.80	9	2
5	0.50	10	3

the maximum permissible RPM change rate $\partial RPM/\partial t$ are tested as well as a reference case where the acceleration is unlimited. The tested constraints are listed in Table 6.4.

Controllers 2-5 performs similarly in terms of surge motion compared to controller 1, significant differences are only seen for controllers 6-10. In Figures 6.2, 6.3 and 6.4, the forward speed, surge and RPM for controllers 1, 7 and 10 are shown. Finally, the delivered power, which can be calculated as $P_D = 2\pi QRPM/60$ is shown in Figure 6.5.

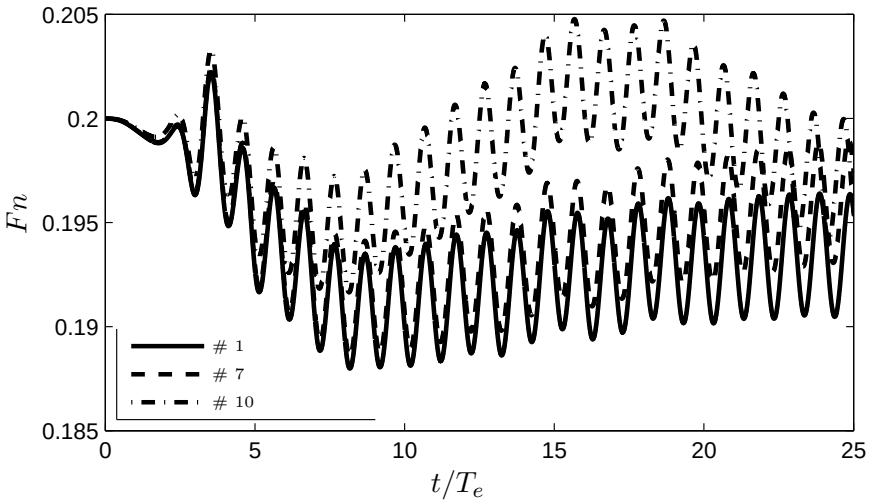

FIGURE 6.2: Changes in forward speed due to waves with different values of $\partial RPM/\partial t$ allowed.

As seen in Figure 6.2, the hull experiences a periodical oscillation in forward speed due to the waves. There is also a drop in the mean velocity. This is due to the mean increase in resistance due to waves R_{AW}. It is clear that none of the controller constraints are generous enough to influence the periodical velocity notably. The RPM in all cases follows the maximum permitted increase. However, the higher the permitted value of $\partial RPM/\partial t$ is, the faster the ship can overcome R_{AW} with an increased thrust and return to the original forward speed. This however comes at the cost of a higher power delivered to the propeller as seen in Figure 6.5. Controller 8 is very successful in keeping constant

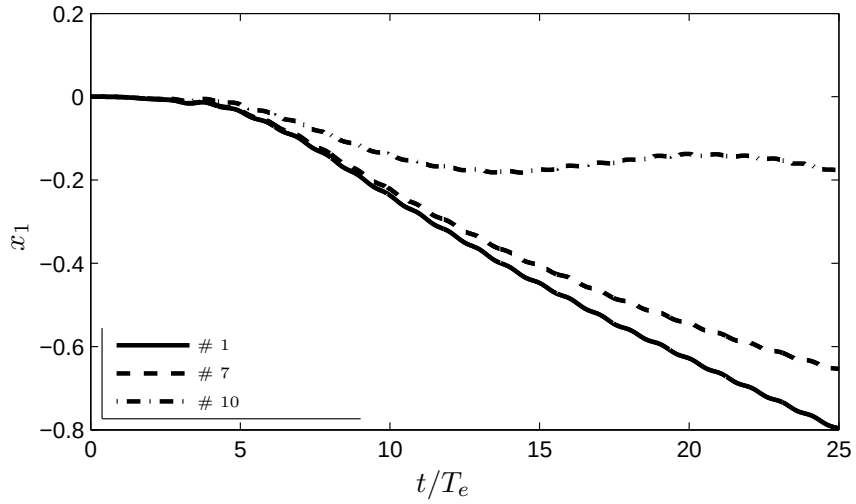

FIGURE 6.3: Changes in surge due to waves with different values of $\partial RPM/\partial t$ allowed.

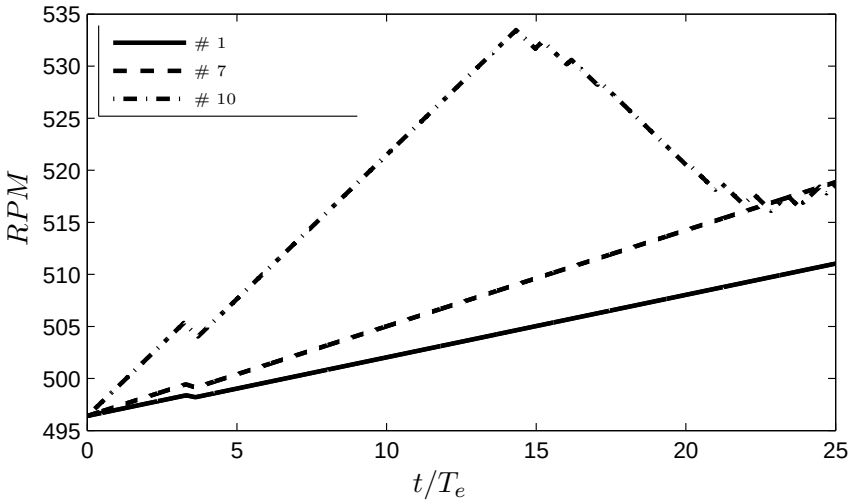

FIGURE 6.4: Development of propeller RPM with different values of $\partial RPM/\partial t$ allowed.

forward speed, however the RPM increases (and subsequent power) required to do so are not in any way related to reality.

As seen in Figure 6.3, even though the hull returns to its initial forward speed, the integral value of the velocity means that it has been given a large distortion in surge. While this is not a problem in real applications, in this case it means that the mesh has been distorted. In the interest of accuracy future implementations should take this into consideration. If the actual powering performance in waves is sought, it would not be suitable to construct a controller that puts a penalty on the surge drift. Instead it would be preferable to initialise the simulation from a fixed hull in waves and use the RPM needed to overcome R_{AW} as the initial condition.

Figure 6.6 shows the variation of surge force and thrust force over one period of encounter for controllers 1,7 and 10. Here it can be seen that the mean values of force are very similar as a consequence of the fixed speed criteria. On the other hand, the amplitude of

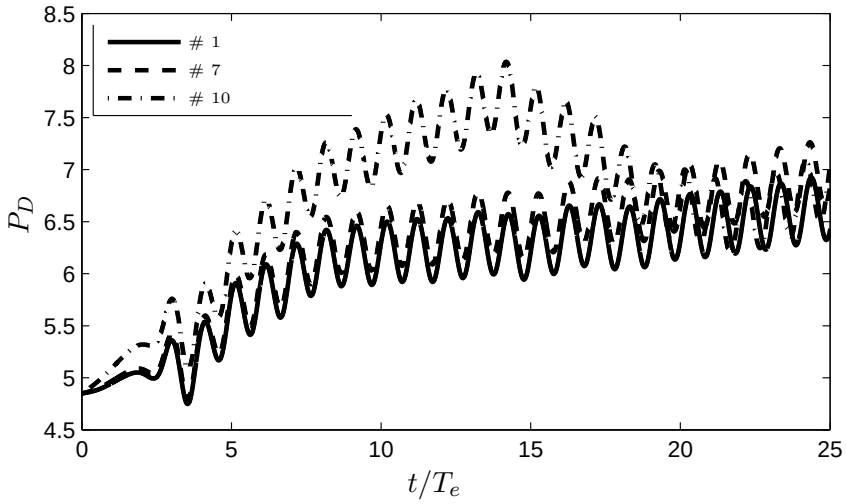

FIGURE 6.5: Changes in delivered power with different values of $\partial RPM/\partial t$ allowed.

the surge force is much higher than the one of the thrust force. Furthermore, the thrust force is phase shifted with approximately 90 degrees relative to the surge force. The phase shift stems mostly from the phase lag of the surge motion, but also to a small extent from small RPM variations for controller 10. The phase lag between different controllers stems from the different values of surge displacement meaning that the locations of the hull in the wave system are different.

Finally, Figure 6.7 shows how the mechanical power of the surge force ($F_x u_x$) together with the delivered power vary over one period of encounter.

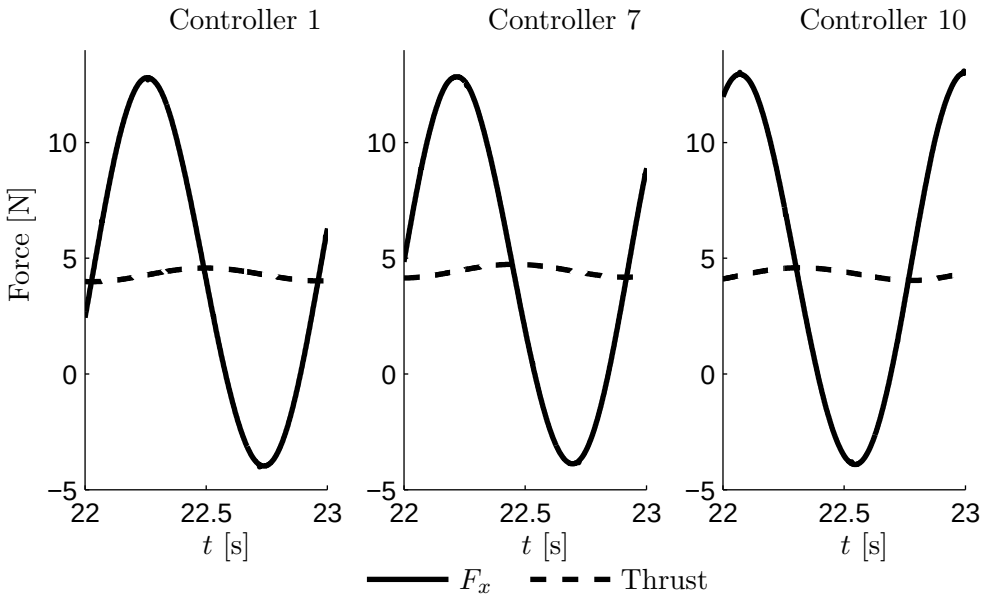

FIGURE 6.6: Variations in resistance and thrust over one period of encounter with different values of $\partial RPM/\partial t$ allowed.

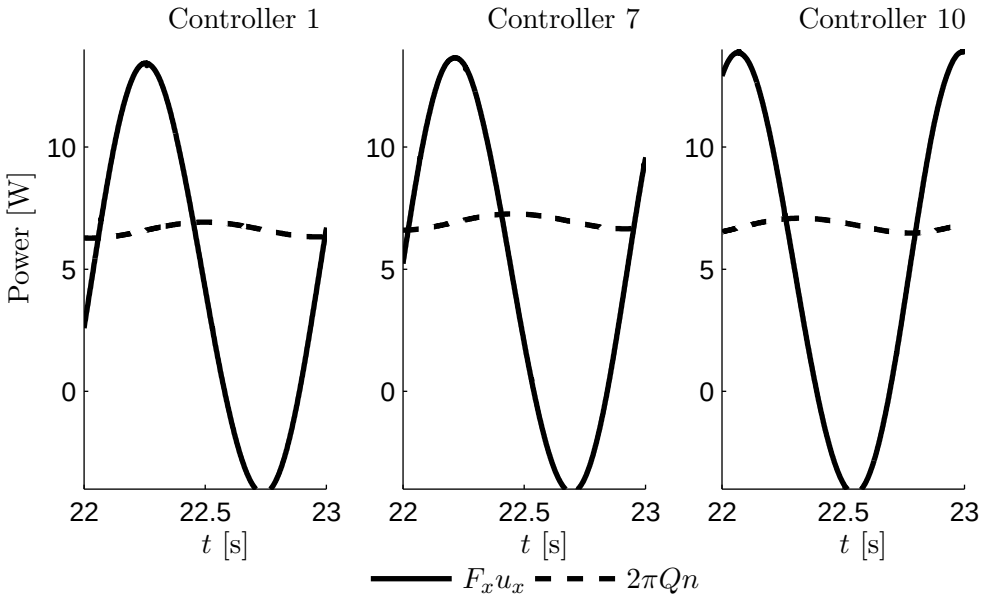

FIGURE 6.7: Variations in power over one period of encounter with different values of $\partial RPM/\partial t$ allowed.

6.4 Conclusions

Fast RPM variations are not feasible for large merchant ships powered by marine diesels. However, with the possibility of an advent of electrical propulsion for large ships in the future, discussions around RPM control are likely to be more common. Furthermore, while this thesis focuses on large merchant vessels, most of the methodology is applicable in a smaller scale. For smaller vessels the engines are smaller and faster variations of the RPM are possible. This chapter, together with the set up of the numerical towing tank and the self propulsion model shows how the impact of RPM control on the performance in waves can be studied numerically. It is shown that the model can represent surging motion and speed changes due to different RPM control schemes. However, the initial conditions set on the controller and the overall unsteady simulations will have a large impact on their success, something that should be improved in future studies.

The results in this chapter also demonstrates the ability of the described model to facilitate a model that is free to surge. Finally, it should be noted that varying the PID coefficients in Table 6.2 may have a similar impact on the performance as varying the maximum permissible increase.

Chapter 7

Modelling self propulsion of the KCS

The described methodology for modelling the ship and its propulsor in interplay is applied in this chapter to model the KCS hull and propeller in unsteady conditions. Firstly, the ability to find the model self propulsion point in calm water is compared with experimental data from the Gothenburg 2010 workshop. Experimental data is also available from the SIMMAN2014 workshop regarding the propulsion coefficients at a fixed RPM in calm water. Comparisons with these studies are made to demonstrate the ability of the RANS-BEMt coupling to capture the influence of the non uniform wake. Finally the self propelled KCS in head waves is presented although without experimental data. The particulars of the used KCS model are given in Table 7.1. Positions are given relative to the waterline amidships. Following the results in Section 5.5.5, the disk thickness in the propeller model is set to $d_d = 0.2R$.

The boundary conditions and overall set up follow the ones presented in Chapters 4 and 5. To accommodate the larger hull, the width of the domain is increased to $B_b = 16m$.

Table 7.2 shows the meshes used for these studies together with the computational effort required by the framework in the simulations.

Table 7.1: Particulars of the KCS model hull.

Scale			1:52.667		
L_m	=	4.3671 m	B_m	=	0.6114 m
T_m	=	0.2051 m	∇_m	=	0.3562 m^3
I_{xx}/B_m	=	0.4	I_{zz}/L_m	=	0.25
R	=	0.0750 m	r_H	=	0.0126 m
$\mathbf{CG}_0$	=	(-0.0647 -0.0668 0) m	$\mathbf{x}_{p0}$	=	(2.139 -0.1273 0) m

TABLE 7.2: KCS meshes.

	Mesh size	BEMt mesh size	Cells in disk	Time spent on framework
Fine	17.7M	10x10x1	3500	2.4%
Medium	10.8M	10x10x1	2600	1.6%
Coarse	3.1M	10x10x1	400	1%

7.1 KCS in calm water

To provide an initial condition for the unsteady simulation and to assess the ability of the framework to find the self propulsion point in calm water without the need for an iterative process, the KCS in calm water is studied initially. Two speeds are studied corresponding to $Fn = 0.260$ and $Fn = 0.201$. To correspond to the two sets of available experimental data, the RPM is fixed to 840 at $Fn = 0.201$ while being free to change at $Fn = 0.26$.

7.1.1 Wave profiles

For $Fn = 0.26$, experimentally measured wave profiles are available for comparison. Figure 7.1 shows the wave pattern around the KCS at $Fn = 0.26$ compared with experimental data by Kim et al. (2001). The contours in the upper and lower part of Figure 7.1 are of identical range and spacing namely between $\zeta/Lpp = \pm 0.005$ with a spacing of 0.0005. Figure 7.2 shows a detail of the bow wave where the contours are drawn between $0 \leq \zeta/Lpp \leq 0.01$ with a spacing of 0.0005.

Figures 7.3 to 7.6 show the longitudinal wave profiles at the hull, at $z/Lpp = 0.0741$, $z/Lpp = 0.1509$ and $z/Lpp = 0.4224$ respectively. These are compared with experimentally measured profiles by Van et al. (1998) and Kim et al. (2001). Near the hull some very high frequency, low amplitude waves are present in the computational results. These are due to non physical noise generated by the method in areas of changing mesh density near the hull. For better readability of the contours, these have been filtered away from Figure 7.2 but can still be seen in Figure 7.3.

Overall, the wave pattern is well predicted. A discrepancy in terms of a phase shift and amplitude reduction is found far downstream of the hull. The predicted shape of the bow wave near the hull is also less accurate than the remaining near hull wave profile. These results indicate that the mesh and set up is suitable for capturing the flow around the KCS hull form in calm water with good accuracy. This is important for the confidence in subsequent results for which less detailed experimental data is available.

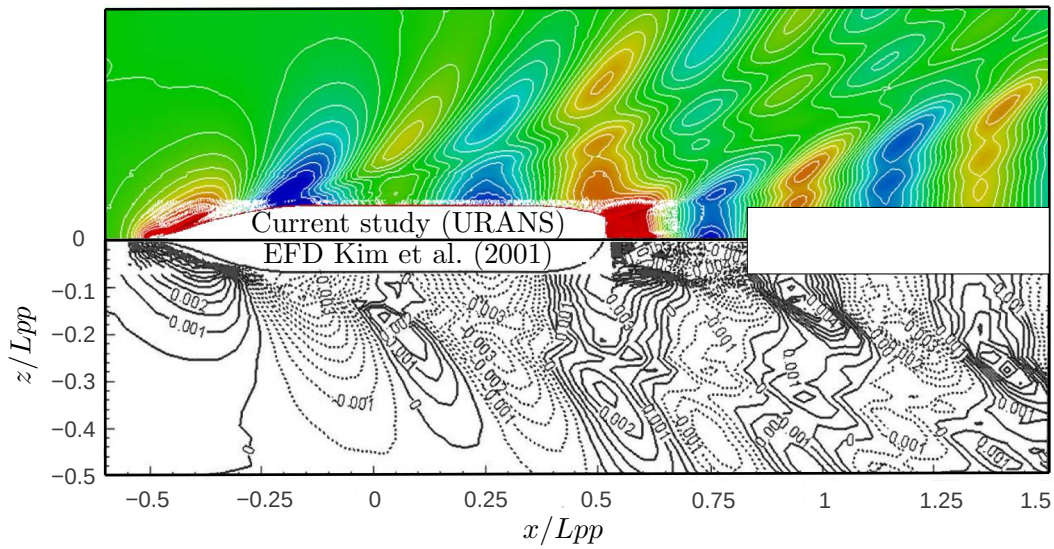

FIGURE 7.1: Contours of ζ/Lpp around the KCS at $Fn = 0.26$, computational (top) and experimental (bottom) results.

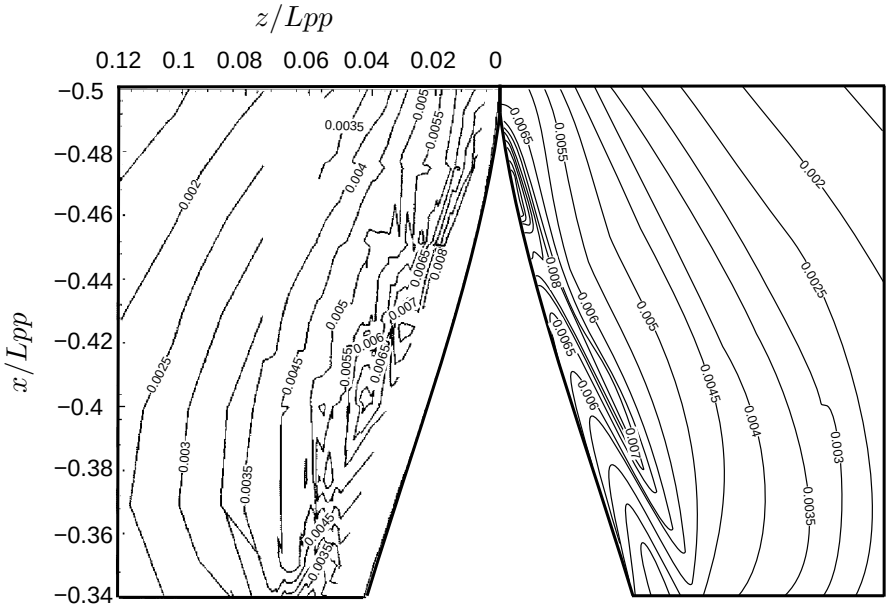

FIGURE 7.2: Detail of KCS bow wave contour at $Fn = 0.26$, computational results (right) and experimental results by Kim et al. (2001)(left.)

7.1.2 Propulsion data

The resistance and propulsion coefficients are presented here where the total resistance is normalised as $C_t = R/(0.5\rho U^2 0.1803 Lpp^2)$. For $Fn = 0.26$, experimental data is available for the bare hull resistance (Test case 2.2a of the Gothenburg 2010 workshop (Larsson et al., 2010).) This is presented in Table 7.3 for comparison with the accuracy in the later self propelled simulations.

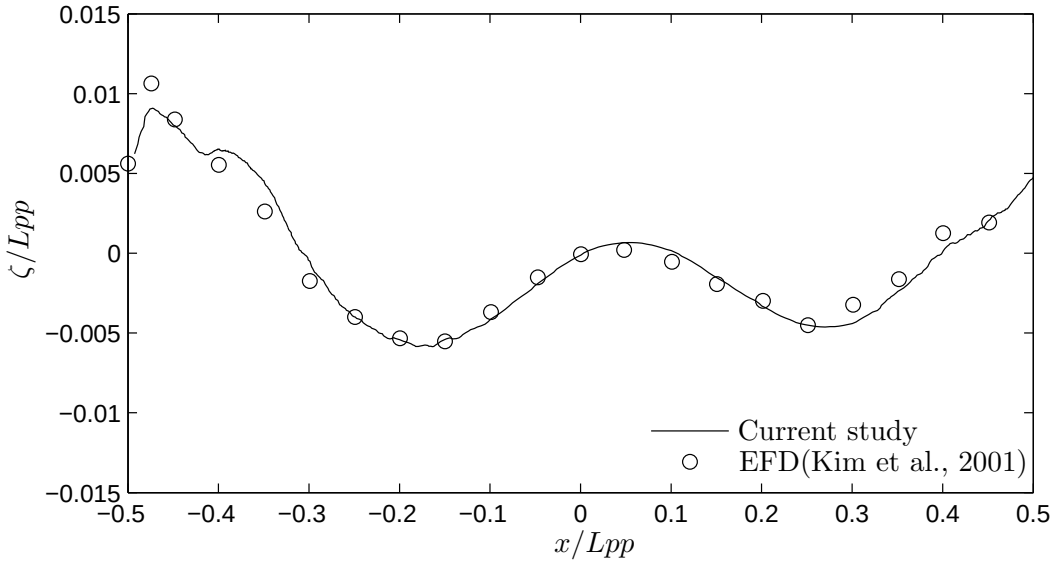

FIGURE 7.3: Calculated wave contour along the hull compared to experiments.

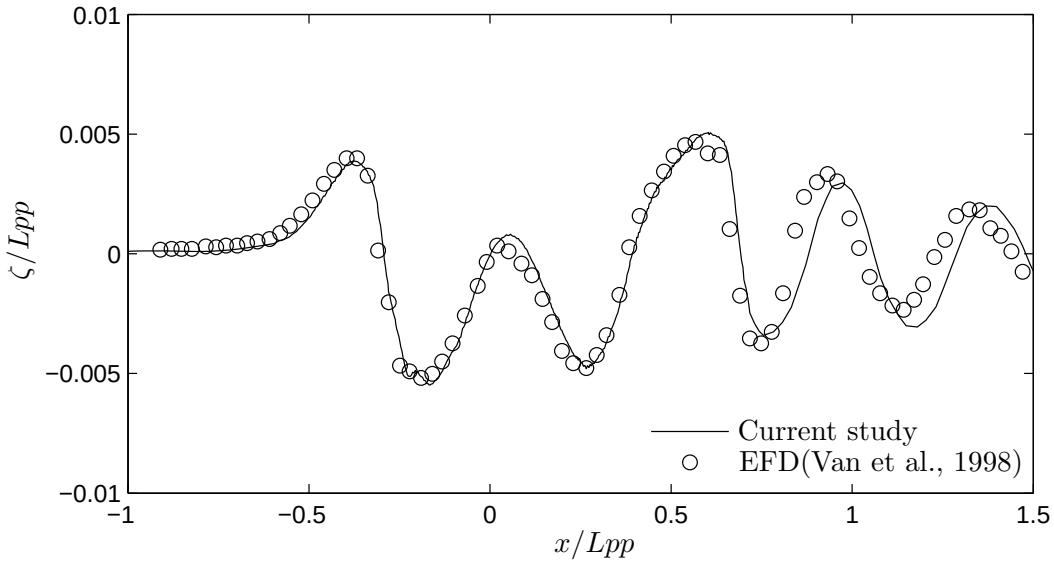

FIGURE 7.4: Calculated wave contour at $z/Lpp = 0.0741$ compared to experiments.

For $Fn = 0.26$, experimental data is also available for the self propelled KCS (Test case 2.3b of the Gothenburg 2010 workshop (Larsson et al., 2010).) Table 7.4 shows how the thrust, torque and propeller RPM compare to those obtained in the experiment. Table 7.4 also shows the thrust deduction factor t based on the calm water resistance in Table 7.3. However, since the experimentally measured bare hull resistance is based on a fixed model whereas the self propelled model was free to heave and pitch, no experimental value for t is provided here. Here, the *Self propulsion point finder* controller is used to find the point where $R = T$. This was done by using the PID controller and defining the error as $\varepsilon_c = R - T$. In these simulations, the model is fixed in heave and pitch.

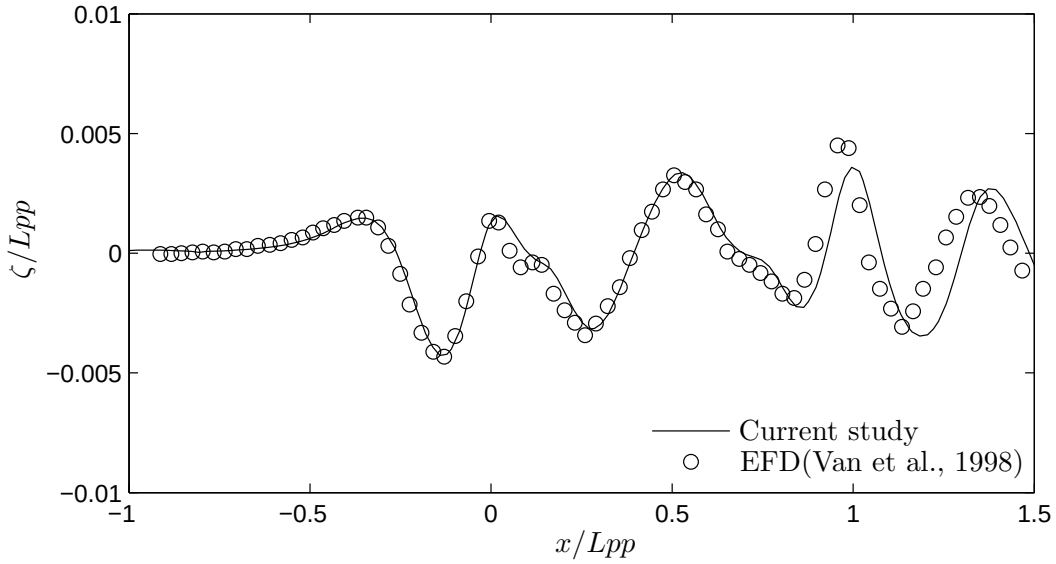

FIGURE 7.5: Calculated wave contour at $z/Lpp = 0.1509$ compared to experiments.

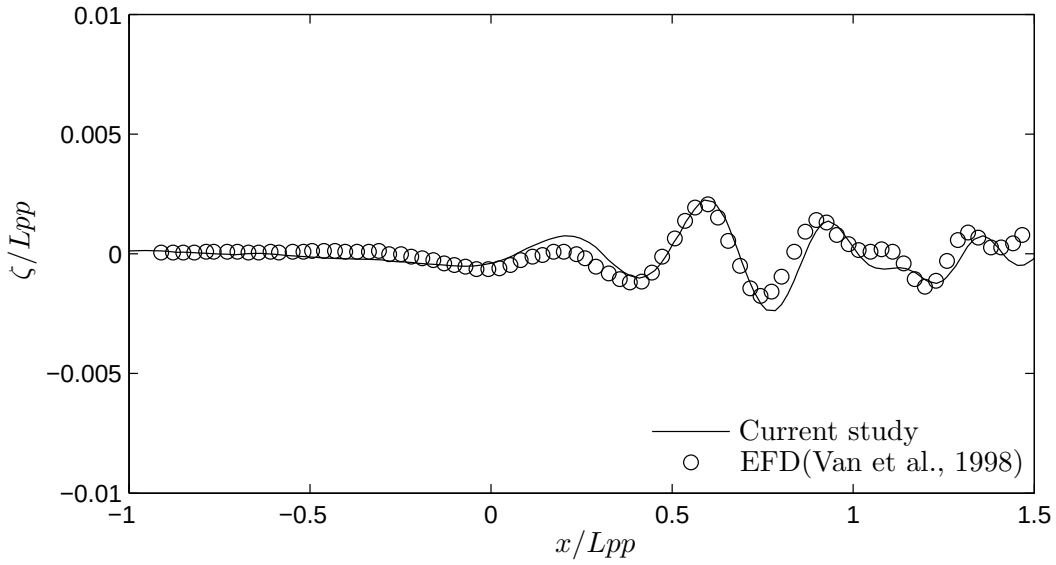

FIGURE 7.6: Calculated wave contour at $z/Lpp = 0.4224$ compared to experiments.

This differs from the experiment where a pitch of 0.143° and a sinkage of 0.00833 m was measured.

The results and the errors in Table 7.4 are comparable with others reported at the Gothenburg workshop. The large error on K_T however, is just above the upper range of the reported errors. It is important to point out that these results are obtained with a very fast propeller model without any particular treatment of the wake apart from what is handled automatically in run time by the framework. Furthermore, because the framework is designed to work with an arbitrary RANS mesh, no particular attention is given to fitting the mesh to the propeller region. These factors make this method a more

TABLE 7.3: Bare hull resistance of KCS at $Fn = 0.26$ compared to experimental data.

		EFD	Coarse	Medium	Fine
$1000C_t$	recorded	3.557	-	3.618	3.544
	error	-	-	1.715%	-0.365%

TABLE 7.4: Propulsion properties (at model self propulsion point) for KCS at $Fn = 0.26$ compared to experimental data.

		EFD	Coarse	Medium	Fine
$1000C_t$	recorded	5.222	-	4.885	4.8305
	error	-	-	-6.473%	-7.50%
K_T	recorded	0.2530	-	0.2170	0.2215
	error	-	-	-14.22%	-12.45%
K_Q	recorded	0.0408	-	0.0381	0.0381
	error	-	-	-6.62%	-6.62%
n	recorded	14.15	-	14.91	14.76
	error	-	-	5.418%	4.31%
t	recorded	-	-	0.263	0.278
	error	-	-	-	-

TABLE 7.5: Propulsion properties (at 840 RPM) for KCS at $Fn = 0.201$ compared to experimental data.

		EFD	Coarse	Medium	Fine
$1000C_t$	recorded	5.318	5.0898	5.154	5.563
	error	-	-4.296%	-3.083 %	4.608%
K_T	recorded	0.302	0.262	0.2808	0.281
	error	-	-13.245%	-7.020%	-6.954%
K_Q	recorded	0.0429	0.0425	0.460	0.0461
	error	-	-0.932%	7.226 %	7.459%

convenient approach to finding the self propulsion point than others that are currently available.

For $Fn = 0.201$, experimental data is available at the fixed RPM of 840 from the SIMMAN2014 workshop (FORCE, 2013). Table 7.5 shows how the thrust and torque compare to those obtained in the experiment. Here , the *Fixed RPM* controller is used. In this case, the model is fixed in heave and pitch in accordance with the experimental set up.

7.2 KCS in regular head waves

After a steady solution is found at $Fn = 0.26$ and at the RPM where self propulsion was found, the model is subjected to regular head waves of $\lambda/L_m = 0.85$ and $\zeta_0 = 0.015$ m. The RPM is kept fixed at the obtained calm water self propulsion RPM throughout

the unsteady analysis. The resulting wave pattern, taken at the time where a crest of the regular wave passes at the stern is shown in Figure 7.7.

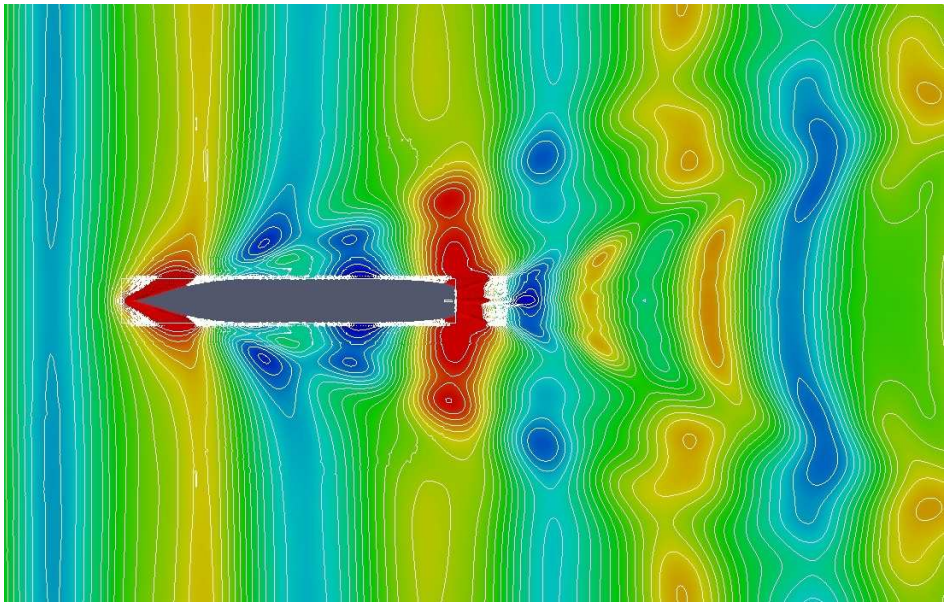

FIGURE 7.7: Wave pattern around KCS in regular head waves at time of wave crest passing at stern. Contour scale and increment is the same as in Figure 7.1.

7.2.1 Distribution of surge force variation on the hull

In this simulation the local distribution of the pressure and viscous force components are also recorded. By subtracting the distribution of forces in calm water, the areas where the viscous and pressure forces vary in waves can be identified.

Figures 7.8 and 7.9 show how the pressure and viscous components of the surge force vary in waves as compared to calm water. Here a relative difference is used to illustrate areas of the underwater hull where the force in waves differs more than 0.5% from the one in calm water. The calm water reference distributions of forces were taken with the propeller active and at the converged self propulsion RPM. The relative increase in force is calculated as

$$\Delta F_{px} = \frac{|F_{px\ waves} - F_{px\ calm}|}{F_{px\ calm}} \tag{7.1}$$

$$\Delta F_{\mu x} = \frac{|F_{\mu x\ waves} - F_{\mu x\ calm}|}{F_{\mu x\ calm}} \tag{7.2}$$

Furthermore, the average difference from calm water over one period of encounter in waves for both the pressure- and viscous surge forces is shown in Figure 7.10. Note that for the pressure force, variations from calm water aft of amidships contribute to

lowering the surge force while variations from calm water forward of amidships contribute to increasing the surge force. For the viscous component, all variations contribute to an increase in the surge force since the areas where the force is smaller than in calm water are very few.

Figures 7.8 and 7.9 also show the current wave elevation in black and white as well as the location and distribution of the applied volume force for reference.

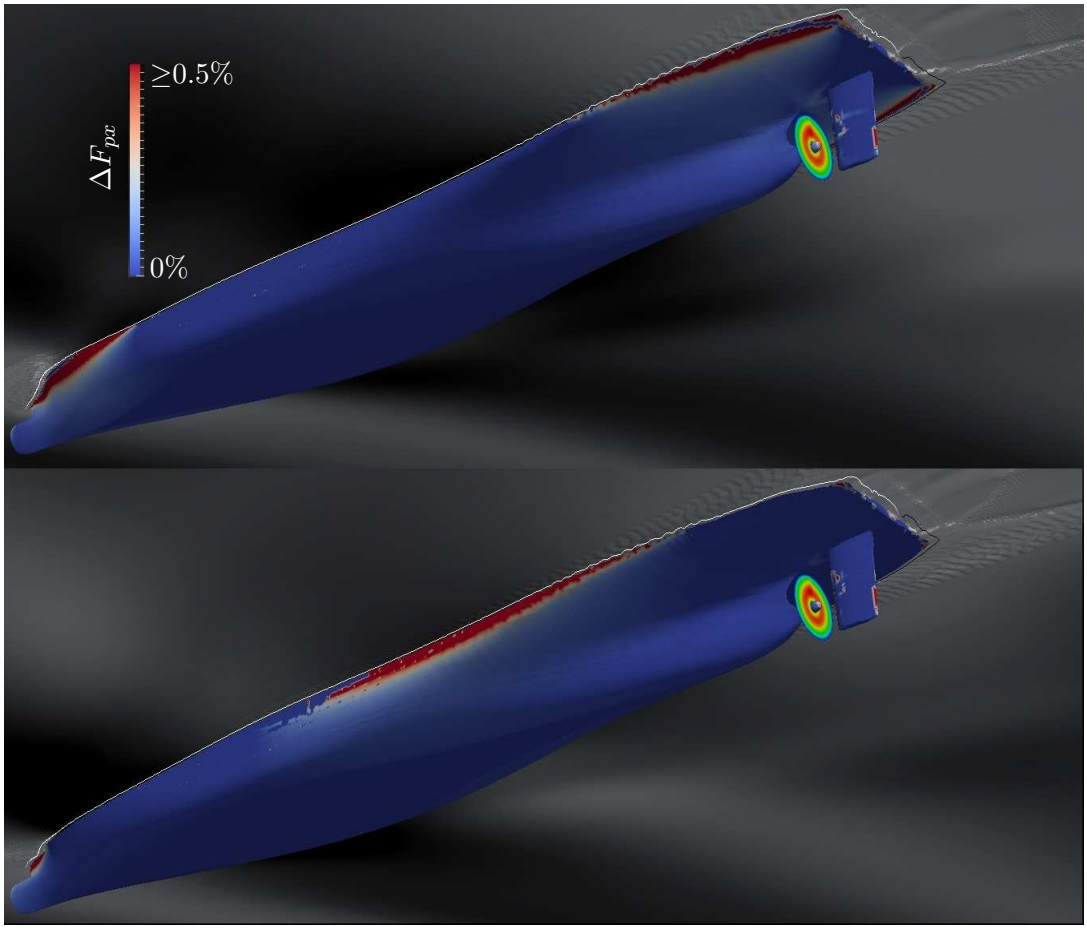

FIGURE 7.8: KCS underwater body, coloured by pressure surge force variation in waves compared to calm water at time of wave crest passing at stern (top) and wave trough passing at stern (bottom.)

The variation of the viscous surge force appears to stem from two sources. Firstly, a disturbance to the onset of the boundary layer near the bow water line and on the bulbous bow is generated by the oscillating bow wave. This disturbance travels downstream with a velocity somewhere between the freestream velocity and the wave celerity. Furthermore, the disturbance is pulsating with the wave frequency due to the orbital velocities of the passing waves. An animation showing this (of which Figure 7.9 represents two frames) has been published by Windén (2014). The variation of the pressure surge force follows the passing of the waves and decreases very rapidly with increasing depth.

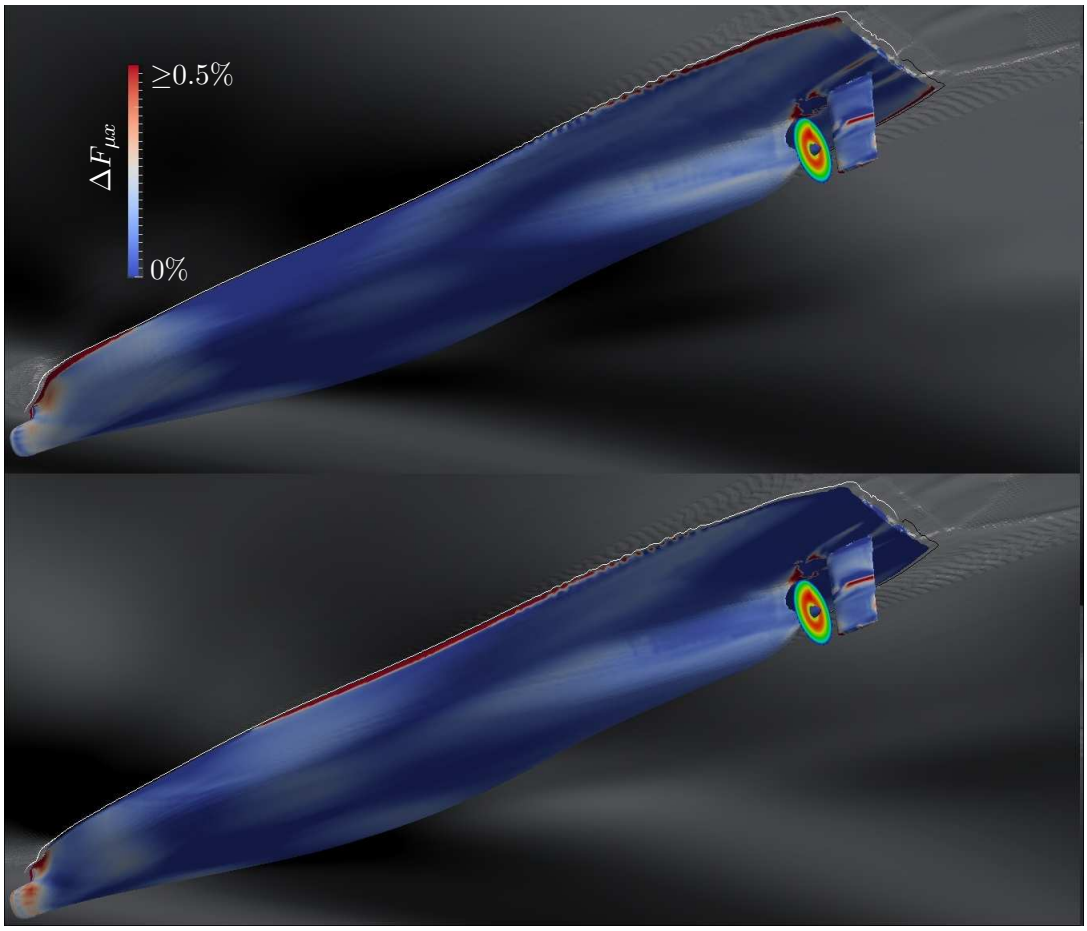

FIGURE 7.9: KCS underwater body, coloured by viscous surge force variation in waves compared to calm water at time of wave crest passing at stern (top) and wave trough passing at stern (bottom.)

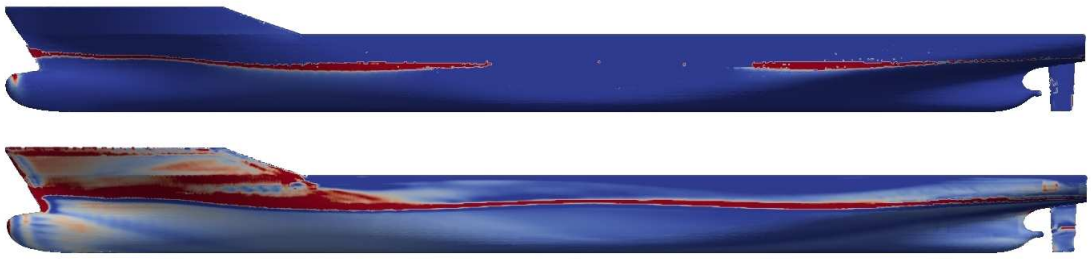

FIGURE 7.10: Average increase of pressure surge force (top) and viscous surge force (bottom) over one period of encounter. The colour scale is the same as in Figures 7.8 and 7.9.

The results for the pressure force are somewhat consistent with previous discussions in Section 2.6 about the local distribution of added resistance. There, it was argued that added resistance due to short waves stem from a pressure force increase along a narrow strip corresponding to the amplitude of the incoming wave. This is also true in this case even though the wave length is relatively long. Here, the pressure surge force only increases with more than 0.5% on average in a very narrow strip along the calm water wave profile. This is likely to be because the hull is fixed. This is also true in principle in short waves of small amplitude where motions are negligible. The viscous force increase is more spread out on the under water body due to the fact that the boundary layer is changed by the passing waves as was discussed in Section 4.7.

Even though the oscillations of the viscous force away from the free surface are small, they indicate that the boundary layer changes character slightly which has an impact on the flow into the propeller. It can be seen in Figure 7.9 that the disturbances travel all the way to the propeller plane. They also appear to increase in amplitude slightly near the stern before they reach the propeller.

7.2.2 Axial velocity variations in and around the propeller plane under waves

Figure 7.11 shows contours of axial velocity (as a fraction of U_∞) in three different planes, half a diameter upstream of the propeller plane, at the propeller plane and one diameter downstream of the propeller plane. Contours are drawn between 0 and 114% of U_∞ with an increment of 6%.

Consistent with previous findings, the thickness of the shear flow region oscillates somewhat in front of the propeller plane due to the waves. This, together with wave orbital velocities and general unsteadiness due to the waves leads to a slight oscillation on the inflow to the propeller. The rotation induced by the propeller also leads to a slight asymmetry of the axial flow in the propeller plane, however, this is not noticeable further upstream.

7.2.3 Variation of propulsion coefficients in waves

Due to the oscillating inflow shown in Figure 7.11, K_T, K_Q and the average advance ratio oscillate when the hull is subjected to waves. This, together with oscillations in the resistance leads to oscillating powering performance in the regular wave train. Figures 7.12 to 7.16 show the development of the relevant quantities. Here, the whole time series from propeller switch on, through the self propulsion point finding process in calm water as well as the regular wave train is shown. This illustrates the various abilities of the framework in a single time series.

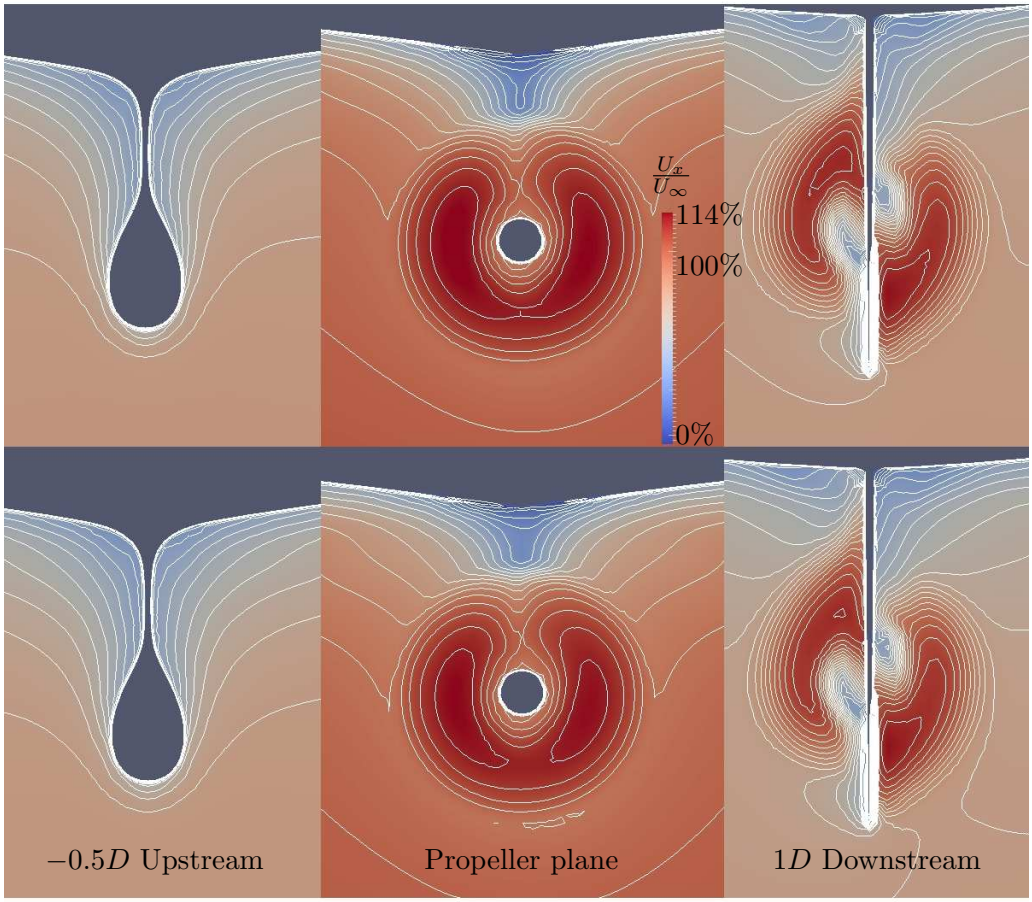

FIGURE 7.11: Contours of axial velocity at time of wave crest passing (top) and wave trough passing (bottom) at different longitudinal locations. Contours at every 6% of U_∞.

Figure 7.12 shows the development of the total surge force over time. Due to the use of URANS rather than steady RANS in the calm water simulations, an oscillating value of the calm water resistance is found. The obtained calm water resistance is taken as the mean value of this oscillation.

Figures 7.13 and 7.14 show the development of the propeller RPM and the resulting average advance coefficient respectively. Finally, Figures 7.15 and 7.16 show the development of K_T and K_Q throughout the simulation.

All coefficients experience a rapid initial variation due to the RPM changing and due to the flow at the stern reacting to the presence of the propeller. The variations are stabilised and steady values of J, K_T and K_Q are reached. After an unexplained initial reduction of the mean value after three encountered waves, the oscillation returns to a steady mean value after six encountered waves. The mean values of the oscillations in waves correspond roughly to the calm water equivalents. This can be related to previous discussions in Section 2.10 where it was suggested based on previous literature that the

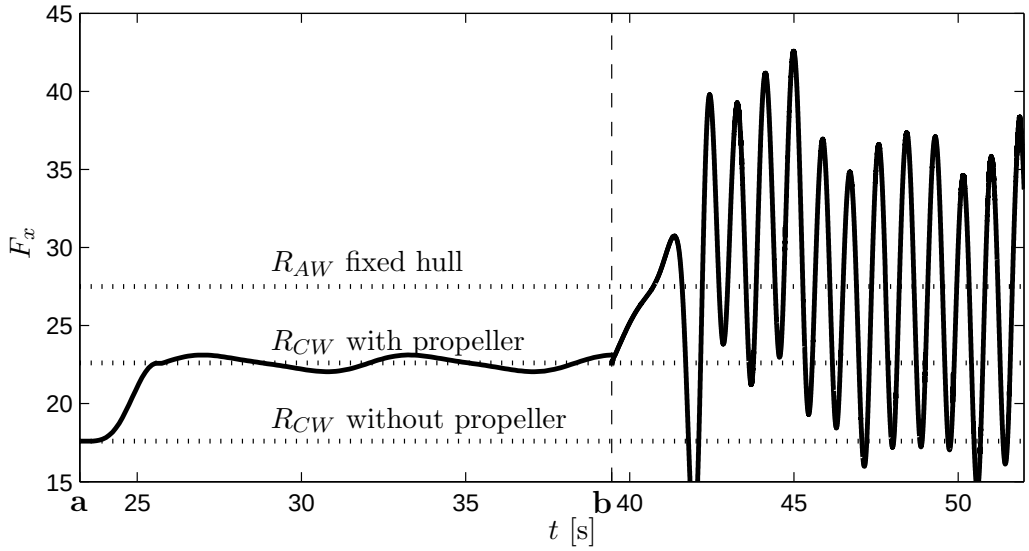

FIGURE 7.12: Development of surge force after propeller switch on (a) and after wave switch on (b).

open water coefficients remain at the same average value even under waves. This seems to hold true even in this case when the hull is present.

7.3 Conclusions

The described flow model is able to capture the steady flow around the KCS container ship with good accuracy. Wave profiles are consistent with experiments with a slight discrepancy far downstream. This gives confidence in the fact that the flow in the unsteady case is also modelled with good accuracy.

The steady self propulsion properties are also captured with reasonable accuracy with current international standards. The difference here is that self propulsion modelling is achieved with very little additional computational effort and with no special regard for the propeller in the generation of the mesh. This means that it can be conducted with not much extra effort compared to a bare hull simulation. Such simulations are commonplace in ship design. If self propulsion modelling can be achieved with the same amount of effort, it is encouraging for the introduction of more holistic methods as design tools. The fact that reasonable accuracy is found on the thrust and torque indicates that the RANS-BEMt coupling is able to separate the propeller induced velocities from the probed total wake at the propeller plane. Even though the unsteady simulations are not supported by experimental data, this gives confidence that the presented variations are close to reality.

In waves, it is shown how the propulsion coefficients, force- and velocity distributions vary due to the unsteady flow. Animated versions of the figures shown in this chapter

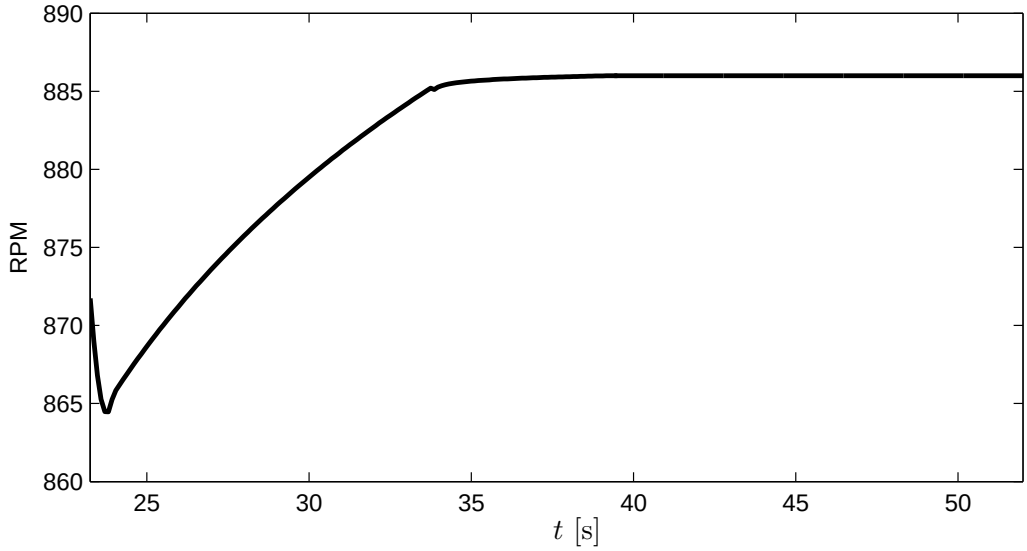

FIGURE 7.13: Development of propeller RPM after propeller switch on.

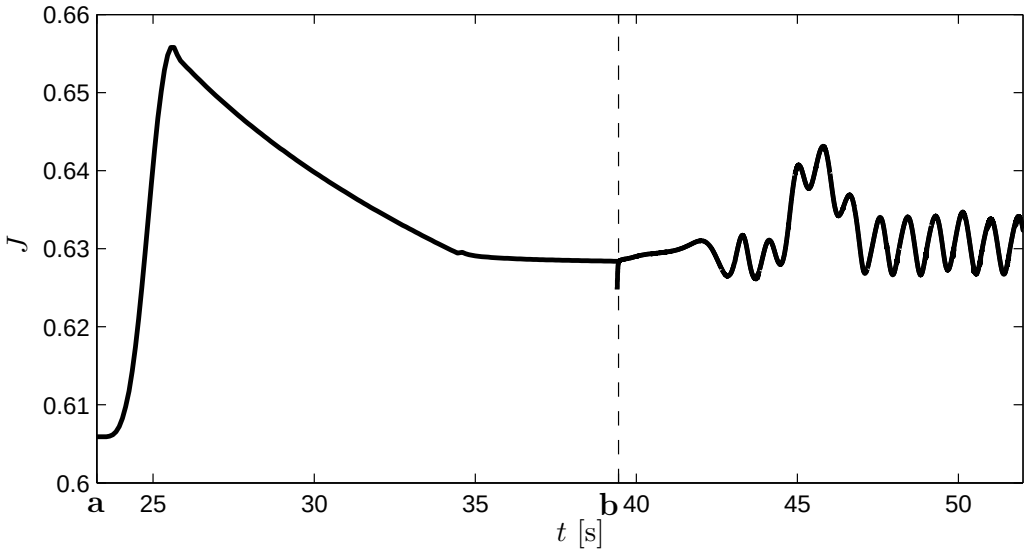

FIGURE 7.14: Development of average J after propeller switch on (a) and after wave switch on (b).

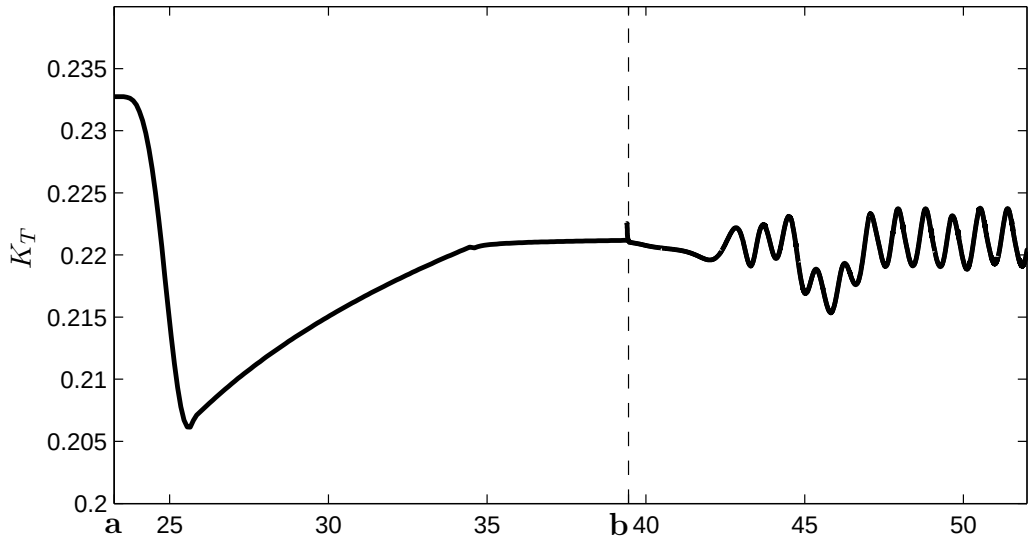

FIGURE 7.15: Development of K_T after propeller switch on (a) and after wave switch on (b).

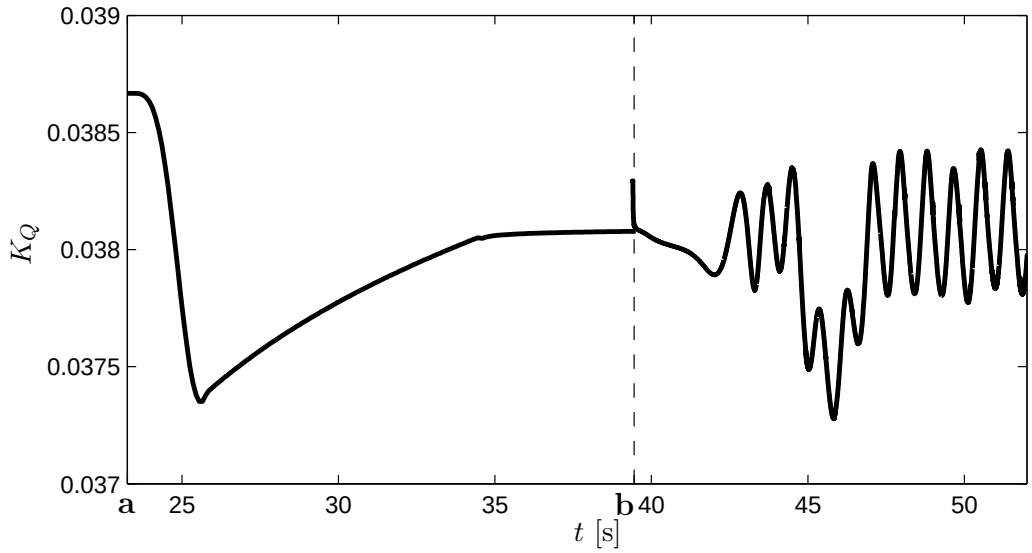

FIGURE 7.16: Development of K_Q after propeller switch on (a) and after wave switch on (b).

showing the variations of force- and velocity distributions are available through a publication by Windén (2014). The oscillations of the propulsion coefficients are of relatively small amplitude which is to be expected in small amplitude waves. The mean of the unsteady oscillations also roughly follows the calm water values of thrust, torque and the advance coefficient. These simulations serve to demonstrate the ability of the framework to facilitate studies on self propulsion in waves.

Chapter 8

Concluding remarks

Accurately predicting the powering performance of a ship when travelling in waves is of high importance to improve the design of new ships. Typically this is done with mean additions to the calm water resistance and open water curves for the propeller. This approach is flawed in that it fails to consider interactions between many phenomena such as between the boundary layer, the viscous wake, the propeller and the waves.

Chapter 1 of this thesis presents the engineering system that needs to be modelled for performance in waves of ships to be estimated in a more holistic way. This is separated into an external and an internal system. This thesis focuses on modelling the external system, i.e. the system that describes how the ship interacts with its surroundings. It is argued that, by separating this from internal factors such as the behaviour of the captain and the characteristics of the engine, all modelling can be conducted in the same scope namely the dynamics of the flow around the hull and the propeller. Factors such as weather, routes and the captains response to changes in these are seen as relatively slow varying compared to the instantaneous loading conditions due to wind and waves. The external system can therefore be modelled independently of such factors at fixed headings and at fixed sea states. However, the interaction between the internal system and the external system in terms of the propeller RPM is seen as a factor that is of a similar temporal scale. Therefore it should be included in the modelling of the external system.

Varying the propeller RPM to better match the unsteady inflow conditions in waves is a potentially novel way to improve performance in waves. It is not feasible to vary the RPM quickly enough on current marine diesels to match changes in the wake due to e.g. surge motions and wave orbital velocities. However, it remains to be investigated if the average performance in an irregular seaway can be improved by slowly varying the RPM. This approach is also of interest when considering a possible future expansion of electrical propulsion where much faster RPM changes will be possible. Furthermore, while this thesis mostly discusses large merchant ships, many of the methods discussed

are also applicable to smaller craft where more control over the RPM exists. Being able to accurately model the interaction of the ship, the propeller and their surroundings together with controlling the propeller RPM will allow for the feasibility of RPM varying systems to be investigated. Furthermore, modelling self propelled ships and being able to vary the RPM to find the self propulsion point is currently the state of the art of numerical predictions of ship propulsive performance. This is most commonly done in calm water conditions. Developments in modelling of the external system for a ship travelling in waves with the ability to vary the propeller RPM will therefore bring benefit to conventional performance predictions by improving their applicability to realistic sea states.

8.1 Choice of modelling technique

When considering the options for modelling the interaction between the ship and its surroundings, two main approaches exist. Experimental and numerical modelling. It is concluded that while both play a major role in the prediction of ship performance, numerical methods have more potential for improvement. Numerical models are also more efficient tools in the ship design process. Therefore, this thesis is mostly focused on developing a numerical method. However, experimental methods play a vital role in this task in order to validate new approaches and study physical phenomena. With this in mind one chapter of this thesis is dedicated to new experiments. These are aimed at highlighting shortcomings and strengths of current methods when it comes to predicting certain phenomena, especially regarding the surge force amplitude in waves. This information is used to improve how the numerical modelling is approached.

In Chapter 2 it is concluded that much understanding exists regarding how the mean surge force on the hull is affected by waves through almost a century of studies of added resistance in waves. However, the amplitude of the force variations has received less attention. This is relevant to this thesis since the amplitude of the surge force will influence the surge motion and thus the variations in the wake and in turn the performance of the propeller. The experimental study presented in Chapter 3 shows that the amplitude is not always strongly related to the mean increase and appears to be affected by more non linear effects. For example, while an increase in forward speed (at the same period of encounter) leads to a larger mean increase of the surge force, it also leads to a smaller amplitude. Furthermore, the amplitude does not show a quadratic increase with wave height which is the general trend and known relation for the mean force. From this it is concluded that representation of the surge motions is important in the numerical model. Currently this can be problematic due to the inability of common models to accurately represent the phase of the surge force variation. Finally, the experimental study hints towards viscous effects on for example heave damping influencing the validity of non viscous numerical methods for predicting the added resistance itself.

Overall, non viscous potential flow models commonly used today are concluded to be sufficient to compare the average added resistance of different hull shapes. However, to be able to model interaction between the waves, the hull and the propeller in one scope as mentioned before and thus provide a suitable design tool, a more advanced model is needed. Here a RANS based modelling technique is chosen.

8.2 Numerical model

The base set up of a numerical towing tank suitable for modelling a ship travelling in waves is presented in Chapter 4 and is implemented in the open source CFD package OpenFOAM. This is supported by a custom algorithm for generating a suitable mesh. Particular emphasis is put on the interaction between the waves and the boundary layer. The nature of this interaction is not well studied but the accurate prediction of the viscous flow will have a large impact on how well the stern flow and thus the propeller inflow is predicted. It will also affect the viscous forces, the accurate prediction of which is one of the arguments for using a RANS based model over a simplified potential flow model.

The effect of numerical convection schemes is studied and it is found that, by varying the convection scheme, the predicted phase of the viscous surge force on a flat plate can vary with up to 10°. Furthermore, the upwind convection scheme is found to be too dissipative to accurately represent the propagation of waves with the current set up. The effect of the convection scheme is also found to be stronger if the simulation time is shorter. If more energy is fed into the wave pattern over a longer period of time, even a more dissipative convection scheme can achieve more accurate representation of the wave amplitude.

When adding the capability to model the propeller in the numerical towing tank, an approach where the flow around the propeller and the flow around the hull are considered using separate models is favoured. By doing so, each model can be better tuned to the local flow conditions. Furthermore, geometrically modelling the propeller in the RANS solution requires a very high level of computational effort. However, to maintain the benefits of modelling the flow around the hull and the propeller together, a strong coupling between the two modelling approaches is needed.

Chapter 5 of this thesis presents a framework, implemented in OpenFOAM for coupling a RANS model for the flow around the hull with a body force model for the propeller. The framework is able to identify the location of the body force on a moving hull. It also provides run time mapping of field variables between the RANS model and an arbitrary propeller model. Templates are provided for the creation of new propeller models and RPM control schemes within the framework. To demonstrate how this can be used, a BEMt model is implemented in the framework. The BEMt is able to give

predictions of the thrust and torque distribution for a non uniform wake for a specific geometry. By implementing it together with the framework and run time probing of the total wake and separation of propeller induced velocities, this allows for prediction of unsteady propeller/hull/wave interaction. The shortcomings of the simplified propeller model are discussed and it is found that, when using the proposed model, the coupling between RANS and BEMt is not reliable because of an inability to correctly calculate the propeller induced velocities. These need to be deducted from the probed total wake. A correction is introduced to compensate for this inability. The correction is shown to be scalable for a large range of radii, inflow velocities and rotation speeds for the same propeller geometry. However, a new correction will be needed for each propeller geometry and indeed for each variation of the propeller model. Using the correction, the coupling is successful in separating the propeller induced velocities from the effective wake in open water. Furthermore, no relaxation is needed to the calculated wake even though there will be a large initial discrepancy in the coupling. The initial discrepancy is due to the fact the the RANS solution develops slowly due to inertia while the BEMt instantly yields the induced velocities for a converged flow field. With an initial drop, the predicted advance ratio will return to the open water value if the simulation is left for a sufficient amount of time.

The numerical towing tank with the BEMt implemented in the framework for propulsion modelling is used to verify if this approach is suitable to model the external system which is the goal set up for this thesis. Several control options for the RPM are discussed in Chapter 6. Here, the influence of the initial conditions and the allowed rate of change of RPM are discussed for a free to surge hull. It is found that in order to achieve a more efficient simulation, the propeller RPM could be initiated as the one that will overcome the added resistance in waves. When free to surge, this prevents the hull from experiencing a static displacement in surge due to the waves before the thrust can compensate for the increased resistance. Furthermore, the RPM rate of change required to overcome periodic variations in surge far exceeds what is possible in reality. However, different constraints on the allowed rate of change lead to differences in the delivered power and the speed loss.

Finally, the results obtained from the combined methodology described in this thesis applied to the KCS container ship are presented in Chapter 7. Here, the flow solver is shown to give satisfactory results for the calm water wave pattern. Furthermore, the framework, with the described RANS-BEMt coupling is able to predict the self propulsion RPM with reasonable accuracy compared to experiments. Reasonable accuracy compared to experiments is also found for the propulsion coefficients at a fixed RPM. When the hull is subjected to waves, the unsteady wake generates oscillations of the propulsion coefficients around a mean value which is very close to the steady value in calm water. These results demonstrate the ability of the framework to model self propulsion in waves with little additional effort compared to conventional simulations of the

bare hull.

8.3 Final conclusions

The final conclusions of this thesis are listed below.

- When predicting the performance of a ship in waves from a hydrodynamic point of view, many factors such as course and weather, which are slow varying can be considered as fixed. The propeller RPM is more strongly linked to the instantaneous flow variations and, even though it is traditionally varied slowly due to restrictions of the engine, the control system for the RPM should be considered together with the hydrodynamic model. This allows for numerical studies on how varying the RPM can affect performance in waves by giving a more favourable loading on the propeller in unsteady conditions.

- To be able to truly assess the performance in waves of a ship when considering both resistance and propulsion, a holistic approach is needed. For quickly estimating the average resistance increase, a century of research has provided very fast and reliable methods as is shown in Chapter 2. These have been the workhorses of the industry for estimating performance in waves. Unfortunately, the deficiencies of the basic potential flow based methods, which take a more holistic view have lead to an increasingly piecemeal approach where accurate modelling of separate phenomena is sought. Ultimately, the only way to encourage the use of a more holistic approach as the workhorse for performance prediction is to establish more confidence in NS based methods.

- Chapter 3 shows that the amplitude of the surge force does not follow the same well established patterns as the mean surge force (added resistance) in waves. The amplitude seems to be more influenced by non linear phenomena and is thus harder to predict with simpler methods. The amplitude of the surge force influences the surge motion and thus the unsteady inflow to the propeller.

- The chosen convection scheme has a significant impact on both the phase of the viscous forces on a surface piercing object and the amplitude of the propagating waves which is demonstrated in Chapter 4. This leads to the conclusion that better attention to how the boundary layer is predicted around surface piercing objects may give improvements for RANS based modelling of ships in waves. This is true both because of the predicted forces and because of the predicted inflow to the propeller which depends strongly on predicting the viscous flow regime with sufficient accuracy.

- For propeller modelling, a separate model to the main RANS solver is favoured to be able to better tune it to the local flow conditions while keeping the RANS solver tuned to best predict the flow around the hull. A body force approach is chosen here where the body force is calculated by means of Blade Element Momentum theory. Chapter 5 of this thesis presents an open source framework for coupling the RANS solver with any body force based model. The framework provides automatic calculation of the extent and position of the propeller disk behind a ship moving in waves. It also provides automatic mapping of field variables between the RANS and the propeller domain.

- This framework makes it simple to test new propeller models which will aid in the development of self propelled simulations in waves. It does so by facilitating a wider range of present and future studies on self propulsion in waves by allowing for easy modification of both the overall modelling and control schemes and the specific parameters therein.

- Chapter 5 also demonstrates that it is possible to achieve a satisfactory coupling procedure between the RANS solver and the BEMt if the propeller induced velocities are corrected for discrepancies between the BEMt assumptions and the RANS assumptions. This correction is shown to yield a coupling which is able to separate the propeller induced velocities from the total wake in open water.

- The coupled RANS BEMt solver is also able to predict hull-propeller interaction with reasonable accuracy compared to experiments. This indicates that the coupling is able to separate the propeller induced velocities from the total wake behind the hull.

- The coupled RANS BEMt solver is able to represent fluctuations in thrust and torque due to an unsteady wake as shown in Chapter 7. It is thus suitable for studying the interplay of the ship and its propeller in waves. This allows for numerical studies regarding the influence of RPM control schemes.

- The methods developed and conclusions drawn in this thesis are of benefit for further development of self propelled simulations of ships in waves. The results also give indications on how accuracy can be improved in several areas. In doing so this thesis represents a contribution towards better tools for predicting ship performance in realistic sea states. With ever stricter requirements on environmental performance of ships, there will be more demand for such tools. More importantly, more demand will be put on their accuracy.

8.4 Future work

Suggestions for future studies that can build from or improve on this one are listed below.

- The simulations in this thesis have been run with fine meshes to ensure accurate representation of the flow. However, no systematic study on grid independence has been conducted. Confidence is instead based on benchmark values of individual mesh parameters such as y_1^+ and the number of cells per wave length and -height. To establish better confidence in the results a more systematic grid independence study should be conducted.
- Even though the presented inflow correction produces satisfactory results it is not fully reliable when the wake is non uniform. Furthermore, a new correction has to be found for every geometry. Developing improvements in the BEMt to better calculate the expected induced velocities in the RANS domain would render the correction unnecessary and improve the reliability of the coupling. Suggested studies include how the Goldstein correction can be improved to work better in a coupled solver as well as with an unsteady inflow. Alternatively, the correction could be extended to determine if a general correction valid for a wider range of propeller geometries can be found.
- This thesis has presented a framework for self propulsion. This allows for future studies on how the propeller model can be modified to achieve better results. The real time mapping of field variables allows for studies on how propeller models can be made to take advantage of this by e.g. including the inbound turbulence kinetic energy in the calculations. It also allows for more comprehensive and focused verification studies regarding the propeller model discretisation itself. This therefore fulfils the aim of facilitating a broader range of future studies on the subject.

Appendix A

Example code

```
// ——————————————————————————————//
if(explicitRPM)
{
    // The controller has noticed that the model has calculated an explicit RPM.
    newRPM = explicitRPMvalue;
}
else
{
    //A controlling function (PID) is needed to calculate new RPM.
    //the target Torque setTorque is read from a dictionary.
    newRPM = RPM + pControlFcn→control(setTorque-Torque,deltaT);
}
// Apply RPM limiters (also updates RPM in controller.)
propellerControl::limitRPM(newRPM,deltaT);
// Invoke selected propeller model to calculate body force.
propellerControl::actOnFluid(mesh,runTime,volumeForce,active);
// ——————————————————————————————//
```

FIGURE A.1: Example propeller controller attempting to keep a fixed torque.

```
// ------------------------------------------------------------//
//Update Concentric Mesh position and orientation and probe inflow.
Cmesh_.update();
//Invoke chosen formulation for calculating KT and KQ distribution on conc. mesh
#include "my_Thrust_Torque_Equations.H"
//Calculate derivatives for mapped fields
if(mO>1){KT_.derivatives();KQ_.derivatives();}
//Loop over all cells to mark which are inside propeller region
forAll(mesh.C(),celli)
{
    //Length of projected vector from origin to current point onto prop. plane (|R_I|)
    dr = mag(pC_.cellRadius(celli));
    //Distance from prop centre to cell centre along prop axis (|d_I|)
    dps = mag(pC_.cellOffset(celli));
    //If point is not outside thickness and within the correct radius, assign body force
    if(dps<=thickness_/2 && dr>=hubRadius_ && dr<=radius_)
    {
        cellsinside.append(celli); //Save cell
        theta = pC_.cellAngle(celli); //Angle of cell
        //Interpolation (order=mO) of KT and KQ distribution on concentric mesh
        //to thrust and torque distribution on RANS mesh
        axF.append(KT_.interpolate(dr,theta,dps,mO)*rho*pow(RPM/60,2)
        *pow(2*radius_,4)/dr);
        tanF.append(KQ_.interpolate(dr,theta,dps,mO)*rho*pow(RPM/60,2)
          *pow(2*radius_,5)/pow(dr,2));
        //Sum up total force to be able to correct later. Also include cell volume
        totAxF += axF[ninside]*mesh.V()[celli];
        totTanF += tanF[ninside]*mesh.V()[celli]*dr;
    }
}
//Assign body force to active cells
forAll(cellsinside,cellI)
{
    //Find tangential direction
    tanDirM = -pC_.diskOrientation()^(pC_.cellRadius(mesh.C()[cellsinside[cellI]]));
    tanDirM = tanDirM/mag(tanDirM);
    //Assign body force, correct with total values of thrust and torque
    (*volumeForce)[cellsinside[cellI]] =
        -pC_.diskOrientation()*Thrust*axF[cellI]/totAxF
        +tanDirM*Torque*tanF[cellI]/totTanF;
}
//Updtate propeller controller with current state.
if(updateStat){ pC_.updateStatus(Thrust,Torque,RPM,avgJ,false);}
// ------------------------------------------------------------//
```

FIGURE A.2: Example propeller model using concentric mesh.

```
/*--------------------------------*- C++ -*----------------------------------*\
| =====                 |                                                   |
| \\      /  F ield     | OpenFOAM: The Open Source CFD Toolbox             |
|  \\    /   O peration | Version:  2.0.0                                   |
|   \\  /    A nd       | Web:      www.OpenFOAM.com                        |
|    \\/     M anipulation |                                                 |
\*---------------------------------------------------------------------------*/
FoamFile
{
    version     2.0;
    format      ascii;
    class       dictionary;
    location    "system";
    object      propellerDict;
}
// * * * * * * * * * * * * * * * * * * * * * * * * * * * * * * * * * * * * \\
//////////////////////
//Limiters and controls
applyRPMincreaseLimiter true;
RPMincreaseLimitValue 10;
applyMaxRPM true;
maxRPM 1000;

//Force simulation to start from startRPM rather than from previous time step value
//at restart
forceStartRPM false;
startRPM 840;
allowExplicitRPM false;
U0 1.318;

g (0 -9.81 0);

//Density of fluid that propeller is working in
rhoProp 1000;

//Propeller shaft orientation in initial state.
//Will determine direction of propeller force on the hull.
propShaftOrientation (-1 0 0);

//Centre of propeller, used to define propeller location in initial state.
propOrigin (2.139 -0.1273 0);

//Propeller options
propellerModel BEMt;
propellerControl fixedRPM;
```

```
//Model-specific properties
BEMtCoeffs
{
    radius 0.0750;
    hubRadius 0.0126;
    thickness 0.015;

    //Number of sectors in BEMt code
    nSectors 10;
    nRad 9;

    mapOrder 2;

    //Number of reference values given
    nRefRads 8;

    //Radii for reference values (r/R)
    rR (0.168 0.3 0.4 0.5 0.6 0.7 0.8 0.9);
    //Pitch Distribution along blade length relative to pitch distribution at R=0.7
    PA (0.888 1.008 1.055 1.060 1.039 1.000 0.948 0.888);
    // Chord distribution along blade
    C2 (0.208 0.241 0.263 0.276 0.279 0.269 0.241 0.184);
    correctTanWake false;
    P_D 1;
    BARatio 0.7;
    NosBlades 5;
    rho 1000;
}

//Control-specific properties
fixedRPMCoeffs
{

    RPM 840;

    controlFunction "PIDController";
    PIDControllerCoeffs
    {
        Tolerance 1e-6;
        Kp 1.2;
        Ki 0.5;
        Kd 0;
    }
}
```

```
//Probe-specific properties
probeCoeffs
{

    maxIterations 10000;

    probedCONCMeshFields
    {
        Ulocal
        {
            interpolationVariable
            {
                U cellPoint;
            }
            location centrePlane;
            offset 0;
        }
    }
}



// ************************************************************************//
```

FIGURE A.3: Example of input parameters to framework (propellerDict.)

```
/*--------------------------------*- C++ -*----------------------------------*\
| =====                 |                                                   |
| \\      /  F ield     | OpenFOAM: The Open Source CFD Toolbox             |
|  \\    /   O peration | Version:  2.0.0                                   |
|   \\  /    A nd       | Web:      www.OpenFOAM.com                        |
|    \\/     M anipulation |                                                 |
\*---------------------------------------------------------------------------*/
FoamFile
{
    version     2.0;
    format      ascii;
    class       dictionary;
    location    "system";
    object      hullDict;
}
// * * * * * * * * * * * * * * * * * * * * * * * * * * * * * * * * * * * * \\

// Name of patch containing main hull
hullPatchName "hull_patch0";

// Patches of any appendages
appendageNames ("rudder_patch0");

// Density name
rhoName "rho";

// Reference density for force calculations
rhoInf 1000;

//Hull centre of rotation (in initial state)
hullCofR ( -0.0647 -0.0668 0 );

//Hull centre of mass (in initial state)
centreOfMass ( -0.0647 -0.0668 0 );

//Moment of inertia of entire hull
momentOfInertia (10 10 424.5807);

// Mass of entire hull
hullMass 356.2;

//Name of mesh region containing hull (region0 if only one region is present)
hullRegionName "region0";

//Report status of motion
report on;
```

```
////////////////////
//DOFs
////////////////////

//Defines which direction is positive forward speed
surgeDirection (-1 0 0);

//Defines which direction is positive heave
heaveDirection (0 1 0);

//Reference "0" time for PMM oscillations
refTime 0;

DOFs
{
    surge
    {
        type "locked";
        persistency "hard";
    }
    sway
    {
        type "PMM";
        persistency "hard";
        amplitude 0.392;
        frequency 0.4712;
    }
    heave
    {
        type "free";
        persistency "hard";
    }
    yaw
    {
        type "locked";
        persistency "hard";
    }
    pitch
    {
        type "free";
        persistency "hard";
    }
    roll
    {
        type "locked";
        persistency "hard";
    }
}

// ************************************************************* //
```

FIGURE A.4: Example of input parameters to framework (hullDict.)

Appendix B

RANS modelling

This section is meant to give an overview of the overall methods used for flow modelling, the combination of which is referred to in the main thesis as RANS modelling.

The equations of motion for a viscous fluid were introduced by Navier (1823) and Poisson (1831) and correctly derived by Saint-Venant (1843) and Stokes (1845). They have consequently come to be called the Navier-Stokes equations.

$$\frac{\partial u_i}{\partial t} + \frac{\partial u_i u_j}{\partial x_j} = -\frac{1}{\rho}\frac{\partial p}{\partial x_i} + \nu\left(\frac{\partial^2 u_i}{\partial x_j \partial x_j}\right) \tag{B.1}$$

where i and j represent the spatial dimensions 1, 2 and 3. Together with the continuity equation

$$\frac{\partial u_i}{\partial x_i} = 0 \tag{B.2}$$

these equations can be applied to model the pressure and velocity fields of viscous fluids.

B.1 Turbulence modelling

The benefit of solving the full Navier-Stokes equations is the inclusion of viscosity. This introduces damping through viscous stresses stemming from the fluid velocity. However, solving the full Navier-Stokes equations with the presence of turbulence requires the grid to be designed for coping with very large as well as very small eddies (see Section B.2.) Solving the Navier-Stokes equations without somehow simplifying the way turbulence is dealt with is known as Direct Numerical Simulation (DNS) and requires immense computational effort.

Since this is not practical in most cases, it is convenient to approximate the turbulent variations in the flow as disturbances around a mean value, for example

$$u_i = \overline{u_i} + u_i' \tag{B.3}$$

$$p = \overline{p} + p' \tag{B.4}$$

This is known as Reynolds decomposition. Inserting Eqns. B.3 and B.4 into Eqn. B.1 will yield different properties depending on how the average and fluctuating quantities are treated. The approach to doing this depends on what level of turbulence needs to be modelled. Popular choices include filtering to include only larger scale eddies known as Large Eddy Simulation (LES.) In LES, a sub-grid model is needed to resolve energy contained in flow features below the resolved scale, this means more computational effort is needed.

An alternative is to define the averaging operator as an ensemble average (over all statistically defined turbulent fluctuations.) This assumes statistically steady turbulence and provides a series of key simplifications due to the nature of the averaging operator. Using the ensemble average and inserting Eqns. B.3 and B.4 into Eqn. B.1 yields the Reynolds-Averaged Navier-Stokes (RANS) equations.

$$\frac{\partial \overline{u_i}}{\partial t} + \overline{u_j}\frac{\partial \overline{u_i}}{\partial x_j} = -\frac{1}{\rho}\frac{\partial \overline{p}}{\partial x_i} + \nu\left(\frac{\partial^2 \overline{u_i}}{\partial x_j \partial x_j}\right) - \overline{u_i' u_j'} \tag{B.5}$$

This is very similar to Eqn. B.1 but now relates to the mean flow. The stresses introduced by the turbulent fluctuations are represented by the non linear term $\overline{u_i' u_j'}$. These stresses are know as Reynolds stresses and a common terminology is to say that $\tau_{ij} = \overline{u_i' u_j'}$. Using this substitution together with the averaged continuity equation

$$\frac{\partial \overline{u_i}}{\partial t} + \overline{u_j}\frac{\partial \overline{u_i}}{\partial x_j} = -\frac{1}{\rho}\frac{\partial \overline{p}}{\partial x_i} + \nu\left(\frac{\partial^2 \overline{u_i}}{\partial x_j \partial x_j}\right) - \tau_{ij} \tag{B.6}$$

$$\frac{\partial \overline{u_i}}{\partial x_i} = 0 \tag{B.7}$$

to model turbulent viscous flows is referred to as RANS modelling. With this formulation, the stresses stemming from all the averaged components are combined into one *Reynolds stress* τ_{ij} representing the effects of the turbulent variations. A hybrid approach combining the strengths of LES and RANS modelling is known as Detached Eddy Simulation (DES) (Spalart et al., 1997). In a DES model, the formulation is switched between a LES and RANS type depending on the fineness of the grid. This saves computational effort by using a RANS formulation in areas not experiencing high

levels of separation and LES to resolve the separated eddies. However, a RANS-only formulation is still the one that is the most computationally efficient for moderately separated flows.

To close the RANS equations, a model for the Reynolds stress is required. This can be achieved by relating it to the mean flow via an artificial eddy viscosity ν_T acting on the average velocity variation as well as the kinetic energy k of the turbulent variations. This is known as the Boussinesq hypothesis (Boussinesq, 1877).

$$\tau_{ij} = \nu_T \left(\frac{\partial \overline{u_i}}{\partial x_j} + \frac{\partial \overline{u_j}}{\partial x_i} \right) - \frac{2}{3} \delta_{ij} k \tag{B.8}$$

The local eddy viscosity is related to the local velocity- and lengthscales characterising the turbulence. The velocity scale is related to the turbulence kinetic energy whereas the lengthscale is usually related to the dissipation rate of kinetic energy. The RANS equations can thus be closed by adding transport equations for the intensity and dissipation rate of turbulence kinetic energy. Usually it is preferred to add equations for both the kinetic energy and the rate of dissipation. Such a model is referred to as a two equation model and the most common ones are the k-ε and k-ω models.

For ship hydrodynamics problems, the k-ε turbulence model (Launder and Sharma, 1974) was shown early on to give good predictions of the behaviour of the viscous wake and the transport of turbulent kinetic energy within it. However the k-ε model experiences stability problems when integrating the equations through the viscous sublayer leading to stiffness issues (Menter, 1993, 1994). This means that it does not model the turbulence in the near-wall boundary layer correctly leading to poor separation prediction. These stability issues have been addressed with the k-ω model (Wilcox, 1988) which takes the near wall grid spacing into account. This model is significantly better at predicting the near field turbulence and separation. Ship hydrodynamics problems require accurate calculation of both the boundary layer behaviour, separation as well as the far field turbulent energy transport. A mix of these two models is therefore needed. This is achieved with the k-ω SST model (Menter, 1994) which uses a blending function to switch between a k-ω and a k-ε formulation based on the wall distance. For the purposes of modelling ships in waves, this is the most suitable approach. The k-ω SST model was updated by Menter et al. (2003). According to Menter et al. (2003), the eddy viscosity is defined as

$$\nu_T = \frac{a_{k\omega} k}{max[a_{k\omega}\omega \ , \ SF_2]} \tag{B.9}$$

with

$$S = \sqrt{2 S_{ij} S_{ij}} \tag{B.10}$$

$$S_{ij} = \frac{1}{2} \left(\frac{\partial u_i}{\partial x_j} + \frac{\partial u_j}{\partial x_i} \right) \tag{B.11}$$

Two transport equations are added for the kinetic energy k and the specific dissipation ω as

$$\frac{\partial k}{\partial t} + \frac{\partial u_j k}{\partial x_j} = P_k - \beta^* k\omega + \frac{\partial}{\partial x_j}\left((\nu + \sigma_k \nu_T)\frac{\partial k}{\partial xj}\right) \tag{B.12}$$

$$\frac{\partial \omega}{\partial t} + \frac{\partial u_j \omega}{\partial x_j} = \frac{\gamma}{\nu_T} P_k - \beta\omega^2 + \frac{\partial}{\partial x_j}\left((\nu + \sigma_\omega \nu_T)\frac{\partial \omega}{\partial xj}\right) + 2(1 - F_{k\omega 1})\sigma_{\omega 2}\frac{1}{\omega}\frac{\partial k}{\partial x_i}\frac{\partial \omega}{\partial x_i} \tag{B.13}$$

Unless given a number in Eqn. B.12 and Eqn. B.13, the constants are blended using the blending function $F_{k\omega 1}$ as

$$\gamma = F_{k\omega 1}\gamma_{k\omega 1} + (1 - F_{k\omega 1})\gamma_{k\omega 2} \tag{B.14}$$

$$\beta = F_{k\omega 1}\beta_{k\omega 1} + (1 - F_{k\omega 1})\beta_{k\omega 2} \tag{B.15}$$

$$\sigma_k = F_{k\omega 1}\sigma_{k\omega 1} + (1 - F_{k\omega 1})\sigma_{k\omega 2} \tag{B.16}$$

$$\sigma_\omega = F_{k\omega 1}\sigma_{\omega 1} + (1 - F_{k\omega 1})\sigma_{\omega 2} \tag{B.17}$$

The blending functions $F_{k\omega 1}$ and $F_{k\omega 2}$ are defined based on the wall distance y as

$$F_{k\omega 1} = tanh\left\{\left(min\left[max\left\{\frac{\sqrt{k}}{\beta^*\omega y}\ ,\ \frac{500\nu}{y^2\omega}\right\}\ ,\ \frac{4\sigma_{\omega 2}k}{CD_{k\omega}y^2}\right]\right)^4\right\} \tag{B.18}$$

$$F_{k\omega 2} = tanh\left\{\left(max\left[\frac{2\sqrt{k}}{\beta^*\omega y}\ ,\ \frac{500\nu}{y^2\omega}\right]\right)^2\right\} \tag{B.19}$$

with

$$CD_{k\omega} = max\left[2\rho\sigma_{\omega 2}\frac{1}{\omega}\frac{\partial k}{\partial x_i}\frac{\partial \omega}{\partial x_i}\ ,\ 10^{-10}\right] \tag{B.20}$$

and P_k is defined as

$$P_k = min\left[\tau_{ij}\frac{\partial u_i}{x_j}\ ,\ 10\beta^* k\omega\right] \tag{B.21}$$

The constants vary slightly depending on the implementation but the ones used in OpenFOAM v1.7.1 which are very close to the ones provided by Menter et al. (2003) are defined in Table B.1.

TABLE B.1: Coefficients in the k-ω SST turbulence model.

$\gamma_{k\omega 1} = 0.5532$	$\gamma_{k\omega 2} = 0.4403$	$a_{k\omega} = 0.31$
$\beta k\omega 1 = 0.075$	$\beta_{k\omega 2} = 0.0828$	$\beta^* = 0.09$
$\sigma_{k1} = 0.85034$	$\sigma_{k2} = 1$	
$\sigma_{\omega 1} = 0.5$	$\sigma_{\omega 2} = 0.85616$	

B.2 Solving the RANS equations

Solving the RANS equations when departing from very simple geometries requires some form of discretisation of the fluid domain. Most commercial codes today use a Finite Volume (FV) method to achieve this (Tu et al., 2008). In a finite volume approach, the domain is split into a number of finite volume elements (cells.) The network of interconnected cells making up the domain is usually referred to as the mesh or the grid. The field variables (u_i and p etc.) are assumed to be constant in each cell and defined discretely in the cell centroid. This is known as a collocated grid. As an alternative, the vector variables (velocity) could be defined at the cell faces which is known as a staggered grid approach. Here, a collocated grid is used. To allow a numerical scheme to be applied to solve Eqn. B.5 and all the other governing equations, the derivatives must be estimated using algebraic representations.

B.2.1 First order spatial derivatives

Firstly, it is seen that if the volume of the cell is decreased, the integral value of the derivative will approach the discrete centroid value since

$$\frac{\partial \Phi}{\partial x_i} = \lim_{\Delta V \to 0} \left(\frac{1}{\Delta V} \int_V \frac{\partial \Phi}{\partial x_i} dV \right) \tag{B.22}$$

where Φ is a transport variable. In real applications $\Delta V > 0$ so an approximation has to be made to say that

$$\frac{\partial \Phi}{\partial x_i} \approx \frac{1}{\Delta V} \int_V \frac{\partial \Phi}{\partial x_i} dV \tag{B.23}$$

This means that Eqn. B.23 will be less accurate the more the actual value of $\frac{\partial \Phi}{\partial x_i}$ varies within the control volume. A large cell covering an area of a quickly changing gradient will thus produce inaccurate results. Since Eqn. B.23 is a basic assumption of the FV method, the relation between the variation in gradient and the local cell size must

be seen as a major factor influencing the results. This will have implications for the generation of the mesh which is discussed in this thesis.

From Eqn. B.23, the derivative can be estimated by applying Gauss' divergence theorem to relate it to the flux through the boundary of each cell as

$$\frac{1}{\Delta V}\int_V \frac{\partial \Phi}{\partial x_i} dV = \frac{1}{\Delta V}\int_A \Phi dA_i \tag{B.24}$$

where A_i is the projected area of the cell in the x_i-direction and A is the surface of the cell. In an FV approach, the surface A will be divided into a number of shared faces with neighbouring cells. Again the value on these faces are said to be constant which is consistent with the approximation in Eqn. B.23. The integral over the cell boundary is approximated as

$$\frac{1}{\Delta V}\int_A \Phi dA_i \approx \frac{1}{\Delta V}\sum_{k=1}^{N_f} \Phi^k A_i^k \tag{B.25}$$

where N_f is the number of faces making up the boundary of the cell and A_i^k is the projected area of face k in the x_i-direction. To calculate the value of Φ_J^k (i.e the value of Φ on face k of cell J an interpolation scheme is needed since the values are by definition only known in the cell centres. This can be done by simply assuming a linear gradient between the cell centres sharing the face. If the mesh is uniform so that the distance from the face to the cell centres of both the neighbouring cells are equal, the value on the face is

$$\Phi_J^k = \frac{\Phi_J + \Phi_{J^k}}{2} \tag{B.26}$$

where Φ_{J^k} is value of Φ in the cell that face k of cell J is shared with. If the mesh is not uniform or a higher order interpolation is wanted, a more well developed expression is needed.

B.2.2 Second order spatial derivatives

For calculating the second order derivative $\frac{\partial^2 \Phi}{\partial x_i^2}$ the same logic is applied as for the first order derivative so that

$$\frac{\partial^2 \Phi}{\partial x_i^2} \approx \frac{1}{\Delta V}\int_V \frac{\partial^2 \Phi}{\partial x_i^2} dV \approx \sum_{k=1}^{N_f} \left(\frac{\partial \Phi}{\partial x_i}\right)^k A_i^k \tag{B.27}$$

This means that the derivative of Φ on the face k, $\left(\frac{\partial \Phi}{\partial x_i}\right)^k$ must be calculated. Again, this can be done by assuming that there is a linear variation of the gradient between the cell centres so that

$$\left(\frac{\partial \Phi}{\partial x_i}\right)^k = \frac{\Phi_{J^k} - \Phi_J}{\Delta x_i} \tag{B.28}$$

where Δx_i is the distance between the centres of cell J and cell J^k in the x_i direction.

B.2.3 Upwind schemes

Since the velocity u_i is one of the field variables to be resolved in the RANS equations, and because this is directional, the local flow direction has a big influence on the interpolation.

The estimated derivatives in a cell depend on those on all of it's faces as shown in Eqns. B.25 and B.27. This is calculated from neighbouring cell values and the own value as shown in Eqns. B.26 and B.28. Considering a cell which starts to experience a flow coming in from the left, the faces on the left should see an increase in flux. However, the cell itself and the cells on the right, all being downwind of the flow front, have not yet seen an increase in the flow. Since the own value appears both in the expression for the right faces as well as the left faces, the downwind cells will prevail in the interpolation. This can create artificial blocking and divergence of the solution. Even though the influence of downwind bias is most tangible for the velocity u_i, the gradient across the face of other variables such as k may also cause the same effects and may need to be given an upwind correction.

It is therefore necessary to first determine the local flow direction, determine which direction is upwind and give cells in this direction higher weight in the interpolation. Such a scheme is known as an upwind scheme and several exist of which the third order QUICK scheme is widely used. Other methods for achieving an upwind formulation for the interpolation is to use Total Variation Diminishing (TVD) schemes (Versteeg and Malalasekera, 2007) where the weighting is done using polynomial extrapolation.

B.2.4 Solving the algebraic equations

The algebraic representation of the governing equations is a system of equations relating the values in each cell centre to those of the cells around it. This system of equations can be solved by defining it as a matrix operation. For very small matrices, the solution to the equation system can be found using e.g. Gauss elimination but for very large matrices this is not computationally efficient. The usual approach for large matrices is

to iteratively solve the equation system using the previous result as a start guess for the next iteration. When the values are no longer changing beyond a lower threshold value between iterations, convergence of the solution is found and the equation system can be considered as solved. The discrepancy found for a specific variable in each iteration when solving the algebraic equations iteratively is known as a *residual*.

Since the value in a specific cell is only related to a few neighbouring cells and is unrelated to most cells in the mesh, the matrix giving the relation between cells will be sparse. Because of this, various preconditioning methods or Algebraic Multi-Grid (AMG) (Trottenberg et al., 2001) methods can be employed to reduce the computational time for performing the matrix algebra numerically in each iteration.

B.2.5 Pressure-velocity coupling

A problem that occurs when trying to solve the RANS equations for an incompressible fluid is that there is no independent transport equation for pressure. In the momentum equations (Eqn. B.5), the velocity field is partly driven by the pressure gradient $\partial\overline{p}/\partial x_i$. The velocity field is also governed by the continuity equation Eqn. B.7. Even though the system of equations is therefore self contained (four unknowns in $u_{1,2,3}$ and p as well as four equations) the continuity equation is only a constraint on the velocity field and does not contain the pressure. Coupling of the pressure and velocity fields is therefore not straightforward since no independent check exist that the driving pressure gradient is correct.

This can be addressed by checking if the pressure field *drives* the velocity fields in a way that satisfies the continuity equation. The SIMPLE scheme proposed by Patankar and Spalding (1972) achieves this by using a guessed pressure field to solve the momentum equations. The scheme then assumes that the resulting discrepancy from the continuity equation (*mass residual*) is due to a discrepancy in pressure which can be corrected accordingly. The velocities are then changed to correct for the new pressure gradients. This creates a coupling between the pressure and velocity fields by sequentially changing them to reduce the mass residual. The number of iterations where the pressure is corrected to reduce the mass residual is usually referred to as the number of inner corrector steps. The number of times the pressure field is recycled to produce a better start guess for the momentum equations is known as the number of outer corrector steps. When the pressure and velocity fields are considered to be converged, they can be used to apply a chosen turbulence model.

The PISO scheme (Issa, 1986) is an extension of the SIMPLE scheme with further corrections for the pressure to enhance the convergence. The criteria for the residuals and the desired level of convergence are set by the user to ensure a good trade-off between the number of iterations and the computational time.

B.2.6 Time marching

The process is not only iterated to ensure that the residuals are minimised, the convergence of the fields themselves must also be checked. The RANS equations represent an unsteady process since they contain the temporal derivative of the velocity field $\frac{\partial \overline{u_i}}{\partial t}$. An appropriate scheme must therefore be found to advance the solution in time. This is done in an outer time loop within which the inner process for finding convergence of the residuals must be performed in each step. For a case where a steady equilibrium can be found (such as when finding the calm water resistance of a ship) $\frac{\partial \overline{u_i}}{\partial t}$ is said to be zero and the outer loop is maintained until the field variables have reached steady values. Maintaining the temporally unsteady term in the equations is usually referred to as Unsteady RANS (URANS.)

For a steady average solution, the time step is less important since the flow situation at intermediate time steps are only important to maintain stability. For an unsteady process where time history of the flow is important, more attention has to be paid to the way time is advanced in the solver.

Furthermore, for the time derivatives to be accurately represented, the flow cannot skip through several cells in one timestep hence

$$\Delta x_i \geqslant u_i \Delta t \tag{B.29}$$

where Δt is the time step. This condition can be expressed as a condition on the constant C, called the Courant number as

$$C = \frac{u_i \Delta t}{\Delta x_i} \leqslant C_{max} \tag{B.30}$$

where $C_{max} = 1$ would satisfy Eqn. B.29.

References

Aalbers, A. and van Gent, W. (1984), Unsteady Wake Velocities due to Waves and Motions Measured on a Ship Model in Head Waves, *in* 'Proceedings of the 15th Symposium on Naval Hydrodynamics, Hamburg'.

Abell, W. (1918), 'Problems of the Future in the Design and Construction of Merchant Ships', *Transactions of the Institution of Naval Architects* .

Abels, W. (2013), Calculation of unsteady inflow conditions for ruder vibration analyses, *in* 'Proceedings of the PRADS2013, Changwon City, Korea'.

Andersson, B., Andersson, R., Håkansson, L., Mortensen, M., Sudiyo, R. and van Wachem, B. (2012), *Computational Fluid Dynamics for Engineers*, Cambridge University Press.

Anon. (2011), 'DNV and Oshima present ECO-Ship 2020 bulk carrier concept', *Sustainable Shipping News, 27 May* .

Bazari, Z. and Longva, T. (2011), Assessment of IMO mandated energy efficiency measures for international shipping, Technical report. IMO, Marine Environment Protection Committe 63/INF. 2 Annex.

Behroozi, F. (2004), 'Fluid viscosity and the attenuation of surface waves: a derivation based on conservation of energy', *European Journal of Physics* **25**, 115–122.

Benini (2004), 'Significance ofblade element theory in performance prediction of marine propellers', *Ocean Engineering* **31**, 957–974.

Bennett, S., Brooks, C., Windén, B., Taunton, D., Forrester, A., Turnock, S. and Hudson, D. (2014), 'Measurement of ship Hydroelastic Response using Multiple Wireless Sensor Nodes', *Ocean Engineering* **79**.

Bennett, S., Windén, B., Brooks, C., Turnock, S. and Hudson, D. (2012), High speed video analysis of freak wave-ship model encounters, *in* 'Proceedings of International Conference on Violent Flows, Nantes, France, September 25-27'.

Bennett, S., Windén, B., Brooks, C., Turnock, S., Hudson, D., Forrester, A. and Taunton, D. (2012), A Wireless sensor network for measuring ship responses in abnormal waves, *in* 'Proceedings of 29th Symposium on Naval Hydrodynamics, Gothenburg, Sweden, 26-31 August'.

Bernitsas, M., Ray, D. and Kinley, P. (1981), Kt, kq and efficiency curves for the Wageningen B-series propellers, Technical report. Department of Naval Architecture and Marine Engineering College, The University of Michigan, Ann Arbor.

Beukelman, W. (1983), Vertical Motions and Added Resistance of a Rectangular and Triangular Cylinder in Waves, Technical report. DUT, SHL Report No. 594.

Bhushan, S., Xing, T., Carrica, P. and Stern, F. (2007), Model- and Full-Scale URANS/DES Simulations for Athena R/V Resistance, Powering, and Motions, *in* '9th International Conference on Numerical Ship Hydrodynamics, Ann Arbor, Michigan, 5-8 August 2007'.

Bingjie, G., Steen, S. and Deng, G. (2012), 'Seakeeping prediction of KVLCC2 in head waves with RANS', *Applied Ocean Research* **35**, 56–67.

Blok, J. (1987), A Research Note on the Added Resistance due to Waves, *in* 'Proceedings of the International Towing Tank Conference', p. 256.

Boese, P. (1970), 'Eine einfache Methode zur Berechnung der Widerstandserhöhung eines Schiffes im Seegang', *Journal Schiffstechnik* **17 (86)**.

Boussinesq, J. (1877), 'Essai sur la theorie des aux courantes', *Memoires presentes par divers savantas a l'academie des Sciences* **23**(1), 1–680.

Bulten, N. and Nijland, M. (2011), On the Development of a Full-Scale Numerical Towing Tank Reynolds Scaling Effects on Ducted Propellers and Wakefields, *in* 'Second International Symposium on Marine Propulsors, Hamburg, Germany, June 2011'.

Burrill, L. (1944), 'Calculation of marine propeller performance characteristics', *Transactions of NECIES* **60**.

Carlton, J. (2007), *Marine Propellers and Propulsion*, second edn, Elsevier.

Carlton, J. (2012), *Marine Propellers and Propulsion*, third edn, Elsevier.

Carrica, P., Castro, A. and Stern, F. (2010), 'Self-propulsion computations using speed controller and discretized propeller with dynamic overset grids', *Journal of Marine Science and Technology* **15**.

Carrica, P., Ismail, F., Hyman, M., Bhushan, S. and Stern, F. (2013), 'Turn and zigzag maneuvers of a surface combatant using a URANS approach with dynamic overset grids', *Journal of Marine Science and Technology* **18**(2), 166–181.

Carson, I. (2012), 'Slow steaming uphill', *The Economist, August 1st 2012* .
URL: *www.economist.com/node/21559869*

Castro, A., Carrica, P. and Stern, F. (2011), 'Full scale self-propulsion computations using discretized propeller for the KRISO container ship KCS', *Computers & Fluids* **51**(1).

Choi, J. and Kinnas, S. (2000), An Unsteady Three-Dimensional Euler Solver Coupled with a Cavitating Propeller Analysis Method, *in* 'Proceedings of the 23rd Symposium on Naval Hydrodynamics, Val de Reuil, France, September', p. 616.

Coleman, H. and Steele, W. (1999), *Experimentation and uncertainty analysis for Engineers*, second edn, Wiley-interscience, New York.

Comstock, J. (1967), *Principles of naval architecture*, Society of Naval Architects and Marine Engineers.

Crossland, P., Wilson, P. A. and Bradburn, J. (1992), The Free Decay of Coupled Heave and Pitch Motions of a Model Frigate, Technical report. Defence Research Agency, TM(AWMH)92340.

Denchfield, S. (2011), An Investigation of the Influence of Rogue Waves on a Travelling Ship, Phd thesis, The University of Southampton.

Denchfield, S., Windén, B., Brooks, C., Turnock, S., Hudson, D., Forrester, A. and Taunton, D. (2011), Wireless sensor network for determining boat motions and hydroelastic responses, *in* 'The Second International Conference on Advanced Model Measurement Technology for EU Maritime Industry', pp. 126–139.

Dugan, J. (1969), 'Viscous Drag of Bodies Moving near a Free Surface', *Physics of Fluids* **12**(1).

Eckhardt, M. and Morgan, W. (1955), 'A Propeller Design Method', *Transactions of SNAME* **63**, 325–374.

Faltinsen, O. (1983), 'Bow Flow and Added Resistance of Slender Ships at High Froude Number and Low Wave Lengths', *JSR* **27 , 3**.

Faltinsen, O. and Løken, A. (1979), 'Slow drift oscillations of a ship in irregular waves', *Applied Ocean Research* **1 , no. 1**.

Faltinsen, O., Minsås, K., Liapis, N. and Skjørdal, S. (1980), Prediction of Resistance and Propulsion of a Ship in a Seaway, *in* 'Proceedings of the 13th Symposium of Naval Hydrodynamics'.

FORCE (2013), Experimental data for appended KCS hull in deep water, Technical report. Data gathered by FORCE Technology for the SIMMAN2014 workshop on ship manouvering.
URL: *http://www.simman2014.dk*

Froude, W. (1861), 'On the rolling of ships', *Transactions of Institution of Naval Architects* **2**, 180.

Fu, H., Michael, T. and Carrica, P. (2010), A method to perform self-propulsion computations with a simplified body-force propeller model, *in* 'Proceedings of the 2010 CFD Worksop in Gothenburg'.

Fujii, H. and Takahashi, T. (1975), 'Experimental study on the resistance increase of a ship in regular oblique waves', *JSNA* **137**.

Gao, Q., Jin, W. and Vassalos, D. (2012), 'The Calculations of Propeller Induced Velocity by RANS and Momentum Theory', *Journal of Marine Science Applications* **11**.

Gerritsma, J. and Beukelman, W. (1967), Analysis of a Modified Strip Theory for the Calculation of Ship Motions and Wave Bending Moments, Technical report. Netherlands Ship Research Center, Report no. 96s.

Gerritsma, J. and Beukelman, W. (1972), 'Analysis of the Resistance Increase in Waves of a Fast Cargo Ship', *International Shipbuilding Progress* **19, no. 20**.

Gerritsma, J. and Journée, J. (1978), Unnamed Entry, *in* 'Proceedings of the International Towing Tank Conference pt.2', p. 70.

Gerritsma, J., Van der Bosh, J. and Beukelman, W. (1961), 'Propulsion in Regular and Irregular Waves', *International Shipbuilding Progress* **8, no. 82**, 285–293.

Godderidge, B., Turnock, S., Earl, C. and Tan, M. (2009), 'The effect of fluid compressibility on the simulation of sloshing impacts', *Ocean Engineering* **36**(8).

Godderidge, B., Turnock, S., Tan, M. and Earl, C. (2009), 'An investigation of multiphase CFD modelling of a lateral sloshing tank', *Computers & Fluids* **38**(2).

Goldstein, S. (1929), 'On the Vortex Theory of Screw Propellers', *Proceedings of the Royal Society of London* **123**(792), 440–465.

Haase, M., Binns, J., Thomas, G. and Bose, N. (2012), Resistance Prediction of Medium-speed Catamarans Using Free-surface Viscous Flow Simulations, *in* 'Proceedings of the 15th Numerical Towing Tank Symposium, 7-9 October, Cortona, Italy'.

Hänninen, S., Mikkola, T. and Matusiak, J. (2012), 'On the numerical accuracy of the wave load distribution on a ship advancing in short and steep waves', *Journal of Marine Science and Technology* **17**(2).

Hänninen, S., Mikkola, T. and Matusiak, J. (2014), 'Computational and experimental study on local ship loads in short and steep waves', *Journal of Marine Science and Technology* **19**(1).

Hanoka, T. (1957), Theoretical Investigation Concerning Ship Motion in Regular Waves, *in* 'Proceedings of the Symposium on the Behaviour of Ships in a Seaway', pp. 266–285.

Hanoka, T. (1963), 'Researches on Seakeeping Qualities of Ships in Japan - Chapter 5 - Resistance in Waves', *The Society of Naval Architects of Japan, 60th Anniversary Series* **8**.

Haskind, M. (1946*a*), 'The Hydrodynamic Theory of Ship Oscillations in Rolling and Pitching', *Prikladnaya Matematika i Mechanika* **10**, 33–66.

Haskind, M. (1946*b*), 'The oscillation of a ship in still water', *Izv. Akad. Nauk SSSR. Otd. Tekhn. Nauk 1946, 23* .

Haskind, M. (1946*c*), 'Waves arising from oscillation of bodies in shallow water', *Prikladnaya Matematika i Mechanika* **10**, 475–480.

Haskind, M. (1953), 'Two Papers on the Hydrodynamic Theory of Heaving and Pitching of a Ship', *S.N.A.M.E. Technical and Research Bulletin, 1-12* .

Havelock, T. (1937), 'The resistance of a ship among waves', *Proceedings of the Royal Society* **161**, 299–308.

Havelock, T. (1940), 'The Pressure of Water Waves upon a Fixed Obstacle', *Proceedings of the Royal Society* **175**, 409–421.

Havelock, T. (1942), 'The drifting force of a ship among waves', *Philosophical Magazine* **33**, 467–475.

Hill, J. (1949), 'The Design of Propellers', *Transactions of SNAME* **57**.

Hino, T. (2005), CFD Workshop Tokyo 2005, Technical report. National Maritime Research Institute, Japan.

Hirota, K., Matsumoto, K., Takagishi, K., Yamasaki, K., Orihara, H. and Yoshida, H. (2005), Development of bow shape to reduce the added resistance due to waves and verification of full scale measurement, *in* 'Proceedings of the International Conference on Marine Research and Transportation', pp. 63–70.

Hosoda, R. (1973), 'The Added Resistance of Ships in Regular Waves', *JSNA* **133**.

Hosoda, R. (1974), 'The Added Resistance of Ships in Regular Oblique Waves', *Selected Papers from the Journal of theSociety of Naval Architects of Japan* **12**.

Huh, K., Golay, M. and Manno, V. (1986), 'A Method for Reduction of Numerical Diffusion in the Donor Cell Treatment of Convection', *Journal of Computational Physics* **63**, 201–221.

IMO (2011), MARPOL Annex VI energy efficiency amendments, Technical report. Resolution MEPC.203(62).

Ismail, F., Carrica, P., Xing, T. and Stern, F. (2010), 'Evaluation of linear and nonlinear convection schemes on multidimensional non-orthogonal grids with applications to KVLCC2 tanker', *International Journal for Numerical Methods in Fluids* **64**, 850–886.

Issa, R. (1986), 'Solution of implicitly discretized fluid flow equations by operator splitting', *Journal of Computational Physics* **62**, 40–65.

ITTC (2005), Recommended Procedures and Guidelines 2005 Rev. 02 7.5-02 07-02.1, Technical report.

ITTC (2011), Recommended Procedures and Guidelines 2011 Rev. 04 7.5-02-07-02.2, Technical report.

Jacobsen, N. G., Fuhrman, D. R. and Fredsøe, J. (2012), 'A Wave Generation Toolbox for the Open-Source CFD Library: OpenFoam©', *Int. J. Numerl. Meth. Fluids* **70**(9), 1073–1088.

Jasak, H. (1996), Error Analysis and Estimation for the Finite Volume Method with Applications to Fluid Flows, PhD thesis, Imperial College, London.

John, F. (1950), 'On the motion of floating bodies', *Communications on Pure Applied Mathematics* **3**, 45–101.

Johnsson, C. (1968), On Theoretical Predictions of Characteristics and Cavitation Properties of Propellers, Technical report. Swedish State Shipbuilding Experimental Tank Publication No. 64.

Joosen, W. (1966), Added Resistance of Ships in Waves, *in* 'Proceedings of the Sixth Symposium on Naval Hydrodynamics, Washington'.

Journée, J. (1976*a*), Motions and Resistance of a Ship in Regular Following Waves, Technical report.

Journée, J. (1992), Experiments and Calculations on 4 Wigley Hull Forms in Head Waves, Technical Report May 1992. Report 0909, Delft University of Technology, Ship Hydromechanics Laboratory.

Journée, J. M. J. (1976*b*), Motions, Resistance and Propulsion of a Ship in Regular Head Waves, Technical report. DUT-SHL Report 0428.

Kashiwagi, M., Kawazoe, K. and Inada, M. (2000), 'A Study on Ship Motion and Added Resistance in Waves', *JKSNAJ* **234**, 85–94.

Kempf, G. (1937), Discussion around subject no. 6: Additions in the transition form model to ship, *in* 'Proceedings of the Internationale Tagung der Leiter der Schleppversuchsanstalten'.

Kent, J. (1922), 'Experiments on Mercantile Ship Models in Waves (First Series)', *Transactions of the Institution of Naval Architects* .

Kent, J. (1924), 'The Effect of Wind and Waves on the Propulsion of Ships', *Transactions of Institution of Naval Architects* .

Kihara, H., Naito, S. and Sueyoshi, M. (2005), 'Numerical analysis of the influence of above-water bow form on added resistance using nonlinear slender body theory', *Journal of Ship Research* **49**(3), 191–206.

Kim, H. (1987), On the Added Resistance Components of Container Ship S-175, *in* 'Proceedings of the 18th ITTC', p. 247.

Kim, K. and Kim, Y. (2010), Numerical Analysis on Added Resistance of Ships, *in* 'Proceedings of ISOPE2010'.

Kim, W., Van, D. and Kim, D. (2001), 'Measurement of flows around modern commercial ship models', *Experiments in Fluids* **31**, 567–578.

Kjellberg, M. (2011), Fully Nonlinear Unsteady Three-Dimensional Boundary Element Method for Force Predictions on a Restrained Hull in Waves, Technical report. Thesis for the Degree of Licentiate of Engineering, Chalmers University of Technology.

Kochin, N. (1937), On the wave resistance and lift of bodies submerged in a fluid, *in* 'Proceedings of the Conference On the Wave Resistance Theory, Moscow, TsAGI', pp. 65–134.

Kochin, N. (1940), 'The theory of waves generated by oscillations of a body under the free surface of a heavy incompressible fluid', *Transactions of Moscow State University* **46**.

Kornev, N. V., Taranov, A., Shchukin, E. and Kleinsorge, L. (2011), 'Development of hybrid URANS-LES methods for flow simulation in the ship stern area', *Ocean Engineering* **38**(16), 1831–1838.

Kreitner, H. (1939), 'Heave, Pitch, and Resistance of Ships In A Seaway', *Transactions of the Institution of Naval Architects* .

Krylov, A. (1896), 'A new theory of the pitching motion of ships on waves and of the stresses produced by this motion', *Transactions of the Institution of Naval Architects* **37**, 326–359.

Krylov, A. (1898), 'A general theory of the oscillations of a ship on waves', *Transactions of the Institution of Naval Architects* **40**, 135–190.

Lagally, M. (1922), 'Berechnung der Kräfte und Momente die strömende Flussigkeiten auf ihre Begrenzung ausüben', *Zeitschrift für Angewandte Mathematik und Mechanik* **2**, 409.

Landweber, L. and Patel, V. (1979), 'Ship Boundary Layers', *Annual Review of Fluid Mechanics* **11**, 173–205.

Larsson, L., Regnström, B., Broberg, L., Li, D. and Janson, C. (1998), Failures, fantasies and feats in the theoretical/numerical prediction of ship performance, *in* '22nd Symp. Naval Hydrodynamics, Washington D.C., U.S.A.'.

Larsson, L., Stern, F. and Bertram, V. (2003), 'Benchmarking of computational fluid dynamics for ship flows: the Gothenburg 2000 workshop', *Journal of Ship Research* **47**(1), 63–81.

Larsson, L., Stern, F. and Visonneau, M. (2010), Gothenburg 2010, A Workshop on Numerical Ship Hydrodynamics, Technical report. Chalmers University of Technology.

Larsson, L., Stern, F. and Visonneau, M. (2014), *Numerical Ship Hydrodynamics - An assessment of the Gothenburg 2010 Workshop*, Springer.

Launder, B. and Sharma, B. (1974), 'Application of the Energy Dissipation Model of Turbulence to the Calculation of Flow Near a Spinning Disc', *Letters in Heat and Mass Transfer* **1**(2), 131–138.

Lewis, E., Cummins, W., Goodrich, G., Grim, O., Kaw, S., Lofft, R., Swaan, W. and Vosnezsensky, A. (1963), Report of the Seakeeping Committee, *in* 'Proceedings of the 10th International Towing Tank Conference', p. 178.

Lewis, F. (1929), 'The inertia of water surrounding a vibrating ship', *Transactions of the Society of Naval Architects and Marine Engineers* **37**, 1–20.

Lewthwaite, J., Molland, A. and Thomas, K. (1985), 'An Investigation into the Variation of Ship Skin Frictional Resistance with Fouling', *Transactions of the Royal Institution of Naval Architects* **127**.

Lipnikov, K. and Shashkov, M. (2006), 'The Error-Minimization Based Strategy for Moving Mesh Methods', *Communications in Computational Physics* **1**(1), 53–80.

Lloyd, A. (1998), *Seakeeping, Ship Behaviour in Rough Weather*, Ellis Horwood, Chichester, United Kingdom.

Loukakis, T. and Sclavounos, P. (1978), 'Some Extensions of the Classical Approach to Strip Theory of Ship Motions, including the Calculation of Mean Added Forces and Moments', *JSR* **22 , 1**.

Lübke, L. (2005), Numerical simulation of the flow around the propelled KCS, *in* 'Proceedings of the 2005 CFD Worksop in Tokyo'.

Maruo, H. (1957), 'The Excess Resistance of a Ship in Rough Seas', *International Shipbuilding Progress* **4, no 35**.

Maruo, H. (1960*a*), 'The drift of a body floating on waves', *Journal of Ship Research* **4, 3rd ed.**

Maruo, H. (1960*b*), 'Wave Resistance of a Ship in Regular Head Seas', *Bulletin of the Faculty of Engineering, Yokohama National University* **9**.

Maruo, H. (1963), 'Resistance in Waves', *Society of Naval Architects Journal* **8**.

Maruo, H. and Ishii, T. (1976), 'Calculation of Added Resistance in Head Sea Waves by Means of a Simplified Formula', *JSNA* **140**.

Masuya, T. (2009), Calculation of the Resistance Increase in Waves Taken Into Account the Effects of the Above Waterline Hull Form, *in* 'Proceedings of Methods for the Development and Evaluation of Maritime Technologies 2009, Nara Japan', pp. 131–152.

Matsumoto, K., Naito, S., Takagi, K., Hirota, K. and Takagishi, K. (1998), BEAK-BOW to Reduce the Wave Added Resistance at Sea, *in* 'Proceedings of PRADS', pp. 521–526.

Mencinger, J. and Žun, I. (2007), 'On the finite volume discretization of discontinuous body force field on collocated grid: Application to VOF method', *Journal of Computational Physics* **221**(2).

Menter, F. (1993), Zonal Two Equation k-w Turbulence Models for Aerodynamic Flows, *in* '24th Fluid Dynamics Conference, July 1993'.

Menter, F. (1994), 'Two-equation eddy-viscosity turbulence models for engineering applications', *AIAA Journal* **32**(8), 269–289.

Menter, F., Kuntz, M. and Langtry, R. (2003), Ten Years of Industrial Experience with the SST Turbulence Model, *in* 'Proceedings of the 4th International Symposium on Turbulence, Heat and Mass Transfer', pp. 625–632.

Michell, J. H. (1898), 'Wave Resistance of a Ship', *Philosophical Magazine* **45**, 113.

Molland, A., Turnock, S. and Hudson, D. (2011), *Ship Resistance and Propulsion: Practical Estimation of Ship Propulsive Power*, Cambridge University Press.

Moor, D. and Murdey, D. (1968), 'Motions and Propulsion of Single Screw Models in Head Seas', *Transactions of the Royal Institution of Naval Architects* **110, no. 4**.

Moor, D. and Murdey, D. (1970), 'Motions and Propulsion of Single Screw Models in Head Seas, part II', *Transactions of the Royal Institution of Naval Architects* **112, no. 2**.

Muscari, R. and Di Mascio, A. (2011), Numerical simulation of the flow past a rotating propeller behind a hull, *in* 'Second International Symposium on Marine Propulsors, Hamburg, Germany'.

Naito, S. and Kihara, H. (1993), 'Mutual Relation between Record Length and Accuracy of Measuring Data in Irregular Waves', *SNAJ* **174**.

Naito, S., Kodan, N., Takagi, K. and Matsumoto, K. (1996), 'An Experimental Study on the Above-Water Bow Shape with a Small Added Resistance in Waves', *JKSNAJ* **226**, 91–98.

Naito, S., Nakamura, S. and Nisiguchi, A. (1985), 'Added Resistance in Short Length Waves on Ships With Blunt Bows', *JKSNA* **197**.

Naito, S., Nakamura, S. and Nisiguchi, A. (1987*a*), Added resistance in regular head waves of a ship with blunt bow, *in* 'Proceedings of PRADS'.

Naito, S., Nakamura, S. and Nisiguchi, A. (1987*b*), Added resistance in regular head waves of a ship with blunt bow, *in* 'Proceedings of PRADS', number pp. 291-301.

Naito, S. and Takagishi, K. (1995), Practical Formula of Added Resistance in Short Crested Irregular Wave and Bow Form, *in* 'Proceedings of PRADS', pp. 1382–1393.

Naito, S. and Takagishi, K. (1996), 'Research on Added Resistance in Short Crested Irregular Waves and Bow Form of Water Line', *KSNAJ* **225**, 157–167.

Naito, S. and Ueda, T. (1992), 'Relation Between Bow Form and Added Resistance in Short Waves', *JKSNAJ* **217**, 103–113.

Nakamura, S., Hosoda, R., Naito, S. and Inoue, M. (1975), 'Propulsive performance of a container ship in waves (4th Report)', *Journal of the Kansai Society of Naval Architects* **159**.

Nakamura, S. and Naito, S. (1977), 'Propulsive performance of a container ship in waves', *Journal of the Society of Naval Architects of Japan* .

Nakamura, S. and Naito, S. (1981), Involuntary and Voluntary Speed Loss, *in* 'Proceedings of the International Towing Tank Conference'.

Nakamura, S., Naito, S. and Inoue, R. (1975), 'Open-water characteristics and load fluctuations of a propeller in waves', *Journal of the Kansai Society of Naval Architects* **159**.

Nakamura, S., Naito, S., Matsumoto, K., Susukida, K. and Nisiguchi, A. (1983), 'Experimental Study on Resistance Increase of a Ship With Blunt Bow in Regular Head Waves', *Journal of the Kansai Society of Naval Architects* **190**, 73–81.

Nakatake, K. (1976), Free Surface Effect on Propeller Thrust, *in* 'International Seminar On Wave Resistance'.

Navier, C. (1823), 'Mémoire sur les lois du mouvement des fluides', *Mém. Acad. R. Sci. Paris* **6**, 389–416.

Newman, J. (1974), Second Order Slowly Varying Forces on Vessels in Irregular Waves, *in* 'International Symposium on the Dynamics of Marine Vehicles and Structures in Waves, London'.

Ogiwara, S. and Yamashita, S. (1996), 'On Resistance Increase in Waves of Short Wavelength', *JKSNAJ* **225**, 37–46.

Ohkusu, M. (1980), Added Resistance in Waves in the Light of Unsteady Wave Pattern Analysis, *in* 'Proceedings of the 13th Naval Hydrodynamics Conference', pp. 413–426.

Ohkusu, M. (1984), Added resistance in waves of hull forms with blunt bow, *in* 'Proceedings of the 15th ONR, Hamburg', pp. pp. 135–148.

Ohkusu, M. (1986), 'Added resistance of blunt bow ships in very short waves', *JKSNAJ* **No. 202**, 39–42.

Ohkusu, M. (1998), Radiation and Diffraction Waves of a Ship at Forward Speed, *in* 'Proceedings of the 21st Symposium on Naval Hydrodynamics', pp. 29–44.

OpenCFD and The OpenFOAM Foundation (2010), 'OpenFOAM (Open source Field Operation And Manipulation) Version 1.7.1'.
URL: *www.openfoam.org/archive/1.7.1/download/*

Patankar, S. and Spalding, D. (1972), 'A calculation procedure for heat, mass and momentum transfer in three-dimensional parabolic flows', *International Journal of Heat and Mass Transfer* **15**, 1787.

Payne, M. (1934), Ship Performance in Relation to Tank Results, *in* 'Proceedings of the Seventy-Fifth Session and International Conference on Experiment Tank Work'.

Pearce, M., Thomas, T. and Hudson, D. (2012), Using SPHysics to simulate a Wigley hull in head waves, *in* '7th International Smoothed Particle Hydrodynamics European Research Interest Community (SPHERIC) Workshop'.

Phillips, A., Turnock, S. and Furlong, M. (2008), Comparisons of CFD Simulations and In-service Data for the Self Propelled Performance of an Autonomous Underwater Vehicle, *in* 'Proceedings of 27th Symposium on Naval Hydrodynamics, Seoul, Korea 5-10 October'.

Phillips, A., Turnock, S. and Furlong, M. (2009), 'Evaluation of manoeuvring coefficients of a self-propelled ship using a blade element momentum propeller model coupled to a Reynolds averaged Navier Stokes flow solver.', *Ocean Engineering* **36**(15-16), 1217–1225.

Pierson, W. and St. Denis, M. (1953), 'On the Motion of Ships in Confused Seas', *Transactions of the Society of Naval Architects and Marine Engineers* **61**, 280–357.

Poisson, S. (1831), 'Mémoire sur les équations générales de léquilibre et du mouvement des corps solides élastiques et des fluides', *Journal de lEcole Polytechnique de Paris* **13**, 139–416.

Prpić-Oršić, J. and Faltinsen, O. (2012), 'Estimation of ship speed loss and associated CO_2 emissions in a seaway', *Ocean Engineering* **44**, 1–10.

Réthoré, R. and Sørensen, N. (2008), Actuator disc model using a modified Rhie-Chow/SIMPLE pressure correction algorithm. Comparison with analytical solutions, *in* 'Proceedings of the European Wind Energy Conference and Exhibition, Brussels'.

Rhee, S. and Stern, F. (2001), 'Unsteady RANS method for surface ship boundary layer and wake and wave field', *Int. J. Numerl. Meth. Fluids* **37**, 445–478.

Rhie, C. and Chow, W. (1983), 'Numerical study of the turbulent fow past an airfoil with trailing edge separation', *AIAA Journal* **21**.

Roe, P. (1986), 'Characteristic-based schemes for the Euler equations', *Annual Review of Fluid Mechanics* **18**, 337–365.

Rood, E. (1996), Validation strategy for RANS Computational ship hydrodynamics, *in* 'Proceedings of the 2nd International. Conference on Hydrodynamics, Hong Kong,', p. 6 p.

Saint-Venant, J. (1843), 'Note a joindre au mémoire sur le dynamique de fluides', *Comptes Rendu de lAcademie des Sciences Paris* **17**, 1240–1243.

Salim, S. and Cheah, S. (2009), Wall y^+ Strategy for Dealing with Wall-bounded Turbulent Flows, *in* 'Proceedings of the International MultiConference of Engineers and Computer Scientist 2009 (IMECS2009) Vol II, March 18-20,Hong Kong'.

Seo, M., Park, D., Yang, K. and Kim, Y. (2013), 'Comparative study on computation of ship added resistance in waves', *Ocean Engineering* **73**.

Seol, D., Seo, J. and Rhee, S. (2013), 'Towed underwater PIV measurement for free surface effects on turbulent wake of a surface-piercing body', *Int. J. Naval Archit. Ocean Eng.* **5**, 404–413.

Sharma, R., Kim, T., Storch, R., Hopman, H. and Erikstad, S. (2012), 'Challenges in computer applications for ship and floating structure design and analysis', *Computer-Aided Design* **44**(3), 166–185.

Shibata, K., Ikogo, Y. and Ohtakagi, Y. (1983), A Study of Tanker Design with Whaleback Shaped Bow for Energy Saving in Rough Seas, *in* 'Proceedings of PRADS'.

Shirani, E., Jafari, A. and Ashgriz, N. (2006), 'Turbulence Models for Flows with Free Surfaces and Interfaces', *AIAA Journal* **44**(7).

Sibul, O. (1966), An Experimental Study of Ship Resistance and Motions in Waves A test for Linear Superposition, Technical report. The University of California, Berkeley, College of Engineering Report NA-66-3.

Simonssen, C. and Stern, F. (2005), 'RANS Maneuvering Simulation of Esso Osaka With Rudder and a Body-Force Propeller', *Journal of Ship Research* **49**(2).

Söding, H., Shigunov, V., Schellin, T. and el Moctar, O. (2014), 'A Rankine Panel Method for Added Resistance of Ships in Waves', *Journal of Offshore Mechanics and Arctic Engineering* p. Accepted Manuscript.

Spalart, P., Jou, W., Strelets, M. and Allmaras, S. (1997), Comments on the feasibility of LES for wings and on a hybrid RANS/LES approach, *in* 'Proceedings of the first AFOSR International conference on DNS/LES, 4th-8th August, Ruston'.

Steen, S. and Faltinsen, O. (1998), Added resistance of a ship moving in small sea states, *in* 'Proceedings of the Seventh International Symposium on Practical Design of Ships and Mobile Units', pp. 521–526.

Stern, F., Hwang, W. and Jaw, S. (1987), Effects of waves on the boundary layer of a surface-piercing flat plate: experiment and theory, Technical report. Iowa Institute of Hydraylic Research, Report No. 318.

Stern, F., Wilson, R. and Shao, J. (2006), 'Quantitative V&V of CFD simulations and certification of CFD codes', *International Journal for Numerical Methods in Fluids* **50**, 1335–1355.

Stern, F., Yang, J., Wang, Z., Sadat-Hosseini, H., Mousaviraad, M., Bhushan, S. and Xing, T. (2013), 'Computational ship hydrodynamics: Nowadays and way forward', *International Shipbuilding Progress* **60**.

Stokes, G. (1845), 'On the effect of the internal friction of fluids on the motion of pendulums', *Transactions of Cambridge Philosophical Society* **9 part II**, 8–106.

Strøm-Tejsen, J. and Yeh, H. Y. H. (1973), Added resistance in waves, *in* 'Trans SNAME', Vol. Vol. 81, p. p.109.

STX Europe (2011), 'STX Europe Brochure - Sustainable design for all weather conditions'.
URL: *www.tu.no*

SVA (2008), Propeller Open Water Data for Stockpropeller VP1193, Technical report. Schiffbau-Versuchsanstalt Potsdam, available as benchmark data for the SIMMAN2014 workshop.
URL: *www.simman2014.dk*

Sweby, P. (1984), 'High resolution schemes using flux limiters for hyperbolic conservation laws', *SIAM Journal on Numerical Analysis* **21**, 995–1011.

Tachmindij, A. and Milan, A. (1957), The calculation of the Circulation for Propellers wit Finite Hub having 3, 4, 5 and 6 Blades, Technical report. DTMB Report N0. 1141.

Tahara, Y., Wilson, R., Carrica, P. and Stern, F. (2006), 'RANS simulation of a container ship using a single-phase level-set method with overset grids and the prognosis for extension to a self-propulsion simulator', *Journal of Marine Science and Technology* **11**, 209–228.

Tang, A. (1985), Propeller Performance Estimates using Blade Element-Momentum Theory, B.sc thesis, report no. ss204, University of Southampton.

Thomson, W. (Lord Kelvin). (1886), 'On stationary waves in flowing water', *Philosophical Magazine* **22**, 353.

Trottenberg, U., Oosterlee, C. W. and Schüller, A. (2001), *Multigrid*, Academic Press.

Tsukada, Y., Hinatsu, M. and Hasegawa, J. (1997), 'Measurement of unsteady ship wakes in waves', *Journal of the Kansai Society of Naval Architects* **228**.

Tu, J., Yeoh, G. and Liu, C. (2008), *Computational Fluid Dynamics, A Practical Approach*, Elsevier.

Turnock, S., Lewis, S., Philips, A., Banks, J., Windén, B., Hudson, D. and Molland, A. (2010), Evaluating the self-propulsion of a container ship in a seastate using computational fluid dynamics, *in* 'William Froude Conference: Advances in Theoretical and Applied Hydrodynamics - Past and Future', p. 12.

Turnock, S., Pashias, C. and Rogers, E. (2006), Flow feature identification for capture of propeller tip vortex evolution, *in* 'Proceedings of 26th Symposium on Naval Hydrodynamics, Rome, Italy'.

Ubbink, O. and Issa, R. (1999), 'A Method for Capturing Sharp Fluid Interfaces on Arbitrary Meshes', *Journal of Computational Physics* **153**, 26–50.

Ueno, M., Tsukada, Y. and Tanizawa, K. (2013), 'Estimation and prediction of effective inflow velocity to propeller in waves', *Journal of Marine Science and Technology* **18**(3).

Ulstein Group (2011), 'Ulstein X-bow Hull Line Design Brochure'.
URL: *www.ulsteingroup.com*

van Leer, B. (1979), 'Towards the Ultimate Conservative Difference Scheme, V. A Second Order Sequel to Godunov's Method', *Journal of Computational Physics* **32**, 101–136.

Van, S., Kim, W., Yim, G., Kim, D. and Lee, C. (1998), Experimental Investigation of the Flow Characteristics Around Practical Hull Forms, *in* 'Proceedings of the 3rd Osaka Colloquium on Advanced CFD Applications to Ship Flow and Hull Form Design, Osaka, Japan'.

van Sluijs, M. (1972), Propeller load fluctuations and performance in regular and irregular waves, Technical report. Report from Netherlands Ship Model Basin Wageningen, presented at ITTC'72 subject Seakeeping.

Vassilopoulos, L. (1967), 'The application of statistical theory of non- linear systems to ship motion performance in random seas', *International Shipbuilding Progress* **14 (150)**.

Vaz, G., Jaouen, F. and Hoekstra, M. (2009), Free surface Viscous Flow Computations. Validation of URANS Code FRESCO., *in* 'Proceedings of ASME 28th International Conference on Ocean, Offshore and Arctic Engineering OMAE2009 May 31-June 5, 2009, Honolulu, Hawaii'.

Versteeg, H. and Malalasekera, W. (2007), *An Introduction to Computational Fluid Dynamics: The Finite Volume Method*, Pearson.

Villeger, F. and Alessandrini, B. (1992), Interaction between free surface flow and boundary layer around a ship model, *in* 'Proceedings of IWWWFB07, 24-27 May, Val d Reuil, France'.

Vossers, G. (1961), Fundamentals of the Behaviour of Ships in Waves, Technical report. Netherlands Ship Model Basin, Publication No. 151a.

Wang, X. and Walters, K. (2012), 'Computational Analysis of Marine-Propeller Performance Using transition-Sensitive Turbulence Modelling', *Journal of Fluids Engineering* **134**.

Watson, D. (1998), *Practical Ship Design*, Elsevier Ocean Engineering Book Series; vol. 1.

Weymouth, G., Wilson, R. and Stern, F. (2005), 'RANS Computational Fluid Dynamics Predictions of Pitch and Heave Ship Motions in Head Sea', *Journal of Ship Research* **49**(2), 80–97.

Wilcox, D. (1988), 'Re-assessment of the scale-determining equation for advanced turbulence models', *AIAA Journal* **26**(11), 1299–1310.

Windén, B. (2014), Visualisation of the flow and force distribution around a self propelled container ship in head waves, Technical report. Dataset and report, University of Southampton.
URL: *http://eprints.soton.ac.uk/id/eprint/365546*

Windén, B., Badoe, C., Turnock, S., Phillips, A. and Hudson, D. (2013), Self propulsion in waves using a coupled RANS-BEMt model and active RPM control, *in* 'Proceedings of the 16th Numerical Towing Tank Symposium, 2-4 September, Duisburg Germany'.

Windén, B., Turnock, S. and Hudson, D. (2012), Validating Force Calculations using OpenFOAM© on a Fixed Wigley Hull in Waves, *in* 'Proceedings of the 15th Numerical Towing Tank Symposium, 7-9 October, Cortona, Italy', pp. 170–175.

Windén, B., Turnock, S. and Hudson, D. (2013*a*), A RANS modelling approach for predicting powering performance of ships in waves, *in* '12th International Symposium on Practical Design of Ships and Other Floating Structures (PRADS13), Changwon City, Korea'.

Windén, B., Turnock, S. and Hudson, D. (2013*b*), Predicting powering performance changes for ships in offshore conditions from small design modifications, *in* 'Proceedings of the 23rd International Offshore and Polar Engineering Conference (ISOPE13), June 30th - July 5th, Anchorage, Alaska'.

Windén, B., Turnock, S. and Hudson, D. (2014*a*), 'A RANS modelling approach for predicting powering performance of ships in waves', *International Journal of Naval Architecture and Ocean Engineering* **6**(2).

Windén, B., Turnock, S. and Hudson, D. (2014*b*), 'CFD Modelling of a Self Propelled Ship Using Body Force Propeller Models: A Framework for Creating Coupled Solvers', *Journal of Marine Science and Technology* (Pending submission).

Windén, B., Turnock, S. and Hudson, D. (2014*c*), 'Influence of waves on the computation of boundary layer development around surface piercing bodies', *Computers & Fluids* (Pending review).

Windén, B., Turnock, S. and Hudson, D. (2014*d*), Self propulsion modelling of the KCS container ship using an open source framework, *in* 'Proceedings of the 17th Numerical Towing Tank Symposium, Marstrand, Sweden 28-30 September'.

Wyatt, D., Fu, T., Taylor, G., Terrill, E., Xing, T., Bhushan, S., O'Shea, T. and Dommermouth, D. (2008), A comparison of full-scale experimental measurements and computational predictions of the transom-stern wave of the R/V Athena I, *in* 'Proceedings of 27th Symposium on Naval Hydrodynamics, Seoul, Korea 5-10 October'.

Xing, T., Bhushan, S. and Stern, F. (2012), 'Vortical and turbulent structures for KVLCC2 at drift angle 0, 12, and 30 degrees', *Ocean Engineering* **55**.

Xiros, N. (2002), *Robust Control of Diesel Ship Propulsion*, Springer-Verlag, London.

Yamzsaki, R. (1966), 'On the Theory of Screw Propellers in Non-uniform Flows', *Memoirs of the Faculty of Engineering, Kyushu University* **25**(2).

Zhou, Y., Yan, C. and Kang, H.-l. (2008), Numerical Dissipation Effect Analysis of Upwind Schemes, *in* '46th AIAA Aerospace Sciences Meeting and Exhibit, AIAA 2008-759'.

Zurigat, Y. and Ghajar, A. (1990), 'Comparative Study of Weighted Upwind and Second Order Upwind Difference Schemes', *Numerical Heat Transfer* **18**, 61–80.